

This electronic thesis or dissertation has been downloaded from the King's Research Portal at <https://kclpure.kcl.ac.uk/portal/>



Development of glycosyltransferase inhibitors for the glycoengineering of therapeutic antibodies

Li, Shasha

Awarding institution:
King's College London

The copyright of this thesis rests with the author and no quotation from it or information derived from it may be published without proper acknowledgement.

END USER LICENCE AGREEMENT



Unless another licence is stated on the immediately following page this work is licensed

under a Creative Commons Attribution-NonCommercial-NoDerivatives 4.0 International

licence. <https://creativecommons.org/licenses/by-nc-nd/4.0/>

You are free to copy, distribute and transmit the work

Under the following conditions:

- Attribution: You must attribute the work in the manner specified by the author (but not in any way that suggests that they endorse you or your use of the work).
- Non Commercial: You may not use this work for commercial purposes.
- No Derivative Works - You may not alter, transform, or build upon this work.

Any of these conditions can be waived if you receive permission from the author. Your fair dealings and other rights are in no way affected by the above.

Take down policy

If you believe that this document breaches copyright please contact librarypure@kcl.ac.uk providing details, and we will remove access to the work immediately and investigate your claim.



Development of glycosyltransferase inhibitors for the glycoengineering of therapeutic antibodies

A thesis submitted to the Faculty of Life Sciences & Medicine
at King's College London for the degree of Doctor of Philosophy

By

Shasha Li

St John's Institute of Dermatology,
School of Basic and Medical Biosciences
King's College London

April 2024

Supervisors: Prof. Sophia Karagiannis & Prof. Gerd Wagner

Declaration

I, Shasha Li, confirm that the work herein presented is my own. All experiments, except where acknowledged, were performed by myself.

Acknowledgement

First and foremost, I would like to sincerely thank my supervisors Prof. Gerd Wagner and Prof. Sophia Karagiannis for their invaluable support, guidance and expertise. I would also like to express my gratitude to King's College London (KCL) and the Chinese Scholarship Council (CSC) for the award of a KCL-CSC studentship. My sincere thanks also go to my thesis progress committee members, Prof. James Mason, Prof. Maria Thanou, and Prof. Katie Doores. Their valuable feedback during each progress meeting has been crucial for the advancement of my project.

The central part of this thesis concerns the chemical synthesis of a novel class of conformationally constrained nucleosides. This work was carried out at Queen's University Belfast. I am grateful to King's College London for agreeing to this arrangement, to Queen's University Belfast for hosting me as a visiting student, and to both institutions for their financial support of my doctoral research.

Moreover, I express my gratitude to Alex McCraw from the Karagiannis group for assessing the cellular activity of my compounds, in particular for IgE glycoengineering, and to Dr Daniel Spencer and Dr Richard Gardner from Ludger Ltd for glycoprofiling of some of the resulting IgE glycoforms. I extend my thanks to Prof. Ulf Ellervik and his PhD student Roberto Mastio (Lund University, Sweden) for evaluating the activity of selected inhibitors towards β 4GalT7.

At Queen's University Belfast, I want to especially thank Dr Irina Tikhonova and her PhD students Abdul-Akim Guseinov and Tianyi Ding for helping me resolve the challenges I faced with the computational simulations. I would also like to thank Dr Stephen Cochrane and his

research group for giving me access to their preparative HPLC and for providing valuable training. Additionally, my appreciation goes to Dr Peter Knipe and Dr Rich Williams and their research groups for facilitating the use of LC/MS equipment. I am also grateful to Prof. Peter Nockemann for offering guidance in single-crystal X-ray diffraction (XRD) training and for assisting with data analysis. I appreciate Dr. Gunnar Neels Schroeder for sharing the AlphaFold models of LtpM and SetA for my molecular modelling work.

I am also grateful to Dr Alice Cross for her guidance in training me in the Malachite Green assay, and to David Matthews for providing recombinant samples of LtpM and SetA, and for training me in the DSF assay. My heartfelt appreciation goes to my lab colleagues Dr Ayesha Khan, Ramya Nuti, Prachi Bendale, Ciyana James, and Catherine Webley for their consistent help whenever it was needed.

I appreciate my family for their unwavering support throughout my journey and thank my boyfriend, Xinshen Ji, for constantly being by my side. Finally, I am grateful to my friends, Qi Huang and Jun Xie, for providing companionship and preventing me from feeling lonely far away from home.

Table of Contents

Acknowledgement	3
Abstract	10
List of inhibitors	13
List of Figures	14
List of Schemes	18
List of Tables	21
Abbreviations	22
1. Introduction	27
1.1 Monoclonal antibody (mAb) glycoengineering.....	27
1.1.1 Immunoglobulins and their glycans.....	27
1.1.2 mAb glycoengineering.....	28
1.1.3 IgE glycoengineering in this project.....	29
1.2 Small molecule inhibitors for mAb glycoengineering.....	30
1.2.1 <i>N</i> -glycan biosynthesis in eukaryotes.....	30
1.2.2 Small molecule inhibitors: advantages & challenges	31
1.3 Glycosyltransferases (GTs) and GT inhibitors	32
1.3.1 Glycosyltransferases (GTs).....	32
1.3.2 Mammalian GTs: β -1,4-Galactosyltransferases (GalTs).....	36
1.3.3 Bacterial GTs: LgtC, SetA and LtpM.....	39
1.3.4 Glycosyltransferase (GT) inhibitors	41
1.4 Conformational restriction as a design strategy for a novel class of glycosyltransferase inhibitors	45
1.4.1 Conformationally restricted macrocycles	46

1.4.2	Conformationally restricted nucleosides.....	49
1.5	Aims and objectives.....	51
2.	5-substituted uridine derivatives (Target Class 1).....	55
2.1	Introduction.....	55
2.1.1	Suzuki-Miyaura coupling.....	55
2.1.2	Suzuki coupling of nucleosides	57
2.2	Objectives	59
2.3	Synthesis of 5-substituted uridine derivatives 1 – 8	60
2.4	β 4GalT1 inhibition assays and molecular modelling of 1 – 4	61
2.4.1	β 4GalT1 inhibition assays of 1 – 4	62
2.4.2	Molecular modelling of 1 – 4 with β 4GalT1	64
2.5	β 4GalT7 inhibition assays of 1 – 4	65
2.6	Cell assays of 5 – 8	68
2.6.1	Effect of uridine derivatives 5 – 8 on cell viability	68
2.6.2	Effect of uridine derivatives 5 – 8 on degranulation.....	69
2.6.3	Initial glycoanalysis of IgE glycoforms obtained in the presence of uridine derivatives 5 and 6	70
2.7	Bacterial enzymes: binding assays with 1 – 4	73
2.8	Summary and conclusions	75
3.	Conformationally restricted uridine derivatives (Target Class 2)	78
3.1	Introduction.....	78
3.1.1	Ring-Closing Metathesis (RCM).....	78
3.1.2	Macrolactonization	81
3.1.3	Heck macrocyclization.....	84
3.2	Objectives	87

3.3	Attempted formation of the macrocycle via macrolactonisation (Route A).....	88
3.3.1	Synthesis of 6-bromoindole-4-boronic acid pinacol ester 12	89
3.3.2	Synthesis of 5-(6-bromoindol-4-yl) uridine derivative 17	94
3.3.3	Heck coupling of 17 with acrylic acid	98
3.4	Formation of the macrocycle via ring-closing metathesis: attempted installation of the side chain at the indole substituent first (Route B)	99
3.4.1	Synthesis of 5-(6-vinylindol-4-yl) uridine derivative 19	100
3.4.2	Synthesis of 5'- <i>O</i> -allyl-6-yl-5-iodouridine derivative 20a	102
3.4.3	<i>N</i> -Protection of the indole substituent.....	105
3.5	Formation of the macrocycle via ring-losing metathesis: installation of the side chain at 5'-position first (Route C).....	109
3.5.1	Synthesis of disubstituted uridine derivatives 21 and 22	110
3.5.2	Ring-Closing Metathesis of 22	110
3.5.3	Synthesis of 5'- <i>O</i> -hexen-6-yl-5-iodouridine derivative 20d	111
3.5.4	Formation of the macrocycle from 20d	114
3.6	Formation of the macrocycle via intramolecular Heck reaction (Route D).....	115
3.6.1	Synthesis and characterisation of macrocycles 27 and 28	115
3.7	Synthesis of final compounds	120
3.7.1	Synthesis of macrocycle 29	121
3.7.2	Synthesis of macrocycle 30	122
3.7.3	Synthesis of macrocycle 31	123
3.7.4	Synthesis of macrocycle 32	130
3.7.5	Synthesis of macrocycle 34	131
3.7.6	Synthesis of uridine derivatives 36 – 41	132
3.8	Summary and conclusions	134

4.	Activity evaluations and molecular modelling of Class 2 target molecules.....	138
4.1	β 4GalT1 inhibition assays and molecular modelling of Class 2 target molecules	138
4.1.1	β 4GalT1 inhibition assays of 29 – 41	138
4.1.2	Molecular modelling of 29 – 37 with β 4GalT1	141
4.2	β 4GalT7 inhibition assays and molecular modelling of Class 2 target molecules	144
4.2.1	β 4GalT7 inhibition assays of 29 – 37	144
4.2.2	Molecular modelling of 29 – 37 with β 4GalT7	145
4.3	Cell assays of Class 2 target molecules	147
4.3.1	Effect of target molecules 29 – 36 on cell viability and IgE production in cell culture	147
4.3.2	Cell permeability of Class 2 target molecules	148
4.4	Bacterial enzymes: activity assays and molecular modelling with Class 2 target molecules	149
4.4.1	Binding assays of 29 – 41 with LgtC, SetA and LtpM.....	150
4.4.2	LgtC inhibition assays with 31	151
4.4.3	Molecular modelling of 31 with LgtC	151
4.5	Discussion on the selectivity of 31 for galactosyltransferases over glucosyltransferases	153
4.6	Summary and conclusions	155
5	Summary, conclusions and outlook.....	158
5.1	Overall summary and conclusions	158
5.2	Future work.....	162
6	Experimental	166
6.1	Chemical synthesis.....	166
6.1.1	Chapter 2 compounds: 1 – 8 (Class 1 inhibitors).....	167

6.1.2	Chapter 3 compounds: 9 – 43 (Class 2 inhibitors).....	175
6.2	Crystallography.....	204
6.3	Malachite-Green inhibition assays.....	206
6.4	β 4GalT7 inhibition assays	213
6.5	Cell assays.....	214
6.6	HPLC-based cell permeability assessment.....	217
6.7	Differential Scanning Fluorimetry (DSF) binding assays	218
6.8	Molecular Modelling	220
7	References.....	222
8	Appendix (^1H and ^{13}C NMR spectra).....	240

Abstract

Immunoglobulin E (IgE)-based antibodies are currently under investigation as promising novel cancer therapeutics. Structure-function studies are complicated by the structural complexity of the IgE glycoforms. The overall goal of this project was to develop glycosyltransferase inhibitors with suitable properties for the application in IgE cell culture and the generation of defined IgE glycoforms. This would provide a novel method for IgE glycoengineering, establishing a basis for structure-function relationship studies of IgE and optimizing its biological and therapeutic properties.

Many existing glycosyltransferase inhibitors are charged molecules with limited cell permeability. The Wagner research group has previously developed a novel class of uncharged galactosyltransferase inhibitors with modest activity in cells. These inhibitors are based on a uridine scaffold with an additional substituent in position 5, which is critical for inhibitor activity. Starting from this existing inhibitor class, two strategies were pursued to improve potency and cellular activity.

In the first series, alternative substituents in position 5 were investigated. Target molecules **1 – 4** were tested for inhibitory activity against two recombinant galactosyltransferases (β -1,4-galactosyltransferase 1 and β -1,4-galactosyltransferase 7) *in vitro* and, in the form of pro-drugs **5 – 8**, for IgE glycoengineering in cell cultures (Chapter 2). Based on these results, a novel class of conformationally restricted analogues with a macrocyclic linkage between the 5-substituent at the uracil base and the 5-position of the ribose was designed. For the generation of target molecules, four different synthetic routes, following three general strategies, were explored, resulting in the delivery of 12 inhibitor candidates, **29 – 41** (Chapter 3). The activity

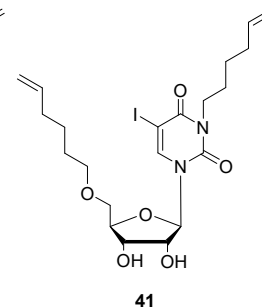
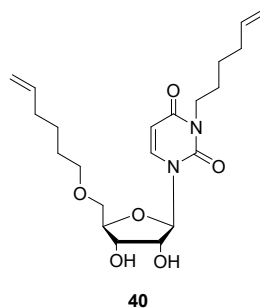
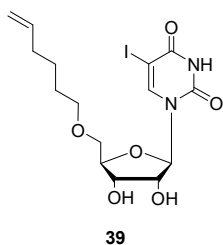
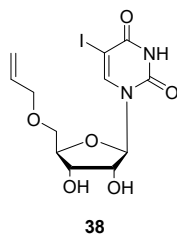
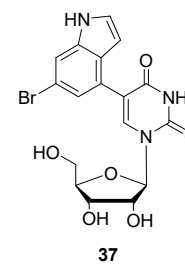
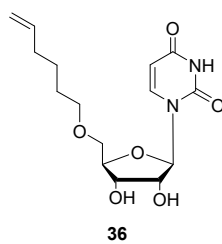
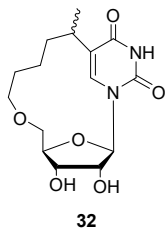
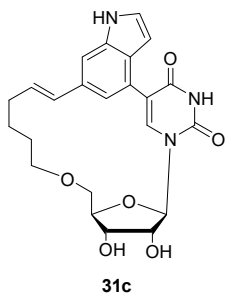
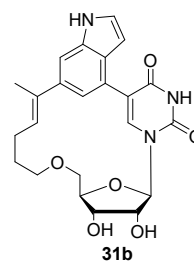
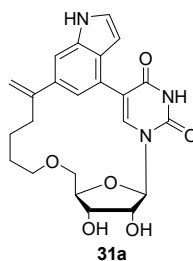
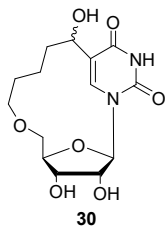
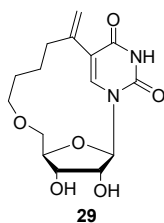
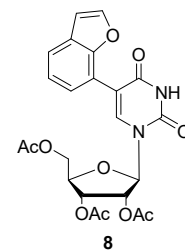
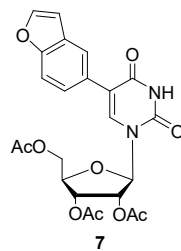
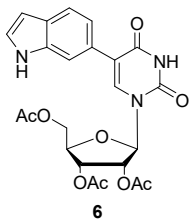
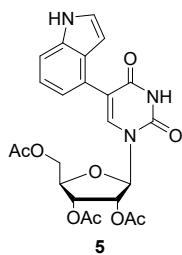
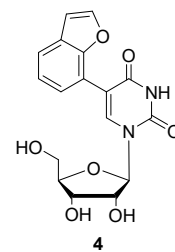
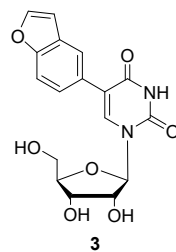
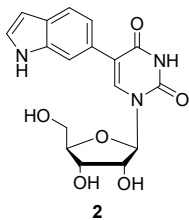
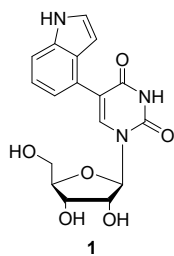
of the conformationally restricted compounds was evaluated against galactosyltransferases *in vitro* and in cell assays (Chapter 4). Molecular modelling was employed to rationalise the experimental outcomes (Chapter 2 and 4). Additionally, the novel inhibitors were investigated against three bacterial sugar-UDP-dependent glycosyltransferases (LgtC, SetA and LtpM) (Chapter 2 and 4).

Findings revealed that the conformationally restricted macrocycle **31** exhibited the most potent activity. **31** displayed 99 % inhibition of β 4GalT1 at 2 mM and 97 % inhibition of β 4GalT7 at 1 mM. In a ligand binding assay based on Differential Scanning Fluorimetry (DSF), **31** demonstrated favourable selectivity for LgtC over SetA and LtpM. Subsequent inhibition assays revealed an IC_{50} of $193 \pm 35 \mu\text{M}$ for LgtC. These suggested **31** could potentially serve as a broad range inhibitor of GalTs (β 4GalT, β 4GalT7 and LgtC) over glucosyltransferases (SetA and LtpM). Molecular dynamics (MD) simulations revealed intermolecular interactions between **31** and key residues in β 4GalT1, β 4GalT7, and LgtC that can explain the observed activities against these enzymes. Conversely, steric clashes were observed between **31** and both SetA and LtpM. These differences may provide an explanation for the experimentally observed target preference of **31**. Compared to its ring-open analogue **1**, the macrocyclic nucleoside **31** appears to exhibit increased inhibitory activity. This suggests that conformational restriction is a successful strategy for improving inhibitory activity. **31** also demonstrated a remarkable 26.0 – 31.0 % cell permeability. Overall, the aim of achieving inhibitors with optimised inhibitory activity, selectivity and cell penetration was successfully accomplished via conformational restriction.

Initial findings from IgE glycoengineering revealed a reduction of four different terminal residues on IgE glycans in the presence of the ring-open nucleoside **5**, as analysed by lectin

blots, while analogue **6** appeared to slightly increase the levels of these residues. Furthermore, there was no noticeable decrease in the prevalence of galactose or sialic acid in the tentative glycan assignment. These unexpected, and seemingly paradoxical, effects may at least in part be influenced by the relatively modest potency of these inhibitors. In contrast, the novel, conformationally restricted nucleoside inhibitors are promising candidates for IgE glycoengineering due to their enhanced inhibitory activity and promising cell permeability. Although some cytotoxicity was observed at 100 μ M for compound **31**, it still stands as a promising candidate with the potential for further structural refinement to increase its activity, thereby reducing the amount required for cellular applications. More generally, the successful evaluation of the conformational restriction strategy has opened a new pathway for designing additional analogues suitable for cellular applications.

List of inhibitors



List of Figures

Figure 1 A schematic representation of immunoglobulin E (IgE) including representative glycans at its glycosylation sites	28
Figure 2 Retaining and inverting transfer reaction catalysed by GTs.....	34
Figure 3 SN2-like mechanism for Inverting GTs	35
Figure 4 Proposed mechanism for retaining GTs	35
Figure 5 Schematic depiction of human β 4GalT proteins.	37
Figure 6 Open conformation (green) and closed conformation (purple) in β 4GalT1.....	38
Figure 7 Structure of LgtC.....	40
Figure 8 Superimposition of SetA (red) and LtpM (green)..	41
Figure 9 Representative GalT inhibitors.....	43
Figure 10 Representative inhibitors for FucT, SiaT and ManT	45
Figure 11 Conformational restriction to improve inhibitory activity, selectivity and cell permeability of existing inhibitors against β 4GalT1	45
Figure 12 Examples of macrocycles for improving binding affinity by conformational restriction	48
Figure 13 Example of macrocycle for improving cellular permeability by conformational restriction	48
Figure 14 Conformational nomenclature of natural nucleosides.	49
Figure 15 Examples of conformationally restricted nucleosides	50
Figure 16 The main project aims	51
Figure 17 Proposed catalytic cycle	56
Figure 18 The GalT reactions and the malachite green assay.....	62
Figure 19 Determination of IC ₅₀ values for 1 – 4 against β 4GalT1.....	63

Figure 20 (a) GAG biosynthesis process. (b) Galactosylation with XylNap as substrate	66
Figure 21 Galactosylation (a) and inhibition (b) of β 4GalT7 via HPLC-based fluorescent assessment.....	66
Figure 22 Activation and inhibition of galactosylation by β 4GalT7 under 1 – 4 at 1 mM. ..	67
Figure 23 Activation of galactosylation by β 4GalT7 under 2	68
Figure 24 Cell viability of 5 – 8	69
Figure 25 Degranulation results of compound 5 and 6	70
Figure 26 Initial glycan analysis performed via lectin blot.	71
Figure 27 The HPLC-FD chromatogram of HEK CSPG ₄ IgE Control	72
Figure 28 HPLC-FD chromatogram of HEK CSPG ₄ IgE-inhibitor 5	72
Figure 29 HPLC-FD chromatogram of HEK CSPG ₄ IgE-inhibitor 6	73
Figure 30 Fluorescence intensity and temperature correlation during the thermal unfolding of proteins in the presence of SYRPO Orange dye.....	74
Figure 31 Common metathesis catalysts.....	80
Figure 32 ¹³ C NMR spectra of alkenylated nucleosides	104
Figure 33 NOESY spectrum of mono-alkenylated nucleoside.....	104
Figure 34 Crystal structure of 27	116
Figure 35 Proposed isomers of compound 28 formed in cross-coupling reaction.....	117
Figure 36 ¹ H NMR of 28a and some isomers.....	117
Figure 37 ¹ H NMRs of two isomers of compound 30	123
Figure 38 Hindered rotation of compound 31	125
Figure 39 Effect of acid and temperature on the proportion of isomers of 31	127
Figure 40 The separation of 31 via analytical HPLC at 254 nm.....	128
Figure 41 ¹ H NMR characterization of the second HPLC peak of 31	128
Figure 42 ¹ H NMR characterization of the third HPLC peak of 31	129

Figure 43 Crystal structure of <i>S</i> isomer of compound 32	131
Figure 44 β 4GalT1 inhibition induced by Class 1 inhibitors and Class 2 inhibitors at single concentrations.	139
Figure 45 Activity comparison of 29 and 39 against β 4GalT1.....	140
Figure 46 Activity comparison of 31ab and 1 against β 4GalT1.....	141
Figure 47 RMSD trajectory plots of 37	142
Figure 48 31b (a) and 37 (b) showed additional interactions with β 4GalT1 in MD simulations	143
Figure 49 Activation and inhibition of galactosylation by β 4GalT7 under compounds 29 – 37 at 1 mM.....	145
Figure 50 Compounds 31a (a) and 37 (b) showed additional interactions with β 4GalT7 in MD simulations.....	146
Figure 51 Effect of Class 2 inhibitors on cell viability and IgE production in cell culture..	148
Figure 52 IC ₅₀ curve of compound 31 against LgtC.....	151
Figure 53 Inhibitor 31b showed additional interactions with R77 and H78 and robust interaction with D105 of LgtC in the MD simulations	152
Figure 54 Superposition of β 4GalT1(Pink), β 4GalT7 (light green) and LgtC (white).....	154
Figure 55 Key interactions between 31 and GalTs in MD simulations	154
Figure 56 Steric clashes are present between 31a and a conserved Trp residue (yellow) in both SetA and LtpM.....	155
Figure 57 Proposed optimisation strategies for inhibitor 31	163
Figure 58 Proposed optimisation strategies for inhibitor 29	164
Figure 59 Proposed optimisation strategies for inhibitor 37	164
Figure 60 Crystal structures of 27 and 32	205
Figure 61 IC ₅₀ values in different donor turnovers	209

Figure 62 UDP calibration curve.	210
Figure 63 Determination of IC ₅₀ values for 5-FU UDP-Gal against β 4GalT1.....	210
Figure 64 Potential inhibition of CIP by inhibitors.....	211
Figure 65 Potential donor-hydrolysis acceleration by 2 and 3	212
Figure 66 GalT activity prediction.....	213
Figure 67 Class 1 and Class 2 inhibitors with SetA in DSF assays.....	219
Figure 68 Compound 31ab with LgtC in DSF assays.	219

List of Schemes

Scheme 1 Sequential processing of the antibody glycan.....	31
Scheme 2 Designed structures of Class 1 inhibitors and Class 2 inhibitors.....	53
Scheme 3 Class 1 inhibitors with various substituents in position 5.....	59
Scheme 4 Synthesis of 5-substituted nucleosides 1 – 4 and their pro-drugs 5 – 8	61
Scheme 5 Mechanism of olefin metathesis	79
Scheme 6 Ring-closing metathesis reactions	80
Scheme 7 Macrolactonization in Peloruside A synthesis.....	81
Scheme 8 Macrolactonization in the synthesis of (+)-Cladospolide D.....	82
Scheme 9 Routes for Macrophelides lactonization	82
Scheme 10 Macrolactonization step in the synthesis of Macrophelide A.....	82
Scheme 11 Macrolactonization with Mitsunobu conditions	83
Scheme 12 Macrolactonization with MNBA reagent	83
Scheme 13 Iodo lactonization	84
Scheme 14 Macrolactonization via rhodium-catalyzed coupling	84
Scheme 15 Mechanism of Intramolecular Heck cyclization.....	85
Scheme 16 Intramolecular Heck reactions	86
Scheme 17 Conformationally restricted Class 2 inhibitors with 3 ring-forming strategies via 4 synthetic routes	87
Scheme 18 The retrosynthetic route A	89
Scheme 19 General synthesis of key reactant 12	90
Scheme 20 General synthesis of 4, 6-diboronic acid pinacol ester 15	91
Scheme 21 Synthesis of 4,7-diborylatedindole 9 and 2,4,7-triborylatedindole 10	91
Scheme 22 Synthesis of 2,4,6,7-tetraborylated indole 13	92

Scheme 23 Synthesis of 11 and 12	92
Scheme 24 Synthesis of 14 and 15	94
Scheme 25 Synthesis of 16	95
Scheme 26 Heck-coupling between 6-bromoindole and acrylic acid	98
Scheme 27 Heck-coupling between 12 and acrylic acid	98
Scheme 28 Heck-coupling between 17 and acrylic acid	99
Scheme 29 The retrosynthetic route B	100
Scheme 30 Synthesis of 19 via vinylation reaction	101
Scheme 31 Allylation of compound 19	103
Scheme 32 Allylation of 5-(<i>N</i> -Boc-6-vinylindol-4-yl) uridine derivative	106
Scheme 33 Proposed mechanism for the Boc-protection	106
Scheme 34 Benzyl protection of 6-bromoindole	107
Scheme 35 Deprotection of <i>N</i> -benzyl-6-bromoindole	107
Scheme 36 Sialylation reaction of 6-bromoindole	108
Scheme 37 Deprotection of <i>N</i> -SiMePh ₂ -6-bromoindole	108
Scheme 38 Suzuki coupling between <i>N</i> -SiMePh ₂ -6-bromoindole and 16	108
Scheme 39 Sialylation of 19	108
Scheme 40 The retrosynthetic route C	109
Scheme 41 Synthesis of 21 and 22	110
Scheme 42 RCM of compound 22	111
Scheme 43 Structures of 24 (left) and 25 (right)	114
Scheme 44 Synthesis of macrocycle starting from compound 20d	115
Scheme 45 One-pot cross-coupling reaction between compound 20d and 12	116
Scheme 46 Deprotection of compound 16 with HCl	121
Scheme 47 Deprotection of macrocycle 27 with <i>p</i> -TsOH	122

Scheme 48 Acid-catalyzed hydration of 27	122
Scheme 49 Mechanism of acid-catalyzed hydration of 27	123
Scheme 50 Deprotection of compound 28 with <i>p</i> -TsOH.	124
Scheme 51 Mechanism of electronic rearrangement from compound 31a to 31b under acidic conditions.....	124
Scheme 52 Proposed constitutional isomers of 28 and 31	126
Scheme 53 Proportions of 31a and 31b with complete addition of 4 equivalent.....	129
Scheme 54 Hydrogenation of 27 with Pt ₂ O catalyst	131
Scheme 55 Compound 34 from acetylation of 27	132
Scheme 56 Deprotection of two <i>O</i> ⁶ ,5'-cyclouridine derivatives.....	134
Scheme 57 General synthesis of Class 2 inhibitors through 4 routes.....	136

List of Tables

Table 1 Root-Mean-Square Deviation (RMSD) and IC ₅₀ of 1 – 4	65
Table 2 Melting temperature (T _m) shifts of 1 – 4 in DSF assay.....	75
Table 3 Optimization of diprotodeborylation of 10	93
Table 4 Optimization of Suzuki coupling between 16 and 12	97
Table 5 Model vinylation reaction between 6-bromoindole and vinyl boronic acid pinacol ester	101
Table 6 Allylation of compound 16	102
Table 7 Boc-protection of indole amine group of 19	105
Table 8 Model olefin metathesis reaction	111
Table 9 Competition between alkenylation and cyclization in 5'-position of 5-iodouridine	113
Table 10 Optimization of intra Heck coupling of 26	118
Table 11 Compound 27 from intramolecular Heck coupling of 20d	119
Table 12 Optimization of synthesis of 26	120
Table 13 Comparison of separation between preparative and analytical HPLC.....	127
Table 14 Hydrogenation of 29 using different catalysts	130
Table 15 Nucleoside analogue deprotection.	133
Table 16 RMSD values of Class 2 inhibitors with β 4GalT1.....	142
Table 17 RMSD values of Class 2 inhibitors with β 4GalT7.....	146
Table 18 Cell permeability of Class 2 inhibitors was assessed through HPLC-based experiments.....	149
Table 19 T _m shifts of Class 2 inhibitors in DSF assay.	150
Table 20 Activities of Class 1 inhibitors (1 – 4) and Class 2 inhibitors (29 – 41).....	159
Table 21 Crystallography data of compound 27 and 32	205
Table 22 Schematic table of Malachite-Green components in 96-well plate.	207

Abbreviations

Å: Angstrom

ADCC: antibody-dependent cellular cytotoxicity

Arg: arginine

β-1,4-GalTs: β-1,4-galactosyltransferases

β4GalT1: β-1,4-galactosyltransferases 1

β4GalT7: β-1,4-galactosyltransferases 7

°C: degree Celsius

CDC: complement-dependent cytotoxicity

CDCl₃: deuterated chloroform

CEL: chicken egg-white lysosome

CIP: calf intestine phosphatase

Cmpd: compound

Conv.: conversion

COSY: correlation spectroscopy NMR

CSPG4: Chondroitin Sulfate Proteoglycan 4

Cys: cysteine

dd: doublet of doublets

DI water: deionised water

DMAP: 4-dimethylaminopyridine

DMF: dimethylformamide

DMSO: dimethyl sulfoxide

DSF: differential scanning fluorimetry

DTT: dithiothreitol

Equiv.: equivalent

ER: endoplasmic reticulum

FcεRI: Fc epsilon receptor I

FcεRII: Fc epsilon receptor II

FucT: fucosyltransferase

5-FT UDP-Gal: 5-formylthiophene UDP-Gal

GAG: glycosaminoglycan

Gal: galactose

GTs: glycosyltransferases

GalTs: galactosyltransferases

Glc: glucose

GlcNAc: N-acetyl glucosamine

HCl: hydrochloride acid

HEPES: 4-(2-hydroxyethyl)-1-piperazineethanesulfonic acid

HILIC: Hydrophilic Interaction Liquid Chromatography

HMBC: heteronuclear multiple bond correlation

HPLC: high pressure liquid chromatography

HSQC: heteronuclear single quantum correlation

Hz: hertz

IC₅₀: half maximal inhibitory concentration

Ig: Immunoglobulin

IPA: isopropanol

J: coupling constant

LC-MS: liquid chromatography coupled with mass spectroscopy

M: molar

m: multiplet

mAbs: monoclonal antibodies

ManT: Mannosyltransferase

MD: Molecular Dynamics

Me: methyl

MeOD: deuterated methanol

mg: milligram

min: minute

mL: millilitre

mmol: millimole(s)

m/z: mass to charge ratio

M⁺: parent molecular ion

MMGBSA: molecular mechanics generalized born surface area

MW: molecular weight

NMR: nuclear magnetic resonance

NOESY: nuclear overhauser effect spectroscopy

Pd: palladium

PDB: protein data bank

ppm: parts per million

RCM: ring-closing metathesis

RMSD: root mean square deviation

RMSF: root mean square fluctuation

rt: room temperature

SAR: structure activity relationship

SD: standard deviation

SiaT: sialyltransferase

SM: starting material

TLC: thin layer chromatography

T_m: melting temperature

UDP: uridine diphosphate

UDP-Gal: uridine diphosphate galactose

UV-Vis: ultraviolet visible

μL: microlitre(s)

μM: micromole(s)

XRD: X-ray diffraction

Xyl: xylose

Chapter 1

Introduction

1. Introduction

1.1 Monoclonal antibody (mAb) glycoengineering

Over the past five years, monoclonal antibodies (mAbs) have become the best-selling drugs in the pharmaceutical market. The market value of mAbs is expected to reach 300 billion by 2025.¹ mAbs have been one of the most important and fastest growing classes of modern medicines. However, the structural complexity of antibody glycosylation limits the synthesis and application of defined antibodies. The identification of a simple and cost-effective strategy for synthesizing defined antibodies is therefore of great importance.

1.1.1 Immunoglobulins and their glycans

Antibodies are divided into five immunoglobulin classes, IgG, IgE, IgA, IgM and IgD, differing in structure, function and activities. In this series, immunoglobulin G (IgG) is the most abundant antibody class in human serum and is also most studied antibody class while our understanding of the other classes is still limited. In general, these antibody classes are composed of two domains, Fab and Fc (**Figure 1**). The Fab domain is engaged in antigen binding, while the Fc domain is responsible for binding with different Fc γ receptors and downstream effector functions (**Figure 1**).² What all these immunoglobulins have in common is that they are glycoproteins which are decorated with diverse glycans.

Glycosylation is a prevalent post-translational modification of immunoglobulins, which fall into two distinct categories including *N*-linked glycans and *O*-linked glycans.³ The specific glycan structure at glycosylation site plays a pivotal role in complement activation and receptor

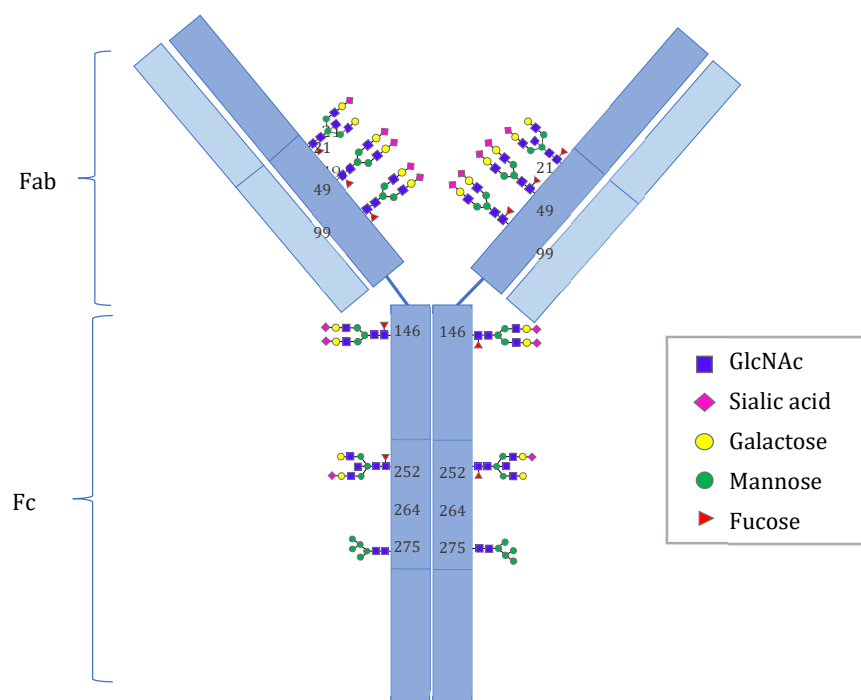


Figure 1 A schematic representation of immunoglobulin E (IgE) including representative glycans at its glycosylation sites⁴

affinity, thereby influencing the effectiveness of mAbs.⁵ Therefore, a comprehensive understanding of glycans at the molecular level is crucial for advancing the development of mAbs with improved effector functions and optimized therapeutic properties.

1.1.2 mAb glycoengineering

It has been well recognized that the manipulation of IgG glycan structure-glycoengineering is a common strategy to control the biological and therapeutic properties of IgG. For example, antibody-dependent cellular cytotoxicity (ADCC) of IgG is enhanced without the core fucose on the Fc *N*-glycans, while the presence of terminal galactose in the Fc domain promotes complement-dependent cytotoxicity (CDC).⁶ Significant evidence indicates that glycoengineering also plays an important role in the other antibody classes.

The IgE class is a key mediator in allergic diseases and represents the least abundant immunoglobulin, but the most glycosylated in human serum. Like other immunoglobulins, IgE consists of two heavy and two light chains, with seven potential *N*-linked glycosylation sites (**Figure 1**). Previous research suggests glycoengineering of IgE is essential for IgE-receptor binding interactions and downstream effector functions. For example, Hunt *et al.*⁷ and Bjorklund *et al.*⁸ demonstrated that FcεRI binding was severely diminished with complete deglycosylation of IgE. Shade *et al.*⁹ revealed that removal of the glycan at glycan site N275 leads to abrogated binding affinity for FcεRI, which prevented allergic reactions. More recently, Shade *et al.*¹⁰ revealed that sialylation was important for IgE functions in allergy. Moreover, Montero-Morales *et al.*¹¹ pointed out that the glycoforms terminating with GlcNAc residues increased the binding to FcεRII compared to the sialylated and galactosylated glycoforms, which indicated that less galactose and sialic acid may contribute to the binding to FcεRII. Glycoproteins with terminal D-galactose residues are directed to asialoglycoprotein receptors on the liver, leading to a shorter in-vivo half-life.¹² Employing GalT inhibitors to reduce the amount of terminal galactose residues may therefore be a promising strategy to prolong the in-vivo half-life of mAbs and other therapeutic glycoproteins.

1.1.3 IgE glycoengineering in this project

All of these findings collectively suggest that glycosylation indeed plays a significant role in modulating the functions of IgE. However, such research on IgE remains relatively limited. Indeed, the significance of IgE glycosylation requires further elucidation and additional supporting evidence. A major obstacle to elucidate the relationship between the glycosylation and IgE activities are the current technological limitations to produce defined glycoforms of IgE. The majority of existing glycoengineering technologies necessitate the creation of

optimized cell lines and/or specific culture conditions. This includes genetic modifications related to glycan biosynthesis, the use of CRISPR/Cas-9 for gene editing,¹³ and the implementation of RNA interference technology for gene silencing¹⁴. These approaches can be time-consuming and costly, often relying on trial-and-error methods for optimization. In this project, an operationally simple alternative was explored: the use of glycosylation inhibitors, in conjunction with established cell lines and culture conditions. In principle, this approach can provide not only a new method for glycoengineering of IgE, but also a basis for structure-function relationships of IgE structure and its biological and therapeutic properties. Hence, glycosylation inhibitors with suitable properties for glycoengineering play a crucial role in this project.

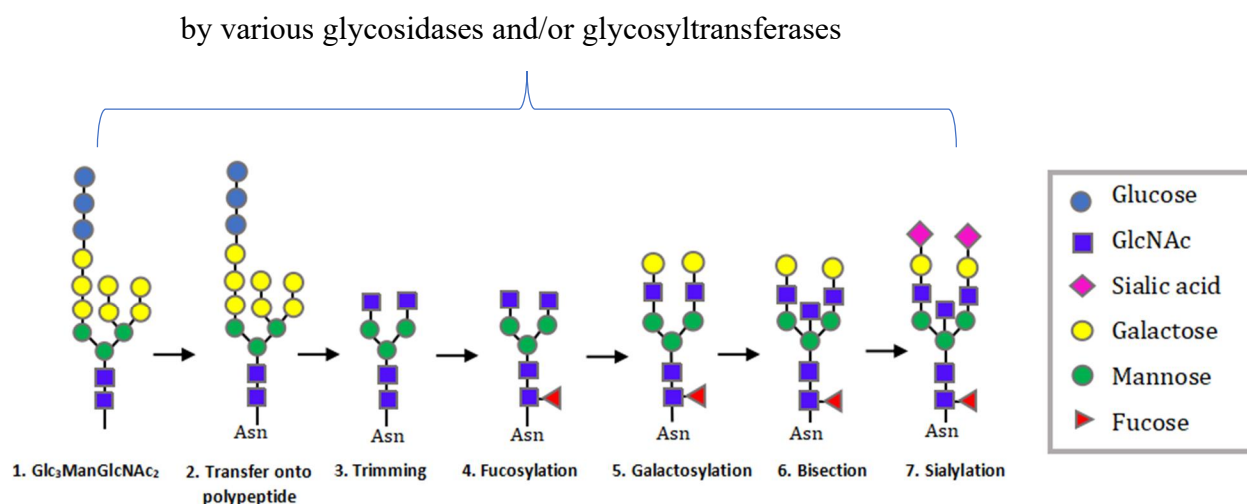
The following sections are overviews of mammalian glycan biosynthesis (see 1.2), glycosyltransferases (GTs) (see 1.3) and a short review of the small molecule inhibitors that have been successfully applied for the glycoengineering of mAbs or are suitable for such applications in principle (see 1.3).

1.2 Small molecule inhibitors for mAb glycoengineering

1.2.1 *N*-glycan biosynthesis in eukaryotes

Small molecule inhibitors of protein glycosylation usually act by inhibiting one or more enzymes involved in *N*-glycan biosynthesis. An abnormal glycosylation pattern is related to differential expression of the glycosidase and glycosyltransferase required for the oligosaccharide biosynthesis in the endoplasmic reticulum (ER) and Golgi (**Scheme 1**).¹⁵ Key steps of biosynthesis of *N*-glycans include (i) The glycan precursor, $\text{Glc}_3\text{Man}_9\text{GlcNAc}_2$ is

initially synthesized in the ER; (ii) The glycan precursor is transferred onto the antibody polypeptide in the ER. (iii) The glycan precursor is gradually trimmed by a highly ordered set of glycosidases and added with a GlcNAc to the intermediate $\text{Man}_3\text{GlcNAc}_2$; (iv) This new precursor is then modified sequentially by specific glycosyltransferases, including fucose, mannose, galactose and sialic acid. Glycosidases and glycosyltransferases play a key role in the release or addition sugar units to the growing oligosaccharide chain. Glycosyltransferase and glycosidase inhibitors are therefore powerful tools to interfere with the glycosylation process and to manipulate the glycan structure of IgE. We will mainly focus on the glycosyltransferase inhibitors, especially galactosyltransferase inhibitors, which are used to decrease the abundance of specific sugar residues (galactose) of IgE.



Scheme 1 Sequential processing of the antibody glycan¹⁵

1.2.2 Small molecule inhibitors: advantages & challenges

Using small molecule inhibitors for manipulating glycosylation is a complementary approach to the genetic disruption of glycan biosynthesis. It offers many practical advantages: compared to most existing methods, it is more cost effective and operationally simple. In addition, small

molecules can simply be added to established culture protocols and used with any number of different cell lines and genetic backgrounds. The level of intervention can also be easily regulated by adjusting the dosage.

The effective use of small molecules also faces some challenges: both poor cell uptake and limited chemical and enzymatic stability could lead to modest activity in cells of small molecular inhibitors. There is usually a trade-off between high uptake and high viability. However, most existing inhibitors are donor-substrate derivatives, which usually exhibit poor cell uptake. In addition, some inhibitors have extensive inhibitory activity on a wide range of glycosylation processes, which hinders research on the relationship between particular glycoforms and function of immunoglobulins. Low/no toxicity is also an important factor to be considered in the application of small molecular inhibitors.

1.3 Glycosyltransferases (GTs) and GT inhibitors

1.3.1 Glycosyltransferases (GTs)

Glycosyltransferases (GTs) constitute a vast group of enzymes that play a role in the formation of glycoconjugates, oligosaccharide and polysaccharides during biosynthesis. They catalyse the transfer a sugar component from a glycosyl donor to a diverse array of appropriate acceptor molecules (including lipid, protein, DNA or glycoconjugates). A prevalent characteristic among GTs is the utilization of glycosyl donors, with a predominant feature being a sugar nucleotide. Nine sugar nucleotide donors have been identified in human cells, including UDP- α -D-Gal (UDP-Gal), UDP- α -D-Glc (UDP-Glc), GDP- α -D-Man (GDP-Man), UDP- α -D-GalNAc (UDP-GalNAc), UDP- α -D-GlcNAc (UDP-GlcNAc), GDP- β -L-Fuc (GDP-Fuc),

CMP- β -D-Sialic acid (CMP-Sialic acid), UDP- α -D-GlcA (UDP-GlcA) and UDP- α -D-Xyl (UDP-Xyl).¹⁶ In all of the above cases, the sugar transfer reaction is enabled by the high energy bond between the sugar and the phosphate. GTs acceptors are predominantly oligosaccharides, although there are cases where they can be monosaccharides.

1.3.1.1 Sequence- and structure-based classification of glycosyltransferases

Glycosyltransferases are classified according to amino acid sequence similarity. Based upon this, 94 GT families have been catalogued.¹⁷ In accordance with their 3D crystal structures, the majority of GTs with established structures exhibit the GT-A, GT-B, or GT-C fold.¹⁸

The GT-A fold comprises a single Rossmann fold, which encompasses open, twisted β -sheets encircled by α -helices. The initial description of the GT-A fold emerged from the crystal structure of *SpsA* from *B. subtilis*,¹⁹ an enzyme of the Leloir pathway. Most GTs with a GT-A fold feature an Asp-x-Asp (DXD) motif positioned at the centre of the active sites. This motif coordinates with the pyrophosphate moiety of the nucleotide donor through metal cations such as Mn^{2+} and Mg^{2+} .

GT-B fold enzymes exhibit a two-domain structure, each domain featuring a Rossmann-like fold. Nonetheless, these two domains exhibit a looser connection with the active sites situated within the resultant crevice.²⁰ Unlike GT-A which relies on a divalent metal ion for nucleotide phosphate stabilization, the interconnected helices within the subdomain of its Rossmann folds establish a binding site for the acceptor.

The recently proposed GT-C fold shares similarities with the GT-A family. Enzymes with the GT-C fold are hydrophobic integral membrane proteins.¹⁸ They typically employ lipid phosphate-linked sugar donors and feature numerous transmembrane helices.¹⁸

1.3.1.2 General enzymatic mechanism of glycosyltransferases

The transfer of the sugar moiety is highly regio- and stereospecific, resulting in the potential occurrence of two distinct stereochemical results. The configuration of the anomeric centre of the donor sugar can be either maintained or reversed. GTs are therefore divided to retaining enzyme or inverting enzyme (**Figure 2**).²⁰

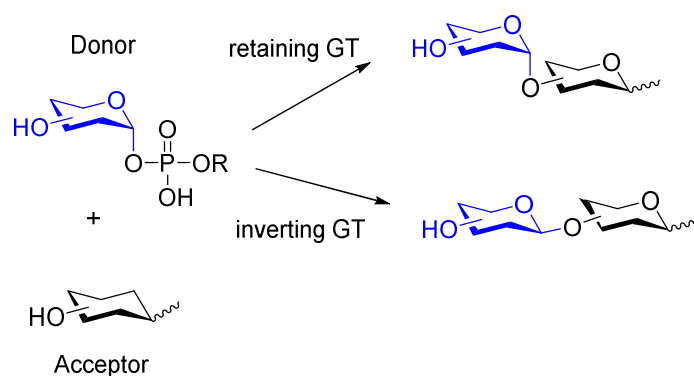


Figure 2 Retaining and inverting transfer reaction catalysed by GTs

While the mechanism of inverting GTs has been thoroughly characterized, there remains some ongoing discussion regarding the mechanism of retaining GTs. The inverting GTs exhibits a single $\text{S}_{\text{N}}2$ -like displacement mechanism and results in an inverted anomeric configuration (**Figure 3**).¹⁸ A catalytic amino acid at the active site of the enzyme acts as a base to deprotonate the hydroxyl group on the acceptor, enabling nucleophile attack of the anomeric centre of the donor. The reaction is followed by the departure of the nucleotide leaving group in a $\text{S}_{\text{N}}2$ -like displacement which leads to the inverted configuration of C1.

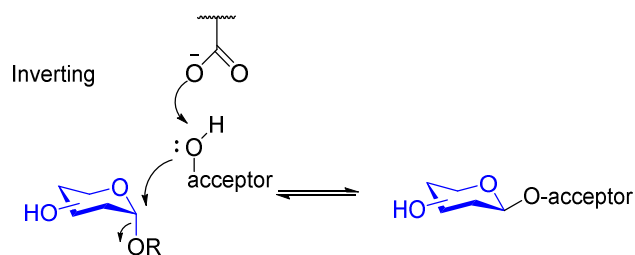
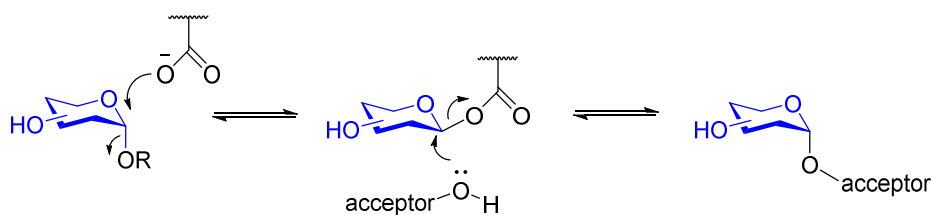


Figure 3 SN₂-like mechanism for Inverting GTs

In contrast, the mechanism behind retaining GTs remains uncertain and two distinct mechanisms have been suggested, respectively a double displacement mechanism and an S_Ni-like mechanism (**Figure 4**).¹⁸ The double displacement mechanism first involves a covalently bound glycosyl-enzyme intermediate with a catalytic amino acid attack. Then a hydroxyl group of the acceptor activated by the base catalyst proceeds a nucleophilic attack to the glycosyl-enzyme intermediate in another S_N2-like displacement. The S_Ni-like mechanism is proposed to involve an enzyme-stabilized oxocarbenium ion-like transition state intermediate, in which the donor leaving group and the acceptor are proposed to be on the same side.

Double displacement mechanism for retaining GTs



S_Ni-like mechanism for retaining GTs

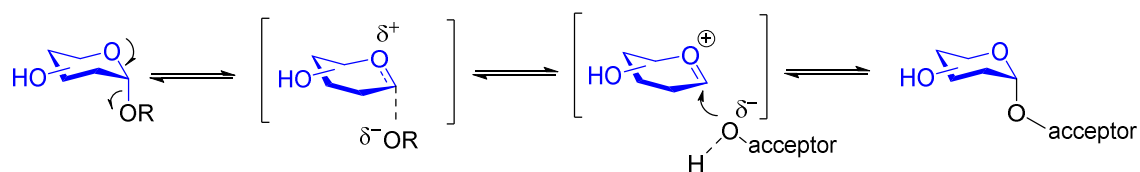
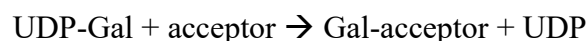


Figure 4 Proposed mechanism for retaining GTs

1.3.2 Mammalian GTs: β -1,4-Galactosyltransferases (GalTs)

1.3.2.1 Classification of β -1,4-GalTs

Within eukaryotic cells, galactosyltransferases (GalT) play a role in various processes such as the creation of several types of glycoconjugates and the biosynthesis of lactose. These enzymes are primarily situated in the Golgi apparatus. In mammals, nineteen GalTs have been identified and studied.²¹ These enzymes are responsible for catalyzing the transfer of galactose using linkages such as β 1-4-, β 1-3-, α 1-4- and α 1-3-, following the below standard reaction for Leloir GTs.²¹



Amongst the subfamily members of GalT, β -1,4-galactosyltransferases (β 4GalTs) are the most extensively researched, containing at least 7 members, β 4GalT1 to β 4GalT7, which share significant homology. β 4GalTs play a critical role in catalysing the transfer of galactose molecules from UDP-Gal to various acceptor molecules. These acceptor molecules can include N-acetylglucosamine (GlcNAc), xylose (Xyl) residues or glucose (Glc), depending on the classification of β 4GalTs.²² β 4GalT1 was the first discovered and represents the most prevalent class of β 4GalTs. Subsequently identified β 4GalTs, based on their higher homology with β 4GalT1, were categorized as β 4GalT2 through β 4GalT7. These enzymes exhibit similarity levels of 55 %, 50 %, 41 %, 37 %, 33 % and 25 % with β 4GalT1, respectively (**Figure 5**).²³ β 4GalT1 through β 4GalT6 each possess four conserved cysteine residues in the putative catalytic domains. In the conserved domain, all human β 4GalTs share several short sequence motifs, including FNRA, NVG, DVD, and WG WG(G/R)EDD(D/E) (**Figure 5**).

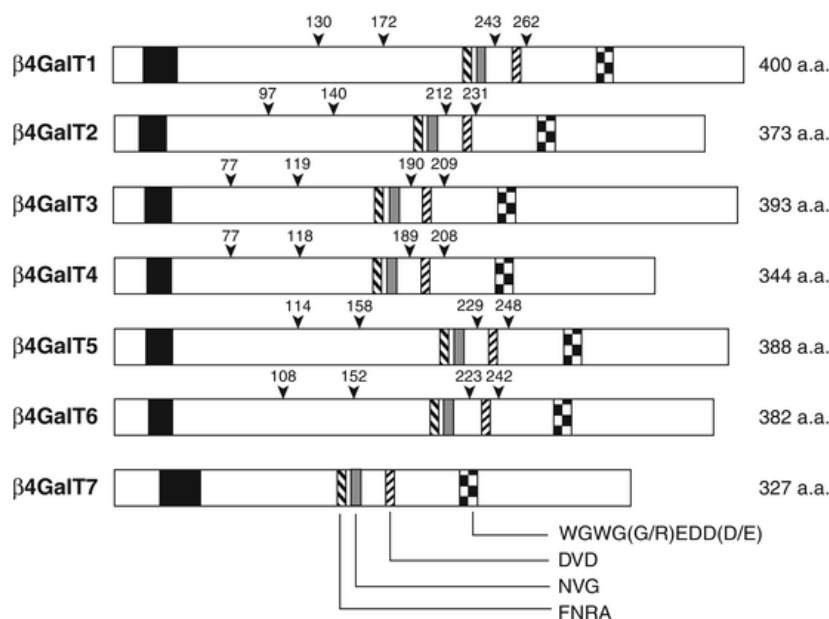


Figure 5 Schematic depiction of human $\beta 4\text{GalT}$ proteins. Solid boxes: putative transmembrane domains. Other boxes: common sequence motifs. Wedges with numbers: conserved Cysteine residues amongst $\beta 4\text{GalT1}$ to $\beta 4\text{GalT6}$.²⁴

Amongst the enzymes involved, only $\beta 4\text{GalT1}$ effectively facilitates the extension of *N*-acetyllactosamine (GlcNAc-Gal) units²⁵ while $\beta 4\text{GalT4}$ serves as a significant regulatory point for controlling glycan branching²⁶. For $\beta 4\text{GalT5}$, *in-vitro* tests demonstrated it can add galactose to *N*-glycans. However, in mice lacking $\beta 4\text{GalT5}$, there were no noticeable changes in *N*-glycan galactosylation. This suggests that the enzyme target may differ *in vitro* and *in vivo* due to limited access to acceptor molecules *in vivo*.²⁷ $\beta 4\text{GalT7}$ catalyses the transfer of galactose from UDP-Gal to xylose (Xyl) residues and, thus participating in the formation of the linkage region that connects core proteins and glycosaminoglycans (GAG).

1.3.2.2 Structure and mechanism of β -1,4-GalTs

The catalytic domain of $\beta 4\text{GalTs}$ contains two flexible loops, one relatively long and one relatively short (**Figure 6**). The main metal binding site is situated at the *N*-terminal hinge region of the elongated flexible loop. When both a metal ion and a sugar-nucleotide bind, a

substantial conformational shift occurs in the flexible loops, transitioning them from an open to a closed conformation. This change in conformation simultaneously generates a binding site for an oligosaccharide acceptor at the C-terminal region of the flexible loop, a site that was previously absent. The loop essentially functions as a lid, covering the attached donor substrate. Following the transfer of the glycosyl unit to the acceptor, the resulting saccharide product is released, and the loop returns to its original state to release the remaining nucleotide.²⁸ The specificity of members within the β 4GalTs family towards the nucleotide sugar UDP-Gal is governed by a tryptophan residue (W314 in β 4GalT1) located in the binding pocket. This tryptophan residue is consistently conserved across different family members from various species. In the open conformation, the side chain of tryptophan is oriented outward from the binding pocket. Conversely, in the enzyme's closed conformation, the side chain of tryptophan towards the binding pocket (**Figure 6**), engaging in the binding of donor and acceptor substrates.^{28,29}

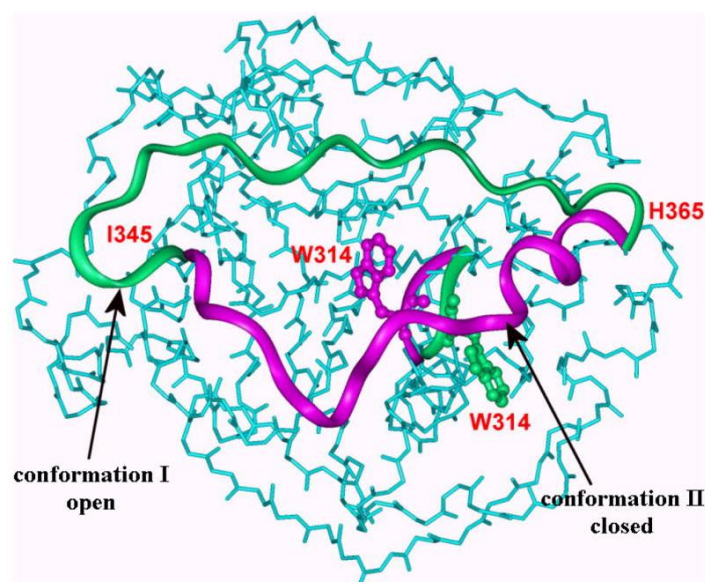


Figure 6 Open conformation (green) and closed conformation (purple) in β 4GalT1 containing a long flexible loop (residues I345-H365) and a short flexible loop (containing W314)²⁸

1.3.3 Bacterial GTs: LgtC, SetA and LtpM

GTs are not only important for mAb glycosylation in mammals, but also for other biosynthetic processes and biological functions. As part of our investigation, we explored three other UDP-sugar-dependant GTs – LgtC, SetA and LtpM – known for their function as bacterial GTs. This exploration offered an opportunity to discern the selectivity of our inhibitors in relation to these target enzymes.

LgtC, also called α -1,4-GalT, from *N. meningitidis* functions as a retaining GalT, facilitating the transfer of α -galactose from UDP-Gal to a terminal lactose acceptor located on the bacterial cell wall.³⁰ Exclusive to Gram-negative pathogenic bacteria, LgtC plays a crucial role in the biosynthesis of the lipooligosaccharide (LOS) envelope found on the bacterial surface. The expression of LgtC has been associated with a significant resistance to serum in non-typeable Haemophilus influenzae (NTHI) strains.³¹ Researchers have therefore investigated inhibiting LgtC involved in LOS biosynthesis as a potential strategy for discovering antimicrobial drugs.³² The crystal structure of LgtC in complex with substrates (**Figure 7a**) was published by Persson *et al.*³³ LgtC contains four Asp-x-Asp (DXD, where x represents any amino acid) motifs, with two of them situated at the active site. Upon binding to the donor substrate, LgtC experiences notable structural alterations, and it is suggested that two flexible loops transition from an open to a closed conformation.³³ However, a crystal structure of LgtC without a substrate is not yet accessible, thus making the positioning of the flexible loops uncertain in the apo (substrate-free) stage. MD simulations could provide a possibility as to how the flexible loops move (**Figure 7b**).³⁴

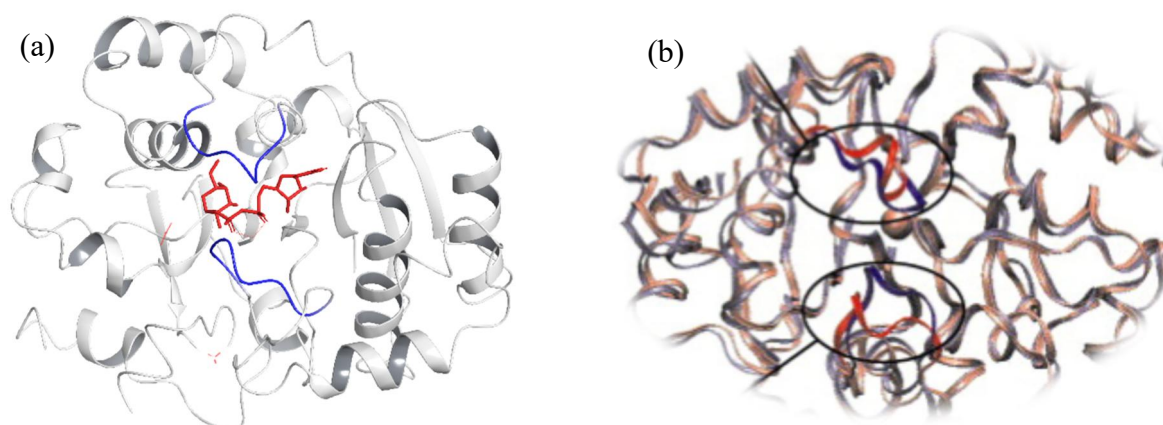


Figure 7 Structures of LgtC. (a) Crystal structure of LgtC with donor (in red) and flexible loops (residues 75 – 80 and 246 – 251) in blue (PDB: 1G9R), visualised with Schrodinger. (b) Comparison of two LgtC structures at the beginning (red) and end (blue) of MD simulations³⁴

Both SetA and LtpM are glucosyltransferases and act as *Legionella pneumophila* effector proteins. *Legionella pneumophila* is a human pathogen responsible for the development of a severe form of pneumonia known as *Legionnaires* disease.³⁵ SetA is more widely studied than LtpM which was published recently. However, neither of them has crystal structure accessibly. SetA displays *O*-glucosyltransferase activity and is a member of the GTA fold glycosyltransferases.³⁶ SetA is referred to as a subversion of eukaryotic traffic A due to its role in sabotaging vesicular transport in yeast.³⁷ The catalytic activity is situated at the *N*-terminus of SetA, while the *C*-terminus (amino acids 401–644) plays a crucial role in directing SetA to vesicular compartments within host cells.³⁵ LtpM is encoded within a recombination hotspot in *L. pneumophila* Paris. Levanova *et al.*³⁸ found that LtpM is both localized and activated by a *C*-terminal phosphoinositide 3-phosphate (PISP)-binding domain. They also discovered the *N*-terminal domain of LtpM represents a novel form of glucosyltransferases, which functions independently of metal ion co-factors and catalytic DxD motif. This is distinct from classic GTAs like SetA.³⁸ In both SetA and LtpM, the AlphaFold models demonstrate the existence of conserved residues, including a tryptophan, aspartic acid and asparagine (**Figure 8**).

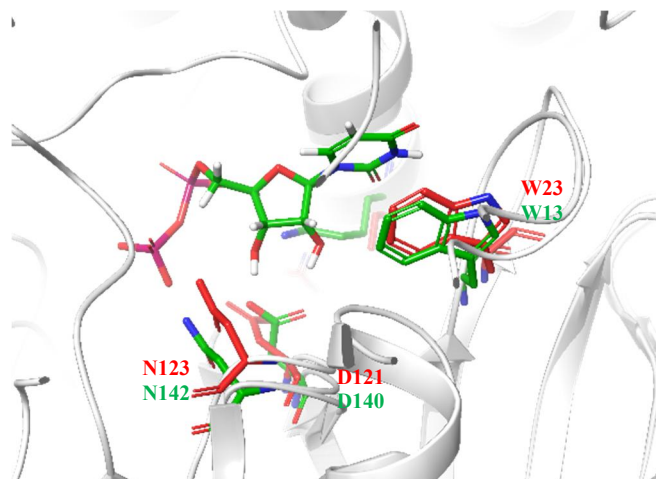


Figure 8 Superimposition of SetA (red) and LtpM (green). Conserved residues within the binding pocket are highlighted in the AlphaFold models of SetA (red) and LtpM (green). UDP (green) was docked with LtpM AlphaFold model using Glide of Schrodinger. The AlphaFold models were generated by Gunnar Neels Schroeder.

1.3.4 Glycosyltransferase (GT) inhibitors

The majority of current GT inhibitors employed in glycoengineering directly focus on inhibiting their respective target GTs. The inhibitors to be discussed below were presented based on the enzymes they specifically target.

1.3.4.1 Inhibitors for GalTs

Terminal galactose residues target glycoproteins to asialoglycoprotein receptors on the liver. This therefore limits glycosylation half-life. Control of the abundance of galactose therefore has biological and pharmacological research value. Galactose residues occur in *N*-glycans most commonly in a β 1-4 linkage. The corresponding β -1,4-GalTs catalyse the transfer of galactose from the sugar-nucleotide donor UDP-Gal specifically to *N*-acetylglucosamine (GlcNAc) residue (acceptor) in the *N*-glycan biosynthesis of IgE.

Several donor analogues have been published as potent GalT inhibitors. Some inhibitors are modified from the sugar (i.e., **1** in **Figure 9**)³⁹ or sugar phosphate moieties (i.e., **2** in **Figure 9**)⁴⁰ of the donor while some others modified from the nucleobase moieties (i.e., **3** and **4** in **Figure 9**)^{41,42} For example, a naphthylmethyl group was introduced to the position 3 of indole group in the inhibitor **1** while a formylthien substitution was introduced to the position 5 of uracil in the inhibitor **3**. These donor analogues can occupy the active site of GalT and therefore affect the sugar transfer. The formylthiophen substitution on the uracil ring was proven to form an additional hydrogen bond with a key residue in the target enzyme. This blocked the enzyme in a catalytically inactive conformation (compound **5** in **Figure 9**).

Despite their potency, these inhibitors have some limitations. The presence of pyrophosphate linkage makes the molecule susceptible to chemical and enzymatic degradation and difficult to penetrate cell membrane. To overcome this, some inhibitors are designed by the substitution of natural glycosidic (*O*-glycosidic) phosphoester bond with *C*-glycosidic bond, such as i.e., **2**, which enhanced chemical and enzymatic stabilization of the structure. Moreover, uncharged inhibitors also attract researcher attention. The Wagner research group has also previously synthesised this type of neutral inhibitor (**4** in **Figure 9**) with promising activity. Inhibitor **3** was altered by eliminating its sugar and pyrophosphate elements while retaining the 5-substituent. This modification resulted in enhanced cell permeability and stability of the inhibitors. Nevertheless, the IC_{50} decreased to 207 μ M from 18 μ M by employing the indol-4-yl- group as the 5-substituent (**4** in **Figure 9**). Aside from these donor analogues, some acceptor analogues (**5** in **Figure 9**)^{43,44} also have been studied, however there are scarce examples.

Apart from inhibitors targeting GalTs, there have been reported inhibitors for fucosyltransferases (FucTs), mannosyltransferases (ManTs), and sialyltransferases (SiaTs).

These inhibitors can play a role in investigating the structure-property relationships of IgE. The predominant design approach for these inhibitors involves the use of analogs of donors, acceptors, or a combination of both.

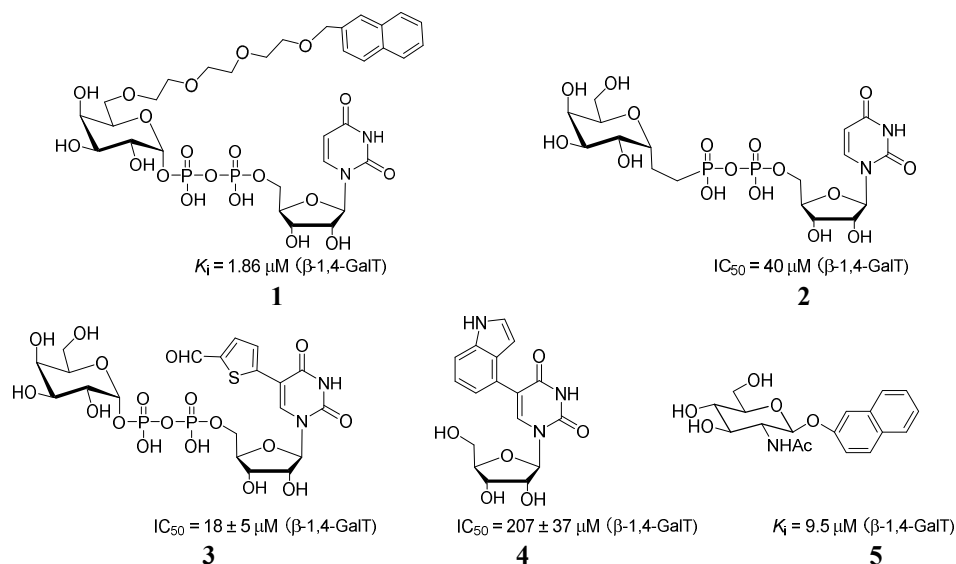


Figure 9 Representative GalT inhibitors

1.3.4.2 Inhibitors for other GTs

Some FucT inhibitors have been successfully applied in IgG glycosylation. Most published FucT inhibitors inhibit fucosylation by depleting the intracellular donor substrate of FucT, GDP-fucose. For example, the use of 2-fluoro-L-fucose per-*O*-acetate (compound **6** in **Figure 10**), involving the replacement of an alcohol group with a fluorine substituent, resulted in the production of completely defucosylated IgG. This outcome was observed in both cell culture and *in vivo* in mice and therefore improved the ADCC functions.⁴⁵ Similarly, 6,6,6-trifluorofucose per-*O*-acetate (compound **7** in **Figure 10**), a prodrug of 6,6,6-trifluorofucose, was successfully used to regulate the fucose glycans on the IgG in a dose-dependent manner.⁴⁶

The sialylation reactions can be inhibited using fluorinated analogs of the donor substrate, cytidine monophosphate (CMP)-SiaFAc. As early as 1999, CMP-SiaFAc was found to have the potential to inhibit sialylation reactions but with poor cell uptake.^{47,48} Its peracetylated metabolic precursor (SiaFAc) was used to enable passive diffusion over the cell membrane and CMP-SiaFAc was activated inside the cell.^{49,50} Such SiaFAc acts as a desired donor substrate-based inhibitor to prevent the de novo synthesis of the natural substrate in human HL-60 cells. More recently, Heise *et al.*⁵⁰ designed and synthesized the similar C-5-modified 3-fluoro sialic acid sialyltransferase inhibitors (i.e., **8** in **Figure 10**) which proved to have drastically improved and prolonged inhibitory ability in multiple mouse and human cell lines.

Mannosyltransferase (ManT) inhibitors are seldom reported. Urbaniak *et al.*⁵¹ published the first inhibitor (compound **9** in **Figure 10**) of the third α -mannosyltransferase (MTIII) of the Glycosylphosphatidylinositol (GPI) biosynthetic pathway. 2'-amino analogue (**9**) of bimannosylglucosaminylphosphatidylinositol (Man₂GlcN-PIC₁₈, M2) blocked the synthesis process of Man₃GlcN-PIC₁₈ (M3) and led to an accumulation of M2 *in vitro* experiments, which indicated that MTIII was inhibited by 2'-amino analogues with low micromolar inhibitory activity (**Figure 10**).

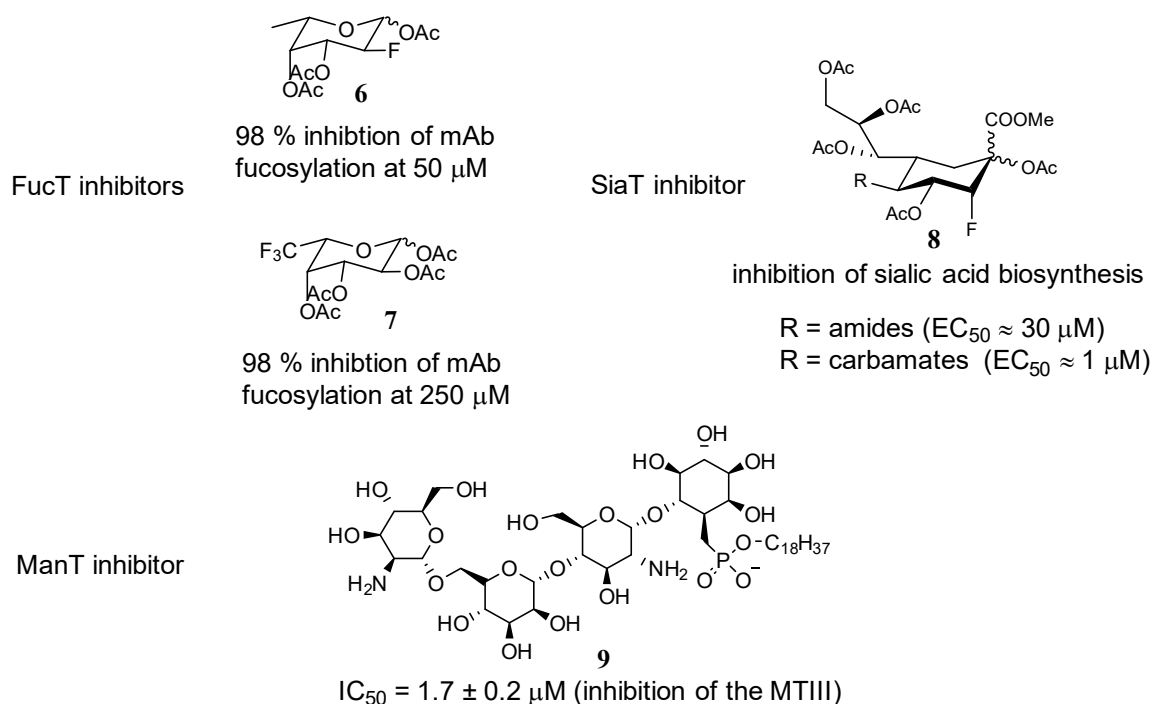


Figure 10 Representative inhibitors for FucT, SiaT and ManT

1.4 Conformational restriction as a design strategy for a novel class of glycosyltransferase inhibitors

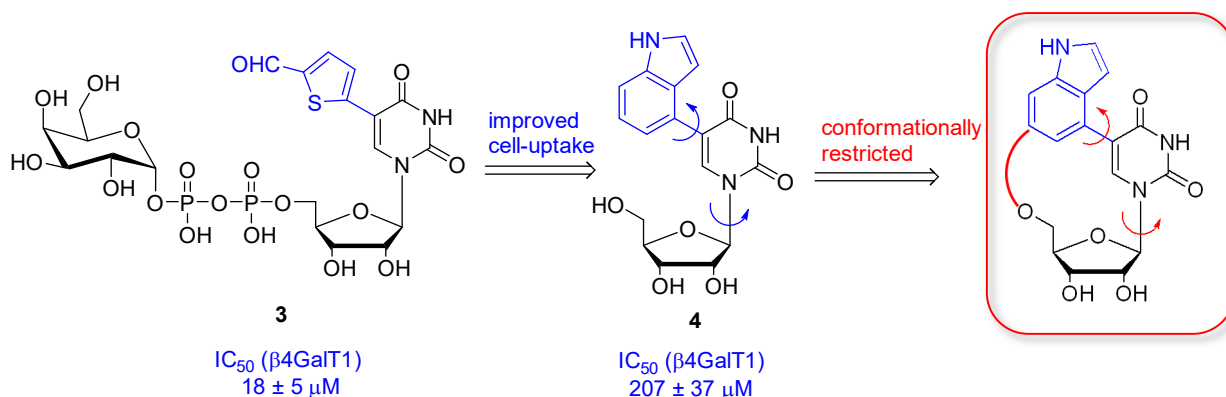


Figure 11 Conformational restriction to improve inhibitory activity, selectivity and cell permeability of existing inhibitors^{52,53} against β4GalT1

The Wagner research group has previously reported a donor analogue 5-FT UDP-Gal (**3**) which was the best GalT inhibitor to date with IC_{50} value of 18 μM towards bovine β4GalT1 (**Figure 11**). It stands out due to the substituent group located at position 5 of its base, which has the

ability to lock the target enzyme in a catalytically inactive state.⁴¹ However, in terms of cellular applications, 5-FT UDP-Gal (**3**) is limited by the charged pyrophosphate linkage, which constrained its application in the glycosylation of IgE. Considering this, Jiang *et al.*⁴² modified 5-FT UDP-Gal by removing its sugar and pyrophosphate component while the 5-substituent remained. Both cell permeability and stability of the inhibitors were improved. However, the IC₅₀ was reduced to 207 μM from 18 μM when using indol-4-yl- group acting as 5-substituent (compound **4** in **Figure 11**). To address this issue, the concept of conformational restriction was pursued. Conformational restriction was going to be achieved by linking the 5'-position of the ribose with the 6-position of the indole substituent, resulting in a new class of macrocyclic nucleoside (**Figure 11**). This conformational restriction was expected to enhance potency and selectivity for the biological targets by minimizing the entropic loss of the ligand being constrained in its preferred conformation. The following sections provide an introduction and brief reviews on conformationally restricted macrocycles (see 1.4.1) and the application of conformational restriction in nucleosides (see 1.4.2).

1.4.1 Conformationally restricted macrocycles

Macrocycles are cyclic structures with 12 or more atoms in their rings. Due to restricted rotation, they offer a certain conformational preorganization. This is crucial for effective binding to proteins, where a molecule needs bioactive conformation. Macrocycles limit the available conformations for unbound molecules, reducing the entropic cost during binding. While not completely rigid, they restrict internal bond rotations, providing conformational constraint. Macrocycles are adaptable, offering flexibility to efficiently interact with proteins' flexible binding sites. This flexibility minimizes the internal entropy penalty when transitioning from the unbound to the bound state.^{54–58}

Entropy is interconnected with other thermodynamic parameters in reversible binding via Gibbs free energy. (**Equation 1**)

$$\Delta G = \Delta H - T\Delta S = -RT\ln K \quad \text{(Equation 1)}$$

ΔG = Gibbs free energy change; ΔH = enthalpy change; T = temperature; ΔS is entropy change; R = gas constant; K is binding constant.⁵⁴

The entropic change is proportional to the binding affinity. In the process of binding between ligand and protein, the whole binding system including ligand was changed from disorder to order. The entropy is therefore decreased during binding (entropy measures the degree of disorder of a system). Thus, a pre-organized ligand is expected to decrease the entropic loss of the binding system, and therefore can increase the binding affinity and the related ligand potency. For example, Tron *et al.*, found an acyclic compound **10** adopted a “U”-shaped conformation in the binding pocket of Mcl-1 (Myeloid cell leukemia-1). By closing the ring and optimization, the IC_{50} value could be decreased by 60-fold (**11**) (**Figure 12**).⁵⁹ Apart from entropy change, enthalpy change may also contribute to binding affinity. In most of the cases of conformationally restricted structures, the entropy change tends to be accompanied by enthalpy change, such as, increased/decreased hydrogen bonds intramolecularly or increased/decreased strength of hydrogen bonds intermolecularly. Delorbe *et al.*⁶⁰ investigated the effect of macrocyclization of a Grb2 SH2 protein-protein interaction inhibitor on the enthalpic and entropic components of binding using isothermal titration calorimetry. They found cyclized **13** had a greater favourable entropic contribution to the free energy of binding, with a smaller enthalpic contribution due to the lack of intramolecular hydrogen bond that existed in the linear ligand **12**. As a result, **13** was still slightly more potent than **12** due to its high positive entropic contribution (**Figure 12**).⁶¹

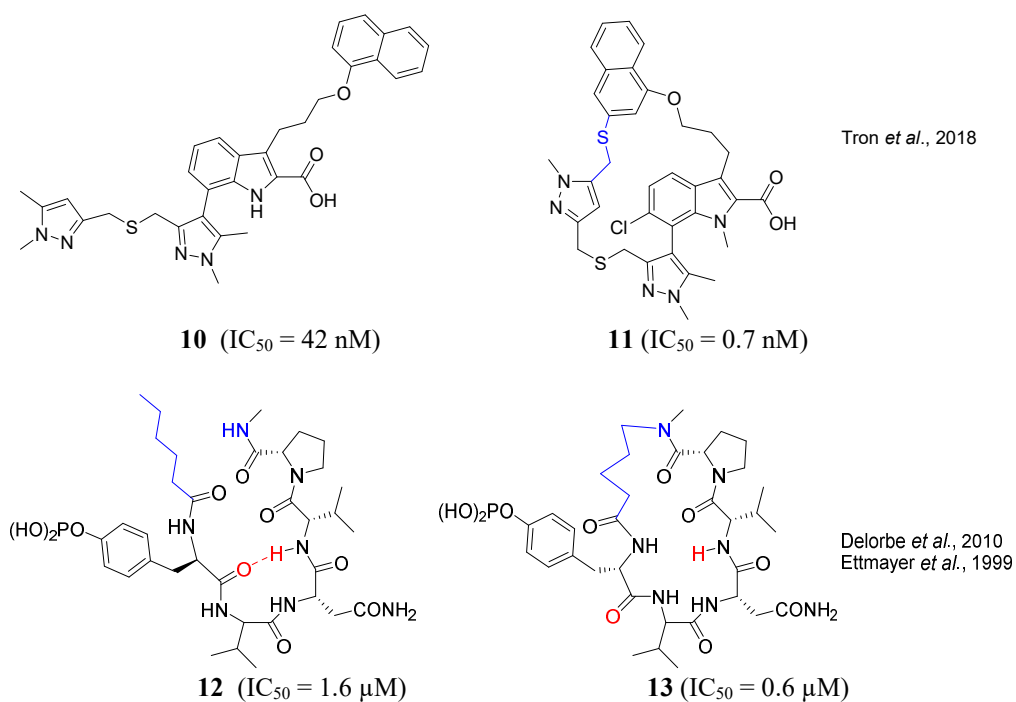


Figure 12 Examples of macrocycles for improving binding affinity by conformational restriction

Research has shown that macrocyclic model compounds may exhibit not only improved potency, but also enhanced permeability across membranes in comparison to their acyclic counterparts. The enhancement is believed to stem from alterations in properties, such as the reduction of flexibility in macrocyclic compounds. Nie *et al.*⁶² discovered that a macrocyclic pyrazolo triazine inhibitors (**15**) of CK2 was less potent than an acyclic one (**14**) in the enzyme assay than the acyclic compound, while more effective in a cell-viability assay. This due to increased cell permeability of the less planar conformation of the macrocyclic structure (**Figure 13**).^{63,64}

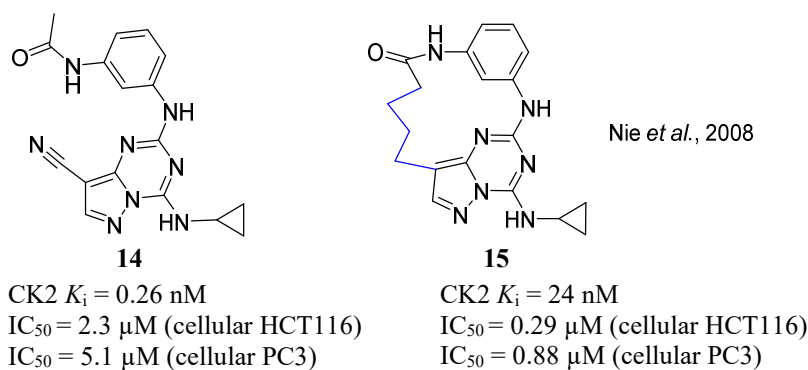


Figure 13 Example of macrocycle for improving cellular permeability by conformational restriction

1.4.2 Conformationally restricted nucleosides

It has been recognized that the binding affinity of nucleosides is affected by the sugar puckering (north/south) and the orientation of the nucleobase (syn/anti) (χ angle). The anti-conformation is mostly preferred in nucleosides. The orientation of the 4'-5' bond (γ angle) is also another essential feature, namely, synclinal (+sc) and antiperiplanar (ap), in which +sc conformation is populated in pyrimidine nucleosides while both are equally preferred in purine nucleosides (**Figure 14**). All these parameters contribute to the design of the modified nucleosides to improve their selectivity and biological activities.

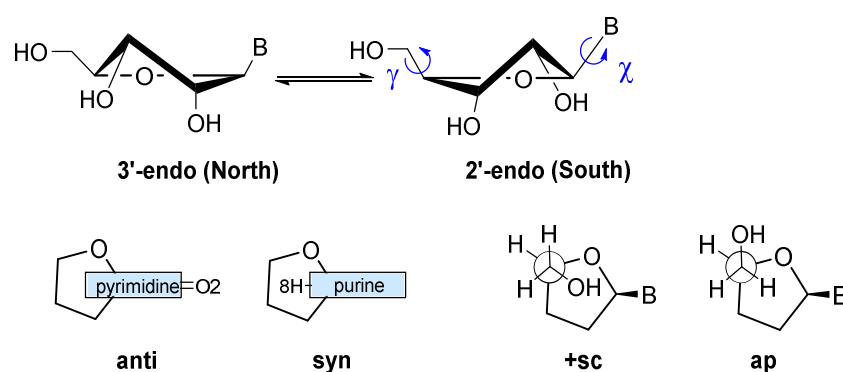


Figure 14 Conformational nomenclature of natural nucleosides. “B” means base.

Existing research predominantly focused on the modification on the pentofurano sugar moiety by chemical approaches. Three to seven-membered ring-fused bicyclic nucleosides have been published, in which, 1',2'- 1',3'-, 1',4'-, 2',3'-, 2',4'-, 3',4'-, 3',5'-conformational constraints are included.⁶⁵⁻⁷² The conformation of the natural nucleoside is well restricted by the inserted ring into the ribose to form a defined conformation. For example, the seven-membered ring linking the 3' to 5' methylene groups of the sugar moiety of **16** produced a nucleoside with South orientation and defined γ angle.⁷⁰ The prodrug exerted modest antiviral activity. Similarly, 3',5'-conformationally constrained **17** was also proved to express improved

stabilization compared to its natural nucleoside.⁷¹ In addition to the furanose-nucleoside, its carbocyclic nucleoside analogue was also studied. A bromo substituent was introduced to the position 3 of adenine (compound **18a** and **18b**)⁷², which locked the conformation into *anti* type by increasing the steric hindrance. The analogue of **18b**, **18a** has no bromo substitution showing less bioactivity. Moreover, the bicyclic[3.1.0]hexane ring constrained pseudo sugar component resulted in a North-conformation. Compared to **19b** with South conformation, **18b** has a more rigid structure showing more potent bioactivity than **19b** (**Figure 15**). All these indicate the importance of the restricted conformation for bioactivity.

Apart from the ribose with an fused ring, different classes of spiro-nucleosides have also been studied, such as anomeric spiro-,⁷³ C-2'-spiro-,⁷⁴ C-3'-spiro-⁷⁵ and C-4'-spiro-nucleosides.⁷⁶ Some of them demonstrated excellent bioactivities.^{74,77} In these cases, hydantocidin (compound **20**)⁷³, a natural spiro-nucleoside, is more than a sugar-restricted nucleoside analogue, its nucleobase is also constrained. In this spironucleoside, the anomeric carbon belongs simultaneously to the base and the sugar ring, which restricts the base in a specific orientation around *N*-glycosidic bond. Hydantocidin was proved to effectively inhibit herbicidal activity. Its analogues were also widely studied, and some showed excellent bioactivities. Other modified nucleosides with sugar or both base and sugar-conformation restricted are still limited (**Figure 15**).

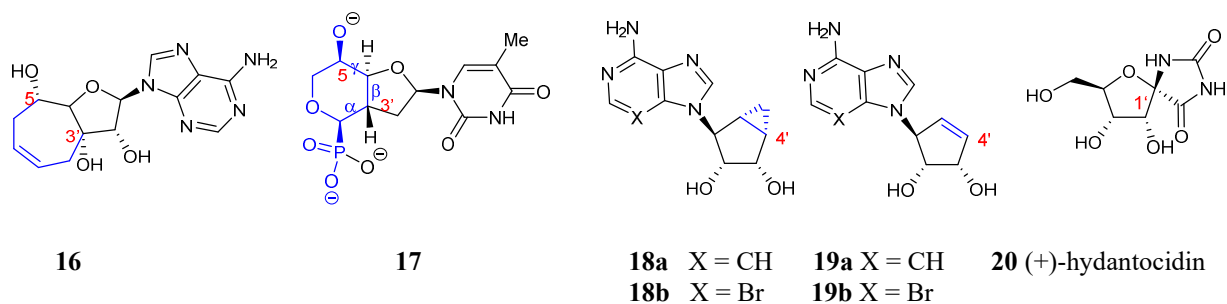


Figure 15 Examples of conformationally restricted nucleosides^{70–73}

1.5 Aims and objectives

The main goal of this project was the development of a novel class of conformationally restricted nucleosides as GalT inhibitors and their application for the glycoengineering of IgE. It was anticipated that these GalT inhibitors would possess suitable properties for applications in cells and could be used in conjunction with established cell lines and culture conditions to control the glycoforms of IgE (**Figure 16**). This would represent a significant technological advance for the generation of defined IgE glycoforms, and help establish the exact role of glycosylation for the biological and therapeutic properties of IgE, which is presently not well understood.

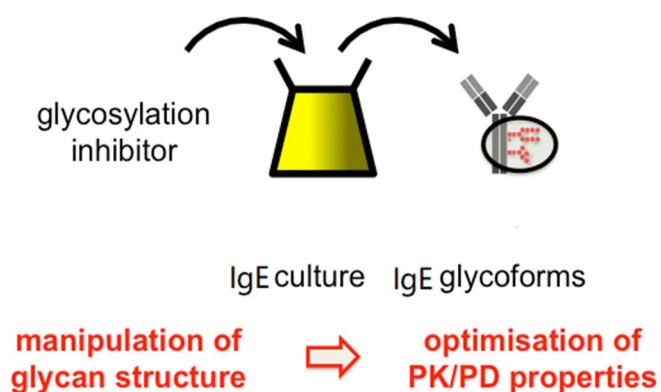


Figure 16 The main project aims

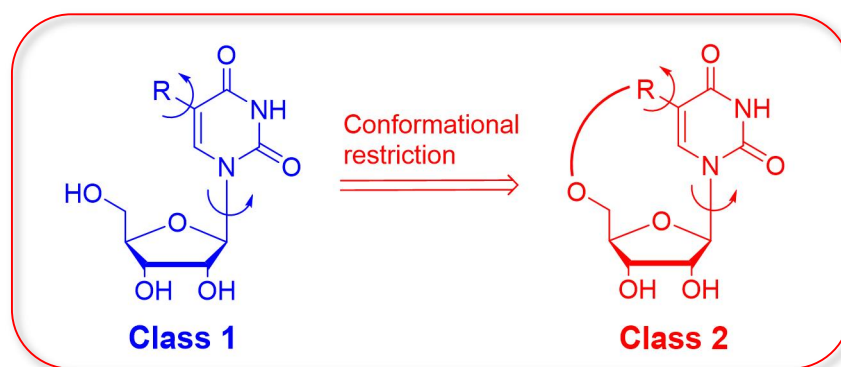
This project pursued four key objectives:

- 1) Rational design and chemical synthesis of novel conformationally restricted GalT inhibitors based on a 5-substituted nucleoside scaffold
- 2) Biochemical assessment of inhibitors against GalTs
- 3) Molecular modelling to rationalise the enzymological behaviour of inhibitors
- 4) Biological evaluations of inhibitors in IgE cell culture

The inhibitor design was based on the previously reported GalT donor analogue 5-FT UDP-Gal, which displayed a low micromolar range inhibitory activity against several GalTs.⁴¹ Due to the 5-formylthienyl substituent at position 5 of the uracil base, 5-FT UDP-Gal can lock its target GalTs in a catalytically inactive state. However, 5-FT UDP-Gal has limited suitability for cellular applications due to its charged pyrophosphate linkage. Removal of the sugar and pyrophosphate linkage improved cell permeability and stability but led to a drop in inhibitory activity.⁴²

In order to regain inhibitory activity and maintain, or further improve, cell permeability, conformational restriction was applied as a design strategy in this project (**Scheme 2**). Starting from an uncharged, 5-substituted nucleoside, internal bond rotations were restricted by introducing a macrocyclic linkage between the 5-substituent at the uracil base, and the 5'-position of the ribose (**Scheme 2**). It was anticipated that this approach may enhance potency and selectivity for biological targets by minimizing the entropic loss associated with the ligand being constrained in its preferred conformation.

Two classes of inhibitors were explored (**Scheme 2**). Class 1 inhibitors were uridine derivatives featuring diverse 5-substituents (**Scheme 2**). The goal was to identify the most favourable substituent and orientation at position 5 of the nucleoside scaffold. Subsequently, installation of a macrocycle at selected Class 1 inhibitors nucleosides delivered a novel class of conformationally restricted Class 2 (**Scheme 2**). The inhibitory activity of Class 1 inhibitors and Class 2 inhibitors was evaluated against two mammalian GTs, β 4GalT1 and β 4GalT7. Selected inhibitors were also applied in IgE glycoengineering studies in cells.



- Class 1 aim: to identify the most favourable substitution and orientation in the 5-position
- Class 2 aim: to enhance inhibitory activity and cellular permeability

Scheme 2 Designed structures of Class 1 inhibitors and Class 2 inhibitors

GTs are not only important for mAb glycoengineering in mammals but also in many other biosynthetic processes and biological functions, including in bacteria. Therefore, the secondary aim of this project was to investigate selected inhibitors against three additional UDP-sugar-dependent GTs of bacterial origin, LgtC, SetA and LtpM. These experiments allowed an initial assessment of the target selectivity of the new inhibitors and their potential as anti-bacterial agents.

The main results from the project are described in three experimental Chapters. Chapter 2 covers the development of 5-substituted nucleoside derivatives (Class 1 inhibitors). It provides an introduction to the synthesis of four ring-open compounds **1** – **4** and their corresponding pro-drug forms **5** – **8**, followed by inhibitory activity assessments of *in-vitro* assays and cellular assays. In Chapter 3 and 4, the conformationally restricted, macrocyclic nucleosides of Class 2 inhibitors are reported, which form the primary focus of this project. Chapter 3 encompasses several different synthetic routes towards the target compounds, while their activity evaluation is described in Chapter 4. Finally, molecular modelling was carried out to rationalise the experimental results and provide a basis for further optimisation.

Chapter 2

5-substituted uridine derivatives

– Target Class 1

2. 5-substituted uridine derivatives (Target Class 1)

2.1 Introduction

This Chapter mainly focuses on the synthesis, activity evaluation and molecular modelling of Class 1 inhibitors. Class 1 inhibitors refer to a group of compounds consisting of 5-substituted uridine derivatives. The key step involved in their synthesis is the Suzuki cross-coupling reaction. A relevant review detailing Suzuki coupling is provided. The activity evaluation involved biochemical assessments, encompassing Malachite-Green inhibition assays and HPLC-based inhibition assays, targeting mammalian GalTs. Subsequently, cellular activity evaluations were conducted, including IgE glycoengineering. Biochemical evaluations of other GTs (LgtC, SetA and LtpM) were employed as target enzyme in DSF binding assay. Molecular modelling was utilized to provide a rational explanation for the observed experimental outcomes.

2.1.1 Suzuki-Miyaura coupling

Suzuki coupling is one of the most widely employed Pd-catalyzed C-C reactions. It comprises the palladium catalyzed cross-coupling between organoboronic reagents and halides. Recent advancements in catalysts and methods have significantly expanded its potential applications, extending beyond aryl halides to alkenyl, alkenyl and alkynyl halides, and replacing boronic acids to boronate esters, organoboranes or potassium trifluoroborates as viable reaction partners. Suzuki-Miyaura reactions present several notable advantages,⁸ including compatibility with aqueous conditions, mild reaction conditions, readily available reagents,

excellent compatibility with various functional groups, high stereo- and regioselectivity and low toxicity.

Suzuki-Miyaura cross-coupling reactions involves three key mechanistic events⁷⁸: (i) oxidative addition, (ii) transmetalation and (iii) reductive elimination (**Figure 17**). The vast majority of cross-coupling reactions catalyzed by Pd(0), Fe(0), and Ni(0) can be explained and understood through this shared catalytic cycle (**Figure 17**).⁷⁹

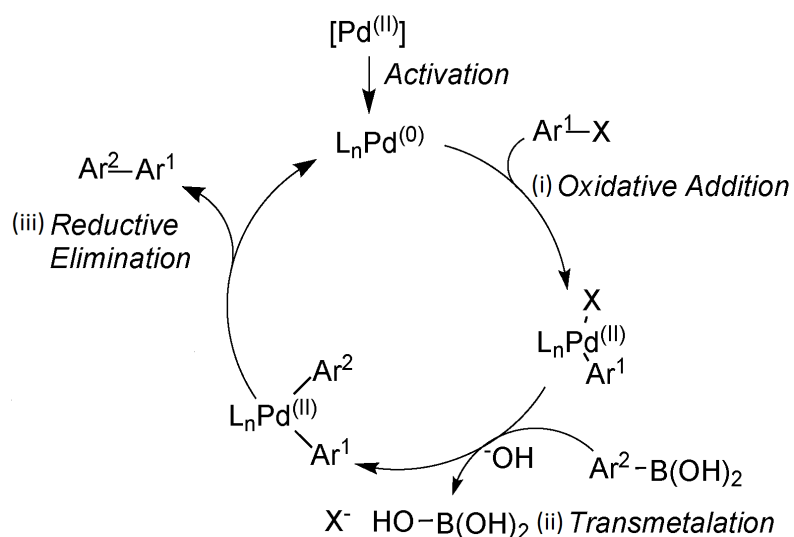


Figure 17 Proposed catalytic cycle⁷⁸

Oxidative addition and reductive elimination are shared amongst most cross-coupling reactions and have been extensively investigated using both molecular and experimental techniques. These two steps are well understood. However, transmetalation step is less well-understood because it is highly dependent on reaction conditions and the nucleophile used.⁸⁰

Oxidative addition, involves the addition of aryl halides or other electrophiles to a Pd(0) complex, resulting in the formation of a stable trans Pd(II)-C complex. $Pd(PPh_3)_4$, $PdCl_2(PPh_3)_2$ and $Pd(OAc)_2$ plus phosphine ligands are commonly used palladium sources. These are air-

stable and readily undergo reduction to form an active Pd(0) complex when exposed to phosphines or organometallics.⁸¹ Oxidative addition often serves as the rate-determining step. It depends on the reactivity of leaving group, is as follows: I >> Br >> Cl > F. In this step, the halides electrophiles are activated by the electron-withdrawing groups, which are more reactive than those with electron-donating groups.⁸²

Transmetalation in Suzuki coupling is an organometallic process involving the transfer of ligands from organoboron to the Pd(II) complex. Simultaneously, the nucleophilic organic groups are also transferred from organoboron to the palladium(II) complex.⁷⁸ In the absence of base, organoboron compounds do not undergo transmetalation. It is widely accepted that the base serves the dual purpose of activating the organoboron compound and facilitating formation of the intermediate from the oxidative addition product.

In the reductive elimination step, Pd(II) eliminates the product with a new C-C bond and restores the Pd(0) catalyst. The stereo effect is involved in this step. This process takes place from the cis complex, causing the trans complexes to isomerize into their corresponding cis isomers. Therefore, the order of reactivity is diaryl->alkyl-aryl>dimethyl-palladium which suggests the potential involvement of the π -orbital of the aryl group.⁸³ Furthermore, the steric bulkiness of the substituents on the phosphine ligand also helps in this reductive elimination reaction. N-heterocyclic carbenes have been employed as an alternative to phosphines because of their greater electron richness and bulkier nature.⁸⁴

2.1.2 Suzuki coupling of nucleosides

Nucleoside derivatives have attracted significant attention owing to their potential bioactivity. Amongst the various synthetic nucleosides, there has been a specific focus on the C5-modified

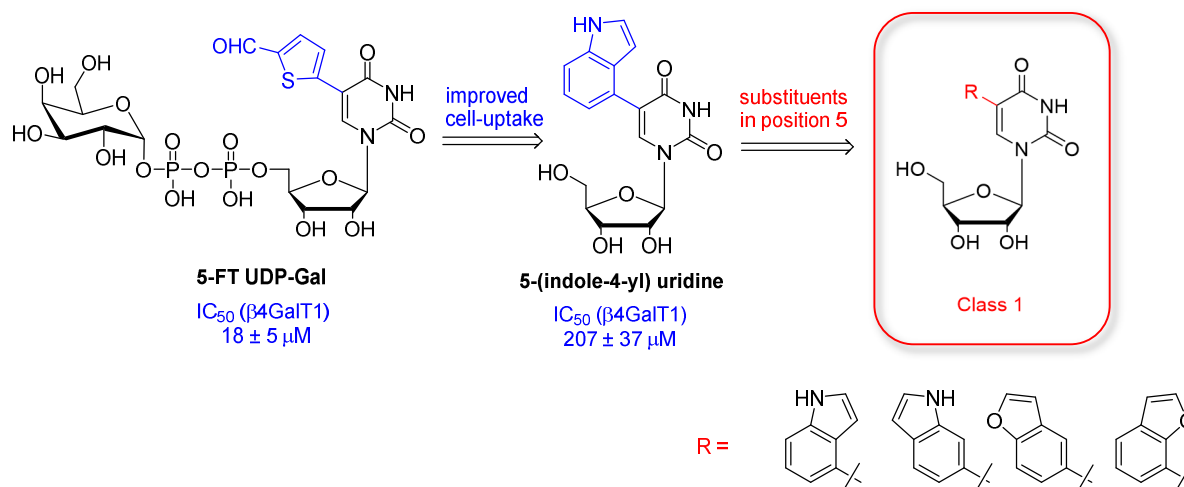
pyrimidines. These are focused upon in this project. In contrast to alternative strategies, Suzuki coupling offers a clear advantage since it can be used in aqueous conditions in the presence and absence of protecting groups. Considering the polarity of nucleosides, the use of aqueous conditions significantly enhances the solubility of the reactants and subsequently addresses yield-related challenges.

In 2002, Wagenknecht *et al.*⁸⁵ published the first procedure for synthesizing unprotected arylated nucleosides via Suzuki coupling. 5-(1-pyrenyl)-2'-deoxyuridine was synthesized in the presence of Pd(PPh₃)₄ and NaOH using a solvent system of THF-MeOH-H₂O. A substantial quantity of catalyst was employed.⁸⁵ Less commonly used boronic acids such as thiophene and furan boronic acids have also been reported as Suzuki coupling reagents by research groups including the Yamamoto group, Wagner group, and Berteina-Raboin group.⁸⁶⁻⁸⁸ While many Suzuki coupling reactions typically require elevated temperatures, often exceeding 80°C, there have been successful instances of Suzuki reactions conducted at rt.^{89,90} For instance, a recent breakthrough by Serrano *et al.*⁹¹ introduced Quadrol-Pd(II) as a phosphine-free catalyst for the aqueous Suzuki synthesis of unprotected nucleoside derivatives at rt.

Suzuki coupling conditions were applied to the unprotected and protected nucleosides. The main purpose of utilizing protected nucleosides was to prevent side reactions between the functional groups of substrates and the ribose hydroxy groups. In recent years, numerous Suzuki-coupling methods have been developed for unprotected nucleosides. Prior to these advancements, Suzuki coupling reactions were conducted using protected nucleosides due to their lipophilic properties, since conventional Suzuki coupling was traditionally performed in organic solvents. Common protecting groups employed Suzuki coupling reactions include the 2'-3'-isopropylidene,^{92,93} silyl groups,^{94,95} and acetylated groups^{96,97}.

2.2 Objectives

The substituent in position 5 of the prototype inhibitor 5-FT UDP-Gal is crucial for GalT inhibitory activity as it blocks the enzyme in a catalytically inactive conformation. Hence, Jiang *et al.*⁴² retained the 5-position fragment but removed the pyrophosphate and sugar of 5-FT UDP-Gal for cell application. While there were improvements in cell permeability and stability, there was a simultaneous decrease in inhibitory activity (**Scheme 3**). Therefore, the objective of this Chapter was to determine the most favourable 5-substituent and orientation for the nucleosides (**Scheme 3**, Class 1 inhibitors). This sought to offer insights for the design of a new class of compounds.



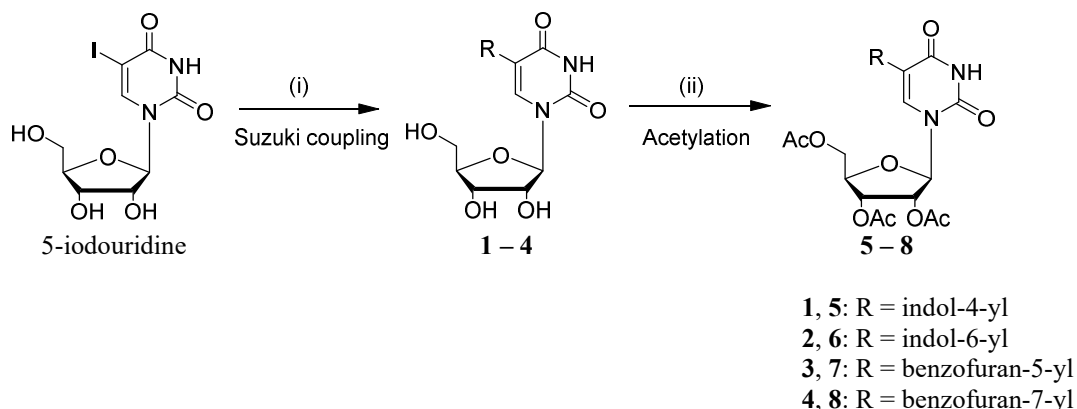
Scheme 3 Class 1 inhibitors with various substituents in position 5

The activity evaluation comprised biochemical assessments, including Malachite-Green and HPLC-based assays, targeting mammalian $\beta 4GalT$ s (see 2.4 and 2.5). Molecular modelling was utilized to offer a rational explanation for the observed experimental outcomes. Following this, cellular activity studies were carried out, including IgE glycoengineering (see 2.6). Additionally, biochemical evaluations of other GTs (LgtC, SetA, and LtpM) were employed

as target enzymes in the DSF binding assay (see 2.7). Each assay is introduced prior to the corresponding results in each section.

2.3 Synthesis of 5-substituted uridine derivatives 1 – 8

At the beginning of the project, compounds **1** and **2**, featuring indol-4-yl and indol-6-yl groups, were chosen as the initial candidates, due to their superior inhibitory activity against β 4GalT1 amongst the tested 5-substituted nucleosides in assays conducted by Jiang *et al.*⁴² **1** and **2** were obtained by Suzuki-Miyaura coupling of 5-iodouridine with corresponding heteroaryl acids (**Scheme 4**). Despite using conventional techniques over microwave reactions, a 99 % conversion of **1** and **2** was observed. These nucleosides possess a relatively polar nature which require purification via reverse phase column chromatography or crystallization. Both purification methods can result in a significant loss of material. Given this, **1** and **2** were directly employed in the subsequent acetylation step without undergoing additional purification. The employment of peracetylated sugars and nucleosides is a well-established pro-drug strategy, given that the acetyl groups can be easily removed by intracellular carboxylesterases. This approach resulted in yields of 70 % and 83 % for **5** and **6** individually over 2 steps, which were intended for use in cell applications. Notably, the yield of inhibitor **5** was substantially improved compared to the published results, which reported a 35 % yield over two steps.⁴² This may be attributed to the omission of column chromatography purification at first step.



Scheme 4 Synthesis of 5-substituted nucleosides **1 – 4** and their pro-drugs **5 – 8**. Reagents and conditions: (i) boronic acid (1.5 equiv.), Na_2PdCl_4 (2.5 mol%), TPPTS (6.3 mol%), Cs_2CO_3 (2.0 equiv.), degassed water, N_2 , 120 °C, 1 – 4 h; (ii) DMAP (0.05 equiv.), Ac_2O (3.5 eq.), pyridine, rt, 14 – 36 h, 70 % – 84 % over two steps.

In order to identify favourable substituents and orientations of the nucleosides against $\beta 4\text{GalT1}$, nucleosides with benzofuran substituents were also designed. This design took into account their expected capacity for hydrogen bonding and/or pi stacking interactions with target enzymes. Specifically, we prepared 5-(benzofuran-5-yl) uridine (**3**) and 5-(benzofuran-7-yl) uridine (**4**), along with their corresponding acetylated derivatives (**Scheme 4**). The combined yields for the two steps of **7** and **8** reached to 78 % and 84 %, respectively (**Scheme 4**).

2.4 $\beta 4\text{GalT1}$ inhibition assays and molecular modelling of **1 – 4**

The inhibitory activity of compounds **1 – 4** against $\beta 4\text{GalT1}$ was initially assessed using Malachite-Green inhibition assays (see 2.4.1). Molecular modelling was employed to rationalise the experimental outcomes (see 2.4.2).

2.4.1 β 4GalT1 inhibition assays of 1 – 4

To evaluate the inhibitory potential of these derivatives, a glycosyltransferase assay coupled with a phosphatase was employed.⁹⁸ The assay utilized calf intestinal alkaline phosphatase (CIP) to efficiently remove inorganic phosphate from the nucleoside diphosphate, which is produced as a secondary reaction product during glycosylation. The concentration of phosphate is measured using a colorimetric assay at 620 nm. When inhibitors are present, the absorbance signal is diminished (**Figure 18**). This assay can be employed to assess the potency of inhibitors by determining their individual IC_{50} values. The published results indicate that an enzyme turnover between 20 – 50 % of the UDP-Gal donor presents a reproducible assay window. In this project, it has been observed that enzyme turnover within the 10 % – 20 % range also yields reproducible and comparable results.

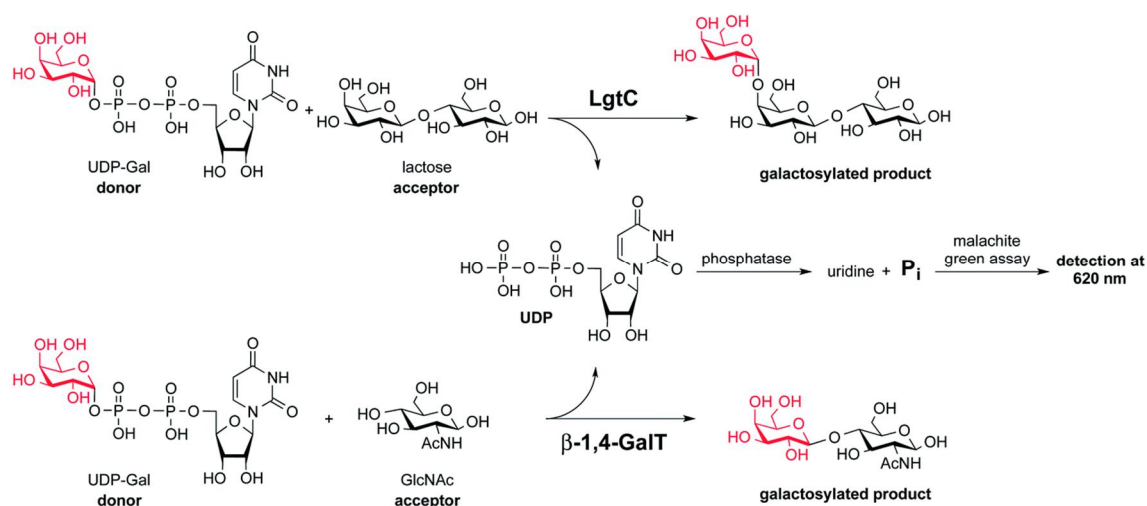


Figure 18 The GalT reactions and the malachite green assay⁹⁸

In the malachite green assay, **1** and **2** exhibited IC_{50} values of 4.8 ± 0.45 mM and 2.4 ± 0.39 mM against β 4GalT1, respectively (**Figure 19**). These values are approximately ten times higher than previous research,⁴² where IC_{50} values of these two identical inhibitors were

reported as $207 \pm 37 \mu\text{M}$ and $250 \pm 24 \mu\text{M}$, respectively. While there is no obvious explanation at the present time for this discrepancy, it may be worth noting that the results were obtained in different laboratories by different operators. The two other inhibitors, **3** and **4**, featuring a benzofuran group at position 5 of the nucleoside, displayed IC_{50} values of $1.9 \pm 0.34 \text{ mM}$ and $3.8 \pm 0.48 \text{ mM}$, respectively (**Figure 19**). Overall, all four compounds demonstrated comparable inhibitory activities, in which 5-(benzofuran-5-yl) uridine **3** exhibited slightly better activity, while 5-(indol-4-yl) uridine **1** displayed slightly less potency.

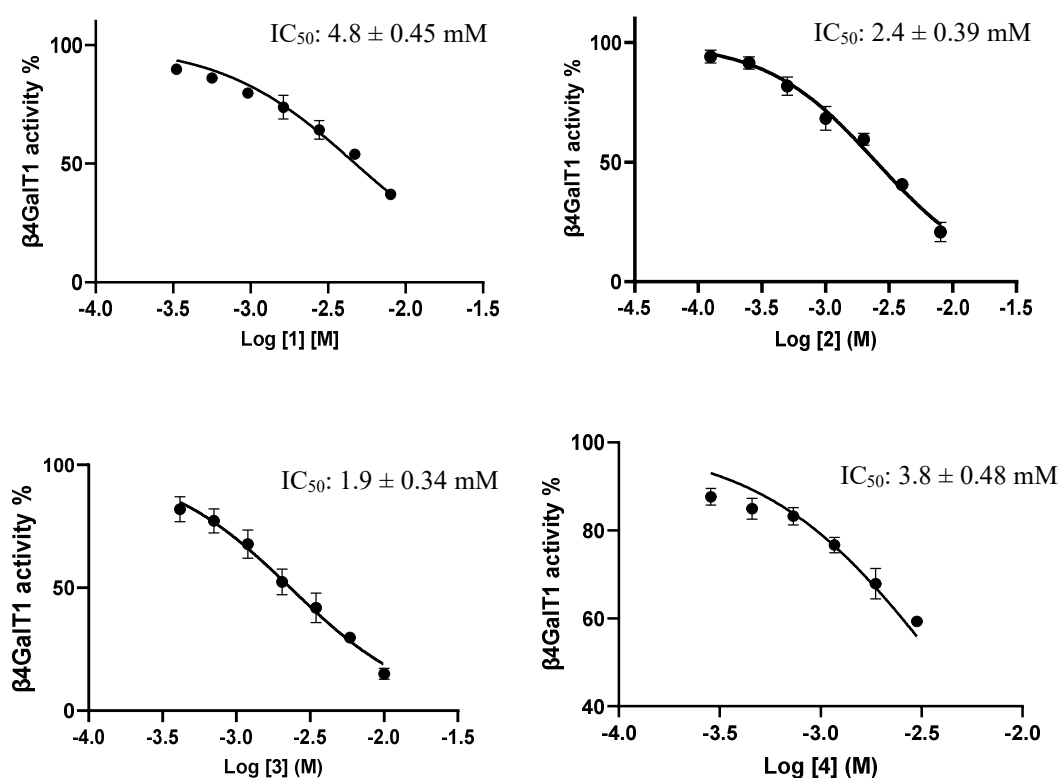


Figure 19 Determination of IC_{50} values for **1** – **4** against $\beta 4\text{GalT1}$. Reagents and conditions: $\beta 4\text{GalT1}$ ($1 \mu\text{g/mL}$, turnover: 17 %, 11 %, 16 % and 22 % for **1** – **4**, respectively), UDP-Gal (33 mM), GlcNAc (10 mM), CIP (10 U/mL), MnCl_2 (5 mM), lysozyme (1 mg/mL), Triton X (0.01 %), MnCl_2 (5 mM), KCl (50 mM), HEPES (pH 7.5, 10 mM), DMSO (10 %) and inhibitors series dilutions were incubated in a 96-well plate at $30 \text{ }^\circ\text{C}$ with shaking for 20 min. The reaction was stopped by adding malachite reagents. The absorbance was measured at 620 nm in 1 h. Bars indicate mean values \pm S.D. of the triplicates in a single experiment. Each experiment was repeated three times.

2.4.2 Molecular modelling of **1** – **4** with β 4GalT1

To further understand the activity results, molecular modelling of β 4GalT1 was conducted. Considering two flexible loops are near the binding sites of β 4GalT1, Molecular Dynamic (MD) simulations were employed to simulate movements and interactions of ligands with target enzymes over time. We chose the pose that exhibited both a good superimposition with natural ligand of β 4GalT1 (PDB: 1FR8) and the highest docking score using Glide docking in Schrodinger, followed by MD simulations using CharmmGui and Amber.

In MD simulations, Root Mean Square Deviation (RMSD) is commonly used parameter that describes the stability of the protein and/or ligand. It quantifies the average movement of atoms during a designated time interval (100 ns was used here), typically expressed in Ångströms (Å). A lower RMSD value for a ligand in a protein-ligand complex indicates a more stable ligand in the binding side. RMSD values on the order of 1 – 2 Å or lower are often considered acceptable for stable structures. RMSD values of **1** and **4** suggested they were unstable within the binding site of the β 4GalT1 (**Table 1**). These results were consistent with experimental IC_{50} values. **1** and **4** demonstrated slightly poorer inhibitory activities compared to **2** and **3**. These results were almost consistent with IC_{50} values (higher RMSD, less potency). In addition, the energy calculations did not reveal significant interactions between the ligands and proteins. This could potentially explain why they did not show the anticipated activity, in contrast to what was reported in the published results⁴².

Table 1 Root-Mean-Square Deviation (RMSD)^a and IC₅₀ of **1** – **4**

Compound	1	2	3	4
IC ₅₀ (mM)	4.8 ± 0.5	2.4 ± 0.4	1.9 ± 0.3	3.8 ± 0.5
RMSD (Å)	4.9 ± 2.9	1.9 ± 0.6	2.2 ± 0.4	3.0 ± 0.5

^a RMSD values were calculated based on non-hydrogen atoms for both the receptor and ligand with VMD. The β4GalT1 structure (PDB: 1FR8) used was from the Protein Data Bank.

2.5 β4GalT7 inhibition assays of **1** – **4**

The inhibitory activity of compounds **1** – **4** against β4GalT7 were assessed in HPLC-based fluorescent assays conducted by Roberto Mastio at Lund University. β4GalT7 plays a vital role in the generation of heparan sulfate (HS) and chondroitin sulfate/dermatan sulfate (CS/DS) glycosaminoglycan (GAG) chains. GAG chains predominantly bind to a core protein, leading to the creation of proteoglycans (PGs), which play crucial roles in regulating various biological functions⁹⁹ and the pathobiology across all stages of cancer progression.^{100–102}

β4GalT7 participates in post-xylosylation (**Figure 20a**)¹⁰³ in the GAG biosynthesis process, which can also be triggered by xylosides containing hydrophobic aglycons (i.e., 2-naphthyl β-D-xylopyranoside (XylNap)), catalyzed by β4GalT7 (**Figure 20b**).^{104,105} Exogenously added xylosides can serve as acceptors within cells and can therefore offer a simplified model system for GAG biosynthesis.

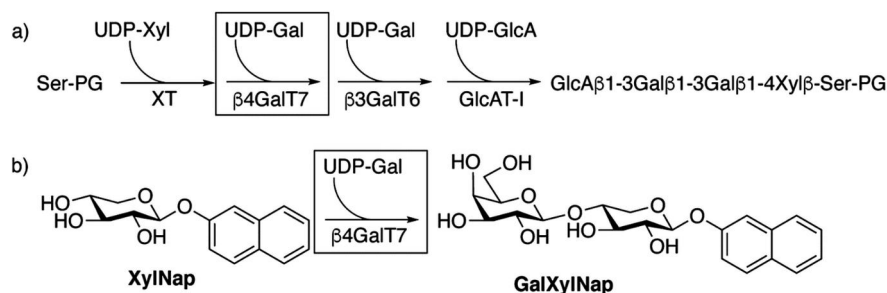


Figure 20¹⁰⁷ (a) GAG biosynthesis process. (b) Galactosylation with XylNap as substrate

For the assessment of galactosylation activity and inhibition of $\beta 4\text{GalT7}$, the Ellervik research group developed a cell-free assay, utilizing a 96-well plate layout suitable for high-throughput analysis.^{106,107} The activity of $\beta 4\text{GalT7}$ was evaluated by employing XylNap as the acceptor substrate, UDP-Gal as the donor substrate. Consequently, GalXylNap emerged as the relevant first-order dependent product. The reaction was examined through HPLC with fluorescence detection. During assessment, a fixed quantity of XylNap was added along with varying concentrations of inhibitors, and the quantity of generated GalXylNap was determined. A reduction in GalXylNap formation, relative to the control, signifies that the substance functions as an inhibitor of $\beta 4\text{GalT7}$ (**Figure 21**).

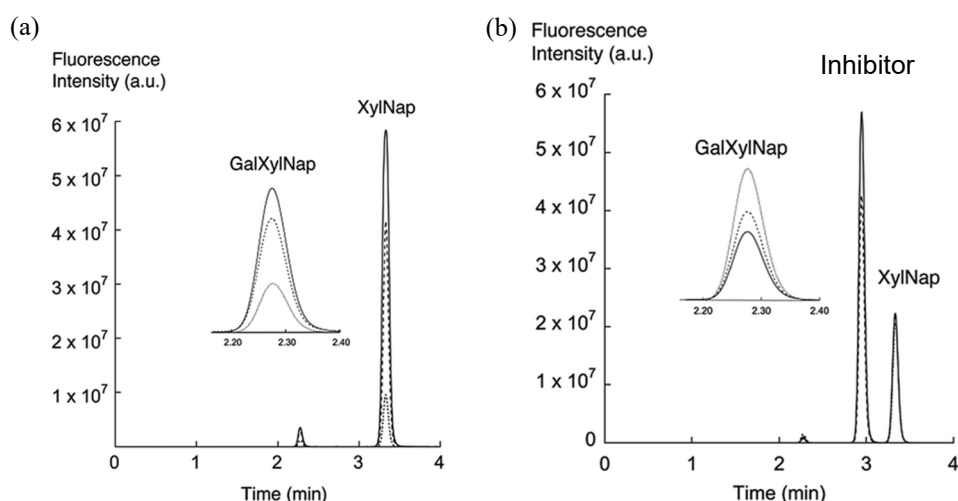


Figure 21¹⁰⁷ Galactosylation (a) and inhibition (b) of $\beta 4\text{GalT7}$ via HPLC-based fluorescent assessment. (a) The peak of GalXylNap shows an upward trend with rising concentrations of XylNap, 0.25 mM, 1.0 mM and 2.0 mM respectively. (b) The peak of GalXylNap demonstrates a downward trend as the inhibitor concentration increases, 0 mM, 0.5 mM and 1.5 mM, respectively.

1 – **4** were examined upon evaluation with the aforementioned assay. **1** and **3** displayed no inhibition towards the enzyme, whereas **4** demonstrated weak inhibition. Unusually, **2** did not show inhibition but strong activation, reaching up to 45 % at 1 mM concentration (**Figure 22**). In the repeated assay with 11 dilution steps, the activation reached to 154 % at 1 mM. The enzyme activity observed in this assay was significantly higher compared to previous single round, potentially attributed to the degradation of the enzyme. The limited amount of UDP-Gal used in this assay might have resulted in an upper activation limit, i.e., all UDP-Gal was used up (**Figure 23**). The activation activity of **2** suggested it might bind at a putative allosteric site of β 4GalT7 rather than the donor binding site. Further investigation of the glycan profile involved in GAG biosynthesis induced by **2** within cells is necessary.

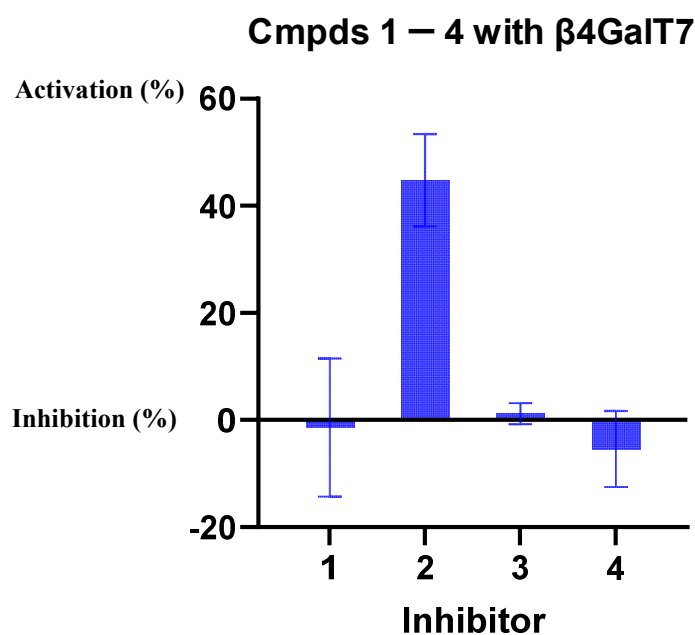


Figure 22 Activation and inhibition of galactosylation by β 4GalT7 in the presence of **1** – **4** at 1 mM. Each experiment was carried out in duplicate. Bars indicate mean values \pm S.D. of the duplicates in a single experiment. The data was obtained by Roberto Mastio.

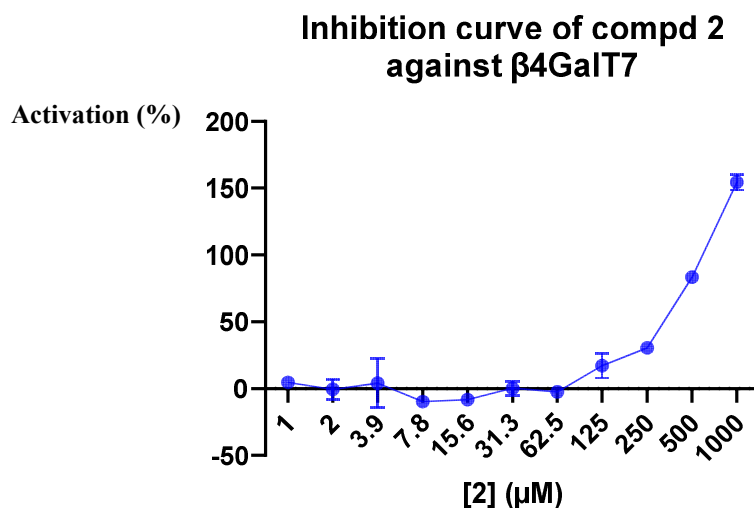


Figure 23 Activation of galactosylation by β 4GalT7 in the presence of **2** from 1 mM with a dilution factor of 2 across a series of 11 sequential dilution steps. Bars indicate mean values \pm S.D. of the duplicates in a single experiment. The data was obtained by Roberto Mastio.

2.6 Cell assays of **5** – **8**

Cellular activity evaluations were conducted by Alex McCraw. The assessment involved cell viability, degranulation and IgE glycoengineering. The IgE analysis included glycan lectin blots and tentative glycan assignment.

2.6.1 Effect of uridine derivatives **5** – **8** on cell viability

In the evaluation of cellular viability for compounds **5** – **8**, which represent the acetylated form of **1** – **4**, they displayed tolerance levels up to 250 μ M (**Figure 24**). However, beyond this concentration, there was a noticeable increase in the number of deceased cells compared to viable ones. Hence, a concentration of 150 μ M was utilized for IgE production and glycan analysis.

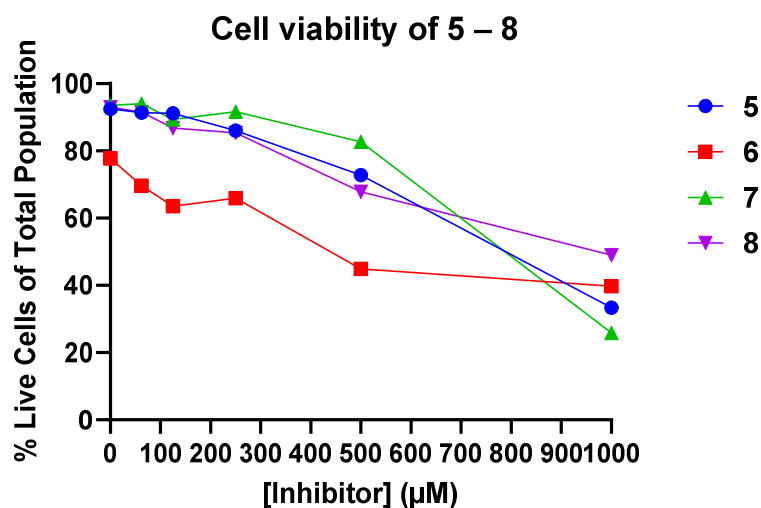


Figure 24 Cell viability of 5 – 8. Expi-HEK293F cells seeded at 5×10^6 cells/ml (standard concentration for protein production) on Day 1 and harvested on Day 3 following incubation with known concentrations of inhibitor. The data was obtained by Alex McCraw.

2.6.2 Effect of uridine derivatives 5 – 8 on degranulation

From the degradation assessment, inhibitors 5 and 6 exhibited reduced degranulation in comparison to the control (**Figure 25**), indicating a potential impairment in their capacity to signal through FcεRI (or potentially even bind it), possibly due to alterations in glycosylation that have likely induced structural or functional modifications.

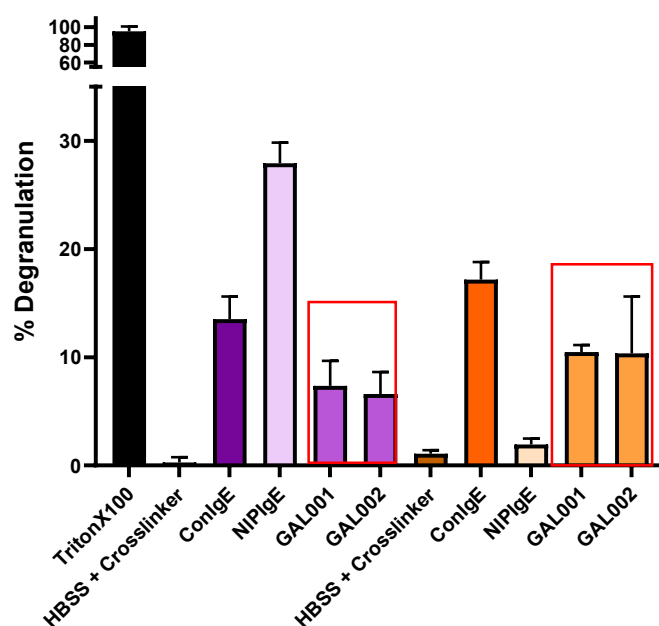


Figure 25 Degranulation results of compound **5** and **6**. Purple: as control, non-specific crosslinker (anti-IgE); Orange: specific crosslinker, A2058 cells expressed with CSPG4 (antigen which all IgEs are specific for). GAL001 = 150 μ M (inhibitor **5**); GAL002 = 150 μ M (inhibitor **6**); ConIgE = unmodified control IgE; NIP-IgE = non-specific control IgE. The data was obtained by Alex McCraw.

2.6.3 Initial glycoanalysis of IgE glycoforms obtained in the presence of uridine derivatives **5** and **6**

Lectin blot assessment was employed to evaluate how the inhibitors affect the glycans expressed in IgE in comparison to the unmodified IgE, exemplified with compound **5** and **6**. Compound **5** exhibited a slight inhibitory effect on all four glycans, whereas compound **6** led to an increase in the levels of all four glycans (**Figure 26**). It appears both inhibitors displayed a lack of selectivity with respect to these four sugars.

There are three possible explanations for the observed results: (1) The inhibitor is not specific for GalTs, instead, it functions as a broad-spectrum inhibitor, affecting other glycosyltransferases like FucTs, SiaTs, and ManTs as well. (2) The inhibitor inhibits a GT in

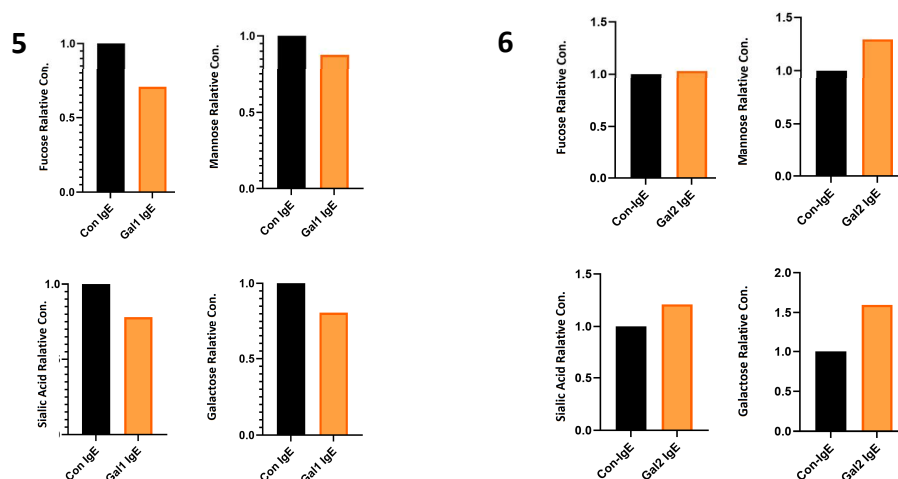


Figure 26 Initial glycan analysis of **5** (left) and **6** (right) performed via lectin blot. Comparing glycosylation of variants produced in Expi-HEK293F cells treated with inhibitors compared to an unmodified IgE produced in the same system (150 μ M). The experiment was carried out in a single instance. The data was obtained by Alex McCraw.

the early stages of glycan biosynthesis, preventing the subsequent addition of molecules such as Gal and Fuc. (3) The inhibitor acts through a distinct mechanism that is independent of GTs. (4) The lectin blots recognised were terminal sugars. The results mentioned above indicated an increase in all four glycans—Galactose, Mannose, Fucose and Sialic acid – which implies the quantity of terminal GlcNAc underwent a corresponding inverse change. (5) The addition of both inhibitors impacted IgE production, subsequently resulting in either an increase or decrease in total glycans.

From the tentative glycan assignment via HPLC-MS of the two IgE variants in relation to compound **5** and **6** at 150 μ M, it appears no apparent reduction exists in the abundance of galactose or sialic acid. (**Figure 27** – **Figure 29**) This suggests that compound **5** and **6** might not be specific galactosyltransferase inhibitors. Considering their poor tolerance and the observed effects, it is probable that they are targeting an enzyme in an early stage of the glycan production process. These unexpected, and seemingly paradoxical, effects may at least in part be influenced by the relatively modest potency of these inhibitors.

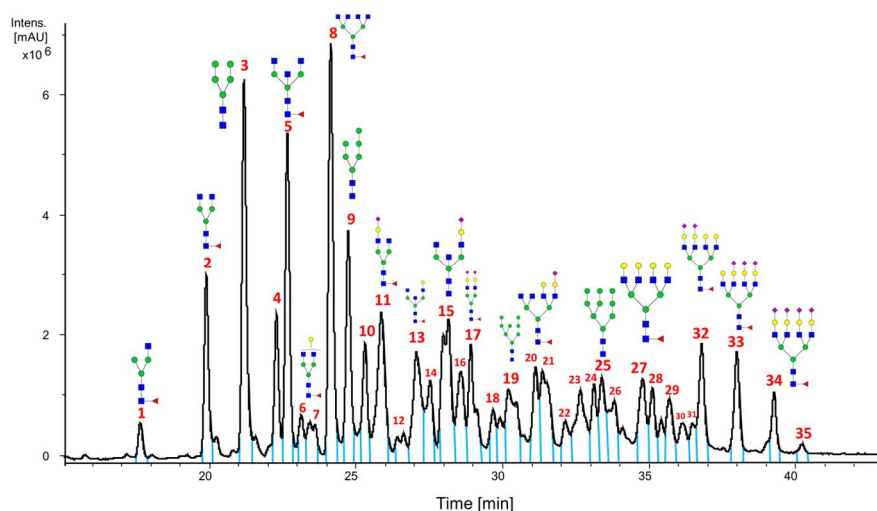


Figure 27 The HPLC-FD chromatogram of HEK CSPG₄ IgE Control, with suggested glycan structures assigned to the main peaks, determined by analyzing m/z masses and predicted monosaccharide compositions. The data was obtained by Alex McCraw, Dr Richard Gardner (Ludger Ltd) and Dr Daniel Spencer (Ludger Ltd).

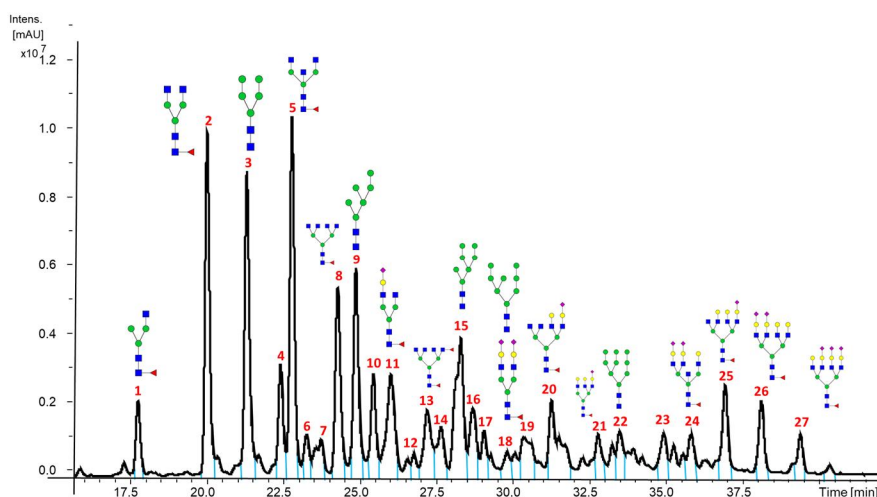


Figure 28 HPLC-FD chromatogram of HEK CSPG₄ IgE-inhibitor **5**, with suggested glycan structures assigned to the main peaks, determined by analyzing m/z masses and predicted monosaccharide compositions. The data was obtained by Alex McCraw, Dr Richard Gardner (Ludger Ltd) and Dr Daniel Spencer (Ludger Ltd).

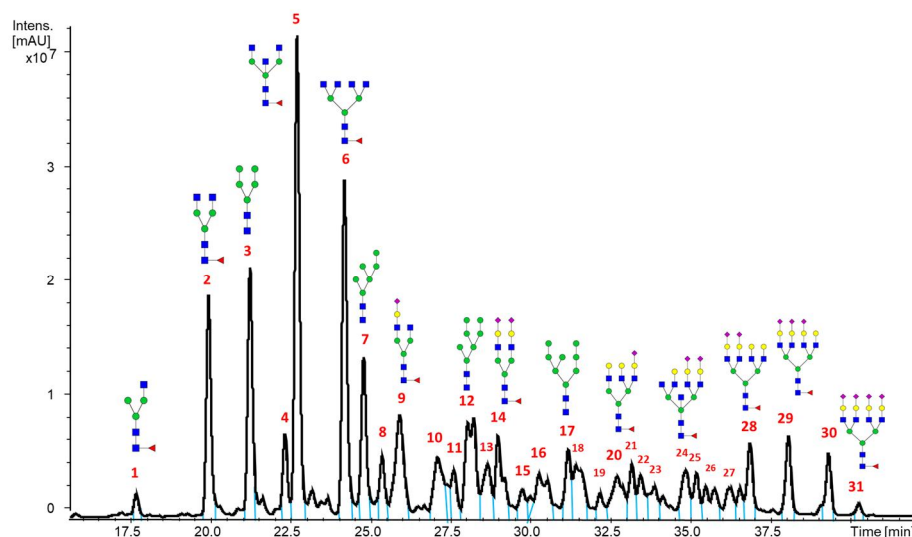


Figure 29 HPLC-FD chromatogram of HEK CSPG₄ IgE-inhibitor **6**, with suggested glycan structures assigned to the main peaks, determined by analyzing *m/z* masses and predicted monosaccharide compositions. The data was obtained by Alex McCraw, Dr Richard Gardner (Ludger Ltd) and Dr Daniel Spencer (Ludger Ltd).

2.7 Bacterial enzymes: binding assays with 1 – 4

To evaluate the binding of our inhibitors to other UDP-sugar-dependant GTs, Differential Scanning Fluorimetry (DSF) was employed. DSF was used to evaluate the binding affinity between the ligands and proteins. Compared to the inhibitory activity assay, DSF is simple and requires minimal sample preparation, making it suitable for high-throughput screening. DSF measures the melting temperature (T_m) of a biomolecule, indicating when it undergoes structural changes like unfolding. DSF works by tracking changes in the fluorescence of a dye binding to exposed hydrophobic regions during proteins unfolding. SYPRO Orange is often used for this purpose. As the temperature rises, proteins undergo structural changes, leading to increased or decreased fluorescence intensity (**Figure 30**).

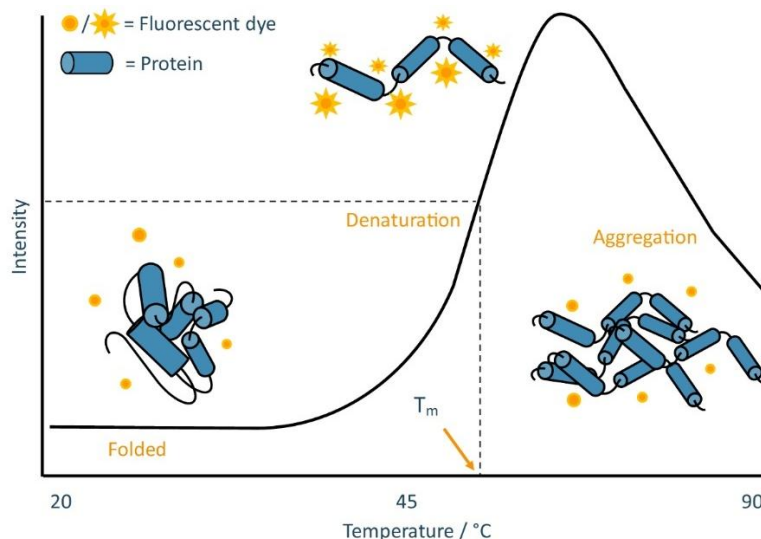


Figure 30 Fluorescence intensity and temperature correlation during the thermal unfolding of proteins in the presence of SYRPO Orange dye¹⁰⁸

The T_m shift caused by an inhibitor reflects its influence on the thermal stability of the protein. If an inhibitor stabilizes the protein, it may result in a higher T_m compared to the control (without the inhibitor). This shift indicates that the protein requires a higher temperature to undergo unfolding, suggesting increased stability in the presence of the inhibitor. Conversely, if an inhibitor destabilizes the protein, the T_m may decrease compared to the control. This shift implies that the protein unfolds at a lower temperature, indicating reduced stability in the presence of the inhibitor.

Compound **1** – **4** were measured in the DSF assay against LgtC, SetA and LtpM. Compound **2** – **4** exhibited moderate binding activity and demonstrated selectivity against SetA over LgtC and LtpM (**Table 2**). These results suggested **2** – **4** can potentially exhibit effective inhibitory activity against SetA. This result is intriguing, given that SetA and LtpM exhibit structural similarity. Both SetA and LtpM serve as glucosyltransferases, acting as effector proteins in *Legionella pneumophila*, and exhibit identical conserved residues in their respective binding pockets. Further elucidation of this finding necessitates additional inhibition assays.

Table 2 Melting temperature (T_m) shifts of **1** – **4** in DSF assay^a

Entry	Compound	ΔT_m (°C)		
		LgtC	SetA	LtpM ^b
1	1	<2	<2	<2
2	2	<2	2.5 ± 0.3	<2
3	3	<2	2.4 ± 0.2	<2
4	4	<2	2.3 ± 0.2	<2

Each experiment was carried out in triplicate. The experiment that demonstrated a deviation of more than two degrees was repeated twice. ^a The concentrations were from 2 to 0 mM with a dilution factor of 2 across 3 sequential dilution steps. The ΔT_m (°C) was calculated at 2 mM. ^b The data was obtained by David Matthews.

2.8 Summary and conclusions

Previously, uncharged 5-substituted nucleosides were discovered to exhibit moderate inhibitory activity and enhanced cell permeability against mammalian β 4GalT1. However, their potency was found to be 20 – 30 times lower than the nucleotide inhibitor, 5-FT UDP-Gal. To find the most favourable substituent and orientation for the nucleosides, alternative substituents at position 5 were investigated. This was expected to provide insights for the design of a new class of compounds. Four target molecules **1** – **4** (Class 1 inhibitors) were synthesized with Suzuki-coupling as the key step. **1** – **4** were investigated to evaluate their biochemical activity. Their pro-drugs **5** – **8** were made through acetylation for cellular applications.

1 – **4** were tested for their inhibitory activities against recombinant mammalian GalTs: β 4GalT1 and β 4GalT7. Malachite Green inhibition assay indicated **1** – **4** shared comparable inhibitory activity against β 4GalT1 (IC_{50} : 1.9 – 4.8 mM), aligning with the results obtained from molecular modelling. An intriguing observation was made by compound **2** which demonstrated

an unexpected activation of up to 154 % towards β 4GalT7. This suggested **2** might bind at a putative allosteric site of β 4GalT7 rather than the donor binding site.

Cell viability assessment showed that **5 – 8** demonstrated tolerance levels of up to 250 μ M. **5** exhibited a slight inhibitory effect on all four IgE sugars, whereas **6** led to an increase in the levels of all four IgE glycans. Both inhibitors appear to lack selectivity with respect to these four sugars. Regarding the IgE level, there appears to be no noticeable reduction in the prevalence of galactose or sialic acid. These unexpected, and seemingly paradoxical, effects may at least in part be influenced by the relatively modest potency of these inhibitors.

Bacterial sugar-UDP-dependant GTs (LgtC, SetA and LtpM) were assessed using a DSF binding assay. **2 – 4** exhibited moderate binding with SetA (ΔT_m : 2.3 – 2.5 $^{\circ}$ C) in comparison with LgtC and LtpM ($\Delta T_m < 2$ $^{\circ}$ C). This observation suggested **2 – 4** had the potential to selectively target SetA over LgtC and LtpM. Further clarification of this result is required through additional inhibition assays.

Chapter 3

Conformationally restricted uridine derivatives – Target Class 2

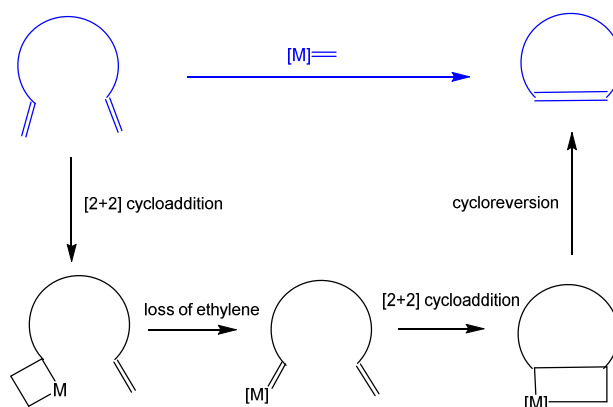
3. Conformationally restricted uridine derivatives (Target Class 2)

3.1 Introduction

This Chapter describes the synthesis of Class 2 inhibitors. The key feature of these uridine analogues is the presence of a macrocycle, which connects the 5'-position of the ribose with the substituent at position 5 of the uracil base. This macrocycle was going to be generated via a ring-closing reaction. Prior to presenting the results, a review on ring-closing reactions is therefore provided. Ring-closing reactions can be challenging because the resultant ring strain poses a significant energy barrier that must be overcome for the reaction to proceed. Common ring-closing reactions include Ring-Closing Metathesis (RCM), lactonization, cross-coupling, etherification, electrophilic substitution reaction and dehydration reaction. Generally, the two uncyclized parts are connected by an alkenyl chain with varying length. In this project, three strategies for macrocyclization were investigated, RCM, macrolactonization and Heck macrocyclization.

3.1.1 Ring-Closing Metathesis (RCM)

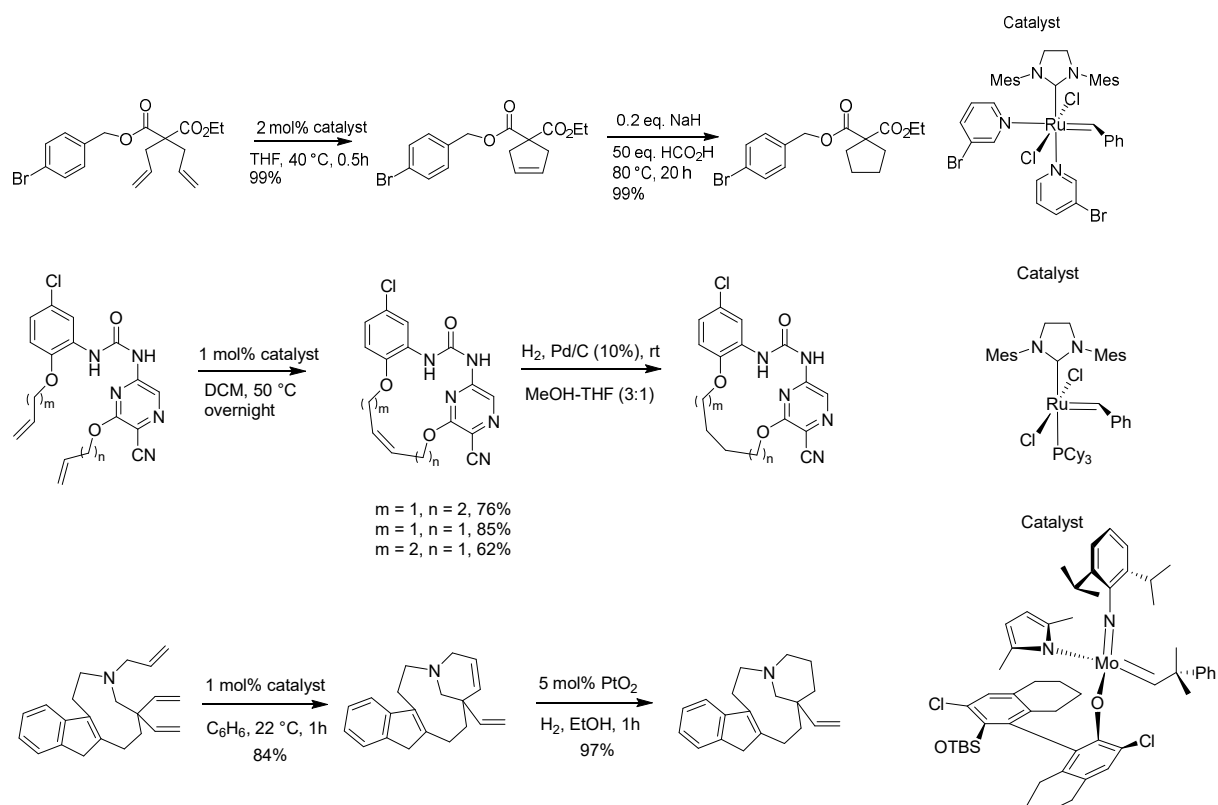
Ring-Closing Metathesis (RCM) is a common approach for creating macrocycles, yielding a double bond that can be subsequently reduced to an alkyl chain. RCM reactions are initiated by transition metals such as ruthenium and advance through an intermediate stage known as metallacyclobutane. The driving force behind the cyclization reaction was ascribed to the entropic advantage achieved through the release of a volatile gas, ethylene (**Scheme 5**).



Scheme 5 Mechanism of olefin metathesis

Robert Grubbs and Richard Schrock significantly advanced the utility of RCM reactions.^{109, 110} The catalysts were represented by Schrock catalyst, Grubbs catalyst I to III, and Hoveyda-Grubbs catalyst (**Figure 31**).¹¹¹ They were widely employed in RCM reactions (**Scheme 6**)^{112–114}. Schrock synthesized the first well-defined single-component metathesis catalysts, which are known for their impressive catalytic activity, but they are constrained by high sensitivity and limited capacity to tolerate various functional groups.¹¹⁵ Apart from changing the chelating metal from molybdenum to ruthenium, Grubbs *et al.* also illustrated that phosphine dissociation stands as a pivotal stage within the olefin metathesis process. Their research indicated that catalysts featuring phosphine ligands possessing both substantial steric clashes and electron-donating properties exhibit the most elevated levels of catalytic activity.¹¹⁶ Therefore in the second-generation ruthenium catalysts, they replaced trialkylphosphines of Grubbs I with N-heterocyclic carbene (NHC) which are notably bulkier and exhibit greater electron-donating characteristics. Apart from that, various other functional groups exert varying degrees of influence on catalytic activity, such as the halogen and benzylidene group.¹¹⁷ Based on this, a multitude of diverse ruthenium catalysts have emerged. However, they still have limitations such as elevated temperatures, the need for high dilution, and extended reaction time.¹¹⁸

Compared to Grubbs catalysts, Hoveyda–Grubbs catalysts also emerged in succession which were famous for their improved stability.¹¹⁹ In the second generation of Hoveyda–Grubbs catalysts, the phosphine group was replaced by an oxygen group, which gives a phosphine-free catalyst. Different from 1st and Class 2 catalysts, the 3rd generation Grubbs catalysts are usually applied in the ring-open metathesis reactions due to their highly fast-initiating rates. Structurally, the phosphine was commonly replaced by two 3- bromopyridine groups.



Scheme 6 Ring-closing metathesis reactions

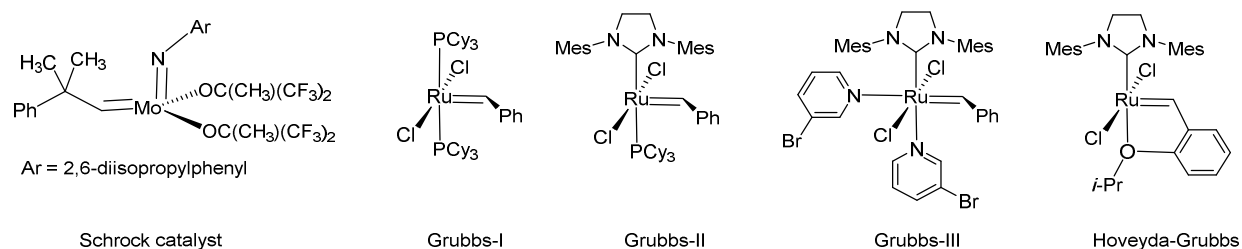
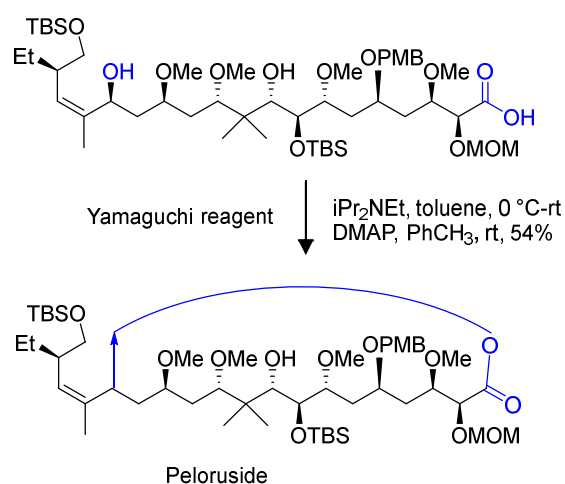


Figure 31 Common metathesis catalysts

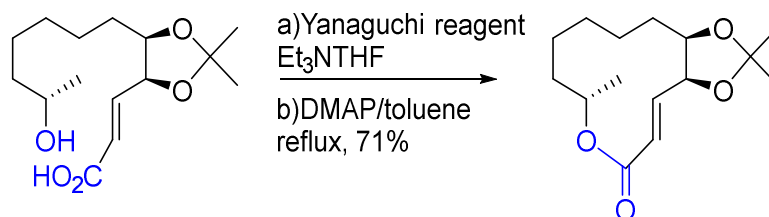
3.1.2 Macrolactonization

Lactonization has been widely applied in the field of macrocyclic synthesis, especially natural products, where the Mitsunobu and Yamaguchi conditions are most widely utilised. Here, the MNBA reagent and substrate of an unsaturated acid were also introduced.

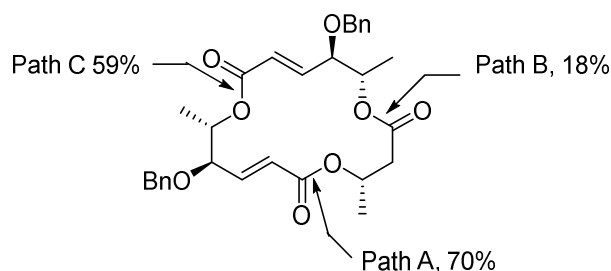
The Yamaguchi reagent is 2,4,6-trichlorobenzoyl chloride. The Yamaguchi esterification involves an alcohol and an aliphatic carboxylic acid, in the presence of the Yamaguchi reagent and DMAP. For example, Hoye *et al.*¹²⁰ achieved the synthesis of Peloruside A, employing the pivotal Yamaguchi cyclization as a key step in their methodology (**Scheme 7**). Si *et al.*¹²¹ successfully produced (+)-Cladospolide D, featuring a 12-membered ring, utilizing Yamaguchi lactonization as the crucial step (**Scheme 8**). In the work by Kobayashi *et al.* Macrophelides were prepared with three ester linkages through Yamaguchi lactonization (**Scheme 9**), and one of the exemplary cases demonstrating a high yield is outlined in **Scheme 10**.¹²²



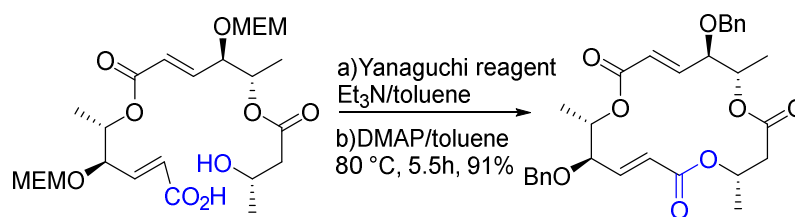
Scheme 7 Macrolactonization in Peloruside A synthesis



Scheme 8 Macrolactonization in the synthesis of (+)-Cladospolide D

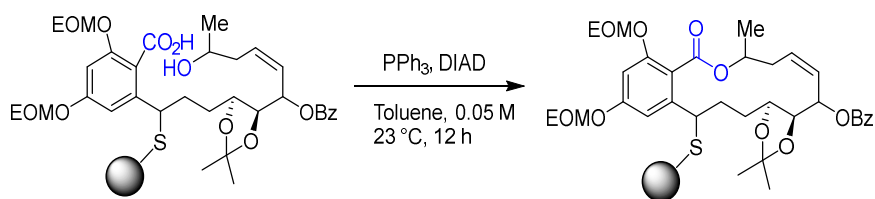


Scheme 9 Routes for Macrophelides lactonization



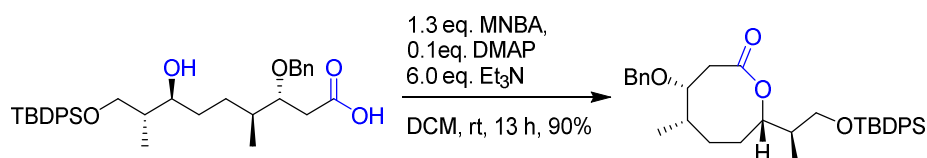
Scheme 10 Macrolactonization step in the synthesis of Macrophelide A

The Mitsunobu reaction is primarily employed to convert primary and secondary alcohols into various functional groups, such as esters, ethers, and other compounds, under mild conditions. It typically relies on the involvement of four essential components: a primary or secondary alcohol, a carboxylic acid, triphenylphosphine (PPh₃), and azo compounds like diethyl azodicarboxylate (DEAD) or diisopropyl azodicarboxylate (DIAD) to facilitate the reaction. As an illustration of ring-forming reaction, Dakas *et al.*¹²³ employed the Mitsunobu conditions as the strategy for conducting macrolactonization in their study (**Scheme 11**). Toma *et al.*¹²⁴ employed the intramolecular Mitsunobu reaction involving a primary alcohol to generate an amine as part of the process to construct a 15-membered ring.



Scheme 11 Macrolactonization with Mitsunobu conditions

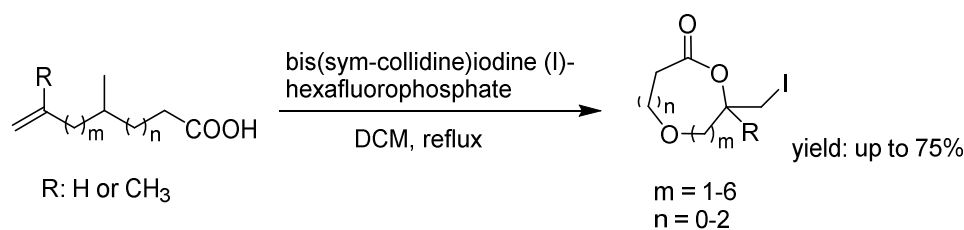
MNBA reagent (2-methyl-6-nitrobenzoic anhydride) is also an interesting lactonization reagent that can be utilized in the formation of macrocycles from hydroxycarboxylic acids. It was developed by Isamu Shinna in 2002. A good example was illustrated in the synthesis of Octalatin, where the macrocycle was formed in the presence of MNBA and a catalytic amount of DMAP with high yield (**Scheme 12**). Additionally, it was demonstrated that under concentrated conditions (100 mM), a dimeric product was obtained with a yield of 32%.¹²⁵ Although they did not provide an example of the macro-lactonization reaction involving a primary alcohol under the MNBA reagent, they did present a series of examples showcasing the regular lactonization process using primary alcohols.¹²⁶



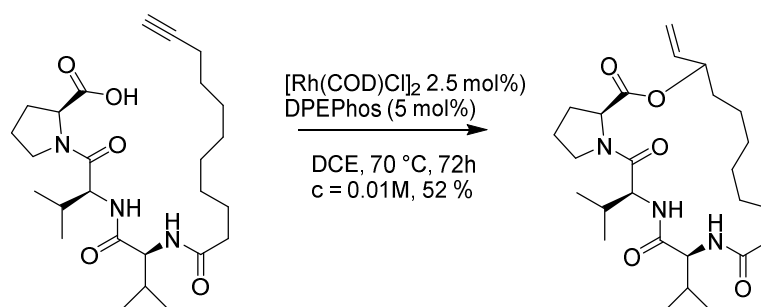
Scheme 12 Macrolactonization with MNBA reagent

In addition to hydroxycarboxylic acids serving as substrate for intramolecular lactonization, there have been reports of unsaturated acids being utilized for this process as well. For example, Simonot *et al.*¹²⁷ illustrated the formation of medium- to large-sized rings using iodo lactonization with bis(*sym*-collidine)iodine (I) hexafluorophosphate, in which an iodo group was introduced (**Scheme 13**). Additionally, Lumbroso *et al.*¹²⁸ reported a process in which

rhodium catalyzed the coupling reaction between carboxylic acids and terminal alkynes, leading to branched allylic esters. They documented the synthesis of macrolactones ranging from 12 to 23 members, featuring various functional groups. Furthermore, these conditions were applied to synthesize a complex natural compound, achieving a yield of 52 % (**Scheme 14**).¹²⁸



Scheme 13 Iodo lactonization



Scheme 14 Macrolactonization via rhodium-catalyzed coupling

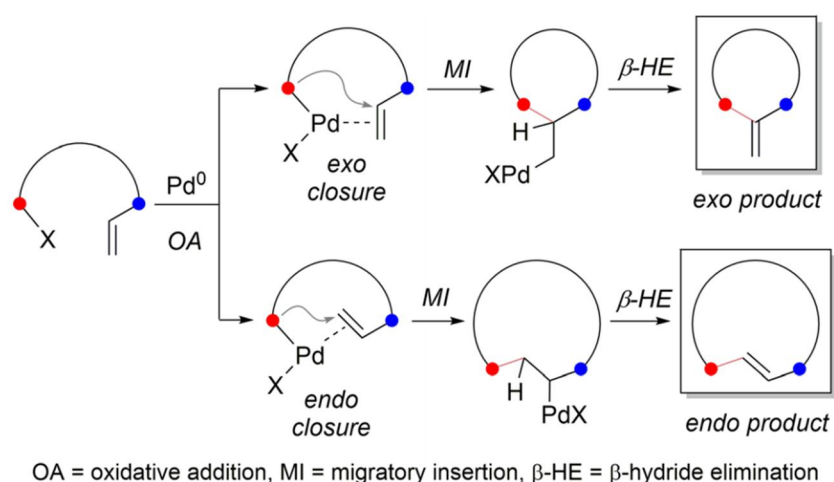
3.1.3 Heck macrocyclization

Intramolecular Heck cyclization naturally extends from the traditional Heck reaction where a covalent linkage forms between an alkene and a haloalkane or haloalkene. The main steps in Heck coupling are summarized as follows (**Scheme 15**):¹²⁹

- 1) pre-activated Pd(0) undergoes oxidative addition into the C(sp²)–X bond, forming an organopalladium species

- 2) the vinyl group coordinates with Pd(II)
- 3) ring-closing via migratory insertion between the C(sp²) and the vinyl group
- 4) the cyclization product (exo or endo) forms via β -hydride elimination

The type of product (exo or endo) is contingent on the size of the ring, which is affected by a complex interplay of electronic, steric and conformational factors. Generally, due to the steric demand of endo cyclization, small rings (3 – 7 members) tend to favor exo cyclization, while the macrocycles (≥ 12 members) predominantly yield endo products. Medium rings, on the other hand, often result in a combination of both.

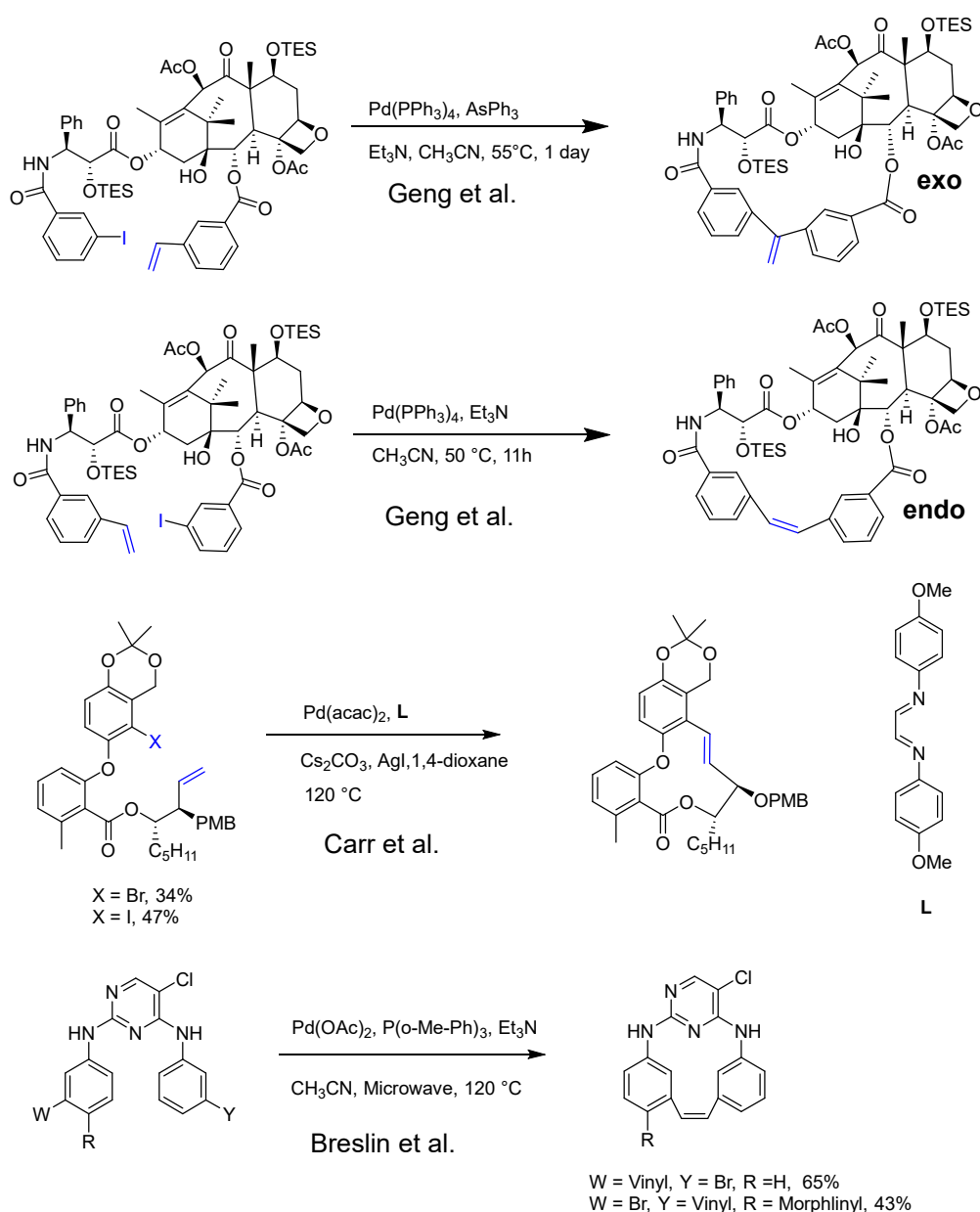


Scheme 15 Mechanism of Intramolecular Heck cyclization¹²⁹

While the intramolecular Heck reaction serves as a viable method for macrocyclization, it has received relatively little attention in recent decades compared to RCM and macrolactonization.

Geng *et al.*¹³⁰ synthesized macrocyclic Taxoids utilizing the intramolecular Heck reaction, which gives highly regioselectivity and functional group tolerance. By strategically altering the positions of the halo- and olefin functionalities, they achieved the formation of endo products

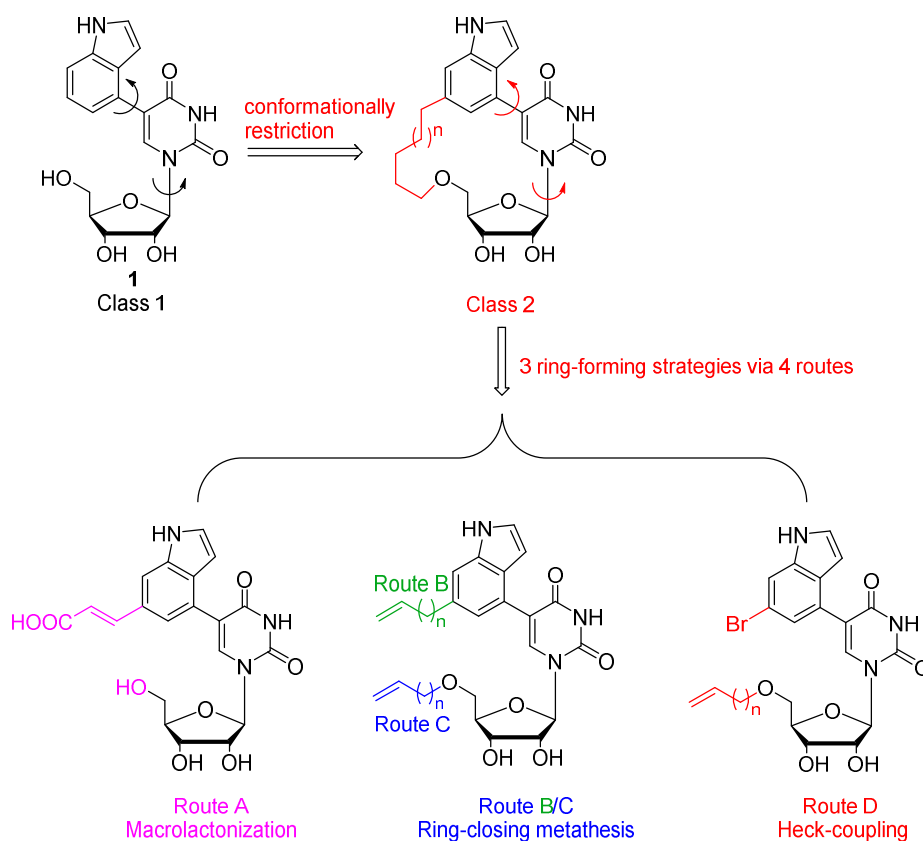
with an impressive regioselectivity of 100 %.¹³⁰ In addition to the widely utilized iodide reagent due to its higher reactivity, Carr *et al.*¹³¹ illustrated the application of Heck macrocyclization with aryl bromides. However, it is worth noting that the use of iodide still resulted in higher product yields in their study. Breslin *et al.*¹³² showcased the application of Heck macrocyclization to synthesize ALK inhibitors, incorporating bromo and olefin moieties in either aromatic position (**Scheme 16**).



Scheme 16 Intramolecular Heck reactions

3.2 Objectives

The results obtained from Class 1 inhibitors indicated that 5-substituted uridine derivatives **1** to **4** all displayed comparable inhibitory activity against β 4GalT1. In addition, **1** was the most synthetically accessible amongst Class 1 inhibitors. Therefore, we chose **1** as the structural basis for developing the conformationally restricted compounds in Class 2 inhibitors (**Scheme 17**). Recognizing the flexibility of the single bonds, a chain was introduced between the indole group and the 5'-O of ribose (**Scheme 17**). This introduction aims to constrain the conformational flexibility of the molecule.

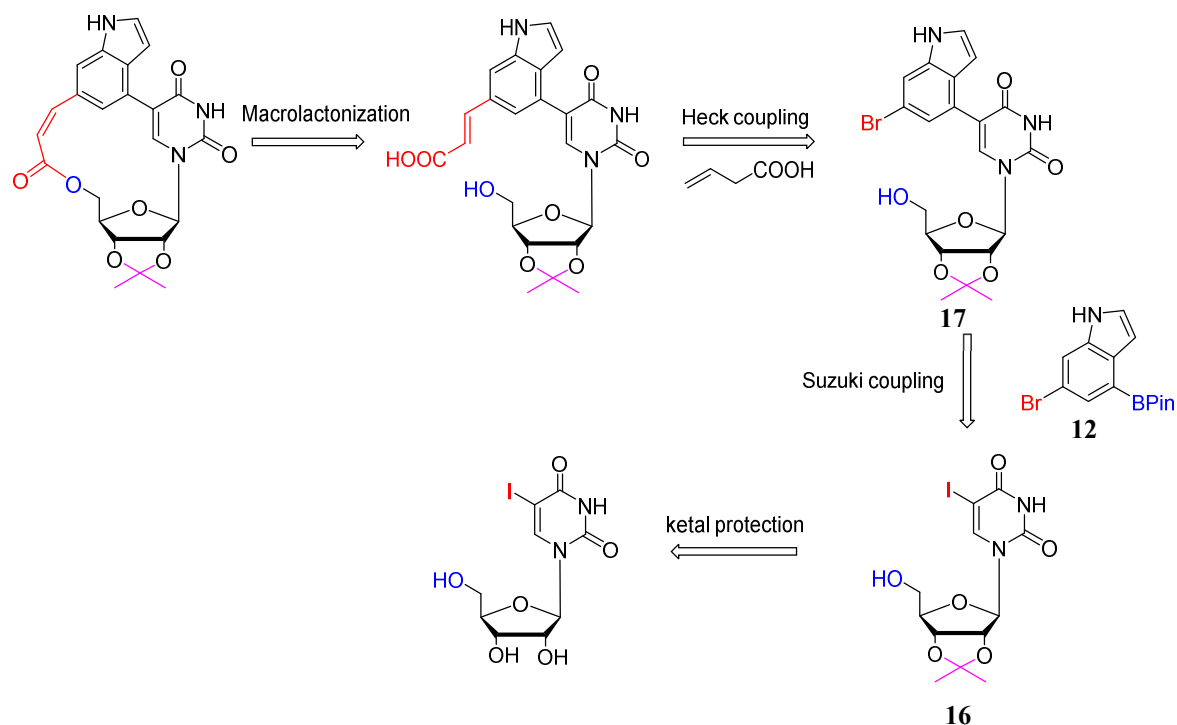


Scheme 17 Conformationally restricted Class 2 inhibitors with 3 ring-forming strategies via 4 synthetic routes

This Chapter provides an overview of the ring-closing reaction which is the pivotal step for the synthesis of Class 2 inhibitors. Three ring-closing strategies were employed in four synthetic routes in this Chapter (**Scheme 17**), including macrolactonization (route A, see 3.3) RCM (route B and C, see 3.4 and 3.5) and Heck macrocyclization (route D, see 3.6). In the case of our project, route D, featuring the Heck macrocyclization as the pivotal step, demonstrated a successful outcome. Whilst the other three routes did not yield the final compounds themselves, they produced several useful intermediates and synthetic insights that proved valuable in the development of the successful synthetic route. Activity assessment and molecular modelling of Class 2 inhibitors will be introduced in Chapter 4.

3.3 Attempted formation of the macrocycle via macrolactonisation (Route A)

To achieve macrocycles, macrolactonization as a ring-forming strategy was employed. One advantage is that only one group with a carboxyl group needs to be added to the indole, allowing the process to be completed in just a few steps. Based on this, the retrosynthetic route was made, including ketal protection of 2'3'-*O*-isopropylidene, Suzuki coupling, Heck coupling and macrolactonization (**Scheme 18**). Successfully, compounds **12**, **16** and **17** were obtained (see 3.3.1 and 3.3.2). Unfortunately, the Heck coupling between **17** and acrylic acid proved unsuccessful (see 3.3.3).



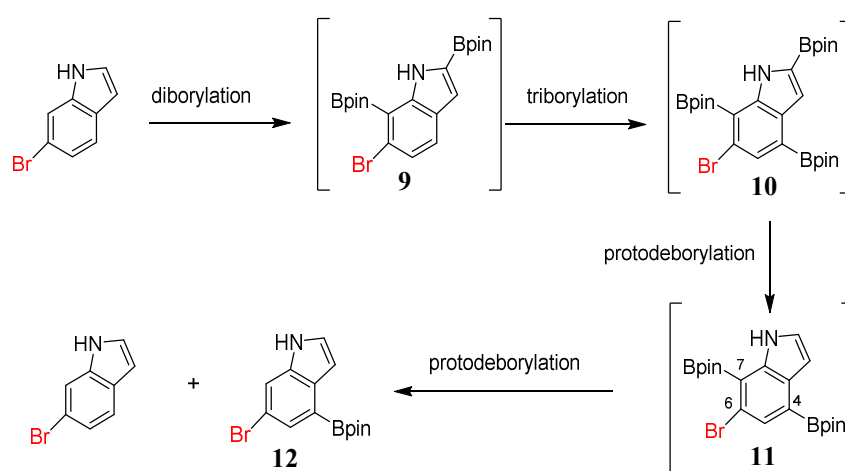
Scheme 18 The retrosynthetic route A

3.3.1 Synthesis of 6-bromoindole-4-boronic acid pinacol ester **12**

To introduce a suitable substituent for macrocyclisation of the ring-open nucleoside **1**, the indole group was functionalized with a bromo group. The formation of 6-bromoindol-4-boronic acid pinacol ester **12** was accomplished through sequential borylation and diprotodeboronation processes.

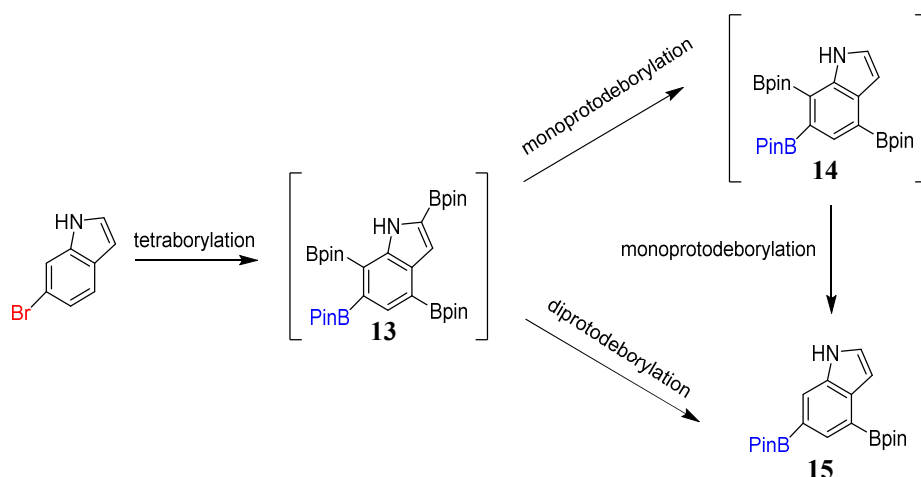
Regioselectivity of aromatic C-H borylation is mainly driven by steric and electronic effects. Thus, Ir-catalysed borylation of unprotected indoles first installs a Bpin group at C2, then C7, and C5 as the following spot. However, when a halogen installs in position 6 first, then C2, C7, C4 would be the sequence of borylation. Shen and co-workers¹³³ illustrated the first Bpin group to be installed during the Ir-catalyzed borylation was also the first to be removed in the protodeboronation.¹³³

For the synthesis of 6-bromo-4-boronate, Nabi and co-workers¹³⁴ gave a good example on this series of reactions. In short, diprotodeborylation was performed after triborylation reaction. 2,4,6-triboronate **10** indole was produced as intermediate and 6-bromoindol-4-boronic acid pinacol ester **12** was obtained as final product (**Scheme 19**). Either two separate steps (65 % yield for two steps) or one-pot reaction gave good yield (70 % yield in one-spot). Intermediates **9** and **11** were also isolated.



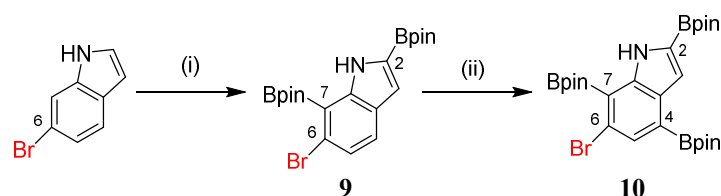
Scheme 19 General synthesis of key reactant **12**

In the process of synthesising target compound **12**, compounds **13**, **14** and **15** were newly found under the different conditions (**Scheme 20**). Equivalent of boronated indole forced the fourth substitution of the indole ring on the position of bromo. **13** was formed using these modified conditions (58 % yield). **14** and **15** were produced using the same conditions as for **11** and **12** (**Scheme 20**).



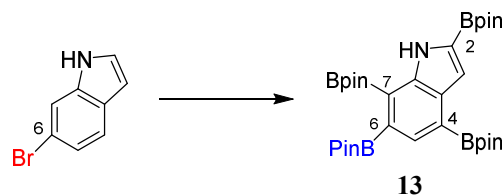
Scheme 20 General synthesis of 4,6-diboronic acid pinacol ester **15**

In detail, 2,4,7-triborylindole **10** was isolated in a good yield of 84 % (**Scheme 21**), with 3.5 equivalent of B_2Pin_2 and 9 mol% iridium catalyst. It was found when reaction time was adjusted from 3 days to 1 day, the yield of **10** decreased while the intermediate **9** increased (**Scheme 21**). Product **9** was not mentioned or characterised by Nabi and coworkers¹³⁴.



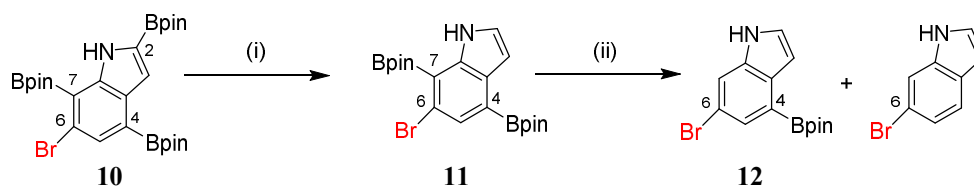
Scheme 21 Synthesis of 4,7-diborylated indole **9** and 2,4,7-triborylated indole **10**. Reagents and conditions: (i) $[Ir(OMe)cod]_2$ (9 mol%), dtbpy (18 mol%), B_2Pin_2 (3.5 equiv.), THF, 85 °C, 12 h; (ii) $[Ir(OMe)cod]_2$ (9 mol%), dtbpy (18 mol%), B_2Pin_2 (3.5 equiv.), THF, 85 °C, 24 h. 84 % yield over 2 steps.

More importantly, when the equivalent of B_2Pin_2 was adjusted from 3.5 to 5.0, the bromo substituent was replaced with Bpin under iridium catalysis. In this way, the unprecedented 2,4,6,7-tetraborylated **13** was obtained in a modest yield of 58 % (**Scheme 22**).



Scheme 22 Synthesis of 2,4,6,7-tetraborylated indole **13**. Reagents and conditions: $[\text{Ir}(\text{OMe})\text{cod}]_2$ (9 mol%), dtbpy (18 mol%), B_2Pin_2 (5.0 equiv.), THF, 85 °C, 24 h, 58 %.

The use of bismuth triacetate to conduct protodeborylation at C2 and C7 sequentially worked as expected (**Scheme 23**). In our studies, a key factor that affects the product yield was found. It was found that a single diborylated product arose when it was carried out with non-anhydrous solvents or when the B_2Pin_2 stoichiometry was adjusted. In addition to solvent quality, the nitrogen atmosphere under high pressure is a crucial factor in protodeborylation. While a mild yield of **12** was achieved with 65 % conversion of the product (**Table 3, entry 4**), a notable increase in nitrogen pressure significantly improved the yield of the desired product, reaching 83 % conversion (**Table 3, entry 6**).



Scheme 23 Synthesis of **11** and **12**. Reagents and conditions: (i) $\text{Bi}(\text{OAc})_3$ (20 mol%), non-anhydrous THF-MeOH, 65 °C; (ii) $\text{Bi}(\text{OAc})_3$ (20 mol%), anhydrous THF-MeOH, 65 °C.

To improve the product yield, the optimization was subsequently performed. It was found product conversion was not improved by use of 40 mol% $\text{Bi}(\text{OAc})_3$ instead of 20 mol% (**Table 3, entry 1 and 2**). Fresh $\text{Bi}(\text{OAc})_3$ did not help to increase the product conversion (**Table 3, entry 8 and 9**). The quality of solvents matters, that is, anhydrous solvents seemed to increase product conversion in comparison with non-anhydrous solvents (**Table 3, entry 1 and 3**). This was in agreement with results from Shen *et al.*¹³³ Completely degassed solvents also slightly

increased product conversion (**Table 3, entry 3 and 4**). The product conversion was dramatically reduced when less MeOH was used (**Table 3, entry 3 and 5**). Nitrogen atmosphere under high pressure and 220 equiv. MeOH gave 83 % product conversion, without diborylindole. However, 17 % degraded compound was observed (6-bromoindole) (**Table 3, entry 6**). Prolonging the reaction time to 2 days resulted in a decrease in product conversion with an increased proportion of degraded compound (**Table 3, entry 7**). Surprisingly, increasing the MeOH content to 440 equiv. slightly decreased the product conversion with a slight increase in diborylindole however the amount of degraded compound was unchanged (**Table 3, entry 6, 8 and 9**). Increased reaction time led to decreased yields, with an overall drop from 83 % in 16 h to 50 % after 73 h (**Table 3, entry 8, 10 and 11**). Longer timescales increased the ratio of product degradation (**Table 3, entry 6, 7, 8, 10 and 11**). No product formation was observed using microwave heating (**Table 3, entry 12**). Optimized reaction conditions led to the 84 % yield of **10** for the first step (**Scheme 21**) and 83 % yield of **12** for the second step (**Table 3, entry 6**). 70 % yield was obtained by a one-pot reaction comparable to separate steps. The one-pot reaction was favoured due to its simpler operation.

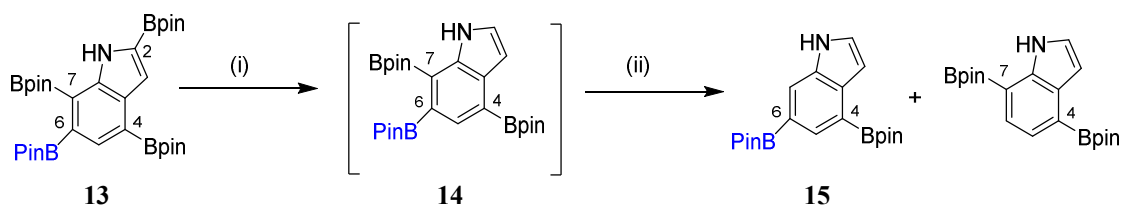
Table 3 Optimization of diprotodeborylation of **10**

Entry	Equiv. of Bi(OAc) ₃ (mol%)	Equiv. of MeOH	N ₂	time (h)	T (°C)	Solvents 2.5:1 MeOH/THF	Conv.(%) ^a 12:11:6-bromoindole
1	20	220	under N ₂	16	65	non-anhydrous	26:69:5
2	40	220	under N ₂	24	65	non-anhydrous	26:69:5
3	20	220	under N ₂	16	65	anhydrous	56:31:13
4	20	220	under N ₂	48	65	anhydrous and degassed	65:28:7
5	20	55	under N ₂	16	65	anhydrous	13:87:0
6	20	220	N ₂ and high pressure	16	65	anhydrous	83:0:17

7	20	220	N ₂ and high pressure	43	65	anhydrous	77:0:23
8	20	440	N ₂ and high pressure	19	65	anhydrous	77:8:15
9	20 (fresh)	440	N ₂ and high pressure	19	65	anhydrous	75:15:10
10	20	440	N ₂ and high pressure	28 h	60	anhydrous	70:14:16
11	20	440	N ₂ and high pressure	73 h	60	anhydrous	50:0:50
12	20	220	under N ₂	30 min	65	anhydrous	no reaction

^a Conversion was determined by ¹H NMR analysis of the crude product.

Similarly, the protodeborylation of **13** was carried using bismuth triacetate (**Scheme 24**). 4,6,7-triborylated (**14**) indole was obtained in the adjustment of reaction time, equivalent of MeOH, the quality of solvents, also the nitrogen pressure. 4,6-diborylated indole (**15**) was also obtained after similar optimization. It's also worth mentioning that **9**, **10**, **11**, **13**, and **14** showed strong fluorescence, even at longer UV wavelengths (365 nm). Hence, they have potential for future fluorescence-based applications.

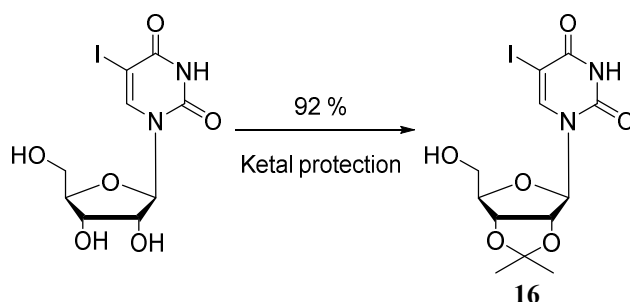


Scheme 24 Synthesis of **14** and **15**. Reagents and conditions: (i) Bi(OAc)₃ (20 mol%), non-anhydrous THF-MeOH, 65 °C; (ii) Bi(OAc)₃ (20 mol%), anhydrous THF-MeOH, 65 °C

3.3.2 Synthesis of 5-(6-bromoindol-4-yl) uridine derivative **17**

In order to install 6-bromoindole at the 5 position of uridine, 5-iodouridine was chosen as a suitable reaction partner, as the iodo group is a good leaving group for the cross coupling of

nucleosides.¹³⁵ Prior to the cross-coupling reaction, the secondary alcohols in positions 2' and 3' of 5-iodouridine were protected in the form of a ketal. Thus, protected **16** was obtained from commercially available 5-iodouridine in a high yield of 92 % under standard conditions (**Scheme 25**).¹³⁶ As indicated by the high yield, this reaction was straightforward, including its work-up: a simple extraction yielded the product as a white powder, without requirement for further purification by column chromatography. It's worth mentioning that NaHCO₃ was a good base here to neutralize the reaction in the work-up step as the following side products were only NaCl, CO₂ and water which were easy to remove. However, Et₃N was suggested in the published paper, which was not appropriate here, as additional Et₃N was difficult to remove and remained in the product even after the silica gel column chromatography.



Scheme 25 Synthesis of **16**. Reagents and conditions: acetone, H₂SO₄, rt, 2 h, 92 %.

With two starting materials **12** and **16** in hand, Suzuki cross coupling was then performed to yield **17**. Compared with previous ring-open **1**, an additional bromo atom was introduced to position 6 of the indole. The aim was to substitute a chain at position 6 to enable ring-formation. Suzuki cross-coupling of nucleoside substrates has been well-studied by the Wagner research group. Suzuki coupling is significantly affected by the type and number of equivalents of base, as well as the catalyst and solvent. Jiang *et al.*⁴² summarized three sets of conditions for unprotected nucleosides. Method A contained 1.5 equivalent boronic acid, 2 equivalent Cs₂CO₃, 2.5 mol% Na₂PdCl₄ and 6.3 mol% TPPTs in degassed water. Method B contained 1.5

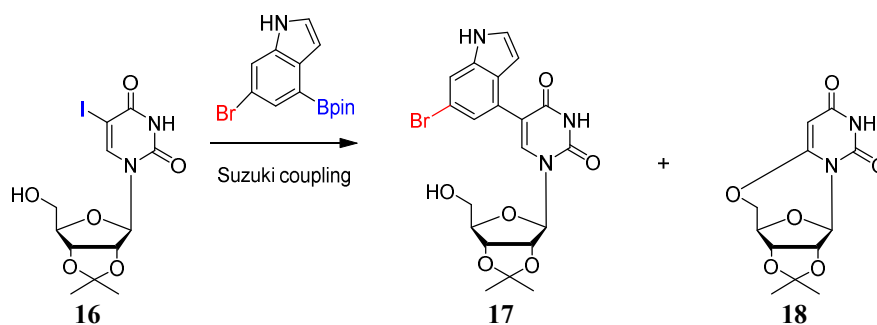
equivalent boronic acid, 3 equivalent NaHCO_3 and 5 mol% $\text{PdCl}_2(\text{dppf})\text{DCM}$ in 3:1 DME/water. Method C contained 1.5 equivalent boronic acid, 3 equivalent NaHCO_3 and 5 mol% $\text{PdCl}_2(\text{dppf})\text{DCM}$ in 3:1 dioxane/water. Starting from this, these conditions were applied into our nucleoside derivatives.

Following method A of Jiang *et al.*⁴², **17** was obtained in an unexpectedly low yield of 26 % (**Table 4, entry 1**), despite the high yield from a previous attempt to synthesize compound **1**. To gain further insight, the side product was isolated characterized by NMR and LC-MS. Results indicated the side product was a protected O^6 -5'-cyclouridine **18** without iodo group. Previous researches^{92,137} suggest **18** can be produced under basic conditions (i.e., $\text{NH}_3 \cdot \text{H}_2\text{O}$ or NaH) from 5-bromo substituted uridine. Qu *et al.*¹³⁷ reported that **18** did not form at rt from 5-iodo substituted uridine. However, this was observed in our Suzuki conditions. It's possible high temperature in the Suzuki conditions accelerated iodo group leaving and subsequent ring formation.

To improve the yield of the desired product **17** and suppress the formation of side product, the cross-coupling reaction was extensively optimized (**Table 4**). By changing the ratio of two starting materials from 1:1.2 to 1.2:1, the yield decreased slightly (**Table 4, entry 2**). The catalyst $\text{PdCl}_2(\text{dppf})\text{DCM}$ in dioxane and water almost doubled the yield of the product in comparison with the catalyst $\text{Na}_2\text{PdCl}_4/\text{TPPT}$ in water, the yield was changed from 26 % to 54 % (**Table 4, entry 3**). Increased equivalent of boronic acid pinacol ester did not lead to increased yield (**Table 4, entry 4**). THF/MeOH solvent was also attempted.¹³⁸ It seems it was not polar enough and therefore was not suitable for $\text{Na}_2\text{PdCl}_4/\text{TPPTS}$ catalyst system. No product was observed under this condition (**Table 4, entry 5**). To understand the role of the bromo group and 2', 3' -*O*-isopropylidene group in the Suzuki cross coupling reaction, 5-(6-

bromo-4-boronic acid pinacol ester)-uridine, 2', 3'-*O*-isopropylidene-5-(6-bromo-4-boronic acid pinacol ester)-uridine and 5-(4-boronic acid pinacol ester)-uridine were synthesized (**Table 4, entry 6, 7 and 8**). The results indicated that the 2',3'-*O*-isopropylidene group facilitates the ring formation of O⁶-5'-cyclouridine.

Table 4 Optimization of Suzuki coupling^a between uridine derivative **16** and indole derivative **12**



Entry	Uridine	Boronate	Equiv. of SMs ^b	Catalyst	Solvent	Base	Conv. ^c (17:18)	Yield (%) ^d
1	2',3'- <i>O</i> -protected	6-bromoindo-1-4-boronic acid pinacol ester	1:1.2	Na ₂ PdCl ₄ /TPPTS	H ₂ O	Cs ₂ CO ₃	1:1	26
2			1.2:1	Na ₂ PdCl ₄ /TPPTS	H ₂ O	Cs ₂ CO ₃	1:1	20
3			1:1.2	PdCl ₂ (dppf)/DCM	dioxane/H ₂ O	NaHCO ₃	1:0.6	54
4			1:1.5	PdCl ₂ (dppf)/DCM	dioxane/H ₂ O	NaHCO ₃	1:0.6	N/A ^e
5			1:1.2	Na ₂ PdCl ₄ /TPPTS	THF/MeOH	Cs ₂ CO ₃	no conv.	N/A ^e
6	unprotected	indol-4-boronic acid	1:1.2	Na ₂ PdCl ₄ /TPPTS	H ₂ O	Cs ₂ CO ₃	1:0	N/A ^e
7	2',3'- <i>O</i> -protected		1:1.2	PdCl ₂ (dppf)/DCM	dioxane/H ₂ O	Cs ₂ CO ₃	1:0.6	N/A ^e
8	unprotected		1:1.5	Na ₂ PdCl ₄ /TPPTS	H ₂ O	Cs ₂ CO ₃	1:0	N/A ^e

^a The reaction was performed under 110 °C.

^b SM: Starting materials

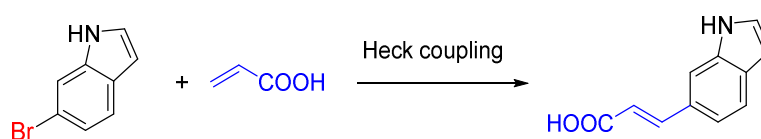
^c Conv.: Conversion; Conversion was determined by ¹H NMR analysis of the crude product.

^d Isolated yield

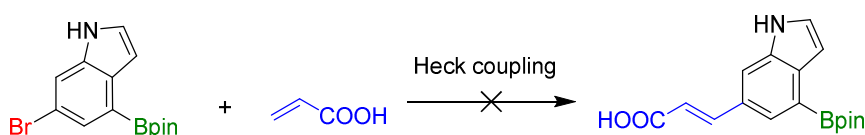
^e N/A: Not applicable

3.3.3 Heck coupling of **17** with acrylic acid

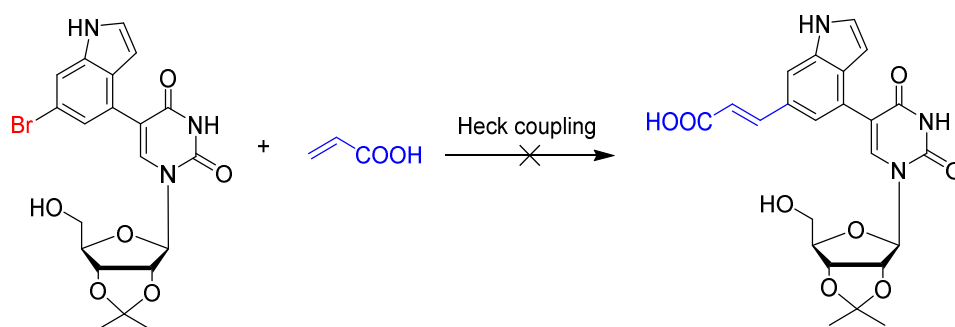
This section aimed to introduce an acrylic acidic group in position 6 of the indole, serving as one of the precursors for the macrolactonization process. Pubill-Ulldemolins *et. al.*¹³⁹ reported optimal conditions for the Heck coupling of indole derivatives with acrylic acid using Na_2PdCl_4 , $^s\text{PPhos}$, Na_2CO_3 in the solvent of CH_3CN and water. To assess the potential efficacy of the reaction conditions, the readily available 6-bromoindole was initially employed as the starting material (**Scheme 26**). Upon reaction with acrylic acid, the product was successfully obtained and characterized through TLC chromatography as well as analysis of the crude ^1H NMR (**Scheme 26**). These conditions were applied to the main reactions. Unfortunately, neither 6-bromoindole boronic pinacol ester **12** nor nucleoside derivative **17** as substrates yielded the desired products via Heck coupling reaction (**Scheme 27** and **Scheme 28**). It is speculated that the presence of the boronic ester or the bulky uridine group may deactivate the bromo functional group, hindering its effectiveness in forming a C-Pd-Br bond with palladium during the oxidative addition step in the Heck coupling reaction (See mechanism in 3.1.3). Therefore, Route A was abandoned at this stage because this key intermediate could not be accessed.



Scheme 26 Heck-coupling between 6-bromoindole and acrylic acid. Reagents and conditions: Na_2PdCl_4 (10 mol%), $^s\text{PPhos}$ (25 mol%), Na_2CO_3 (4 equiv.), degassed CH_3CN : H_2O (1:1), 80 °C, 21 h.



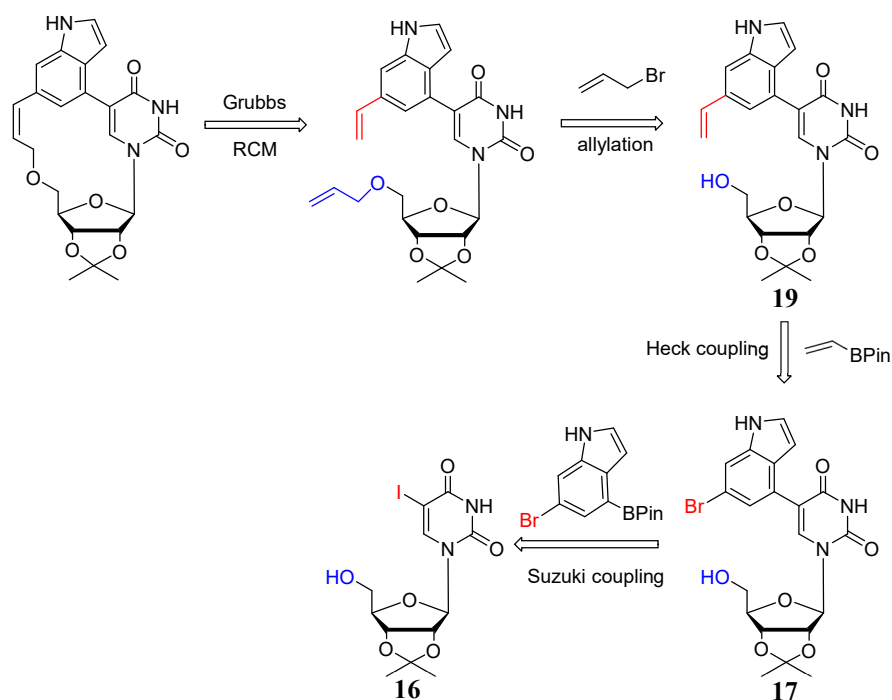
Scheme 27 Heck-coupling between **12** and acrylic acid. Reagents and conditions: Na_2PdCl_4 (10 mol%), $^s\text{PPhos}$ (25 mol%), Na_2CO_3 (4 equiv.), degassed CH_3CN : H_2O (1:1), 80 °C, 22 h.



Scheme 28 Heck-coupling between **17** and acrylic acid. Reagents and conditions: Na_2PdCl_4 (10 mol%), $^s\text{PPhos}$ (25 mol%), Na_2CO_3 (4 equiv.), degassed $\text{CH}_3\text{CN}:\text{H}_2\text{O}$ (3:1), 80 °C, 30 h.

3.4 Formation of the macrocycle via ring-closing metathesis: attempted installation of the side chain at the indole substituent first (Route B)

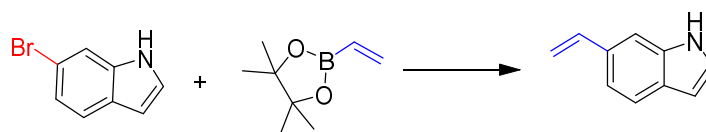
The inability to functionalize the indole with acrylic acid prevented esterification as a ring-forming strategy. An alternative approach, olefin metathesis was carried out, involving the Grubbs catalyst. This is a widely used strategy for ring-formation. It was hypothesised that two alkenyl chains could be introduced to the indole position 6 and position 5'-O. We firstly tried to install the upper alkenyl chain to the nucleoside. The retrosynthetic route encompassed Suzuki coupling, Heck coupling, allylation and Ring-Closing Metathesis (**Scheme 29**). **16** and **17** were achieved following route A (see 3.3.2). Compound **19** was obtained successfully (see 3.4.1). The allylation reaction worked for the model reaction with **16**, but it did not proceed as expected for **19** (see 3.4.2). The difficulty arose because the alkenylation reaction occurred at the indole amine group rather than at position 5'-O. Additional efforts were made to safeguard the indole amine group, employing methods such as Boc-protection, benzylation, and sialylation. Unfortunately, none of these strategies proved successful (see 3.4.3, **Scheme 29**).



Scheme 29 The retrosynthetic route B

3.4.1 Synthesis of 5-(6-vinylindol-4-yl) uridine derivative 19

The starting point of this ring-forming strategy was to replace the bromo substituent with an alkenyl functional group. Gao *et al.*¹³⁸ reported two reactions between a 6-bromoindole derivative and alkenyl boronic ester or organostannanes via Suzuki coupling or Stille reaction, respectively. Due to the high toxicity of organostannanes, the alkenyl boronic ester route was attempted first. Vinyl boronic acid pinacol ester was selected as a starting material due to its good activity and commercial availability. There was a potential selectivity between Suzuki coupling and Heck coupling.¹⁴⁰ Surprisingly, altered catalyst and solvent conditions led to the desired product in high yield following Suzuki coupling (Table 5). Optimal conditions involved use of PdCl₂(dppf)DCM with dioxane/water (Table 5).

Table 5 Model vinylation reaction^a between 6-bromoindole and vinyl boronic acid pinacol ester

Entry	Base	Catalyst	Solvent	Time (h)	Conv. (%) ^b	Yield (%) ^c
1	Cs ₂ CO ₃	Pd(PPh ₃) ₄	4:1 THF/MeOH	16	28	N/A ^d
				43	55	N/A ^d
2	Cs ₂ CO ₃	Na ₂ PdCl ₄ /TPPTS	9:1 dioxane/H ₂ O	45	3	N/A ^d
3	Cs ₂ CO ₃	PdCl ₂ (dppf)DCM	9:1 dioxane/H ₂ O	45	99	92
4	Cs ₂ CO ₃	Na ₂ PdCl ₄ / ^s Sphos	9:1 dioxane/H ₂ O	45	33	N/A ^d

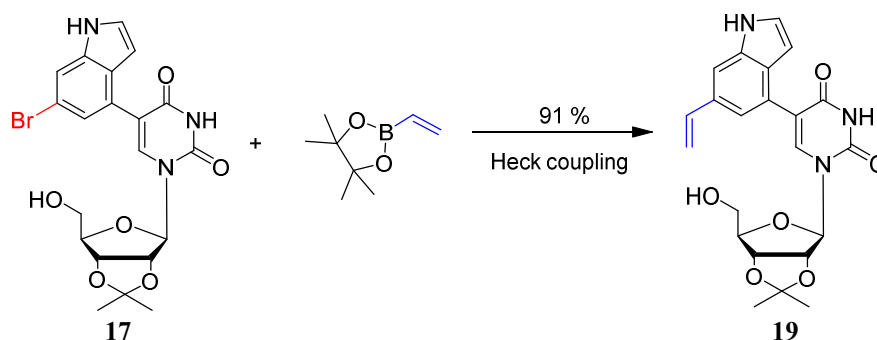
^a The reaction was performed at 115 °C. 2 equivalent vinyl boronic acid pinacol ester was used.

^b Conversion was determined by ¹H NMR analysis of the crude product.

^c Isolated yield

^d N/A: Not applicable

These conditions were then be applied to the target reaction, involving 5-(6-bromoindol-4-yl) uridine **17** as starting material (**Scheme 30**). The target product **19** was isolated with a high yield of 91 %. In the applied conditions, 9:1 dioxane/H₂O was changed to 3:1 dioxane/H₂O because the substrate in the target reaction was more polar than in the model reaction.

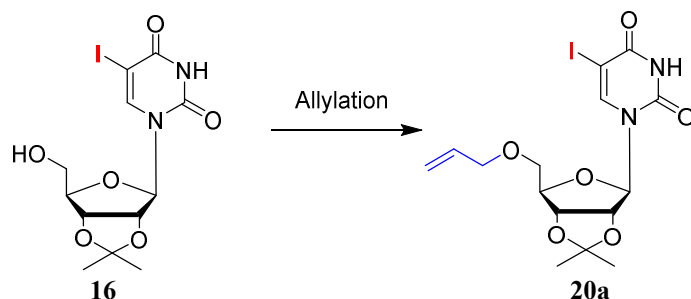


Scheme 30 Synthesis of **19** via vinylation reaction. Reagents and conditions: PdCl₂(dppf)DCM (14 mol%), Cs₂CO₃ (1.1 equiv.), degassed CH₃CN: H₂O (3:1), 115 °C, 17 h, 91 %.

3.4.2 Synthesis of 5'-*O*-allyl-6-yl-5-iodouridine derivative 20a

Following vinyl substitution of the indole group, the aim was to install a second alkenyl group in position 5'-*O*. This would generate the precursor required for formation of the macrocycle. In the model reaction, 1.2 equiv. of both substrates, together with anhydrous THF, at rt with classical stirring, only starting material was observed (**Table 6, entry 1**).¹⁴¹ However, when we replaced classical stirring with sonication at rt, 30 % conversion of **19** can be observed (**Table 6, entry 2**). Following this success, the number of equivalents of bromide and NaH were tuned to improve the reaction yield. Addition of 2.5 equiv. NaH increased the yield to 80 % (**Table 6, entry 3**). Surprisingly, increasing the amount of allyl bromide did not improve but decrease the yield (**Table 6, entry 4**).

Table 6 Alkylation of compound **16**



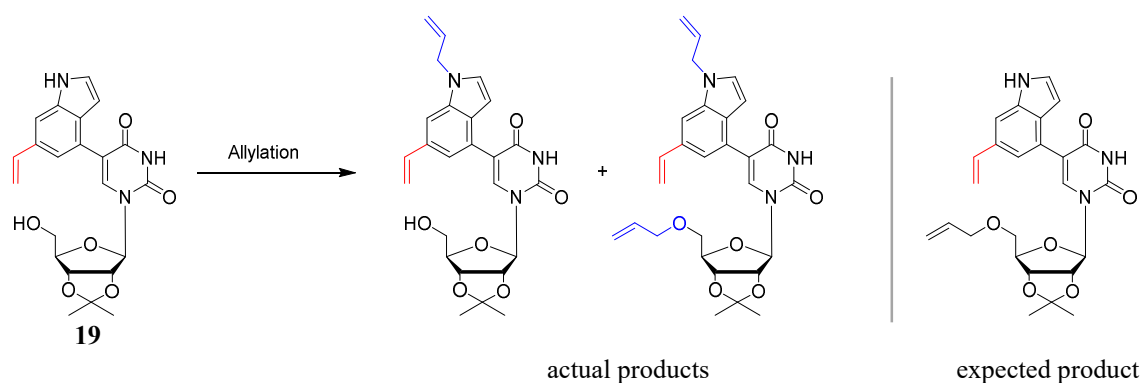
Entry	Equiv. of allyl bromide	Equiv. of NaH	Solvent	Condition	Time (h)	Conv. (%) ^a	Yield (%) ^b
1	1.2	1.2	THF	classical stirring	2.0	0	N/A ^c
2	1.2	1.2	THF	ultrasonication	1.5	30	N/A ^c
3	1.2	2.5	THF	ultrasonication	1.5	99	80
4	2.5	2.5	THF	ultrasonication	0.5	99	60

^a Conv.: Conversion; Conversion was determined by ¹H NMR analysis of the crude product.

^b Isolated yield

^c N/A: Not applicable

Optimal conditions were applied to the target reaction (**Scheme 31**) using **19**. TLC indicated almost complete consumption of the SM and appearance of two new spots. LC-MS indicated these were mono-allylated and di-allylated compounds, respectively (**Scheme 31**). The ^{13}C NMR spectra indicated the mono-allylated compound was *N*-substituted, in which the chemical shift of the $\text{NCH}_2\text{CH}=\text{CH}_2$ was 48.6 ppm, while the general chemical shift of $\text{OCH}_2\text{CH}=\text{CH}_2$ in a 5'-substituted nucleoside is around 70 ppm. Thus, both chemical shifts 48.6 ppm and 70 ppm can be observed in the ^{13}C NMR of the di-allylated compound (**Figure 32**). The results suggested the target compound was not produced. NOESY was used to determine whether the *N*-allylated group of the mono-substituted nucleoside was on the indole nitrogen or the nucleobase. From the NOESY spectrum, a correlation between H-7 of indole and the proton in $\text{NCH}_2\text{CH}=\text{CH}_2$ was observed (**Figure 33**). Results indicated the mono-allylated nucleoside was indole substituted (**Scheme 31**). Chapter 3.4.3 discusses the methods to obtain the *O*-alkenylated compounds.



Scheme 31 Alkylation of compound **19**. Reagents and conditions: NaH (2.5 equiv.), anhydrous THF, allyl bromide (1.2 equiv.), sonication.

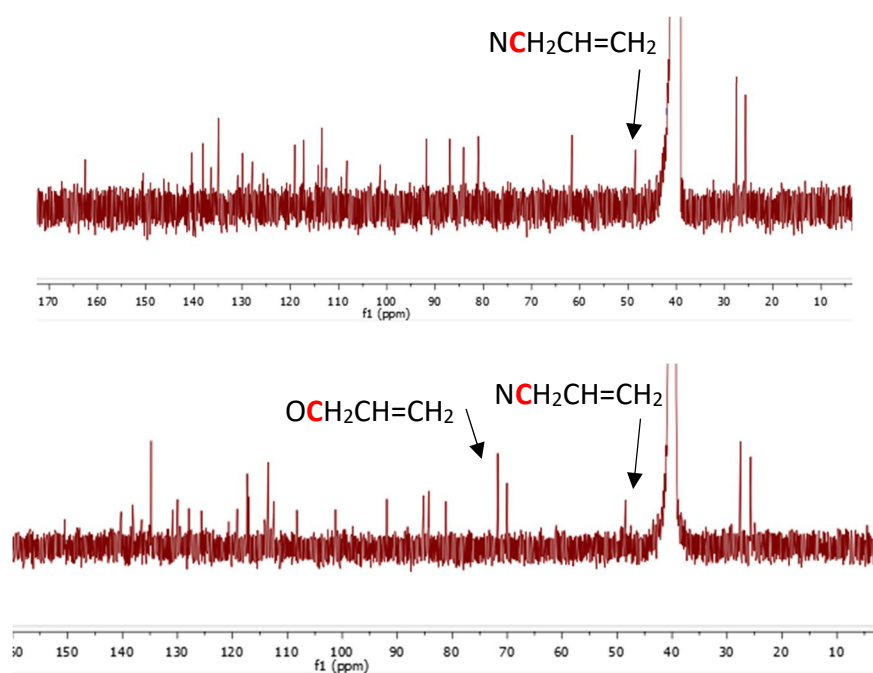


Figure 32 ^{13}C NMR spectra of allylated nucleosides (top: mono-allylated nucleoside; bottom: di-allylated nucleoside)

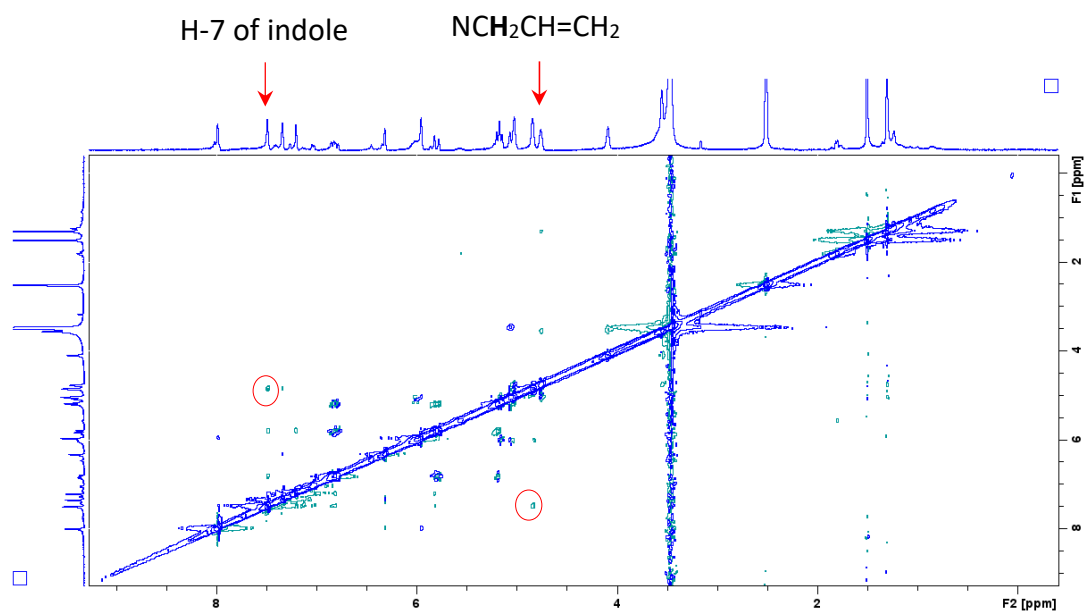
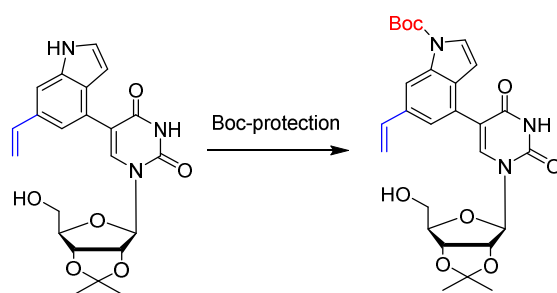


Figure 33 NOESY spectrum of mono-allylated nucleoside

3.4.3 N-Protection of the indole substituent

N-substitution was the predominant product following allylation reaction of compound **19**. To avoid this, the indole nitrogen was Boc protected. Boc protection is a common strategy for the selective modification of a nitrogen in the presence of an alcohol. With protected **19** as the substrate, 4 equivalent Boc₂O in 4:1 pyridine/DCM (**Table 7, entry 1**)¹⁴² gave a mixture of mono-substituted and di-substituted product, diagnosed from LC-MS and crude ¹H NMR. Then the equivalence of Boc₂O was reduced to 1.1 (**Table 7, entry 2**), in order to avoid the produce of di-substituted product. When 10 mol% DMAP was added and anhydrous DMF worked as the solvent, high yield of 99 % was obtained (**Table 7, entry 3**).¹⁴³ ¹H NMR, ¹³C NMR and HSQC were used to identify the *N*-Boc compounds. A change in chemical shift was observed for the indole protons (compared with the SM) whereas the signals for the nucleobase protons remained unchanged.

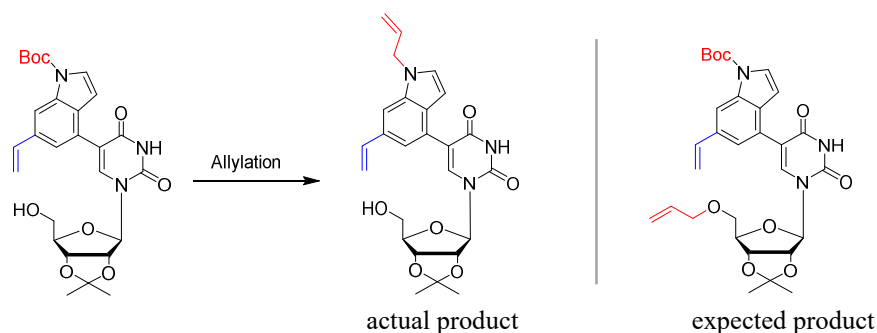
Table 7 Boc-protection^a of the indole substituent of **19**



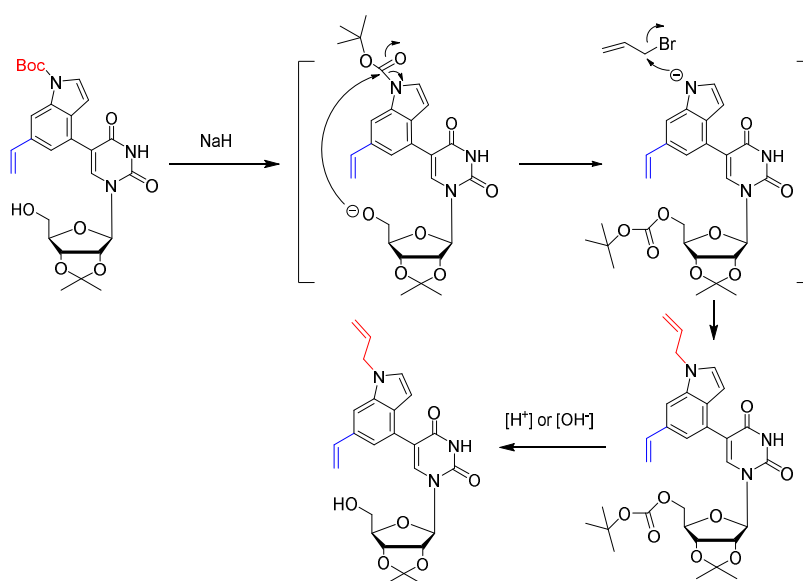
Entry	Equiv. of Boc ₂ O	Addition of DMAP	Solvent	Results
1	4	no	4:1 pyridine/DCM	mixture of di-Boc and mono-Boc
2	1.1	no	4:1 pyridine/DCM	no product
3	1.1	yes	dry DMF	99 % yield

^a The reaction was performed at rt.

Following synthesis of the 5-(*N*-Boc-6-vinylindol-4-yl) uridine derivative and after establishing an appropriate method of allylation, allylation of **19** was performed to introduce another alkenyl chain for ring-closing. Surprisingly, the Boc functional group was dropped during the reaction with transfer of the allyl chain onto the indole nitrogen (Scheme 32). These findings were observed using ^{13}C NMR. There are two possible explanations. The first is the instability of *N*-Boc under strongly basic conditions. Secondly, Xue *et al.*¹⁴⁴ revealed that the alkoxide anion can trigger *N*→*O* Boc migration in an intramolecular pathway under strong condition. The resultant amide anion can react with bromide to produce an intermediate which may be hydrolysed under acidic or basic conditions (Scheme 33).

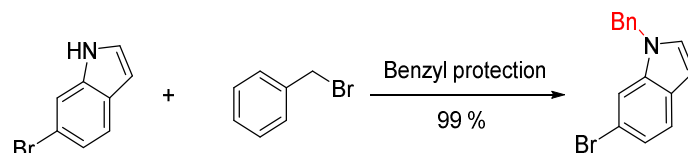


Scheme 32 Allylation of 5-(*N*-Boc-6-vinylindol-4-yl) uridine derivative. Reagents and conditions: NaH (2.5 equiv.), anhydrous THF, allyl bromide (1.2 equiv.), sonication.

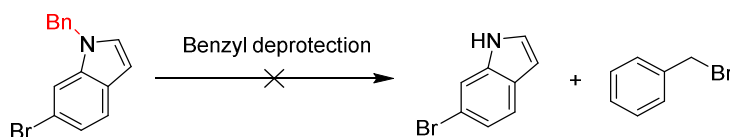


Scheme 33 Proposed mechanism for the Boc-protection

Thus, a benzyl protecting group strategy was alternatively employed. Compared to Boc group, benzyl group has an advantage of being more stable in such strong conditions. However, also due to its stability, the benzyl group was difficult to be removed from *N*-benzyl-6-bromoindole. In the model reactions, the *N*-benzylation reaction proceeded smoothly with 99 % yield (**Scheme 34**).^{145,146} However, the deprotection was not successful (**Scheme 35**).



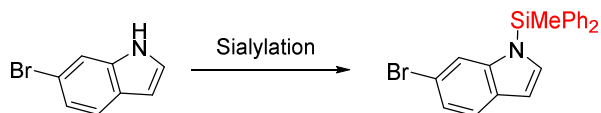
Scheme 34 Benzyl protection of 6-bromoindole. Reagents and conditions: NaH (1.2 equiv.), anhydrous DMF, 99 %



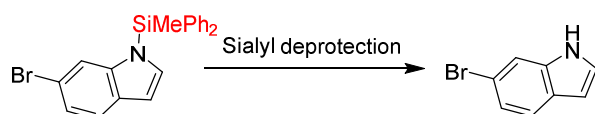
Scheme 35 Deprotection of *N*-benzyl-6-bromoindole. Reagents and conditions: PtO₂, 3:1 MeOH/DCM (3:1) or HOAc, rt.

To overcome this, silylation was used to protect the indole nitrogen. The silyl group can be removed selectively with reagents such as Bu₄NF in THF. Test reactions showed silylation (Zn(OTf)₂ and pyridine)¹⁴⁷ and subsequent deprotection (Bu₄NF in THF)¹⁴⁸ occurred with good conversions (**Scheme 36** and **Scheme 37**, respectively). Suzuki coupling was then performed between *N*-SiMePh₂-6-bromo and compound **16**. Unfortunately, these reaction conditions resulted in deprotection of the silyl protecting group (**Scheme 38**). To investigate this, the temperature and number of equivalents of base and catalyst were modified. Unfortunately, these still yielded the same undesirable outcome (deprotection of the indole nitrogen). The SiMePh₂ group appeared to be unstable under the Suzuki reaction conditions. Considering this, silylation was performed directly with protected 5-(6-vinyl-indol-4-yl) uridine **19** and

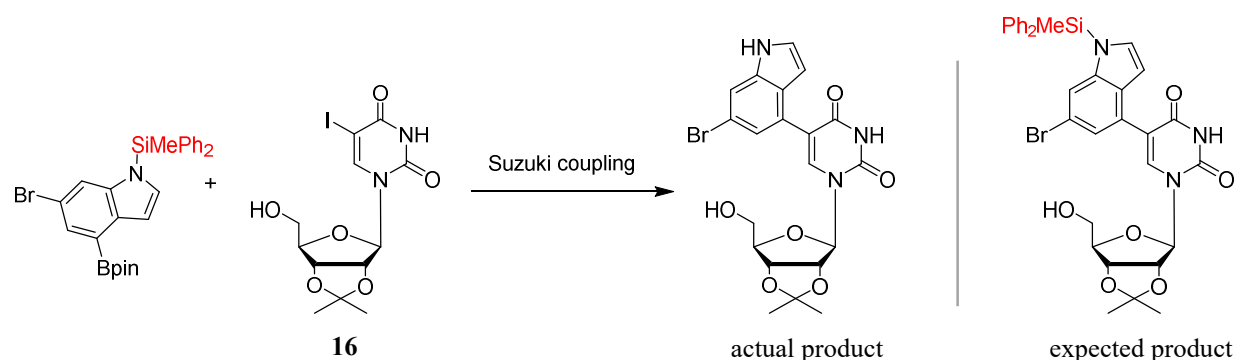
HSiMePh₂. However, this resulted in sialylation on the alcohol rather than the indole nitrogen (Scheme 39). This was diagnosed through the chemical shift of C-5' ribose.



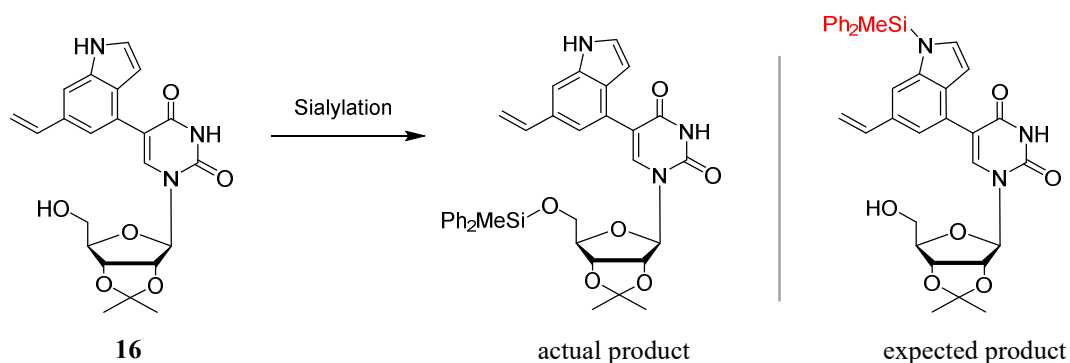
Scheme 36 Sialylation reaction of 6-bromoindole. Reagents and conditions: HSiMePh₂ (1.2 equiv.), Zn(OTf)₂ (10 mol%), pyridine, MeCN, 80 °C, overnight.



Scheme 37 Deprotection of *N*-SiMePh₂-6-bromoindole. Reagents and conditions: Bu₄NF (1 equiv.), THF, 0 °C, N₂, 30 min.



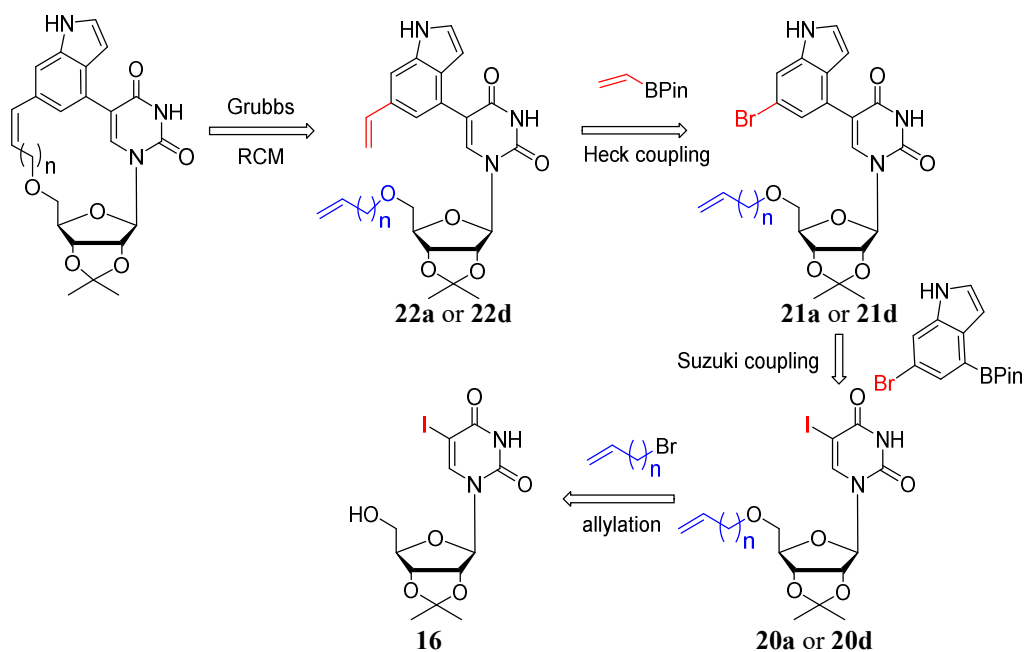
Scheme 38 Suzuki coupling between *N*-SiMePh₂-6-bromoindole and **16**. Reagents and conditions: PdCl₂(dppf)DCM (5 mol%), NaHCO₃ (3 equiv.), degassed dioxane/H₂O (3:1), N₂, 90 °C, 16 h.



Scheme 39 Sialylation of **19**. Reagents and conditions: HSiMePh₂ (1.2 equiv.), Zn(OTf)₂ (10 mol%), pyridine, MeCN, 80 °C, overnight.

3.5 Formation of the macrocycle via ring-losing metathesis: installation of the side chain at 5'-position first (Route C)

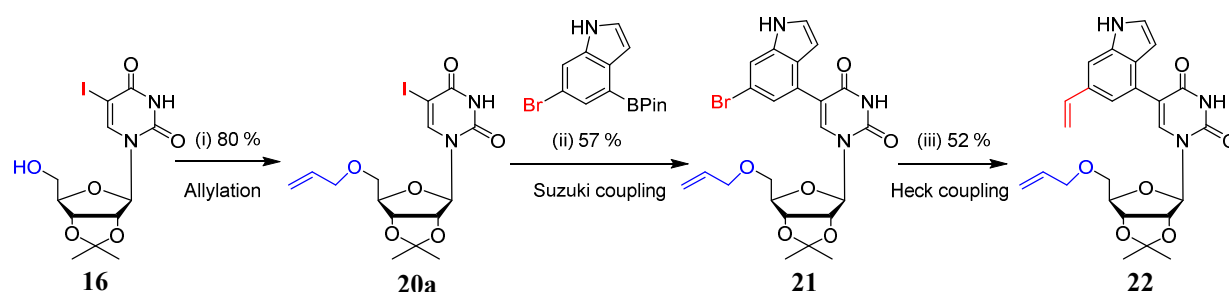
Previous results suggested that it was challenging to introduce an alkenyl chain onto position 5'-O of the ribose following installation of the indole alkenyl chain. We then tried to install the lower alkenyl chain to the nucleoside first. The retrosynthetic route encompassed allylation, Suzuki coupling, Heck coupling and Ring-Closing Metathesis (**Scheme 40**). Compounds **16** and **20a – 22a** were obtained using the optimized methods in route A and B (see 3.5.1). The RCM reaction proved successful for the model reaction involving **20a** and 6-vinylindole, however, it did not work as anticipated for **22a** (see 3.5.2). It was speculated that the target ring may be too strained to form. Considering this, a lengthened chain to position 5'-O of the ribose was synthesized (see 3.5.3). Subsequently, **20d – 22d** were successfully obtained (see 3.5.4). The macrocyclic product resulting from the RCM reaction of **22d** was identified using LC-MS (see 3.5.4). Interestingly, two macrocycles were formed during the Suzuki coupling step. Considering easier accessibility, our initial focus was on identifying these two newly formed macrocycles. Further details will be explored in route D (see 3.6).



Scheme 40 The retrosynthetic route C. (n = 1 (**a**); n = 3 (**d**))

3.5.1 Synthesis of disubstituted uridine derivatives **21** and **22**

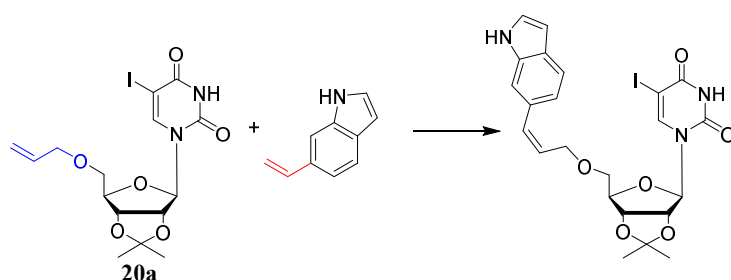
Allylation, Suzuki and Heck coupling reactions were conducted sequentially using the optimized methods in route A and B (see 3.3 and 3.4). This yielded products **21** and **22** in mild yields (**Scheme 41**). The yields were somewhat reduced due to loss of the allyl group of uridine products during step (ii) and (iii) which were performed under relatively harsh conditions. A one-pot reaction of step (ii) and (iii) did not yield product **22**.



Scheme 41 Synthesis of **21** and **22**. Reagents and conditions: (i) NaH (2.5 equiv.), anhydrous THF, allyl bromide (1.2 equiv.), sonication, 2 h, 80 %; (ii) PdCl₂(dppf)DCM (5 mol%), NaHCO₃ (3 equiv.), degassed dioxane/H₂O (3:1), N₂, 130 °C, 4 h, 57 %; (iii) vinyl boronic acid pinacol ester (2 equiv.), PdCl₂(dppf)DCM (5 mol%), Cs₂CO₃ (4 equiv.), degassed DI water, N₂, 100 °C, 24 h, 52 %.

3.5.2 Ring-Closing Metathesis of **22**

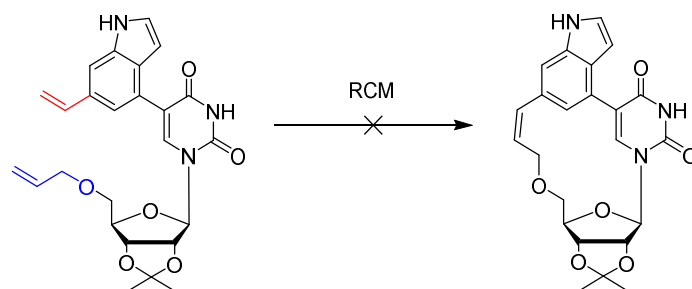
Following its successful preparation, the aim was to carry out an RCM with **22**. A model reaction involving **20a** and 6-vinylindole was performed and optimized using a variety of Grubbs catalysts and solvent. Complete product conversion was observed via Hoveyda-Grubbs II catalyst in anhydrous DCM (**Table 8, entry 3**). However, application of these conditions towards the desired product was unsuccessful (**Scheme 42**). A 3-carbon linkage between the 5'-position and the indole substituent may lead to a macrocycle with considerable strain, which may explain the unsuccessful RCM of **22** under these conditions.

Table 8 Model olefin metathesis reaction^a

Entry	Catalyst	Solvents	Results
1	Grubbs II	dry DCM	no product
2	Grubbs II	anhydrous THF	no product
3	Hoveyda-Grubbs II	dry DCM	99 % conv. ^b
4	Hoveyda-Grubbs II	anhydrous THF	1:1 SM/product

^aThe reaction was performed at 40 °C.

^bConversion was determined by ¹H NMR analysis of the crude product.



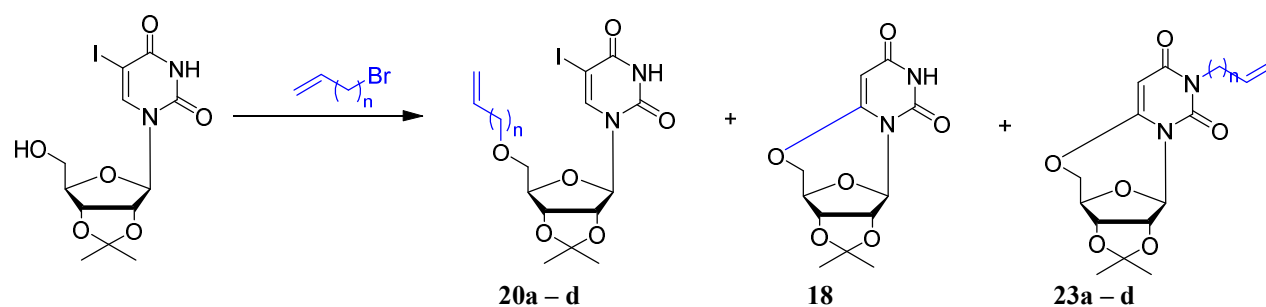
Scheme 42 RCM of compound **22**. Reagents and conditions: Hoveyda-Grubbs II, dry DCM, 40 °C.

3.5.3 Synthesis of 5'-*O*-hexen-6-yl-5-iodouridine derivative **20d**

Starting with **16** and allylbromide, **20a** was obtained at a yield of 80 % (**Table 9, entry 1**) via the conditions in **Chapter 3.4.2**. However, when the substrate 3-bromo-propene was changed to 4-bromo-butene, 5-bromo-pentene or 6-bromo-1-hexene, the resulting product shifted to the side product, namely, 5-iodo-*O*⁶-5'-cyclouridine derivative **18** (**Table 9, entry 2-4**). This suggested the substrate plays an important role in the competition between alkenylation and cyclization (**Table 9**). To circumvent cyclization, numerous changes were applied. First, the

solvent was changed to anhydrous DMF from THF in the case of 6-bromo-1-hexene. However, no 5'-*O*-alkenylated compound was produced but side product **23d** (**Table 9, entry 5**). The first step was then performed using conventional stirring instead of sonication. This facilitated use of lower temperature for the activation step. Sonication was used in the second part. This yielded small amount of alkenylated product (**Table 9, entry 6**). It seems that the low temperature facilitates the alkenylation but slows down the cyclization. Consequently, the entire reaction was performed at low temperature. This led to 50 % conversion of the alkenylated compound (**Table 9, entry 7**). Further optimization was performed to increase the yield. Results were summarised in **Table 9, entry 8 – 10**. The highest yield occurred using both 2.5 equivalents of bromide and NaH (**Table 9, entry 8**). To further circumvent cyclization, diluted protected 5-iodouridine was added to the reaction system drop by drop (**Table 9, entry 11**) because a concentrated solution is able to accelerate the ring-forming reaction. However, no product was found under these conditions. Teste *et al.*¹⁴⁹ reported a close relationship between regioselectivity and dielectric constant of solvent. When the dielectric constant of the solvent is lower than 10 (i.e., THF), the *O*-alkenylated product is favoured over *N*-alkenylated product. Considering this, the reaction was repeated using THF, cold temperature and both sonication and traditional stirring (**Table 9, entry 12 and 13**). Unexpectedly, neither condition yielded the desired product.

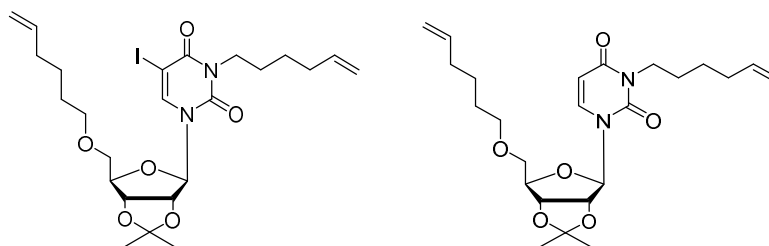
In view of these results, it seems that the selectivity between alkylation, cyclization and temperature are closely linked. In the case of 6-bromo-1-hexene, cyclization is predominant under the conditions of sonication which often leads to uncontrolled heating. Low temperature can slow down cyclization allowing nucleophilic substitution on the 5'-position of the nucleoside. Unusually, applying the optimized conditions to 5-bromo-1-pentene yielded only starting material with neither alkenylated nor cyclic compound observed (**Table 9, entry 14**).

Table 9 Competition between alkenylation and cyclization in position 5'-O of 5-iodouridine derivative. (a – d: n = 1 – 4)

Entry	Bromide	Equiv. of bromide	Equiv. of NaH	Solvent (dry)		Reaction time first/second step	T (°C)	Conv. (%) ^b 20: 18: 23	Yield (%) ^c
1	3-bromo-1-propene	1.2	2.5	THF	sonication	0.5 h/1.5 h	20-50 °C	91:9:0	80
2	4-bromo-1-butene	1.2	2.5	THF	sonication	0.5 h/2 h	20-40 °C	0:100:0	N/A ^d
3	5-bromo-1-pentene	1.2	2.5	THF	sonication	0.5 h/2 h	30-50 °C	0:100:0	N/A ^d
4	6-bromo-1-hexene	1.2	2.5	THF	sonication	0.5 h/3 h	20-50 °C	0:100:0	N/A ^d
5	6-bromo-1-hexene	1.2	2.5	DMF	sonication	0.5 h/0.5 h	20-40 °C	0:0:100	N/A ^d
6	6-bromo-1-hexene	1.2	2.5	DMF	conventional + sonication	30 min/10 min	0 °C/25 °C	23:67:0	N/A ^d
7	6-bromo-1-hexene	1.2	2.5	DMF	conventional	0 h/1 h	0 °C	50:50:0	N/A ^d
8	6-bromo-1-hexene	2.5	2.5	DMF	conventional	0 h/1 h	0 °C	59:31:10	44
9	6-bromo-1-hexene	2.5	5	DMF	conventional	0 h/2.5 h	0 °C	45:55:0	N/A ^d
10	6-bromo-1-hexene	5	2.5	DMF	conventional	0 h/2.5 h	0 °C	0:0:100	N/A ^d
11	6-bromo-1-hexene, diluted	2.5	2.5	DMF	conventional, dropwise	30 min/24h	0 °C	0:0:50	N/A ^d
12	6-bromo-1-hexene	2.5	2.5	THF	conventional	0h/2.5h	0 °C	0	N/A ^d
13	6-bromo-1-hexene	2.5	2.5	THF	sonication	20min	0 °C	0	N/A ^d
14	5-bromo-1-pentene	2.5	2.5	DMF	conventional	0 h/2 h	0 °C	0	N/A ^d

^a The reaction was performed under 110 °C.^b Conv.: Conversion; Conversion was determined by ¹H NMR analysis of the crude product.^c Isolated yield^d N/A: Not applicable

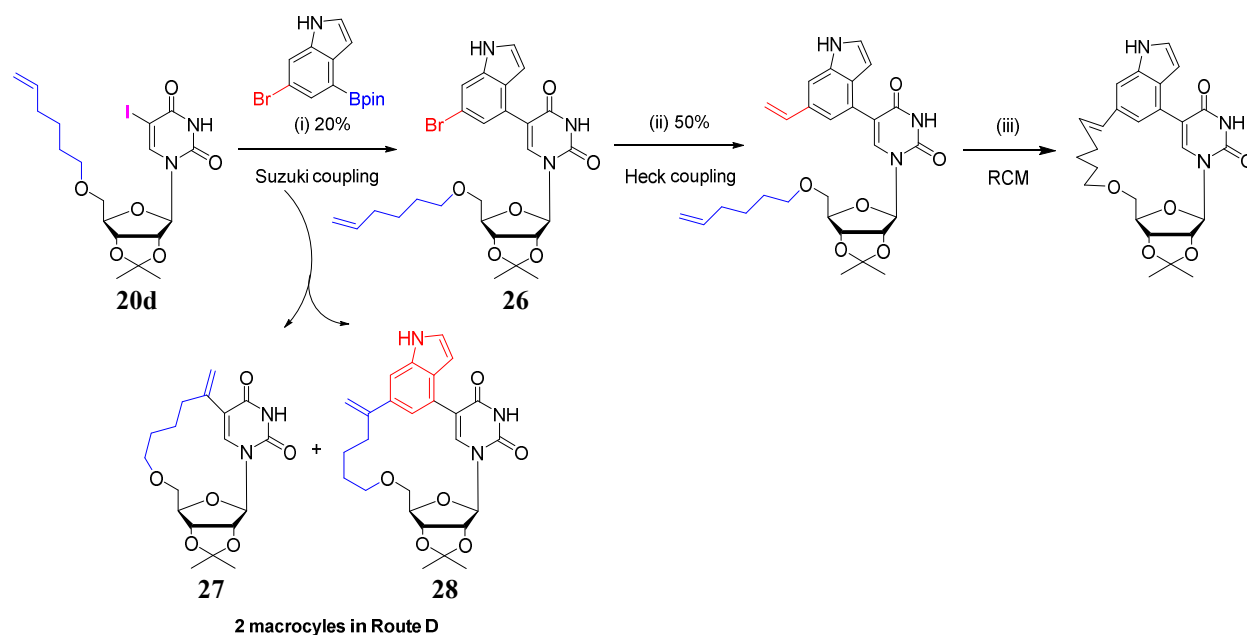
It is worth mentioning that in the 2 g large-scale reaction of **16** and 6-bromo-1-hexene, two by-products, dihexen-substituted nucleosides **24** and **25**, were isolated with yields of 7 % and 5 %, respectively (see experimental). To evaluate the effect of hexene group of uridine derivatives on inhibitory activity, **24** and **25** were deprotected for purpose of activity testing in Chapter 3.7.6.



Scheme 43 Structures of **24** (left) and **25** (right)

3.5.4 Formation of the macrocycle from **20d**

With 5'-*O*-hexen-6-yl-5-iodouridine derivative **20d** in hand, the Suzuki cross-coupling, vinylation and RCM were conducted sequentially based on synthetic strategy from Chapter 3.3.2, 3.4.1 and 3.5.2 (**Scheme 44**). While formation of the desired target molecule was observed by LC/MS, the low yield of the total synthesis precluded its isolation in pure form. Moreover, in addition to **26**, the formation of two macrocycles, **27** and **28**, was observed during the first step of this reaction sequence (**Scheme 44**). Full details of the formation and characterisation of these unexpected side products, **27** and **28**, will be discussed in Chapter 3.6 (Route D)



Scheme 44 Synthesis of macrocycles starting from compound **20d**. Reagents and conditions: (i) PdCl₂(dppf)DCM (5 mol%), NaHCO₃ (3 equiv.), degassed dioxane/H₂O (3:1), N₂, 90 °C, 20 h, 20 %; (ii) Vinyl boronic acid pinacol ester (2 equiv.), PdCl₂(dppf)DCM (5 mol%), Cs₂CO₃ (4 equiv.), degassed dioxane/H₂O (3:1), N₂, 90 °C, 20 h, 50 %; (iii) Hoveyda-Grubbs II (10 mol%), anhydrous DCM, 40 °C, 1 day.

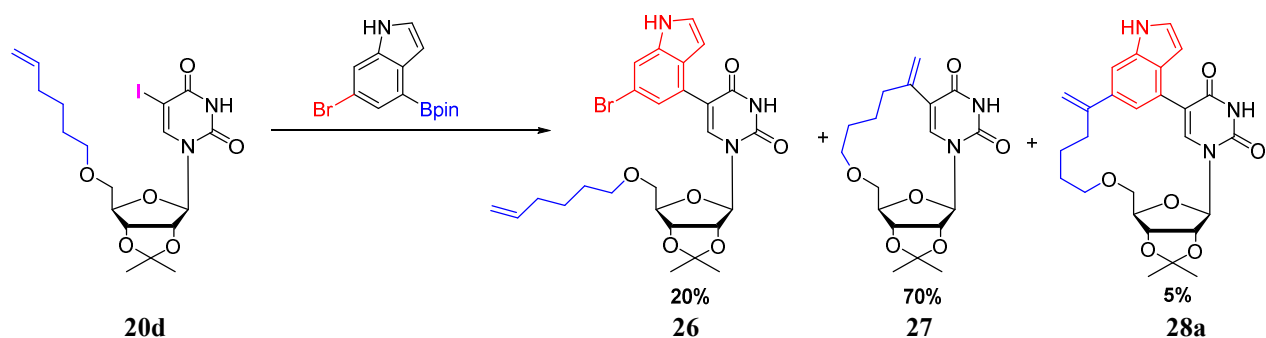
3.6 Formation of the macrocycle via intramolecular Heck reaction (Route D)

The Suzuki coupling of **20d** and **12** unexpectedly resulted in the formation of two macrocycles. Subsequent investigations confirmed that these two products, **27** and **28**, originated from the Heck macrocyclization of **20d** and **26**, respectively.

3.6.1 Synthesis and characterisation of macrocycles **27** and **28**

To fully characterize the side products of Suzuki coupling of **20d** and **12** (Scheme 45), the three products were separated and purified by column chromatography. NMR and LC-MS were used to characterize **27** and **28**. For the initial characterization of compound **27**, the free double bond was shown as terminal double bond in HSQC (or DEPT), and the alkenyl chain showed

correlation with the H-6 of nucleobase in NOESY. In addition, a crystal structure was obtained by X-ray diffraction with high resolution, unambiguously confirming the formation of the macrocycle in **27** (Figure 34). Similarly for compound **28**, the free double bond was shown as terminal double bond in HSQC (or DEPT), and the proton of free double bond showed correlation with H-7 of the indole in NOESY. NMR spectra and LC-MS suggested compound **28** is a mixture of different isomers with an endocyclic or exocyclic double bond (Figure 35). This may be due to electronic rearrangement during Heck reaction. The structural similarities between these isomers may explain the difficulty isolating compound **28** via column chromatography. Thus, in the NMR spectra, some small peaks were shown on the baseline (Figure 36), but it is still clear that the main product was compound **28a**. LC-MS showed an identical value for the mixture of compound **28** which supported the hypothesis that **28** was a mixture of isomers.



Scheme 45 One-pot cross-coupling reaction between compound **20d** and **12**. Reagents and conditions: (i) PdCl₂(dppf)DCM (5 mol%), NaHCO₃ (3 equiv.), degassed dioxane/H₂O (3:1), N₂, 90 °C, 20 h.

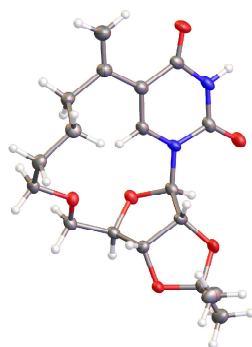


Figure 34 Crystal structure of **27**

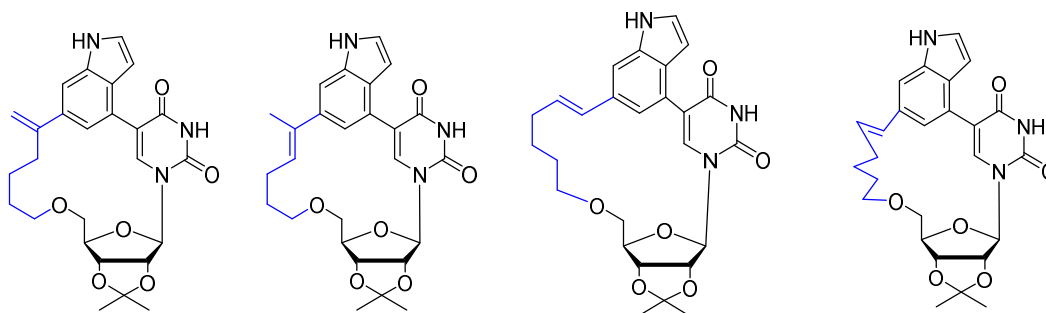


Figure 35 Proposed isomers of compound **28** formed in cross-coupling reaction

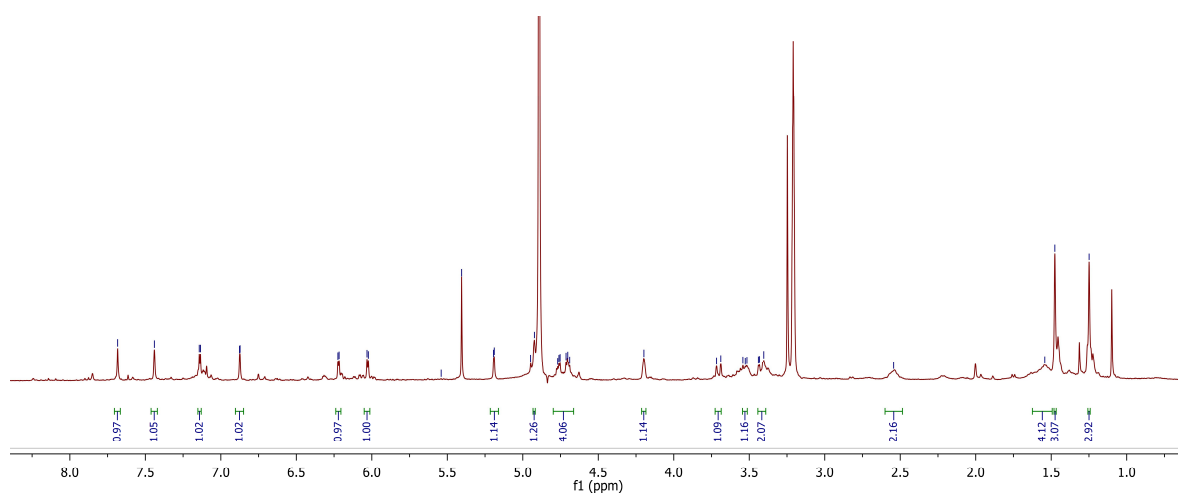
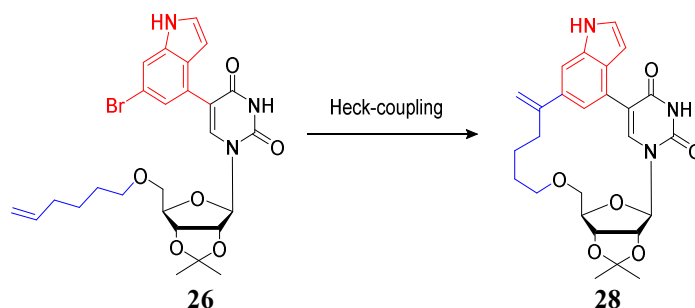


Figure 36 ^1H NMR of **28a** with some isomers

Although **27** and **28a** were not the primary target molecules, they were of interest since they contained a macrocycle with reduced conformational flexibility. While a single example has been reported before for linking positions 5 and 5' of a deoxynucleoside, using Click chemistry,¹⁵⁰ the intramolecular cyclisation that led to the macrocyclic nucleoside **27** has, to the best of our knowledge, never been described before. We reasoned that this might represent an unexpected but versatile method for the generation of the desired class of conformationally restricted molecules as potential GalT inhibitors. **28** on the other hand is exactly one of the target compounds, containing both a macrocyclic linkage and the 5-indole substituent. In the same conditions of Suzuki cross-coupling of **Scheme 45**, compound **26** can be converted to **28** with high conversion. Then by changing the category of base, it's found most of the base could

provide high conversion (**Table 10**). Although high conversion was observed, only 30 % yield of product was obtained after a purification with column chromatography. The Heck macrocyclization of 5'-*O*-hexen-5-(6-bromoindol-4-yl) uridine derivative **26** appears to undergo multiple side reactions.

Table 10 Optimization of intra Heck coupling^a of **26**



Entry	Base	Conv. (%) ^b	Yield (%) ^c
1	NaHCO ₃	80	N/A ^d
2	Na ₂ CO ₃	99	N/A ^d
3	Cs ₂ CO ₃	99	N/A ^d
4	K ₂ CO ₃	99	30
5	Et ₃ N	90	N/A ^d

^a Reagents and conditions: PdCl₂(dppf)DCM (5 mol%), base (3 equiv.), 3:1 dioxane/H₂O, N₂, 90 °C, 16 h.

^b Conversion was determined by ¹H NMR analysis of the crude product.

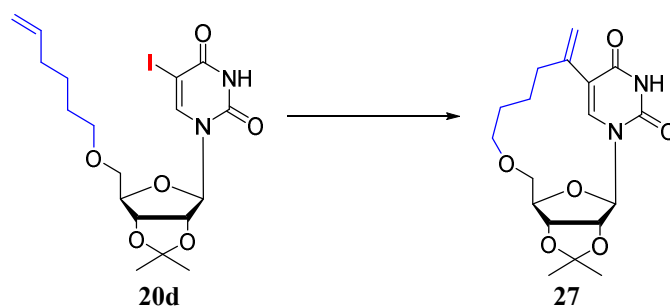
^c Isolated yield

^d N/A: Not applicable

To increase the yield of compound **26** or **28**, we tried to find appropriate conditions to inhibit compound **27** (**Table 11**). The hypothesis was that there was a competition between intra Heck coupling reaction of **20d** and inter Suzuki coupling reaction of **20d** and **12**. We tried to find the appropriate conditions that slow down the intra Heck coupling reaction but improve the inter Suzuki coupling reaction. With different reaction conditions, it provided the highest inhibition of Heck coupling reaction with conditions of Na₂PdCl₄ and ^sSPhos in dioxane/H₂O. 50% conversion can be observed in 1 hour. The majority of reaction conditions yielded good

conversion of the ring-closed compound. This indicated this intra Heck coupling reaction was very active. The selected reaction conditions (**Table 11, entry 3**) were then applied to the target reaction with **20d** and **12**. Unfortunately, **26** and **28a** were not observed.

Table 11 Compound **27** from intramolecular Heck coupling^a of **20d**



Entry	Catalyst	Ligand	Solvent	Time	Conv. (%) ^b	Yield (%) ^c
1	PdCl ₂ (dppf) DCM	-	dioxane/ H ₂ O	1h	99	80
2	Pd(PPh ₃) ₄	-	dioxane/ H ₂ O	1h	99	N/A ^d
3	Na ₂ PdCl ₄	^s SPhos	dioxane/ H ₂ O	1h	50	N/A ^d
				2h	75	N/A ^d
				3h	99	N/A ^d
4	Na ₂ PdCl ₄	TPPTS	H ₂ O	1h	90	N/A ^d

^a The reaction was performed under N₂ at 90 °C.

^b Conv: Conversion; Conversion was determined by ¹H NMR analysis of the crude product.

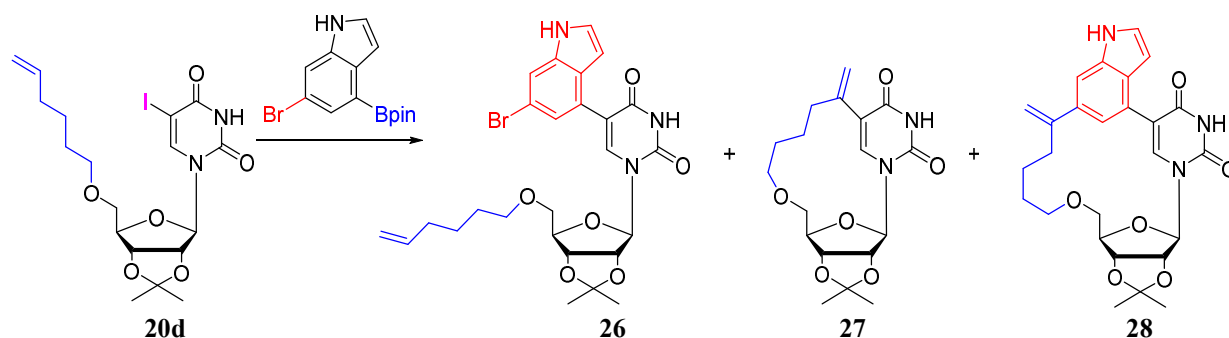
^c Isolated yield

^d N/A: Not applicable

Significant challenges were encountered finding appropriate conditions that favored Suzuki coupling over the intra Heck coupling. To address this, we altered the Suzuki coupling reaction conditions, modifying the Pd source, type of base, solvent, number of equivalents, temperature and substrate concentration (**Table 12**). Although the yield of **27** was not reduced, the yield of **28** can be improved from 5 % to 23 % when the temperature was increased to 130 °C and make the nucleoside concentration to 8 mM (**Table 12, entry 3**). This suggested the final compound

28 could be obtained from **20d** in one step. LC-MS and NMR data indicated fewer side products were being formed at higher temperatures.

Table 12 Optimization of synthesis of **26**



Entry	[Pd]	Base	Solvent	Equiv. (indole)	Temp (°C)	Conc. (20d) ^a mM	Yield (%) ^b (26:27:28)
1	PdCl ₂ (dppf) DCM	NaHCO ₃	dioxane/ H ₂ O	1.2	90	4	20:70:5
2	Na ₂ PdCl ₄ / ^s SPhos	no	dioxane/ H ₂ O	1.2	90	4	most 27
3	PdCl ₂ (dppf) DCM	NaHCO ₃	dioxane/ H ₂ O	2	130	8	0:68:23
4	Na ₂ PdCl ₄ /T PPTS	Cs ₂ CO ₃	H ₂ O	1.2	130	8	most 27
5	PdCl ₂ (dppf) DCM	NaHCO ₃	DME/ H ₂ O	1.2	130	8	0:83:17
6	PdCl ₂ (dppf) DCM	K ₂ CO ₃	DME	1.2	130	8	most 27

^a Concentration of **20d**

^b Isolated yield

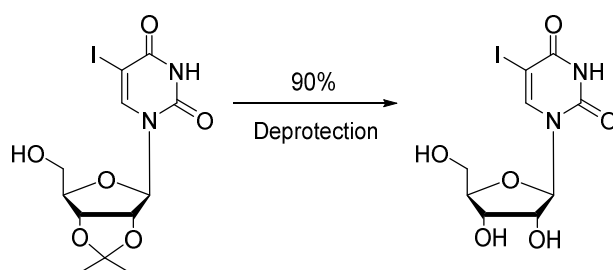
3.7 Synthesis of final compounds

Having obtained two macrocyclic precursors, **27** and **28**, the subsequent step involved their deprotection to generate the final compounds for testing. The deprotection of **27** resulted in the formation of **29**, accompanied by a by-product, **30**, identified as a product of the hydration

reaction. The deprotection of **28** yielded **31**, a mixture of at least five isomers. The hydrogenation of **27** produced **32**, while **34** represented the acetylated form of **27**. Compounds **36** – **41** were deprotected forms of intermediates generated through various synthetic routes. These will be discussed in the following sections.

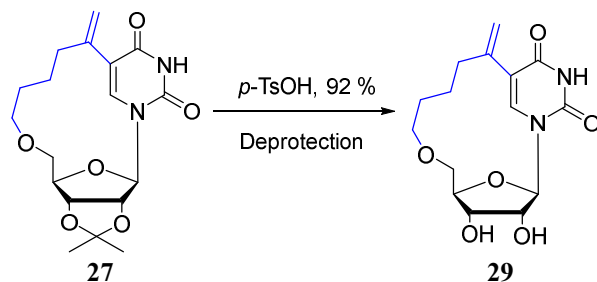
3.7.1 Synthesis of macrocycle **29**

The isopropylene group was removed following the method of Sun *et al.*¹⁵¹ using HCl at 45°C. This method was applied due to the simple reagents and ease of work-up. A test reaction was performed with compound **16**. The reaction was complete in 30 mins with a yield of 90 % (Scheme 46). However, the application of these conditions to compound **27** was not successful.



Scheme 46 Deprotection of compound **16** with HCl. Reagents and conditions: 1N HCl, MeOH, 45 °C, 30 min, 90 %.

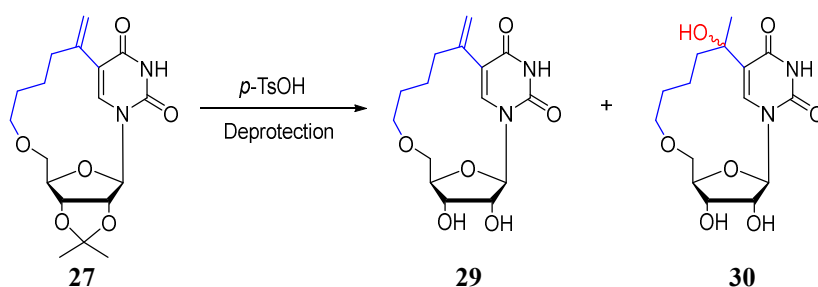
In a separate project carried out at the same time in our laboratory, another PhD student observed that harsher deprotection conditions such as *p*-TsOH¹⁵² are required for cyclo-nucleosides than for the corresponding ring-open nucleosides (Ramya Nuti, unpublished results). These conditions were applied to the ring-closed compounds introduced here. Compound **29** was subsequently obtained in good yield as a pure white powder following simple recrystallisation from DCM. The additional steric bulk and electronic effect associated with ring-closed compounds may explain why stronger acidic conditions were required.



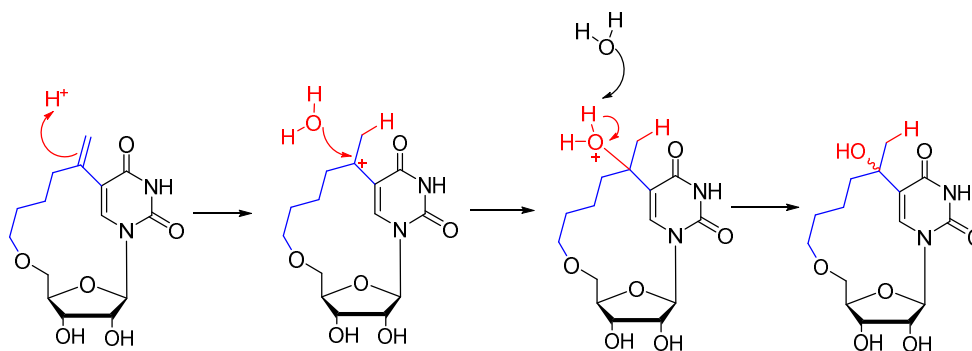
Scheme 47 Deprotection of macrocycle **27** with *p*-TsOH. Reagents and conditions: *p*-TsOH (2 equiv.), THF/H₂O (1:1), 80 °C, 5 h, 92 %.

3.7.2 Synthesis of macrocycle **30**

An interesting observation was made during deprotection of **27** with *p*-TsOH. Acid-catalyzed hydration was observed at the exocyclic double bond of **27**, resulting in **30** (**Scheme 48** and **Scheme 49**). This hydration was concentration dependent. When the concentration of **27** was 22 mM, little trace of compound **30** was observed, while 30 % yield of **30** was obtained with 54 mM of compound **27**. The compound was characterized by NMR, in which, the ¹H NMR spectrum showed disappearance of CH₂ and CH peaks of the free double bond. The ¹H NMR spectrum in DMSO-*d*₆ showed a new OH peak and the NOESY displayed a correlation between the new OH peak and new CH₃ peak. As the new chiral centre was formed in the hydration reaction, compound **30** was a mixture of diastereomers, which can be identified by the NMR and HPLC. Due to their similar properties, they were difficult to separate via column chromatography, but the purity could be improved by washing with MeOH (**Figure 37**). However, the absolute structures of the two isomers were difficult to determine from NMR.



Scheme 48 Acid-catalyzed hydration of **27**. Reagents and conditions: *p*-TsOH (2 equiv.), THF/H₂O (1:1), 5 h, 80 °C.



Scheme 49 Mechanism of acid-catalyzed hydration of **27**

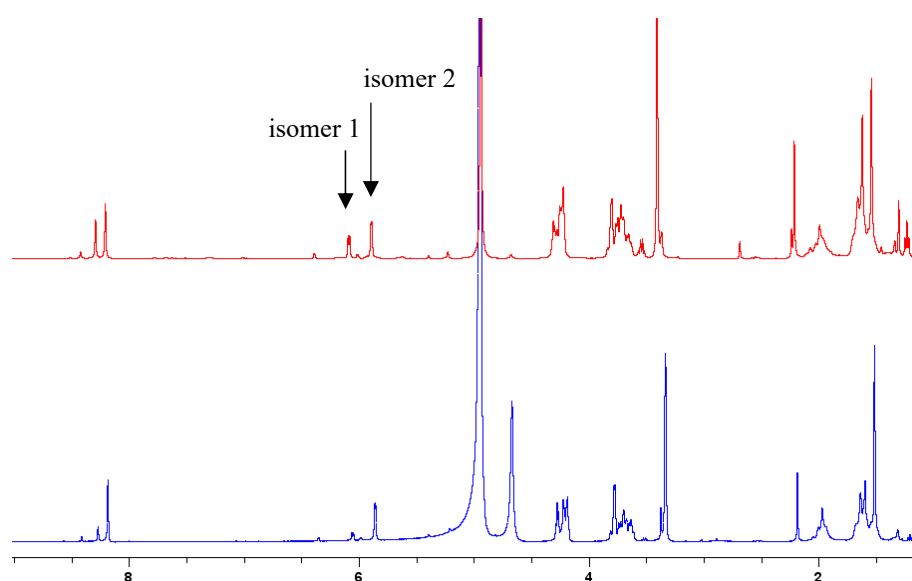
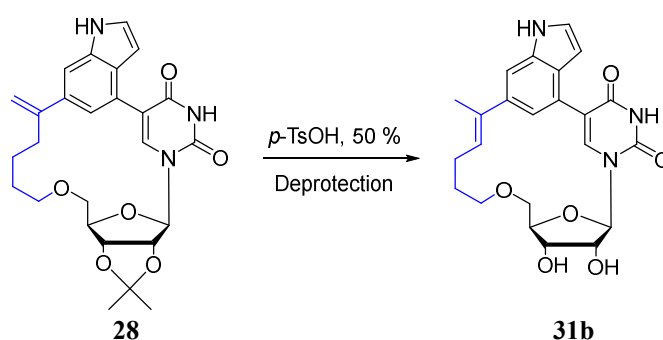


Figure 37 ^1H NMRs of two isomers of compound **30** (top: purified via silica gel chromatography; bottom: washed with MeOH)

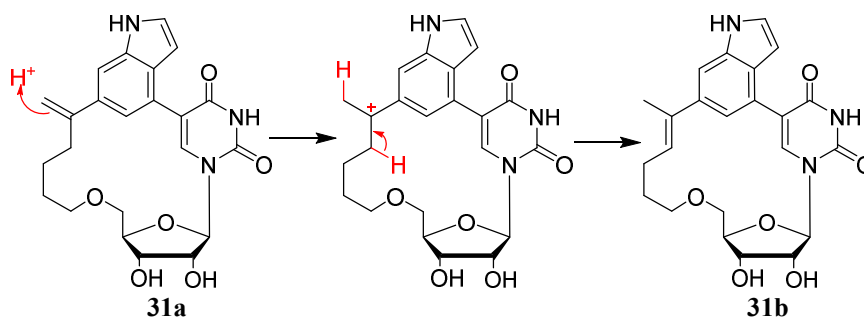
3.7.3 Synthesis of macrocycle **31**

With the experience of deprotection of compound **27**, 2 equiv. *p*-TsOH in THF/H₂O was then applied to the deprotection of compound **28** (**Scheme 50**). The reaction worked well on a small scale (4 mg, 8 μmol). However, when the scale was increased to 20 mg (40 μmol), only half the material was consumed. Then 4 equiv. *p*-TsOH was applied to the reaction. In this way, 50 mg (100 μmol) compound **28** was deprotected in 10 hours. However, the yielded product **31** was still a mixture of isomers. This was determined via LC-MS. Similar to compound **28**, the

structural similarity meant these isomers of **31** could not be entirely separated, hence the NMR results show small peaks on the baseline. Despite the impurities in the NMR spectra, a dominant product was observed. Surprisingly, this predominant isomer was **31b**, not **31a**. This was observed via loss of the protons on the exocyclic double bond and appearance of a new CH₃ group from NMR. NOESY showed correlation between the new CH₃ and the H-7 on the indole. This can be explained by electronic rearrangement under acidic conditions (**Scheme 51**).



Scheme 50 Deprotection of compound **28** with *p*-TsOH. Reagents and conditions: *p*-TsOH (2 equiv.), THF/H₂O (1:1), 80 °C, 10 h, 50 %.



Scheme 51 Proposed mechanism of electronic rearrangement from compound **31a** to **31b** under acidic conditions

Preparative TLC was used to separate the mixture of compound **31**. However, despite the appearance of good separation via TLC, NMR data indicated some small impurity peaks remained. The subsequent HPLC indicated at least 3 compounds were present.

Two hypotheses were used to rationalize the mixture of products observed. The first was that the compounds might be atropisomers which arise from hindered rotation around a single bond. The large energy barrier leads to discrete conformers. The corresponding ring-open compound **1** has two flexible bonds between the indole, nucleobase and ribose (green arrows, **Figure 38**). Once the ring was closed, the rotation became greatly hindered (red arrows, **Figure 38**). In this situation, different isomers with different energy, called atropisomers, might be generated. To verify this, HPLC experiments were performed. Atropisomers were thought to be temperature dependent. Hence, performing HPLC at variable temperatures was sought to provide information about whether the isomer ratio was altered upon temperature changes. Three approaches were applied. First, the HPLC column was preheated to 50 or 60 °C prior to sample injection. Second, the sample was heated to 100 or 165 °C before sample injection at rt. The third approach was a combination of both, whereby the sample was heated to 100 or 165 °C prior to injection to a preheated column (at 50 °C). However, after application of these three techniques, the ratio of compounds was unchanged, suggesting the isomers were not atropisomers.

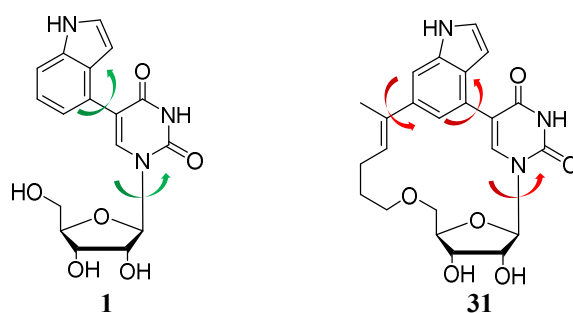
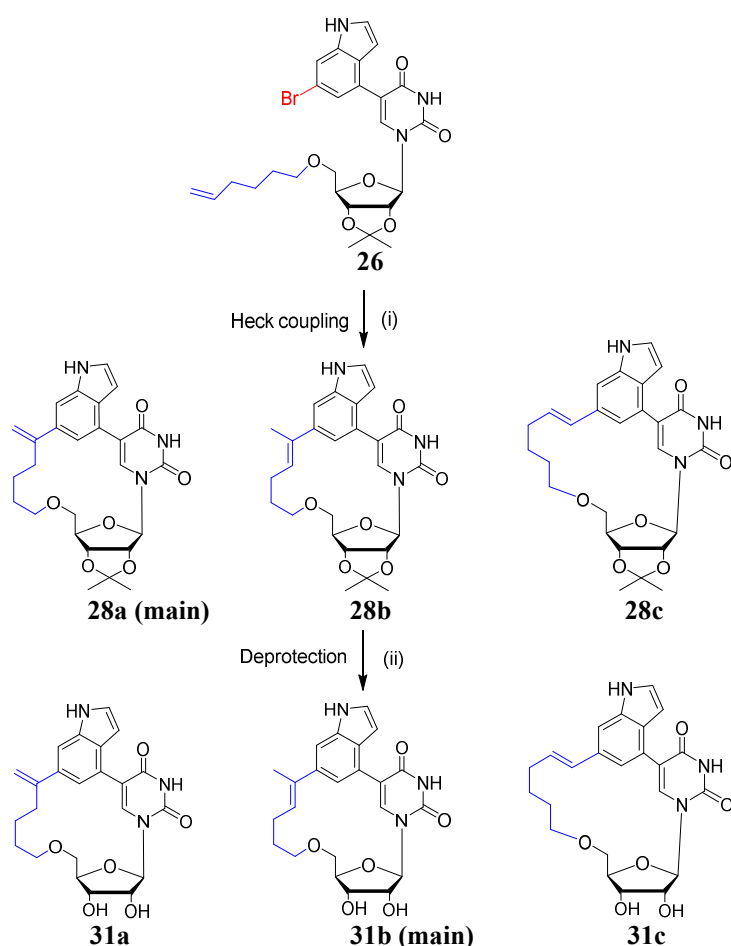


Figure 38 Hindered rotation of compound **31**

As an alternative explanation for the different isomers of **31**, we hypothesised that under Suzuki coupling conditions, **26** may already undergo macrocyclisation to different constitutional isomers (**Scheme 52**). To verify this, compound **31** was stirred with 4 equiv. *p*-TsOH at rt

(15 °C) or 80 °C and then monitored by HPLC with varying timepoints to determine whether the isomer ratios were altered. Findings suggested the isomer ratios were almost unchanged at rt. However, all these three main compounds degraded over time at 80 °C, especially for the first one (red arrow, **Figure 39**). These results suggested the proportion of compound isomers were stable in acid at rt while easy to degrade in acid in high temperature (80 °C). This indicated that incubation of the compounds in acid at different temperatures was an inefficient method for transformation of one isomer to another.



Scheme 52 Proposed constitutional isomers of **28** and **31**. Reagents and conditions: (i) PdCl₂(dppf)DCM (5 mol%), NaHCO₃ (3 equiv.), degassed dioxane/H₂O (3:1), N₂, 130 °C, 20 h; (ii) *p*-TsOH (2 equiv.), THF/H₂O (1:1), 80 °C.

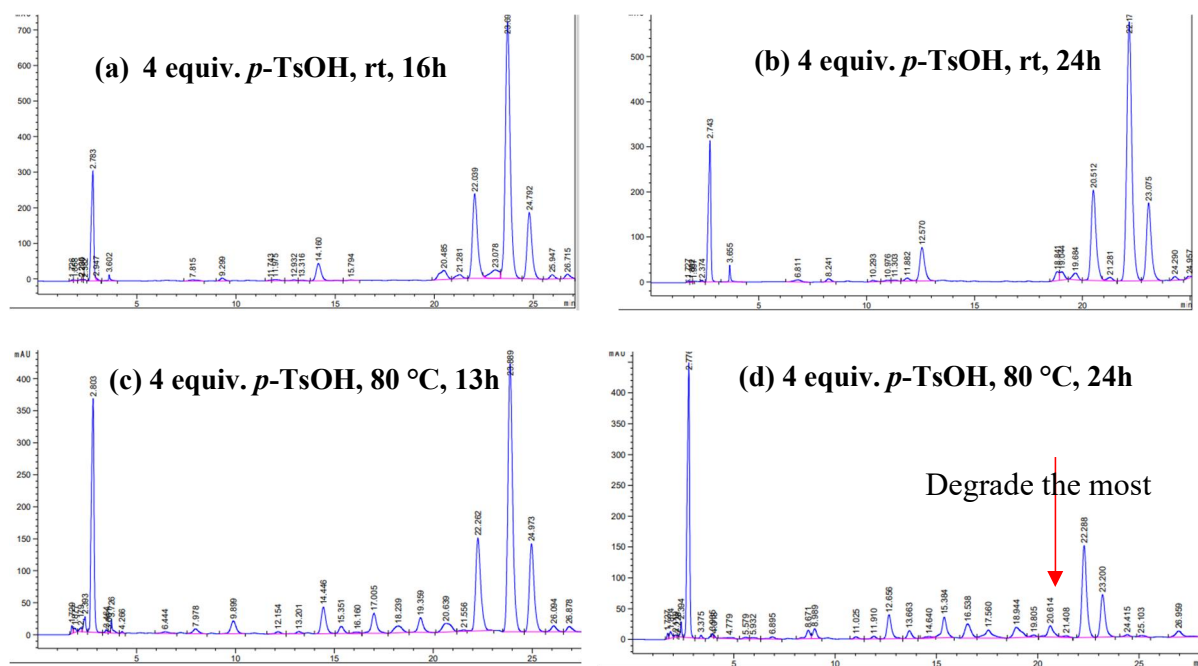


Figure 39 Effect of acid and temperature on the proportion of isomers of **31**. Flow rate: 1 mL/min; Solvent gradient: 40–70 % MeOH in water in 30 min; Wavelength: 254 nm; Retention time of isomers are 22.0, 23.1 and 24.8 min, respectively (varies a little each time).

Thus, further purification and separation was required to identify the different isomers. HPLC was performed. This was first performed on a preparative HPLC however the yield was limited by low sample loading (**Table 13**). This was due to poor solubility in MeCN/H₂O and limited peak separation despite the long retention times. An alternative way was analytical HPLC with manual collection. Limited by the maximum loading concentration and loading volume of the machine, the maximum loading scale was 0.2 mg per hour. This was comparable to the preparative HPLC.

Table 13 Comparison of separation between preparative and analytical HPLC

	Preparative HPLC	Analytical HPLC
Solvent	MeCN/H ₂ O	MeOH/H ₂ O
Rate (mg/mL)	10	1
Retention time (min)	100	20
Maximum loading concentration (mg/mL)	2	1
Maximum loading volume (uL)	300	100
Loading amount (mg/h)	0.3	0.2

The three main peaks were successfully separated by analytical HPLC at retention times of 21.1, 22.8 and 23.8 min, respectively (**Figure 40**). The NMR data showed the first peak was not entirely pure while making it difficult to identify the main compound. However, it was clear that the first peak still contained a mixture of different isomers. The second peak observed via HPLC was the dominant product. The second peak observed in HPLC was also a mixture of two isomers and their structures can be confirmed through NMR analysis. These isomers are **31a** and **31b**, as shown in **Figure 41**, with a ratio 0.7:1. The third peak was also validated by NMR (**Figure 42**). This compound, **31c**, was a macrocycle with an endocyclic double bond. The coupling constant was 11.12 Hz, suggesting its trans configuration.

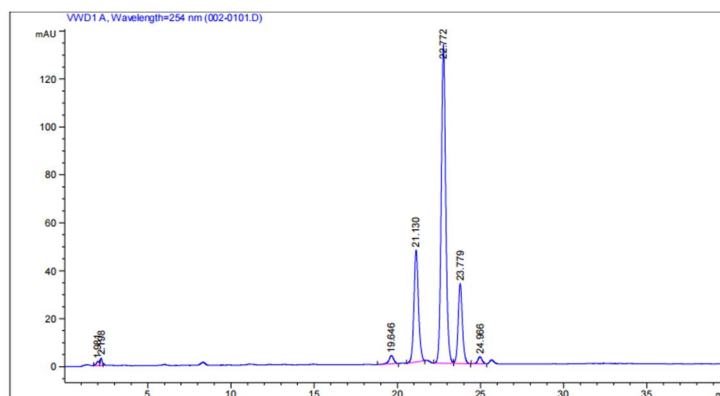


Figure 40 The separation of **31** via analytical HPLC at 254 nm. Flow rate: 1 mL/min; Solvent gradient: 40–70 % MeOH in water in 30 min. Retention times of isomers are 21.1, 22.8 and 23.8 min, respectively.

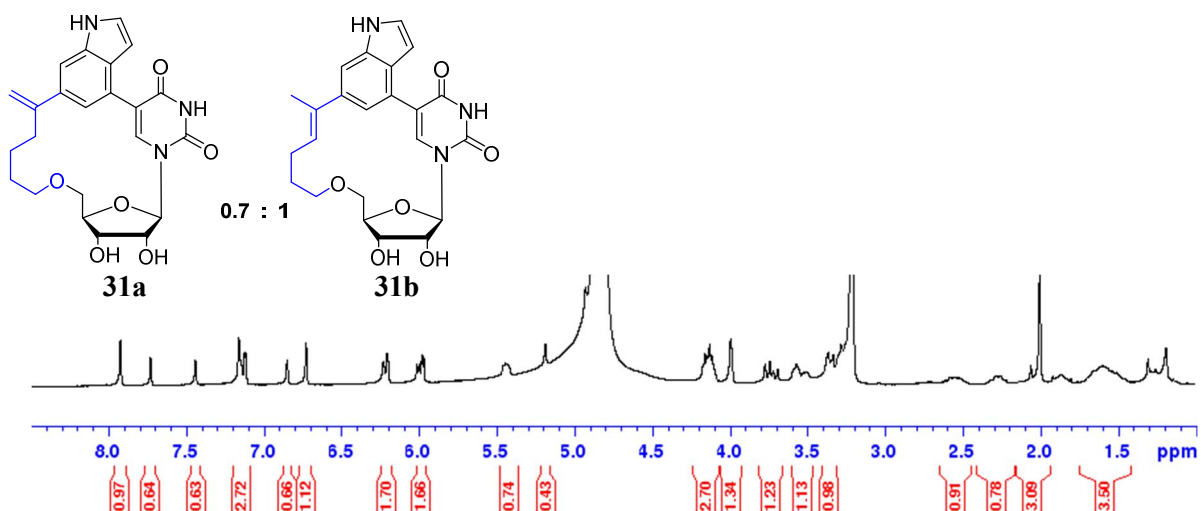


Figure 41 ^1H NMR characterization of the second HPLC peak of **31**

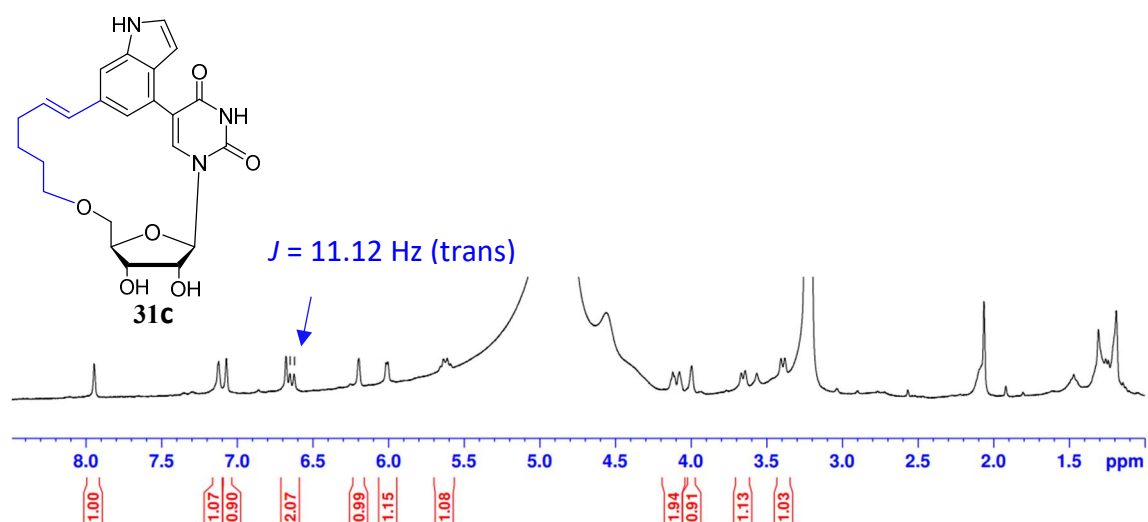
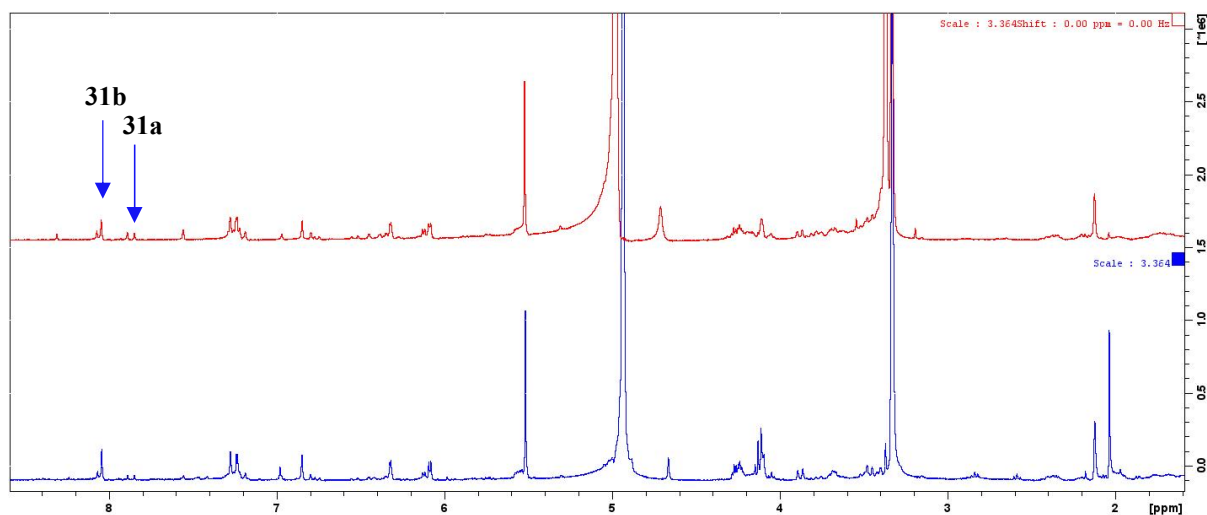


Figure 42 ^1H NMR characterization of the third HPLC peak of **31**

Following identification of the main isomers, this gave confidence in structural assignment of the main peaks present in the NMR of mixtures (**Scheme 53**, top). After addition of 4 equiv. *p*-TsOH in two batches, less **31a** was formed leading to a greater yield of **31b** (**Scheme 53**, bottom).

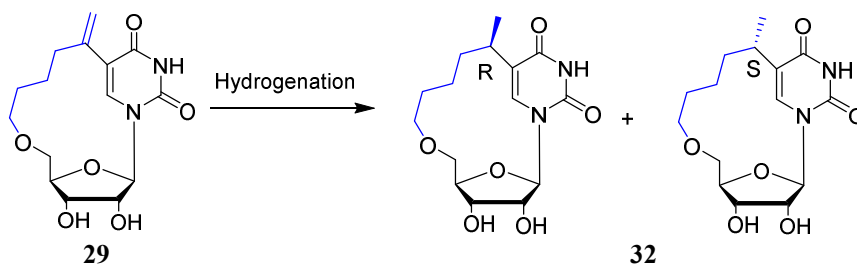


Scheme 53 Proportions of **31a** and **31b** with complete addition of 4 equivalent *p*-TsOH (top) and batch addition of *p*-TsOH (bottom)

3.7.4 Synthesis of macrocycle **32**

To expand the scope of the final compounds, more analogues were synthesized. To understand the impact of rigidity or flexibility on the biological properties, **27** was hydrogenated to increase the conformational flexibility. As expected, a mixture of two diastereoisomers was produced due to formation of a new chiral centre. With Pt₂O as the catalyst, two isomers were isolated in a ratio of approximately 3:7 with a slightly variable in the amount of catalyst (**Table 14, entry 1 – 3**). It is interesting that when the catalyst was changed to Pd/C, the ratio of the two isomers was completely reversed (**Table 14, entry 4**). However, the absolute structures of **32a** and **32b** were difficult to elucidate via NMR. Recrystallisation was proposed to address this. Since the protected nucleoside was less polar, **27** was hydrogenated with 10 % Pt₂O (**Scheme 54**). This took 16 hours, longer than the reaction time for unprotected **29**. Both the HPLC and NMR showed an approximate 3:1 of the two isomers of products **33**. Compound **32** formed a good quality crystal of *S* isomer, enabling high resolution X-Ray diffraction (**Figure 43**). To correlate these structures with the ¹H NMR spectra, HPLC was performed on the crystal to identify the retention time of the *S* isomer. Unfortunately, the HPLC spectrum of the crystal compound was still a mixture of two peaks. Thus, despite obtaining a crystal structure of the *S* isomer, it remains unclear which isomer predominantly formed using different catalysts.

Table 14 Hydrogenation^a of **29** using different catalysts

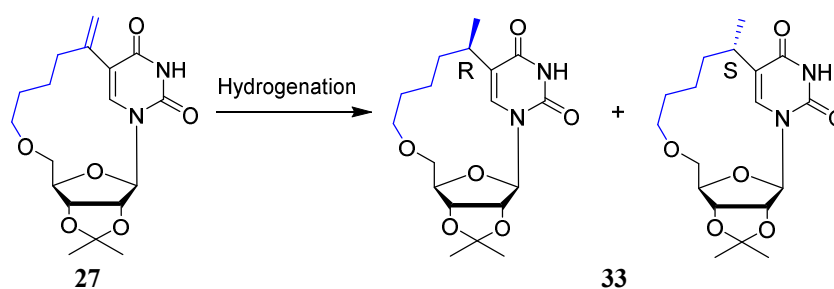


Entry	Catalyst	Amount of catalyst (mmol%)	Ratio of 32 (HPLC)	Ratio of 32 (NMR)	Yield (%) ^b
1	Pt ₂ O	50	30:70	N/A ^c	N/A ^c
2	Pt ₂ O	20	23:77	30:70	85 %
3	Pt ₂ O	10	27:73	N/A	N/A ^c
4	Pd/C	20	80:20	80:20	N/A ^c

^a The reaction was performed under hydrogen at rt for 30 min.

^b Combined yield of two diastereomers.

^c N/A: Not applicable



Scheme 54 Hydrogenation of **27** with Pt₂O catalyst. Reagents and conditions: PtO₂ (10 mol%), H₂, MeOH, rt, 16 h.

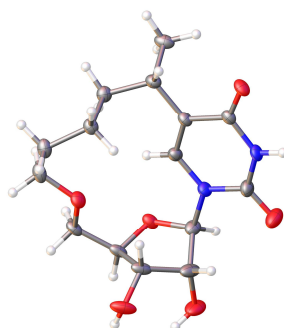
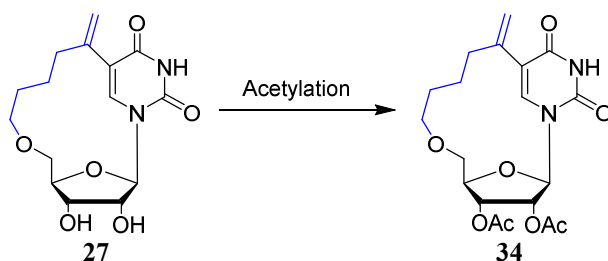


Figure 43 Crystal structure of *S* isomer of compound **32**

3.7.5 Synthesis of macrocycle **34**

To validate the hypothesis that the macrocycle **27** would lead to improved cell permeability, the acetylated form was synthesised. This could enable comparison with the ring-open compounds **5** to **8** under identical conditions (**Scheme 55**). Unfortunately, **34** was unstable at

rt, which was observed through changes in the HPLC/NMR. Hence, the acetylated form of **34** was not utilised for further activity assessment.

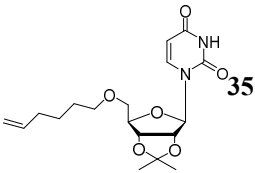
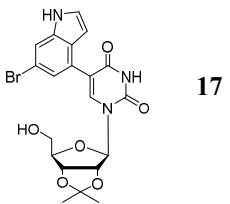
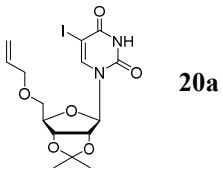
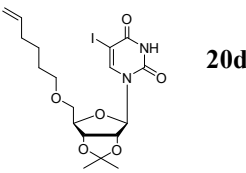
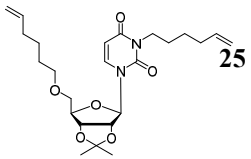
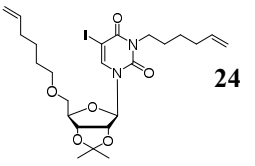
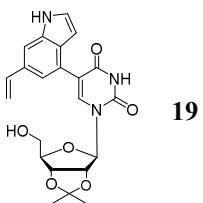


Scheme 55 Compound **34** from acetylation of **27**. Reagents and conditions: DMAP (0.05 equiv.), Ac₂O (3.5 eq.), pyridine, rt, 5 h.

3.7.6 Synthesis of uridine derivatives **36** – **41**

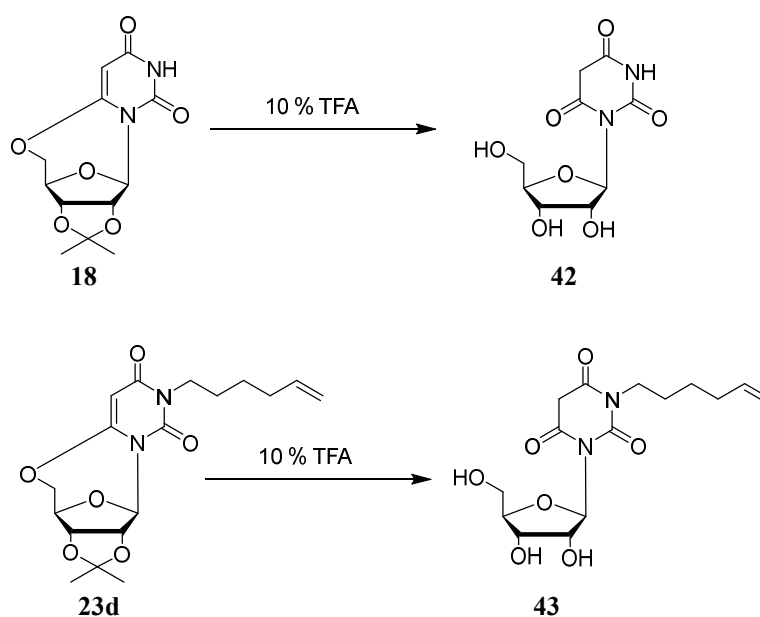
To understand the additional effect of conformational restriction of inhibitory activity, the ring-open analogue of **27**, 2',3'-*O*-isopropylidene-5'-*O*-hexenuridine **35**, was synthesised for comparison. This was done using the same synthetic route as for **20d**, with DMF as solvent. Given that **17**, **19**, **20a**, **20d**, **24** and **25** shared the same uridine scaffold (**Table 15**, **entry 2** – **7**), it was decided that testing the corresponding deprotected compounds would confer the additional benefit of exploring the effect of different functional groups on inhibitory activity. This would expand the overall inhibitor library. Hence, **36**, **37**, **38** and **39** were obtained by applying the deprotection strategy used for **16**, involving 1N HCl in MeOH (**Table 15**, **entry 1** – **4**). Since **24** and **25** had more complex structures, **40** and **41** were obtained using the same conditions as for **27**, using 4 equiv. *p*-TsOH instead of 1N HCl (**Table 15**, **entry 5** and **6**). Neither condition afforded hydrolysis of **19** (**Table 15**, **entry 7**).

Table 15 Nucleoside analogue deprotection.

Entry	Substrate	Conditions	Product ^a	Yield (%) ^b
1	 35	MeOH, 1N HCl 45 °C	36	61
2	 17	MeOH, 1N HCl 45 °C	37	50
3	 20a	MeOH, 1N HCl 45 °C	38	46
4	 20d	MeOH, 1N HCl 45 °C	39	39
5	 25	4 equiv. <i>p</i> -TsOH 1:1 THF/H ₂ O 80 °C	40	30
6	 24	4 equiv. <i>p</i> -TsOH 1:1 THF/H ₂ O 80 °C	41	42
7	 19	MeOH, 1N HCl, 45 °C or 4 equiv. <i>p</i> -TsOH 1:1 THF/H ₂ O, 80 °C	No reaction	N/A ^c

^a The 2'3'-*O*-isopropylidene group was removed from starting material.^b Isolated yield^c N/A: Not applicable

Deprotection was additionally attempted on **18** and **23d** (Scheme 56). In a related project concurrently conducted in our lab, another PhD student found that 10 % TFA effectively deprotects *O*⁶,5'-cyclouridine derivatives (Ramya Nuti, unpublished results). These conditions were applied for deprotection of **18** and **23d**. However, the NMR spectra indicated the desired products were not obtained. Instead, the barbituric nucleosides **42** and **43** were formed, wherein the anhydro bridge was cleaved by the acid.^{92,153,154} The protons in the 5-position are too active to be observed in NMR (Scheme 56).



Scheme 56 Deprotection of two *O*⁶,5'-cyclouridine derivatives. Reagents and conditions: 10 % TFA in H₂O, 70 °C.

3.8 Summary and conclusions

Conformational restriction was expected to improve potency and selectivity for biological targets by reducing the entropic loss with the ligand being constrained in its preferred conformation. Based on the outcome of 5-substituted nucleosides (Class 1 inhibitors, Chapter 2), **1** was chosen as the structural basis of the macrocyclic compounds (Class 2 inhibitors). The complete synthetic steps are summarized in Scheme 57. Three ring-forming strategies across

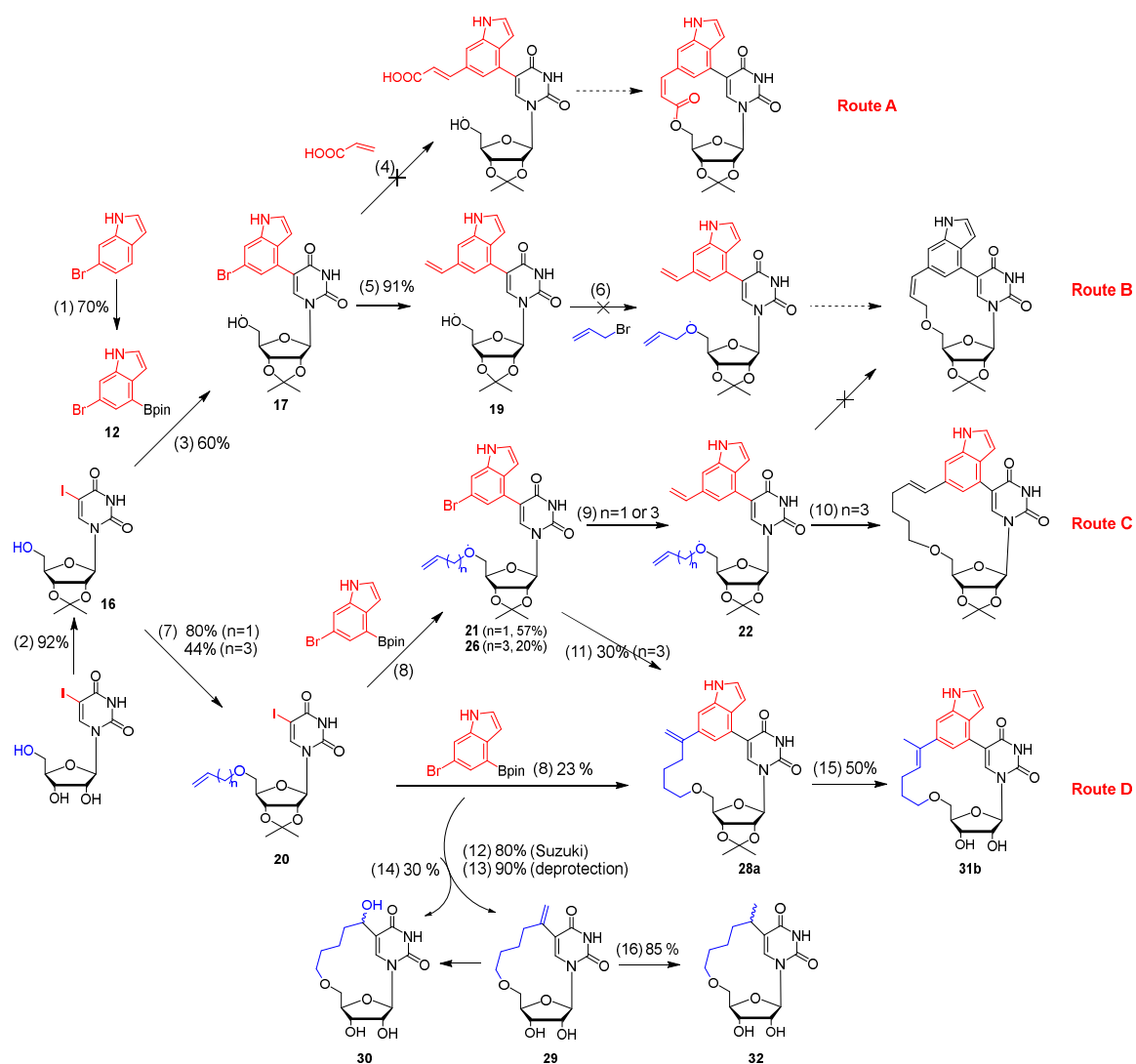
four routes were utilised for the synthesis of Class 2 inhibitors (**Scheme 57**). These strategies include macrolactonization (route A), RCM (route B and C) and the Heck coupling (route D) (**Scheme 57**). Successful route D was characterized by key steps such as borylation, Suzuki-coupling and Heck-coupling. Route D resulted in 6 macrocyclic compounds (**29 – 32**) whilst different routes contributed to an additional 6 ring-open uridine derivatives (**36 – 41**).

29, which merged as a by-product during the Suzuki coupling of **20d** and **12**, attracted our attention due to its exhibited conformational restriction. Two more macrocyclic analogues, **30** and **32**, were further synthesized. **30** resulted from hydration of **29**, whilst **32** from hydrogenation of **29**. A new chiral centre was generated in **30** and **32**. Both are a mixture of two isomers that could not be entirely separated. These processes resulted in the acquisition of two high-resolution crystals, namely, **27** (the unprotected form of **29**) and one isomer of **32**.

31, being the most relevant target macrocyclic compound, was an analogue of the ring-open **1**. Due to the complexity of the reaction leading to **31**, there were at least 5 isomers generated. Following attempts at both preparative and analytical HPLC separations, two isomers, **31a** and **31b**, were identified as a mixture with a ratio of 0.7:1. Pure **31c** was isolated and characterized via NMR.

Several intermediates were generated during synthesis of the target molecules through different routes. To explore the effect of different functional groups on inhibitory activity, **36 – 41** were obtained after deprotection.

With these 12 compounds in hand, both activity assessment and molecular modelling were conducted, and the results are described in Chapter 4.



Scheme 57 General synthesis of Class 2 inhibitors through 4 routes. Detailed reaction conditions are provided in the experimental.

Chapter 4

Activity evaluations and molecular modelling of Class 2 target molecules

4. Activity evaluations and molecular modelling of Class 2 target molecules

This Chapter focuses on activity assessment and molecular modelling of Class 2 inhibitors. The activity evaluation comprised biochemical assessments, including Malachite-Green inhibition assays and HPLC-based inhibition assays, targeting mammalian GalTs. Molecular modelling was utilized to offer a rational explanation for the observed experimental outcomes. Following this, cellular assessment included evaluations of cell viability, IgE production and cell permeability. Additionally, biochemical evaluations in bacterial GTs (LgtC, SetA, and LtpM) were employed as target enzymes in the DSF binding assay. The inhibitor exhibiting promising binding results underwent further assessment using the Malachite-Green inhibition assay.

4.1 β 4GalT1 inhibition assays and molecular modelling of Class 2 target molecules

The inhibitory activity of compounds **29** – **41** against β 4GalT1 was assessed in the Malachite-Green assay. Molecular modelling was employed to rationalise the experimental outcomes.

4.1.1 β 4GalT1 inhibition assays of **29 – **41****

The Malachite Green assay established in Chapter 2.4 was used to evaluate the inhibitory activity of Class 2 inhibitors towards β 4GalT1. The greatest level of inhibition was observed for the macrocycles **29** and **31ab**, with 62 % and 99 % inhibition at 2 mM, respectively (**Figure**

44). This is greatly increased in comparison with the ring-open compounds **1** – **4** (Figure 44). Compounds **38** – **41** were tested to identify the effects of individual functional groups on inhibitory activity. Preliminary screening indicated **38** and **39** had very weak inhibitory activity at 2 mM while **40** and **41** showed almost no inhibition at 0.5 mM (Figure 44). Higher concentrations of **40** and **41** could not be tested due to solubility issues. Higher concentrations of **31c** were not possible due to limited amount of sample.

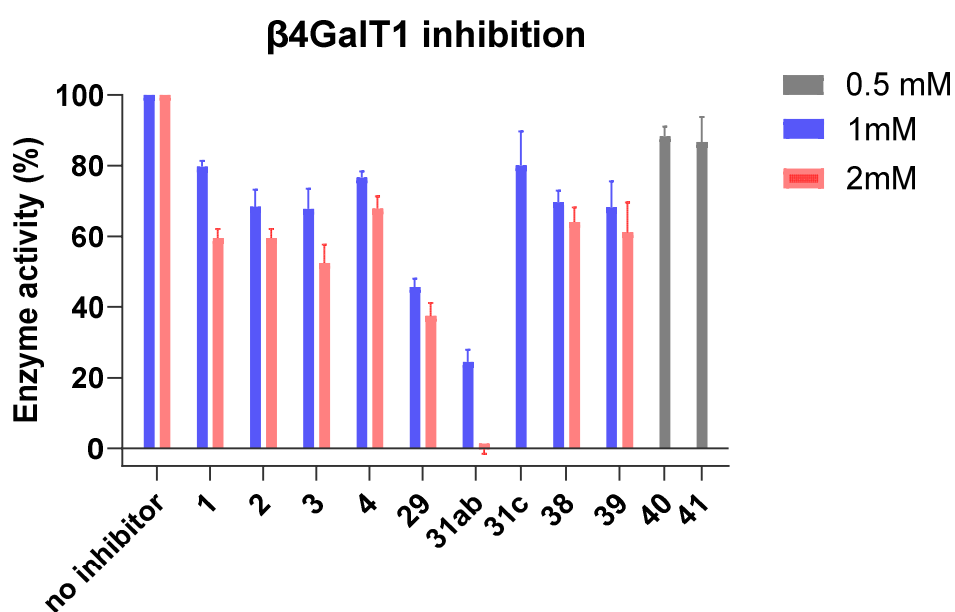


Figure 44 β 4GalT1 inhibition induced by Class 1 inhibitors and Class 2 inhibitors at single concentrations. **31ab** was used as a 0.7:1 mixture of two isomers. Reagents and conditions: β 4GalT1 (1 μ g/mL, turnover: 10 – 50 %), UDP-Gal (33 mM), GlcNAc (10 mM), CIP (10 U/mL), $MnCl_2$ (5 mM), lysozyme (1 mg/mL), Triton X (0.01 %), $MnCl_2$ (5 mM), KCl (50 mM), HEPES (PH 7.5, 10 mM), DMSO (10 %) and inhibitors were incubated on a 96-well plate at 30 °C with shaking for 20 min. The reaction was stopped by adding malachite reagents. The absorbance was measured at 620 nm in 1 h. Bars indicate mean values \pm S.D. of the triplicates in a single experiment.

The IC_{50} of **29** was 1.0 ± 0.16 mM. This was a slight improvement in comparison to Class 1 inhibitors, **1** – **4** (IC_{50} = 1.9 mM to 4.8 mM, Figure 19). Poor solubility precluded the testing of inhibitors at concentrations greater than 2 mM due to precipitation. The macrocycle **29** and its ring-open analogue **39** were assayed to probe the effect of conformational restriction on inhibitory activity. Results are presented in Figure 45. While **39** could only be tested over a

limited range of concentrations, these results suggest that the macrocyclic nucleoside **29** is a more potent inhibitor. This indicates conformational restriction was a successful strategy for improving inhibitory activity towards β 4GalT1.

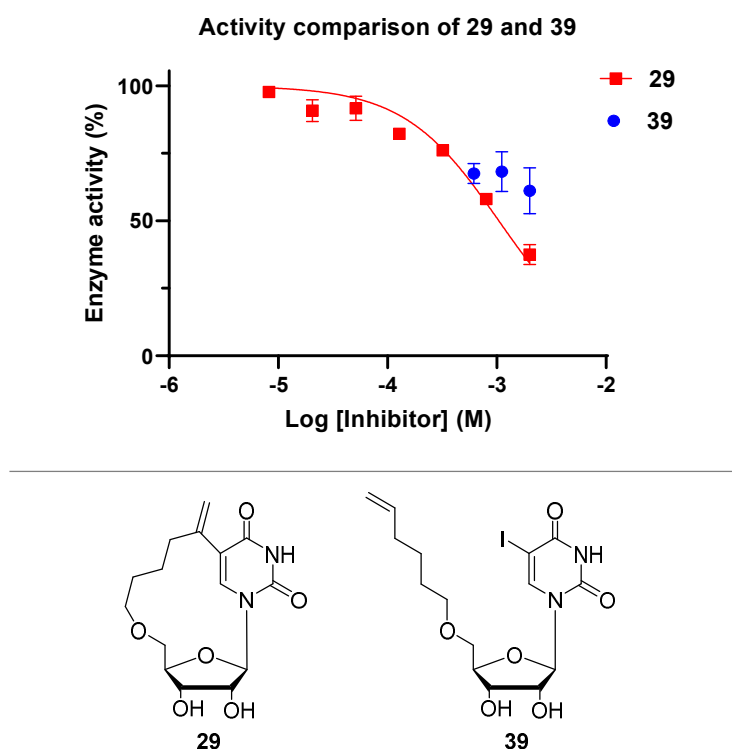


Figure 45 Activity comparison of **29** and **39** against β 4GalT1. Reagents and conditions: β 4GalT1 (1 μ g/mL, turnover: 15 % for **29**, 18 % for **39**) UDP-Gal (33 mM), GlcNAc (10 mM), CIP (10 U/mL), MnCl₂ (5 mM), lysozyme (1 mg/mL), Triton X (0.01 %), MnCl₂ (5 mM), KCl (50 mM), HEPES (PH 7.5, 10 mM), DMSO (10 %) and inhibitors series dilutions were incubated on a 96-well plate at 30 °C with shaking for 20 min. The reaction was stopped by adding malachite reagents. The absorbance was measured at 620 nm in 1 h. Bars indicate mean values \pm S.D. of the triplicates in a single experiment. The experiment of **29** was repeated three times.

Compound **31** was a mixture of three main compounds **31a** – **c**. HPLC purification allowed isolation of **31c**. However, **31a** and **31b** were unseparated. **31ab** was a mixture of two isomers with a ratio of 0.7:1 (**a:b**). It was only possible to do preliminary testing of **31ab** and **31c** due to limited sample material and issues with enzyme stability. Findings are presented in **Figure 46**. At 1.5 mM and 2 mM concentrations of **31ab**, β 4GalT1 activity was reduced by 76 % and 99 %, respectively. This was a significant improvement in comparison with the ring-open

analogue **1** which had an IC_{50} of 4.8 mM. No inhibitory activity was observed upon addition of 1 mM of **31c**. These findings corroborate the initial hypothesis that conformational restriction effectively enhances inhibitory activity.

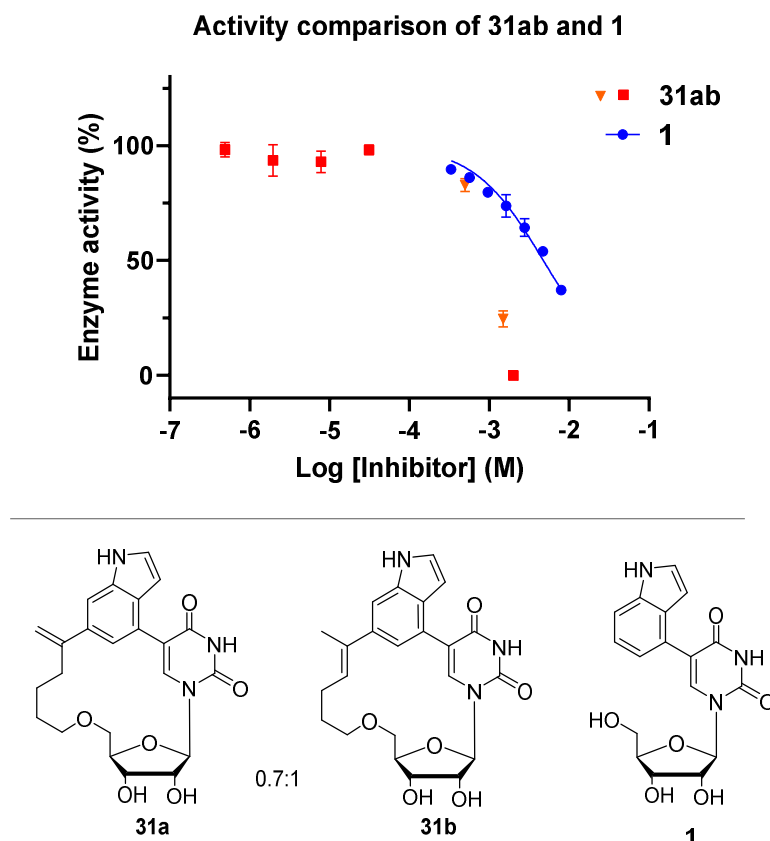


Figure 46 Activity comparison of **31ab** and **1** against β 4GalT1. **31ab** was used as a mixture of **a:b** (0.7:1). Conditions: β 4GalT1 (1 μ g/mL, turnover: 18 % and 21 % for **31ab**, 25 % for **1**), UDP-Gal (33 mM), GlcNAc (10 mM), CIP (10 U/mL), $MnCl_2$ (5 mM), lysozyme (1 mg/mL), Triton X (0.01 %), $MnCl_2$ (5 mM), KCl (50 mM), HEPES (PH 7.5, 10 mM), DMSO (10 %) and inhibitors series dilutions were incubated on a 96-well plate at 30 °C with shaking for 20 min. The reaction was stopped by adding malachite reagents. The absorbance was measured at 620 nm in 1 h. Each experiment was carried out in triplicate. Bars indicate mean values \pm S.D. of the triplicates in a single experiment. The experiment of **1** was repeated three times.

4.1.2 Molecular modelling of 29 – 37 with β 4GalT1

To gain deeper insights into the activity results, molecular modelling of β 4GalT1 was performed. We chose the pose that exhibited both a good superimposition with natural ligand

of β 4GalT1 (PDB: 1FR8) and the highest docking score using Glide docking in Schrodinger, followed by Molecular Dynamic (MD) simulations with CharmmGui and Amber. In MD simulations, **29**, **30b** and **32a** had relatively low RMSD values whereas **36** and **37** had very high scores (Table 16). In this case, an unusual scenario occurred, exemplified with the trajectory of **37** (Figure 47). This indicated the stable binding of **37** in the binding pockets with fluctuations limited to the first few frames (Figure 47). It may be that molecular docking did not identify the most stable pose of **36** and **37**. Thus, the initial pose from docking was rapidly altered in the first frames prior to stabilisation.

Table 16 RMSD values of Class 2 inhibitors with β 4GalT1

Compound	29	30b	31a	31b	32a	36	37
RMSD (Å)	1.3 \pm 0.3	1.0 \pm 0.3	2.0 \pm 0.4	1.8 \pm 0.4	0.9 \pm 0.2	3.6 \pm 0.5	3.5 \pm 0.2

RMSD values were calculated based on non-hydrogen atoms for both the receptor and ligand with VMD. The β 4GalT1 structure (PDB: 1FR8) used was from the Protein Data Bank.

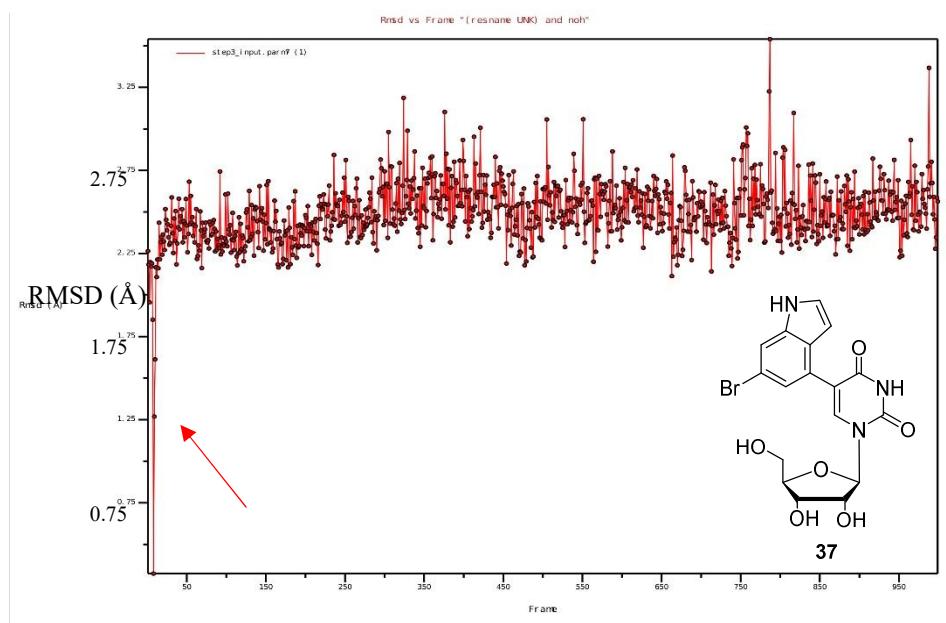


Figure 47 RMSD trajectory plots of **37** indicated instability only in the first few frames but stable in the rest of frames (the fluctuation is within 1 Å). RMSD were calculated based on non-hydrogen atoms for both the receptor and ligand with VMD. The β 4GalT1 structure (PDB: 1FR8) was used from the Protein Data Bank.

Further energy calculations revealed that **31b** and **37** exhibited the most promising interactions with residues amongst all the compounds. **31b** displayed a robust interaction with Arg189 with an energy of -35.5 kcal/mol. The new pi-stacking interaction between the indole group of **31b** and the side chain of Arg189 might contribute to this. Met225 might provide additional hydrophobic interaction (**Figure 48**, left). These findings align with the experiment results, where **31** exhibited a 99 % inhibition of β 4GalT1 at 2 mM. In the MD simulation of **37**, it formed a new pi-stacking interaction with residue Trp314 in a stable state, which showed -7.8 kcal/mol energy (**Figure 48**, right). Trp314 is a key residue in the catalytic cycle of β 4GalT1. This suggested compound **37** might be a promising inhibitor of β 4GalT1.

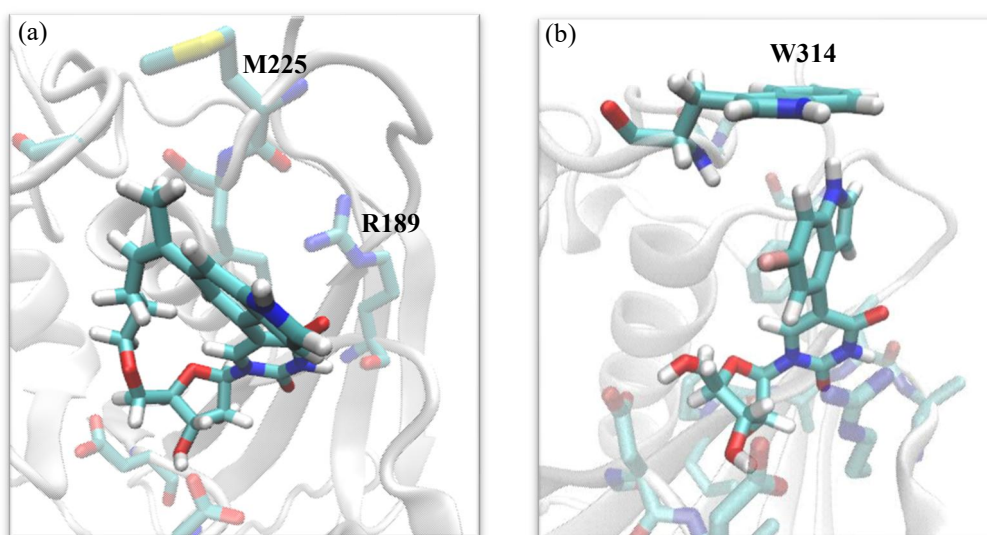


Figure 48 Compounds **31b** (a) and **37** (b) showed additional interactions with β 4GalT1 in MD simulations, visualised in VMD. (a) Inhibitor **31b** exhibited pi stacking interaction with R189 and hydrophobic interaction with M225 of β 4GalT1; (b) Inhibitor **37** displayed pi stacking interaction with W314 of β 4GalT1.

4.2 β 4GalT7 inhibition assays and molecular modelling of Class 2 target molecules

The inhibitory activity of compounds **29** – **37** against β 4GalT7 were assessed in HPLC-based assay by Roberto Mastio. Molecular modelling was employed to rationalise the experimental outcomes.

4.2.1 β 4GalT7 inhibition assays of **29** – **37**

Compounds **29** – **37** were assessed at 1 mM concentrations with 2 mM XylNap as the acceptor substrate against β 4GalT7. **31** mixture and **37** exhibited 97 % and 35 % inhibition. **32** and **36** showed slight β 4GalT7 activation (18 %) whereas **29** and **30** showed almost no activation or inhibition (**Figure 49**). The ring-open analogue **1** showed no activity until 1 mM. It is understood that the best known β 4GalT7 inhibitor was published by the Ellervik group in 2014, which was an acceptor-analogue. Its inhibitory activity was 52 ± 2.6 % after addition of 2 mM.¹⁰⁷ This suggests that inhibitors **31** and **37** (**Figure 49**) could be promising candidates for β 4GalT7 inhibition and subsequent GAG inhibition in cell applications. These results indicated that conformational restriction may be a suitable strategy for the development of potent, nucleoside-based inhibitors.

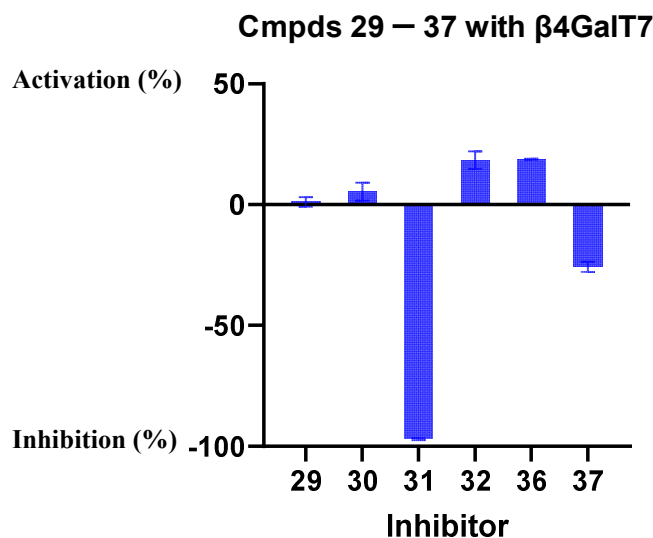


Figure 49 Activation and inhibition of galactosylation by β 4GalT7 under compounds **29** – **37** at 1 mM. **30** was used as a 1:8 mixture of two isomers. **31** was used as a mixture of **a:b:c** (25 %: 35 %: 14 %). **32** was used as a 1:1 mixture of two isomers. **31** and **37** were carried out in biological duplicate. Bars indicate mean values \pm S.D. of the duplicates in a single experiment. The data was obtained by Roberto Mastio.

4.2.2 Molecular modelling of **29** – **37** with β 4GalT7

We chose the pose that exhibited both a good superimposition with natural ligand of β 4GalT7 (PDB: 4IRP) and the highest docking score using Glide docking in Schrodinger, followed by Molecular Dynamic (MD) simulations with CharmmGui and Amber. In MD simulations, the majority of the compounds had good RMSD values (**Table 17**), which suggested stable binding. However, **36**, the ring open analogue of **29**, exhibited relatively high RMSD value. Neither **29** or **36** showed inhibitory activity against β 4GalT7 at 1 mM, while both **32** and **36** exhibited 18 % activation (see 4.2.1). Similar to compound **2**, it is possible that **32** or **36** bind at a putative allosteric site rather than a donor binding site. Compounds **31a** and **37** exhibited most promising interactions (**Figure 50**). This is consistent with the experiment results, where they showed 97 % and 26 % inhibition against β 4GalT7 at 1 mM (see 4.2.1). Compound **31a** displayed a new interaction with residue Arg102 with an energy of -30.3 kcal/mol. Both

hydrogen bonding and pi-pi stacking were involved. Arg138 also provided an additional stabilization with an energy of -4.9 kcal/mol. Compound **37** formed a new interaction with residue Arg270 from flexible loop with an energy of -29.0 kcal/mol. The guanidine group of Arg270 formed a pi-stacking and hydrogen bonding interactions with the indole group and 5' *O* of **37**, respectively (**Figure 50**).

Table 17 RMSD values of Class 2 inhibitors with β 4GalT7

Compd	29	30a & 30b	31a & 31b	31c	32a & 32b	36	37
RMSD (Å)	1.5 \pm 0.6	1.2 \pm 0.6 1.2 \pm 0.3	1.7 \pm 0.3 1.8 \pm 0.3	1.5 \pm 0.3	1.4 \pm 0.3 1.6 \pm 0.4	3.0 \pm 0.6	1.4 \pm 0.5

RMSD values were calculated based on non-hydrogen atoms for both the receptor and ligand with VMD. The β 4GalT7 structure (PDB: 4IRP) used was from the Protein Data Bank.

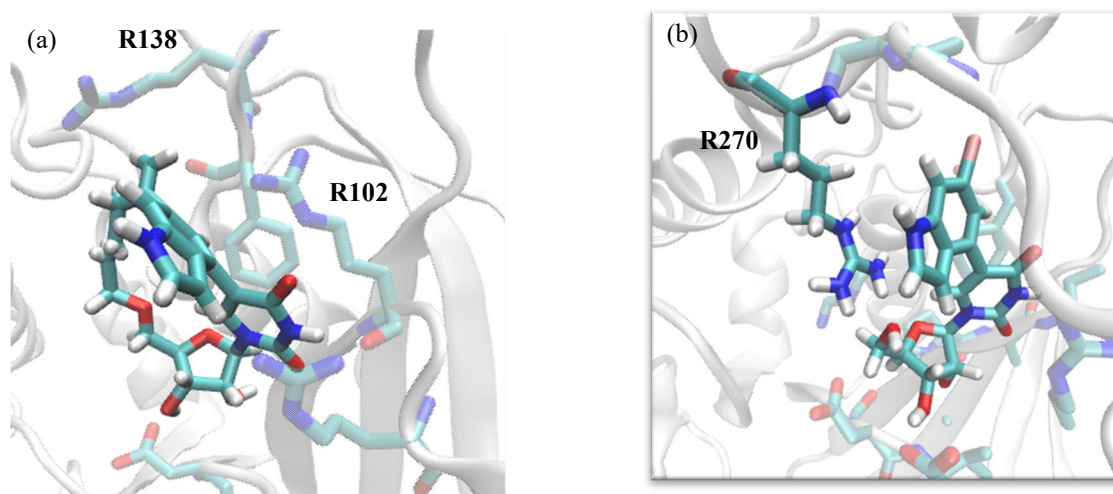


Figure 50 Compounds **31a** (a) and **37** (b) showed additional interactions with β 4GalT7 in MD simulations, visualized in VMD. (a) Inhibitor **31a** exhibited pi stacking interaction with R102 and pi stacking interaction with R138 of β 4GalT7; (b) Inhibitor **37** displayed pi stacking interaction with R270 of β 4GalT7

Overall, MD simulations indicated the appearance of stabilising interactions, involving R102, R138 and R270, which highlight the advantages of conformational restriction. Compound **31a** is a fully conformationally restricted compound whilst **37** is partially restricted owing to the existence of bromo atom. It is worth mentioning that both **31** and **37** exhibited promise against

both β 4GalT1 and β 4GalT7 in the MD simulations. This aligns with the experimental results, where **31** displayed moderate inhibition towards both β 4GalT1 and β 4GalT7, whilst **37** exhibited moderate inhibition against β 4GalT7. This suggests that conformational restriction potentially contributes to their inhibitory activity towards GalTs.

4.3 Cell assays of Class 2 target molecules

Cellular activity evaluations of Class 2 inhibitors were conducted by Alex McCraw. The assessment involved cell viability, IgE production, and cell permeability. IgE glycoengineering of Class 2 inhibitors is set to undergo testing in the future work.

4.3.1 Effect of target molecules 29 – 36 on cell viability and IgE production in cell culture

At concentrations of less than 1 mM, compounds **30**, **32** and **36** did not affect cell viability and IgE production (**Figure 51** (a) and (b)). Cells tolerated **29** up to 0.8 mM with a corresponding decrease in IgE production (**Figure 51** (a) and (b)). **31** mixture demonstrates cellular toxicity even at a relatively low concentration of 100 μ M (**Figure 51a**). **31** also had an impact on IgE production after adding 100 μ M (**Figure 51b**). Overall, results from both classes compounds suggest that the presence of a heterocycle such as indole or benzofuran may be associated with a decrease in cell viability.

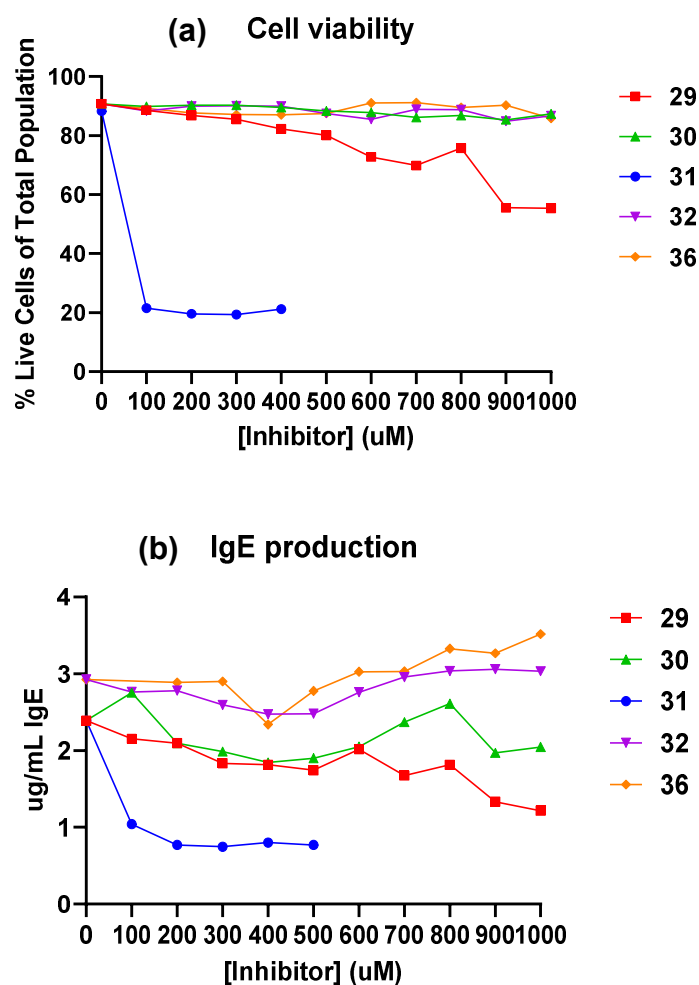


Figure 51 Effect of Class 2 inhibitors **29** – **36** on cell viability and IgE production in cell culture. (a) Expi-HEK293F cells seeded at 5×10^6 cells/ml (standard concentration for protein production) on Day 1 and harvested on Day 3 following incubation with known concentrations of inhibitor. (b) Anti-IgE ELISA was ran using cell supernatants. **30** was used as a 1:8 mixture of two isomers. **31** was used as a mixture of **a:b:c** (25 %: 35 %: 14 %). **32** was used as a 1:2 mixture of two isomers. The data was obtained by Alex McCraw.

4.3.2 Cell permeability of Class 2 target molecules

Cell permeability was assessed by a HPLC-based semi-quantitative experiments.⁵³ The material was used from the cell-viability experiments (see 4.3.1). Following centrifugation and lysis of the cell pellets, the intracellular proportions of compounds **29** to **36** were determined as a percentage of the total concentration. A concentration of 0.5 mM was utilized for compound **31**, while 1 mM was employed for the others. The concentration of the compounds

in the cell pellet or supernatant was calculated based on the area under the curve in HPLC. HPLC data indicated that approximately 26.0 – 31.0 % of 0.5 mM stock solution of compound **31** was taken up by Expi293F cells (**Table 18**). This result was the most promising compared to the others. Compound **29**, **30**, **32** and **36** displayed similar cell permeability, ranging from 5.6 – 7.6 % (**Table 18**).

Table 18 Cell permeability of Class 2 inhibitors was assessed through HPLC-based experiments.

Compound	29	30^a	31^b	32^c	36
Cell permeability (%)	7.6	5.6	26.0-31.0	5.4-6.0	6.8

The cell pellets or supernatants were filtered through a 2 µm filter, and the filter membrane was washed twice with 5 mL MeOH. The filtrate was completely dried in vacuo. The concentrated sample was dissolved in MeOH and loaded into HPLC system. ^a **30** was used as a 1:8 mixture of two isomers. ^b **31** was used as a mixture of **a:b:c** (25 %: 35 %: 14 %). ^c **32** was used as a 1:2 mixture of two isomers.

4.4 Bacterial enzymes: activity assays and molecular modelling with Class 2 target molecules

Biochemical assessments were conducted on additional GTs (LgtC, SetA, and LtpM) as the target enzymes in the DSF binding assay (see 4.4.1). Inhibitor **31** which displayed encouraging binding activity, was further evaluated in the Malachite Green inhibition assay (see 4.4.2). Molecular modelling was employed to provide a rational explanation for the experimental results (see 4).

4.4.1 Binding assays of 29 – 41 with LgtC, SetA and LtpM

Class 2 inhibitors were assessed in DSF binding assay against LgtC, SetA and LtpM. The macrocycle **29** exhibited 2.4 °C T_m shift against SetA whilst another macrocycle **31ab** showed a remarkable 4.5 °C T_m shift against LgtC (Table 19). These results suggested the macrocycles **29** and **31ab** have the potential to exhibit effective inhibitory activity against SetA and LgtC, respectively. These also indicated they might have a selectivity over the other two enzymes.

Table 19 T_m shifts of Class 2 inhibitors in DSF assay.

Entry	Compound	ΔT_m (°C)		
		LgtC	SetA	LtpM
1	29	<2	2.4 ± 0.3	<2 ^e
2	30^a	<2	<2	<2
3	31ab^b	4.5 ± 0.2	<2	<2
4	31c	<2	<2	<2
5	31^c	<2	<2	<2
6	32^d	<2	<2	<2
7	36	<2	<2	<2
8	37	<2	<2	<2
9	38	<2	<2	<2
10	39	<2	<2	<2
11	40	<2	<2	<2
12	41	<2	<2	<2

The ΔT_m (°C) was calculated at 2 mM (**31ab** was calculated at 0.5 mM). The concentrations of all compounds used in initial screening was 2 to 0 mM (**31ab** was from 0.5 to 0 mM) with a dilution factor of 2 across 3 sequential dilution steps. The compounds with distinct T_m shifts were assessed again from 2 to 0 mM with a dilution factor of 2 across 7 sequential dilution steps (**31ab** was diluted from 0.5 to 0 mM). Each experiment was carried out in triplicate. The experiment that demonstrated a deviation of more than two degrees was repeated twice. ^a **30** was used as a 1:8 mixture of two isomers. ^b **31ab** was used as a 0.7:1 mixture of two isomers. ^c **31** was used as a mixture of a:b:c (25 %: 35 %: 14 %). ^d **32** was used as a 1:1 mixture of two isomers. ^e This data was from David Matthews.

4.4.2 LgtC inhibition assays with 31

31ab displayed encouraging binding activity against LgtC in DSF binding assay. This suggested **31ab** could potentially be a LgtC inhibitor. The mixture of compound **31** was assessed using Malachite Green inhibition assay. It showed a promising IC_{50} value of $193 \pm 35 \mu\text{M}$ (**Figure 52**). As previously described, compound **31** is a mixture of three main, and at least two minor, isomers, with **31a** and **31b** representing the main components (25 % and 35 % of the mixture, respectively). It is therefore likely that one or both of these isomers may be primarily responsible for the observed inhibitory activity.

However, due to the limited amount and separation issue of **31ab**, compounds **31ab**, **31a** and **31b** studies will be performed in future work. Its ring-open analogue **1** showed no activity up to 2 mM. These data again support the initial hypothesis that conformational restriction is effective in increasing inhibitory activity.

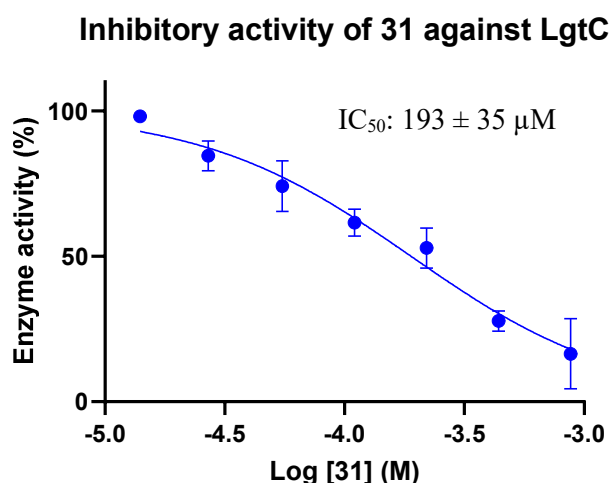


Figure 52 IC_{50} curve of compound **31** against LgtC. **31** was used as a mixture of **a:b:c** (25%:35%:14%). Conditions: LgtC (1 $\mu\text{g}/\text{mL}$, turnover: 16 %, incubated with 5 mM DTT at 30 °C for 20 min for activation), UDP-Gal (33 mM), GlcNAc (10 mM), CIP (10 U/mL), MnCl_2 (5 mM), lysozyme (1 mg/mL), Triton X (0.01 %), MnCl_2 (5 mM), HEPES (PH 7.5, 10 mM), DMSO (10 %) and inhibitors series dilutions were incubated on a 96-well plate at 30 °C with shaking for 20 min. The reaction was stopped by adding malachite reagents. The absorbance was measured at 620 nm in 1 h. Bars indicate mean values \pm S.D. of the triplicates in a single experiment. The experiment was repeated twice.

4.4.3 Molecular modelling of **31** with LgtC

Since good activity was observed with compound **31** against LgtC, the molecular simulations were performed for **31**. For comparison, its corresponding ring-open analogue **1** was also conducted. **31b** was standing out amongst **31a** to **31c** from docking simulations. In MD simulations, both **1** and **31b** exhibited similar RMSD (2.0 Å for both). However, **31b** displayed additional interactions with residue Arg77 and His78 with energies of -1.6 and -1.9 kcal/mol, respectively (**Figure 53**). Moreover, **31b** demonstrated a robust interaction with Asp105 in comparison to compound **1** (-20.9 and -1.4 kcal/mol, respectively, **Figure 53**). Conformational restriction could potentially lead to the enhancement of the additional interactions between **31b** and LgtC.

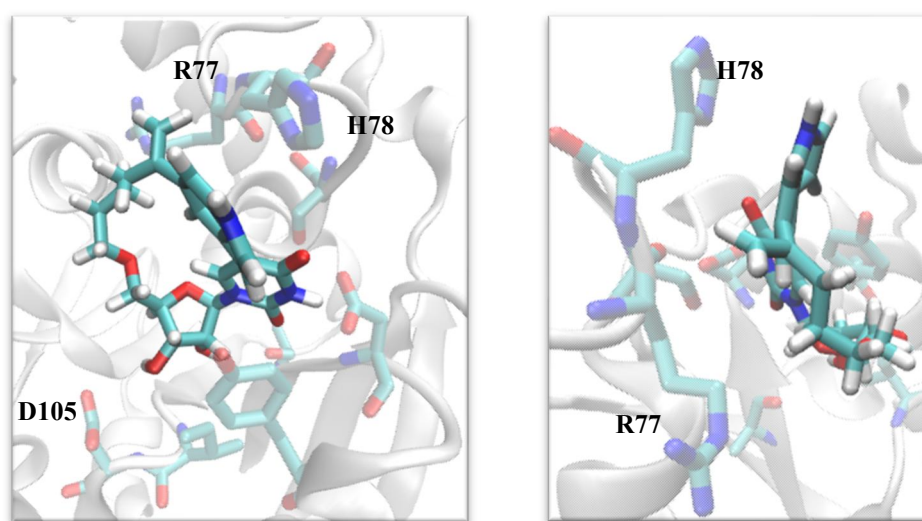


Figure 53 Inhibitor **31b** showed additional interactions with R77 and H78 and robust interaction with D105 of LgtC in the MD simulations, visualised in VMD (Left: front view; Right: top view)

4.5 Discussion on the selectivity of **31** for galactosyltransferases over glucosyltransferases

From the results above, the conformationally restricted macrocycle **31** exhibited selectivity towards galactosyltransferases (β 4GalT1, β 4GalT7 and LgtC) over glucosyltransferases (SetA and LtpM). To understand enzymological behaviour of **31**, molecular modelling was performed.

MD simulations of **31a** or **31b** showed they formed robust interactions with GalTs. As shown in **Figure 54**, β 4GalT1 and β 4GalT7 exhibited conserved residues in the binding pockets. There was an observed pi-stacking between the side chain of the conserved arginine residue (R189 in β 4GalT1 and R102 in β 4GalT7) and the indole group of compound **31** (**Figure 55**). This interaction was not observed in any other compounds in Class 1 inhibitors or 2. In addition, a new hydrophobic interaction was observed between residue Met225 of β 4GalT1 and **31b**, while a pi-stacking interaction was formed between Arg138 of β 4GalT7 and **31a** (**Figure 55**). In contrast, LgtC shared a lower sequence identity with β 4GalT1 and β 4GalT7 (**Figure 54**). Despite this, pi-stacking interactions were observed involving Arg77 and His78 of LgtC with the indole group of compound **31** (**Figure 55**). These suggested the presence of the chain and indole group of **31** could provide additional interactions with the target enzymes. These interactions could be stabilized by the constrained conformation of compound **31**.

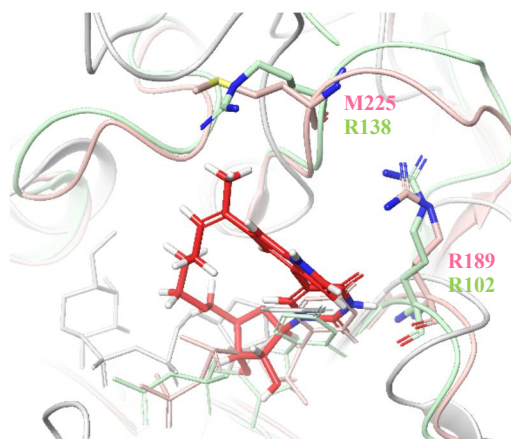


Figure 54 Superposition of β 4GalT1 (Pink, PDB 1FR8), β 4GalT7 (light green, PDB 4IRP) and LgtC (white, PDB 1G9R), visualized in Maestro. The image depicted the natural ligands occupying the binding sites. The pose of **31b** (red) was from the best docking result against β 4GalT1 using Glide in Schrodinger. The key residues of β 4GalT1 and β 4GalT7 were shown in stick representation.

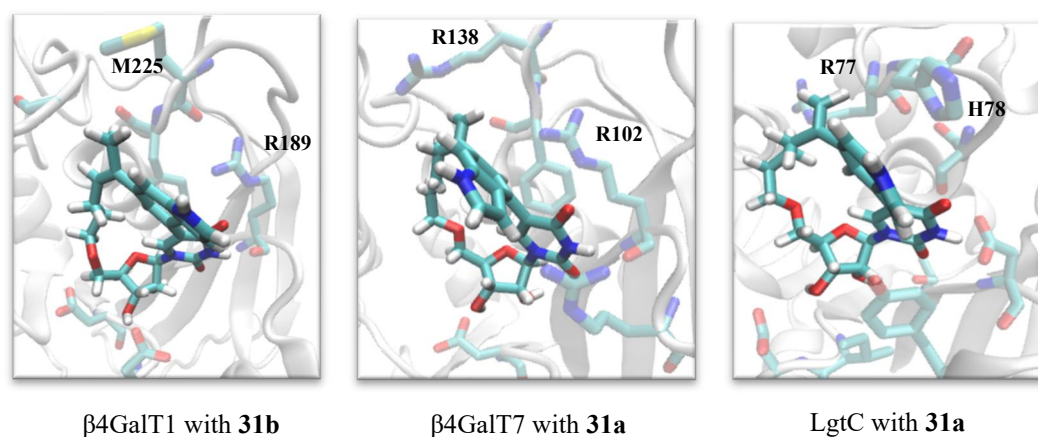


Figure 55 Key interactions between **31** and GalTs in MD simulations visualised with VMD. Corresponding interaction energies: Arg189 and Met225 of β 4GalT1 (PDB 1FR8): -35.5 and -1.1 kcal/mol, respectively; Arg102 and Arg138 of β 4GalT7 (PDB 4IRP): -30.3 and -4.9 kcal/mol, respectively; Arg77 and 78 of LgtC (PDB 1G9R): -1.6 and -1.8 kcal/mol, respectively.

Since no crystal structures is available for SetA and LtpM, we used their AlphaFold models generated by Gunnar Neels Schroeder. It was known that a conserved tryptophan residue is present in both SetA and LtpM, as observed in **Figure 56**. Upon superposing our ligand **31b** with the natural ligands of SetA and LtpM, an apparent clash was observed between indole group of **31b** and tryptophan residue (**Figure 56**). This observation could help explain the absence of binding observed in the DSF assay between **31** and both SetA and LtpM. The

modelling analysis provides a rationale for the observed selectivity of **31** towards galactosyltransferases (β 4GalT1, β 4GalT7 and LgtC) over glucosyltransferases (SetA and LtpM).

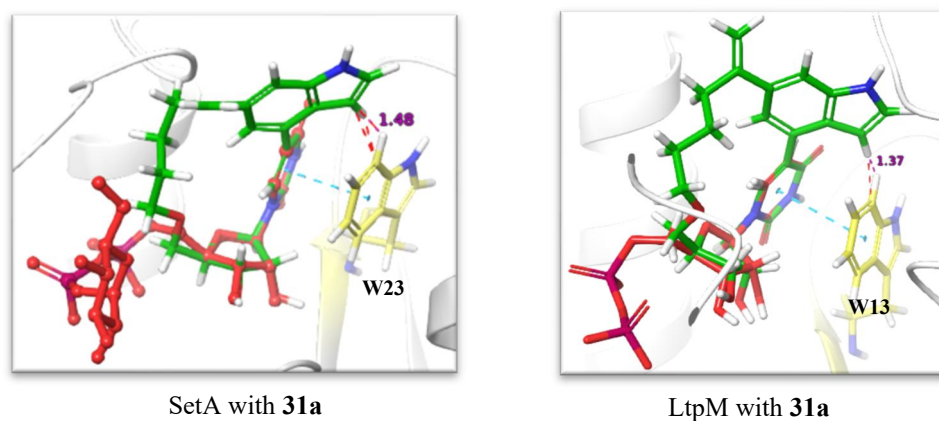


Figure 56 Steric clashes are present between **31a** (Green) and a conserved tryptophan residue (yellow) in both SetA and LtpM. UDP-Glc and UDP (red) were docked with SetA and LtpM, respectively, using Glide in Schrodinger. Both SetA and LtpM are AlphaFold models generated by Gunnar Neels Schroeder.

4.6 Summary and conclusions

This chapter described and discussed activity assessment and molecular modelling of Class 2 inhibitors. Activity assessment involved inhibition assays towards β 4GalT1 and β 4GalT7. Macrocyclic compound **29** exhibited a IC_{50} of 1.0 ± 0.2 mM against β 4GalT1, indicating a slightly increased activity in comparison with Class 1 inhibitors. Macrocyclic compound **31** demonstrated significant 99 % inhibition of β 4GalT1 at 2 mM and 97 % inhibition of β 4GalT7 at 1 mM. The partially conformationally restricted compound **37** exhibited 35 % inhibition of β 4GalT7. These findings suggested employing conformational restriction of inhibitors proved to be a promising strategy for enhancing inhibitory activity towards mammalian GalTs. Molecular modelling provides a rationale for the observed inhibition induced by **31** and **37**.

They formed additional robust interactions with the target enzymes in the MD simulations. These interactions might be strengthened by their restricted conformations. In the cell permeability assessment, **31** displayed a significantly higher value (26 % – 31 %), compared to the rest of tested Class 2 inhibitors (5.4 % – 7.6 %). However, **31** showed cytotoxicity at concentrations exceeding 100 μM . In contrast, **30**, **32** and **36** demonstrated tolerance reaching 1 mM, whilst **29** exhibited tolerance up to 0.8 mM. This suggested there is a trade-off between high uptake and high viability amongst these inhibitors.

In the binding assays of LgtC, SetA and LtpM, **31ab** (a/b 0.7:1) displayed a notable binding affinity with LgtC. Further inhibition assays revealed that **31ab** exhibited a remarkable IC_{50} value of 193 μM . This suggested **31a** or **31b** might have selectivity for LgtC over SetA and LtpM. Considering the observations, **31a** or **31b** exhibited potential selectivity for GalTs (β4GalT1 , β4GalT7 and LgtC) over glucosyltransferases (SetA and LtpM).

Chapter 5

Summary, conclusions and outlook

5 Summary, conclusions and outlook

5.1 Overall summary and conclusions

Immunoglobulin E (IgE)-based antibodies are currently being explored as potential innovative cancer therapeutics. The complexity of the IgE glycoforms presents challenges in conducting structure-function studies. The main goal of this project was to develop GalT inhibitors with suitable properties for application in IgE cell culture. Such inhibitors could subsequently be used to generate defined IgE glycoforms and contribute to establish the exact role of glycosylation for the biological and therapeutic properties of IgE.

The inhibitor design was based on the previously reported GalT donor analogue 5-FT UDP-Gal, which exhibited inhibitory activity in the low micromolar range against several GalTs. The 5-formylthienyl substituent at the 5-position of the uracil base enables 5-FT UDP-Gal to lock its target GalTs in a catalytically inactive state. However, its charged pyrophosphate linkage limited its suitability for cellular applications. The removal of the sugar and pyrophosphate linkage improved cell permeability and stability but resulted in a reduction in inhibitory activity. To regain inhibitory activity and maintain or further enhance permeability, this project employed conformational restriction as a key design strategy. This approach was expected to enhance both potency and selectivity for biological targets by minimizing the entropic loss associated with the ligand being constrained in its preferred conformation. Two classes of inhibitors were investigated.

Table 20 Activities of Class 1 inhibitors (**1** – **4**) and Class 2 inhibitors (**29** – **41**)^a

Entry	Cmpds	Mammalian GTs			Bacterial GTs		
		Galactosyltransferases			Glucosyltransferases		
		Inhibition assay			DSF binding assay (ΔT_m , °C)		
		$\beta 4\text{GalT1}$ (IC ₅₀ , mM)	$\beta 4\text{GalT7}$ (at 1 mM)	LgtC (IC ₅₀)	LgtC (at 2 mM)	SetA (at 2 mM)	LtpM (at 2 mM)
1	1	4.8 ± 0.5	n.a.	n.d.	n.a.	n.a.	n.a.
2	2	2.4 ± 0.4	154 % activation	n.d.	n.a.	2.5 ± 0.3	n.a.
3	3	1.9 ± 0.3	n.a.	n.d.	n.a.	2.4 ± 0.2	n.a.
4	4	3.8 ± 0.5	n.a.	n.d.	n.a.	2.3 ± 0.2	n.a.
5	29	1.0 ± 0.2	n.a.	n.d.	n.a.	2.4 ± 0.3	n.a.
6	30 ^d	n.d.	n.a.	n.d.	n.a.	n.a.	n.a.
7	31	99 % ^b inhibition (at 2 mM)	97 % ^c Inhibition (at 1 mM)	IC ₅₀ 193 ± 35 μM ^c	4.5 ± 0.2 ^b (at 0.5 mM)	n.a. ^b	n.a. ^b
8	32 ^e	n.d.	18 % activation	n.d.	n.a.	n.a.	n.a.
9	36	n.d.	18 % activation	n.d.	n.a.	n.a.	n.a.
10	37	n.d.	35 % inhibition	n.d.	n.a.	n.a.	n.a.
11	38	n.a.	n.d.	n.d.	n.a.	n.a.	n.a.
12	39	n.a.	n.d.	n.d.	n.a.	n.a.	n.a.
13	40	n.a.	n.d.	n.d.	n.a.	n.a.	n.a.
14	41	n.a.	n.d.	n.d.	n.a.	n.a.	n.a.

In the $\beta 4\text{GalT1}$ assay, **31c** was tested at a highest concentration of 1 mM, while compounds **40** and **41** were assessed at a highest concentration of 0.5 mM. The $\beta 4\text{GalT7}$ assay utilised the highest inhibitor concentration of 1 mM, and the DSF assay employed the highest inhibitor concentration of 2 mM. Significant observations were indicated using red highlighting in the table. n.a.: no activity (inhibition, activation, or binding); n.d.: not determined. ^a Class 2 inhibitors comprises macrocyclic compounds **29** – **32** and ring-open uridine analogues **36** – **41**. ^b **31** was used as a mixture of **a:b** (0.7:1) in $\beta 4\text{GalT1}$ inhibition assay and DSF assay. ^c **31** was used as a mixture of **a:b:c** (25%: 35%: 14%) in $\beta 4\text{GalT7}$ and LgtC inhibition assay. ^d **30** was used as a 1:8 mixture of two isomers. ^e **32** was used as a 1:1 mixture of two isomers.

In Chapter 2, the results of Class 1 inhibitors were introduced. Class 1 inhibitors (**1 – 4**) were uridine derivatives with four different 5-substitutions. The purpose was to identify the most favourable substituent and orientation at position 5 of nucleosides. **1 – 4** exhibited comparable inhibition of β 4GalT1 (IC_{50} : 1.9 – 4.8 mM, **Table 20, entry 1 – 4**). Compound **2** demonstrated a significant activation (up to 154 %, **Table 20, entry 2**) towards β 4GalT7, suggesting it might bind at a putative allosteric site rather than the donor binding site. However, the preliminary results from IgE glycoengineering indicated **5** exhibited limited and broad inhibition on the IgE glycans from lectin blots, while, surprisingly, **6** showed a slight increase in glycans broadly. Additionally, there was no noticeable reduction in the prevalence of galactose or sialic acid in the tentative glycan assignment. These unexpected, and seemingly paradoxical, effects may at least in part be influenced by the relatively modest potency of these inhibitors.

In Chapter 3 and 4, the chemical synthesis and activity evaluations of Class 2 inhibitors were introduced, respectively. Based on the comparable activity of Class 1 inhibitors against β 4GalT1 and synthetic accessibility, inhibitor **1** was chosen as the structural basis of conformationally restricted compounds. The synthesis of Class 2 inhibitors employed three ring-forming strategies across four routes. The route featuring Heck coupling for ring formation was successful, resulting in the final macrocycles. Although the other three routes did not yield the target compounds, they generated valuable intermediates and insights that contributed to the development of a successful synthetic route. Twelve Class 2 inhibitors were generated, including 6 macrocyclic compounds **29 – 32** and 6 ring-open uridine derivatives **36 – 41**. The macrocycle **29** exhibited a modest inhibitory activity, with an IC_{50} value of 1.0 ± 0.2 mM against β 4GalT1 (**Table 20, entry 5**). The fully conformationally restricted **31** exhibited the most potent activity. **31** displayed 99 % inhibition of β 4GalT1 at 2 mM and 97 % inhibition of β 4GalT7 at 1 mM (**Table 20, entry 7**). The partially conformationally restricted **37** exhibited

35 % inhibition of β 4GalT7 at 1 mM (**Table 20, entry 10**). Compared to their ring-open analogues **1 – 4**, these conformationally restricted inhibitors exhibited apparent increasing activity. Moreover, **31** also demonstrated 26.0 – 31.0 % cell permeability.

In Chapter 2 and 4, our investigation expanded to three bacterial GTs: LgtC, SetA, and LtpM with Class 1 inhibitors and Class 2 inhibitors. The critical aspect of this research involves evaluating the selectivity of our inhibitors towards these specific GTs. **31** demonstrated favourable selectivity for LgtC over SetA and LtpM in Differential Scanning Fluorimetry (DSF) binding assays (**Table 20, entry 7**). Subsequent inhibition assays revealed an IC_{50} of 193 ± 35 μ M for LgtC (**Table 20, entry 7**). Findings suggested **31** could potentially serve as a broad range inhibitor of GalTs (β 4GalT, β 4GalT7 and LgtC) over glucosyltransferases (SetA and LtpM) (**Table 20, entry 7**). Molecular modelling suggested that the chain and indole group on **31** could offer additional robust interactions with GalTs, and these interactions could be potentially stabilized by the constrained conformation of **31**. However, steric clashes were observed between the rigid structure of **31** and both SetA and LtpM.

In conclusion, the aim of achieving inhibitors with optimised inhibitory activity, selectivity and cell permeability was successfully accomplished via conformational restriction. Inhibitor **31** exhibited the most promising inhibitory potency and cell permeability amongst all the test compounds. This can be potentially attributed to the presence of indole group in the 5-position of nucleobase, with the macrocycle constraining the ligand in its favoured conformation. In IgE glycoengineering, the Class 1 inhibitors did not show a significant decrease in the prevalence of galactose or sialic acid in the IgE glycoengineering, whereas the Class 2 inhibitors are promising candidates for IgE application. This is attributed to their improved inhibitory activity and cell permeability. Some cytotoxicity was observed after

addition of 100 μ M for inhibitor **31**. Despite this, it remains promising candidate with the potential for further structural refinement to enhance its activity, thereby reducing the amount required for cellular applications. Alternatively, successful evaluation of the conformational restriction strategy has offered a new avenue to design additional analogues for use in cellular applications.

5.2 Future work

The future development of this work will include cell assays, *in-vitro* assays, and inhibitor optimizations. Cell assays will involve the application of current inhibitors to IgE glycoengineering and glycosaminoglycan (GAG) biosynthesis. *In-vitro* assays will involve the application of inhibitors to additional target enzymes. Finally, the results from this study, including the synthetic routes described in Chapter 3, provide a strong foundation for the further optimisation of this new class of the glycosyltransferase inhibitors. As the next steps, the following experiments may be particularly worthwhile:

- 1) Conducting IgE studying with conformationally restricted nucleosides. The Class 2 inhibitors inhibitors are promising candidates for IgE application, due to their improved inhibitory activity and cell permeability. The potential candidates include inhibitors **29**, **31** and **37**. The following optimization strategies would provide further investigations of this area.
- 2) Establishing the glycan profile within GAG biosynthesis in cells treated with **31** or **2**. Considering the remarkable inhibitory activity of **31** and activating activity of **2** against β 4GalT7, it is essential to investigate their activities in cell assays.

- 3) Exploring additional sugar-UDP-dependant enzymes, such as UDP-glucosyltransferase, fucosylgalactoside α -N-acetylgalactosaminyltransferase (AA(Gly)B) and β -1,3-galactosyltransferase. This exploration can potentially offer an opportunity to discern the selectivity of our inhibitors in relation to various enzymes.
- 4) Optimizing the structure of **31**. Inhibitor **31** demonstrated the most potent inhibitory potency, selectivity and cell permeability amongst all the test compounds. Its potential optimization strategies involve: (a) performing hydrogenation to increase the ligand flexibility, (b) adjusting the ring size to control ring flexibility, and (c) substituting the hydrophobic alkenyl chain with a hydrophilic chain, such as PEG (**Figure 57**).

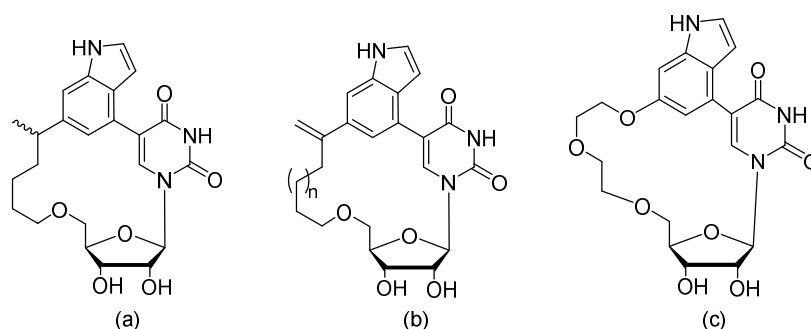


Figure 57 Proposed optimisation strategies for inhibitor **31**

- 5) Optimizing the structure of **29**. Although **29** and **37** are not as potent as **31**, they are promising owing to mild activity and easy synthetic accessibility. Similar to **31**, **29** is a fully conformationally restricted nucleoside. The potential optimization strategies of **29** involve: (a) adjusting the ring size to control ring flexibility; (b) substituting the hydrophobic alkenyl chain with a hydrophilic chain, such as PEG (**Figure 58**).

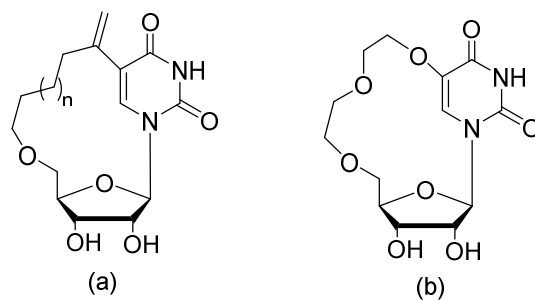
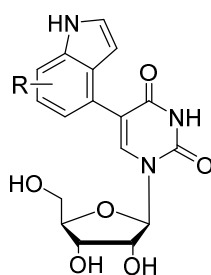


Figure 58 Proposed optimisation strategies for inhibitor **29**

- 6) Optimizing the structures of **37**. Inhibitor **37** is a partially restricted nucleoside due to the presence of the bromo group. Various substituents on the indole moiety can regulate the dihedral angle between indole and the nucleobase, potentially favouring conformations preferred by the target enzymes. Potential optimization strategies of **37** involve substituting bromo group with either electron-withdrawing groups, such as Cl, OH or OCH₃, or electron-donating groups, such as CH₃ and benzyl group in different position of indole (**Figure 59**). A benzyl group also can be utilised to investigate the impact of bulky groups on ligand conformation towards target enzymes and downstream activities.



R = Cl, OH, OCH₃, CH₃, benzyl ... in different position of indole

Figure 59 Proposed optimisation strategies for inhibitor **37**

Chapter 6

Experimental

6 Experimental

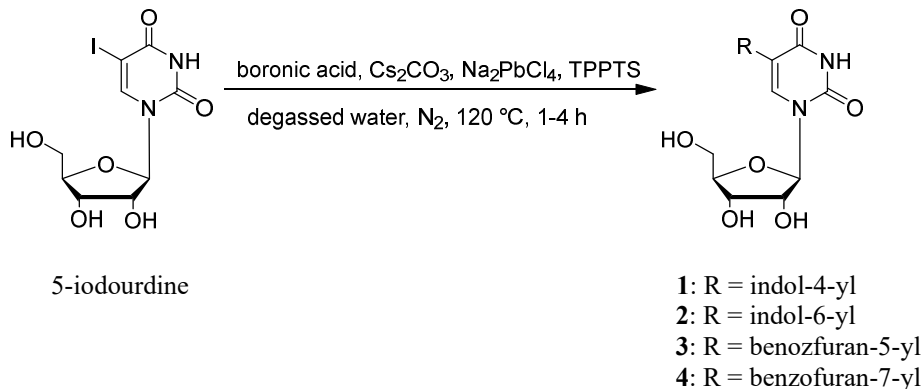
6.1 Chemical synthesis

General. Commercial chemicals and dry solvents were employed as received, except for dry DCM which was dried using preactivated 4Å molecular sieves. Silica gel (particle size 40 – 63 µm) was used for the normal phase chromatography procedure. Precoated aluminium plates (Silica Gel 60 F254, Merck) were utilized for the thin layer chromatography (TLC) procedure. The compounds were visualised using UV light exposure (254/365 nm) and/or through staining with potassium permanganate. All newly synthesized compounds were subjected to analysis using ¹H NMR, ¹³C NMR, COSY, NOESY, HMBC, and LC/MS. For all known compounds, characterization was conducted using ¹H-NMR and ¹³C-NMR. The ¹H NMR spectra were collected at 298K on a ultrasield™ 400 PLUS Bruker machine operating at 400.13 MHz (¹H-NMR) and 100.62 MHz (¹³C-NMR), respectively. The NMR spectra were presented using MestReNova 12.0. Chemical shifts (δ) are indicated in ppm relative to the residual solvent peaks. Analytical HPLC was performed using an Agilent 1220 infinity LC system with an Agilent ZORBAX eclipse XDB-C18 column (5 µm, 4.6 × 250 mm). All final compounds satisfied the necessary purity standards (> 95 % by HPLC) at two wavelengths. The two maximum absorbance wavelengths were validated through UV-VIS spectrophotometry. Notably, compound **30** and **32** comprised two diastereomers, while compound **31** was a combination of at least five diastereoisomers, all of which exhibited a total purity exceeding 95 %. Three diastereomers of compound **31** were separated by automated preparative reversed-phase high-performance liquid chromatography (RP-HPLC). The PerkinElmer HPLC system employed for the separation, which consisted of a 200 series binary

pump, dual Rheodyne 7725i injector, channel UV/vis detector, and a Dr. Maisch ReproSil Gold 120 C18 column (10 μm , 25 \times 250 mm²). The LC-MS analysis was performed utilizing an Agilent Technologies 1290 ultra-performance liquid chromatography (UPLC) system, featuring a 6140 single quadrupole mass spectrometer (MS) detector and a Zorbax Eclipse Plus C18 RRHD column (1.8 μm , 50 \times 2.1 mm). The mobile phase of LC-MS underwent a transition from 100 % H₂O (0.1 % formic acid) to 100 % MeCN (0.1 % formic acid) within a 6-minute period, and UV detection was carried out at two standard wavelengths (210 and 254 nm) for all compounds.

6.1.1 Chapter 2 compounds: 1 – 8 (Class 1 inhibitors)

Suzuki cross-coupling: 1 – 4

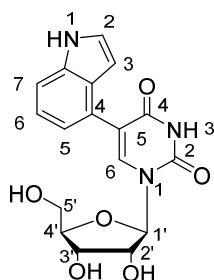


5-Indouridine (1 equiv.), boronic acid (1.5 equiv.) and Cs₂CO₃ (2 equiv.) in 50 mL degassed water were combined in a 100 mL two-necked flask. The reaction mixture was stirred at rt until all the solids were dissolved. Under nitrogen, NaPdCl₄ (0.025 equiv.) and TPPTS (0.0625 equiv.) were added and stirred at rt temperature until all solids were dissolved. The reaction was heated to reflux (120 °C) under nitrogen until TLC (IPA/H₂O/NH₃ 12:3:1) indicated complete conversion. The reaction was cooled to rt. The Pd-complex was removed using cotton

and a glass funnel. The pH was adjusted from basic to neutral with 1N HCl before extraction with ethyl acetate. Then the solution was extracted with ethyl acetate (8×). The organic layers were combined and dried with anhydrous Na₂SO₄ for 30 min. The organic solvent was concentrated in vacuo. The crude product was used in the next step without further purification.

For the purpose of activity testing, the Pd-complex was removed using a DMT chelating agent. The solution was stirred with DMT at 80 °C overnight and subsequently filtered with celite. The following procedures remained consistent with those described above. **1 – 4** were further purified via recrystallization in MeOH.

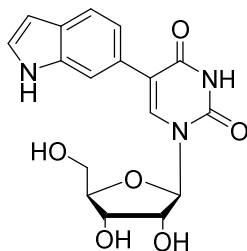
1-((2*R*,3*R*,4*S*,5*R*)-3,4-dihydroxy-5-(hydroxymethyl)tetrahydrofuran-2-yl)-5-(1*H*-indol-4-yl)pyrimidine-2,4(1*H*,3*H*)-dione (1**)⁴²**



White solid, 45 % yield. ¹H NMR (400 MHz, Methanol-*d*₄) δ 8.16 (s, 1H, H-6), 7.34 (d, *J* = 7.8 Hz, 1H, indoyl-H-7), 7.21 (d, *J* = 3.0 Hz, 1H, indoyl-H-2), 7.09 (dd, *J* = 7.8, 7.3 Hz, 1H, indoyl-H-6), 7.03 (d, *J* = 7.3 Hz, 1H, indoyl-H-5), 6.37 (d, *J* = 3.0 Hz, 1H, indoyl-H-3), 6.01 (d, *J* = 5.3 Hz, 1H, H-1'), 4.27 (dd, *J* = 5.3, 4.7 Hz, 1H, H-2'), 4.13 (dd, *J* = 4.7, 4.4 Hz, 1H, H-3'), 3.99 (dt, *J* = 4.4 Hz, 1H, H-4'), 3.72 (dd, *J* = 12.0, 2.7 Hz, 1H, H-5'), 3.62 (dd, *J* = 12.0, 2.7 Hz, 1H, H-5'). ¹³C NMR (100 MHz, Methanol-*d*₄) δ 164.87 (C-4), 152.43 (C-2), 140.62 (C-6), 137.87 (indoyl-C-9), 128.45 (indoyl-C-8), 125.91 (indoyl-C-2), 125.60 (indoyl-C-4), 122.10 (indoyl-C-6), 121.39 (indoyl-C-5), 116.50 (C-5), 112.25 (indoyl-C-7), 101.78 (indoyl-C-3), 90.60 (C-1'), 86.48 (C-4'), 75.78 (C-2'), 71.72 (C-3'), 62.42 (C-5'). LC-MS (*m/z*) [*M* + H⁺]:

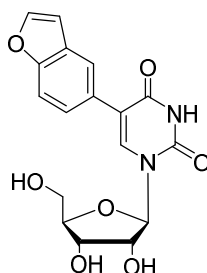
calculated 360.1; found 360.2. HPLC: > 99 % purity at 220 nm and 265 nm; t_R = 2.3 min; flow rate: 1 mL/min; solvent elution: 40 % MeOH in water.

1-((2*R*,3*R*,4*S*,5*R*)-3,4-dihydroxy-5-(hydroxymethyl)tetrahydrofuran-2-yl)-5-(1*H*-indol-6-yl)pyrimidine-2,4(1*H*,3*H*)-dione (2)⁴²



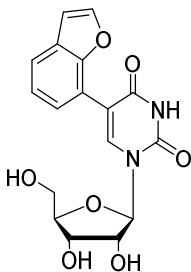
White solid, 48 % yield. ¹H NMR (400 MHz, DMSO-*d*₆) δ 11.48 (s, 1H, uracil-NH), 11.10 (s, 1H, indoyl-NH), 8.20 (s, 1H, H-6), 7.70 (s, 1H, indoyl-H-7), 7.50 (d, *J* = 9.2 Hz, 1H, indoyl-H-4), 7.35 (d, 1H, indoyl-H-2), 7.11 (d, *J* = 9.2 Hz, 1H, indoyl-H-5), 6.41 (d, 1H, indoyl-H-3), 5.88 (d, *J* = 5.5 Hz, 1H, H-1'), 5.44 (s, 1H, OH-2'), 5.18 (s, 1H, OH-5'), 5.10 (s, 1H, OH-3'), 4.21 – 4.14 (m, 1H, H-2'), 4.08 – 4.01 (m, 1H, H-3'), 3.94 – 3.85 (m, 1H, H-4'), 3.68 – 3.63 (m, 1H, H-5'), 3.60 – 3.57 (m, 1H, H-5'). ¹³C NMR (100 MHz, DMSO-*d*₆) δ 162.60 (C-4), 150.36 (C-2), 137.29 (C-6), 135.85 (indoyl-C-9), 126.96 (indoyl-C-8), 126.05 (indoyl-C-6), 125.71 (indoyl-C-2), 119.68 (indoyl-C-4), 119.24 (indoyl-C-5), 114.84 (C-5), 111.42 (indoyl-C-7), 101.00 (indoyl-C-3), 88.06 (C-1'), 84.90 (C-4'), 73.97 (C-2'), 69.99 (C-3'), 60.69 (C-5'). LC-MS (*m/z*) [*M* + *H*⁺]: calculated 360.1; found 360.3. HPLC: > 99 % purity at 240 nm and 300 nm; t_R = 2.2 min; flow rate: 1 mL/min; solvent elution: 40 % MeOH in water.

5-(benzofuran-5-yl)-1-((2*R*,3*R*,4*S*,5*R*)-3,4-dihydroxy-5-(hydroxymethyl)-tetrahydrofuran-2-yl)pyrimidine-2,4(1*H*,3*H*)-dione (3)



White solid, 52 % yield. ^1H NMR (400 MHz, $\text{DMSO-}d_6$) δ 11.55 (s, 1H, NH), 8.27 (s, 1H, H-6), 8.00 (d, 1H, benzofuran-H-2), 7.82 (s, 1H, benzofuran-H-4), 7.57 (d, $J = 8.4$ Hz, 1H, benzofuran-H-7), 7.45 (d, $J = 8.4$ Hz, 1H, benzofuran-H-5), 6.98 (d, 1H, benzofuran-H-3), 5.86 (d, $J = 2.7$ Hz, 1H, H-1'), 5.45 (s, 1H, OH-2'), 5.22 (s, 1H, OH-3'), 5.11 (s, 1H, OH-5'), 4.19 – 4.13 (m, 1H, H-2'), 4.07 – 4.01 (m, 1H, H-3'), 3.91 – 3.87 (m, 1H, H-4'), 3.73 – 3.51 (m, 2H, H-5'). ^{13}C NMR (101 MHz, $\text{Methanol-}d_4$) δ 164.90, 155.94, 152.18, 146.96, 139.79, 128.99, 128.93, 126.09, 122.34, 116.43, 111.85, 107.75, 90.91, 86.25, 76.04, 71.13, 61.87. LC-MS (m/z) $[\text{M} + \text{H}^+]$: calculated 361.1; found 361.2. HPLC: > 99 % purity at 230 nm and 285 nm; $t_{\text{R}} = 2.8$ min; flow rate: 1 mL/min; solvent elution: 40 % MeOH in water.

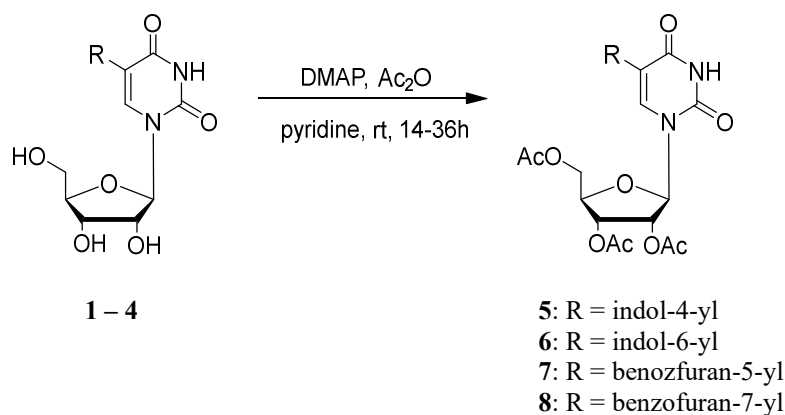
5-(benzofuran-7-yl)-1-((2*R*,3*R*,4*S*,5*R*)-3,4-dihydroxy-5-(hydroxymethyl)-tetrahydrofuran-2-yl)pyrimidine-2,4(1*H*,3*H*)-dione (4)



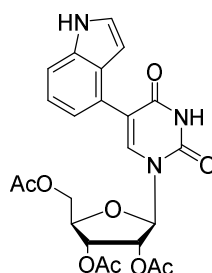
White solid, 49 % yield. ^1H NMR (400 MHz, $\text{DMSO-}d_6$) δ 11.63 (s, 1H, NH), 8.36 (s, 1H, H-6), 7.96 (m, 1H, benzofuran-H-2), 7.62 (m, 1H, benzofuran-H-4 or 6), 7.45 (m, 1H, benzofuran-H-4 or 6), 7.26 (m, 1H, benzofuran-H-5), 6.98 (m, 1H, benzofuran-H-3), 5.90 (m, 1H, H-1'),

5.47 (s, 1H, OH-2'), 5.13 (s, 1H, OH-5'), 4.96 (s, 1H, OH-3'), 4.16 (m, 2H, H-2'), 4.04 – 3.96 (m, 1H, H-3'), 3.91 – 3.83 (m, 1H, H-4'), 3.58 – 3.49 (m, 2H, H-5'). ^{13}C NMR (100 MHz, Methanol- d_4) δ 164.29 (C-4), 152.14 (C-2), 146.36 (benzofuran-C-2), 141.79 (C-6), 129.26 (benzofuran-C-9), 126.33 (benzofuran-C-6), 123.82 (benzofuran-C-5), 121.99 (benzofuran-C-4), 118.32 (benzofuran-C-7), 111.44 (C-5), 107.76 (benzofuran-C-3), 90.86 (C-1'), 86.45 (C-4'), 76.00 (C-2'), 71.54 (C-3'), 62.33 (C-5'). LC-MS (m/z) $[\text{M} + \text{H}^+]$: calculated 361.1; found 361.2. HPLC: > 99 % purity at 225 nm and 285 nm; $t_R = 2.4$ min; flow rate: 1 mL/min; solvent elution: 40 % MeOH in water.

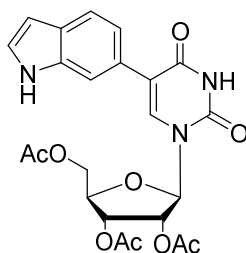
Acetylation of 1 – 4: compounds 5 – 8



To a solution of **1 – 4** (1 equiv.) and DMAP (0.05 equiv.) in pyridine (5 mL) was added acetic anhydride (3.5 equiv.). The reaction was stirred at rt until TLC (hexane/EA 3:1) indicated complete conversion. The reaction was quenched with drops of water. The solvent was removed by evaporation and the residue co-evaporated with toluene (3 \times). The crude product was purified by flash silica chromatography (hexane/EA, gradient: 10:1 to 3:1) to yield target compounds **5 – 8**.

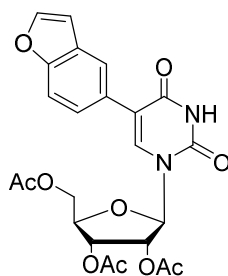
(2*R*,3*R*,4*R*,5*R*)-2-(5-(1*H*-indol-4-yl)-2,4-dioxo-3,4-dihydropyrimidin-1(2*H*)-yl)-5-(acetoxymethyl)tetrahydrofuran-3,4-diyl diacetate (5)⁴²

White solid, 70 % yield over 2 steps. ¹H NMR (400 MHz, Methanol-*d*₄) δ 7.94 (s, 1H, H-6), 7.39 (d, *J* = 6.6 Hz, 1H, indoyl-H-7), 7.24 (d, 1H, indoyl-H-2), 7.18 – 7.08 (m, 2H, indoyl-H-5 and 6), 6.44 (d, 1H, indoyl-H-3), 6.20 (d, *J* = 5.7 Hz, 1H, H-1'), 5.49 (t, *J* = 5.9 Hz, 1H, H-2'), 5.43 – 5.33 (m, 1H, H-3'), 4.48 – 4.37 (m, 1H, H-4'), 4.33 – 4.21 (m, 2H, H-5'), 2.11 (s, 6H, OAc-2' and 3'), 1.41 (s, 3H, OAc-5'). ¹³C NMR (100 MHz, Methanol-*d*₄) δ 171.89 (C of OAc), 171.41 (C of OAc), 171.39 (C of OAc), 164.62 (C-4), 151.96 (C-2), 139.68 (C-6), 137.90 (indoyl-C-9), 128.37 (indoyl-C-8), 126.34 (indoyl-C-2), 125.12 (indoyl-C-4), 122.12 (indoyl-C-5), 121.55 (indoyl-C-6), 116.69 (C-5), 112.39 (indoyl-C-7), 101.29 (indoyl-C-3), 88.42 (C-1'), 81.60 (C-4'), 74.32 (C-2'), 72.02 (C-3'), 64.53 (C-5'), 20.44 (Me of OAc), 20.30 (Me of OAc), 19.88 (Me of OAc). LC-MS (*m/z*) [*M* + *H*⁺]: calculated 486.2; found 486.3 HPLC: > 99 % purity at 210 nm and 265 nm; *t*_R = 1.5 min; flow rate: 1 mL/min; solvent elution: 95 % MeOH in water.

(2*R*,3*R*,4*R*,5*R*)-2-(5-(1*H*-indol-6-yl)-2,4-dioxo-3,4-dihydropyrimidin-1(2*H*)-yl)-5-(acetoxymethyl)tetrahydrofuran-3,4-diyl diacetate (6)

White solid, 83 % yield over 2 steps. ^1H NMR (400 MHz, Methanol- d_4) δ 7.69 (s, 1H, H-6), 7.56 – 7.47 (m, 2H, indoyl-H-7 and H-4), 7.21 (d, 1H, indoyl-H-2), 7.06 (d, $J = 8.2$ Hz, 1H, indoyl-H-5), 6.40 (d, $J = 2.2$ Hz, 1H, indoyl-H-3), 6.04 (d, $J = 5.4$ Hz, 1H, H-1'), 5.50 (t, $J = 5.7$ Hz, 1H, H-2'), 5.37 (t, $J = 5.4$ Hz, 1H, H-3'), 4.38 – 4.23 (m, 3H, H-4' and H-5'), 2.05 (s, 6H, OAc-2' and 3'), 1.76 (d, $J = 1.7$ Hz, 3H, OAc -5'). ^{13}C NMR (100 MHz, Methanol- d_4) δ 172.03 (C of OAc), 171.42 (C of OAc), 164.83 (C-4), 151.84 (C-2), 138.53 (C-6), 137.47 (indoyl-C-9), 129.32 (indoyl-C-8), 126.73 (indoyl-C-2), 126.56 (indoyl-C-6), 121.11 (indoyl-C-4), 120.75 (indoyl-C-5), 118.35 (C-5), 112.66 (indoyl-C-7), 102.33 (indoyl-C-3), 89.44 (C-1'), 81.42 (C-4'), 74.26 (C-2'), 71.74 (C-3'), 64.27 (C-5'), 20.50 (Me of OAc), 20.41 (Me of OAc), 20.32 (Me of OAc). LC-MS (m/z) $[\text{M} + \text{H}^+]$: calculated 486.2; found 486.3. HPLC: > 99 % purity at 210 nm and 290 nm; $t_{\text{R}} = 1.5$ min; flow rate: 1 mL/min; solvent elution: 95 % MeOH in water.

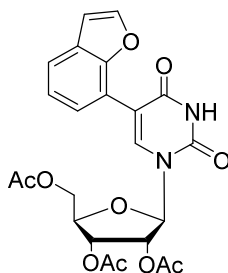
(2*R*,3*R*,4*R*,5*R*)-2-(acetoxymethyl)-5-(5-(benzofuran-5-yl)-2,4-dioxo-3,4-dihydropyrimidin-1(2*H*)-yl)tetrahydrofuran-3,4-diyl diacetate (7)



White solid, 78 % yield over 2 steps. ^1H NMR (400 MHz, Methanol- d_4) δ 7.77 (s, 2H, H-6 and benzofuran-H-2), 7.75 (s, 1H, benzofuran-H-4), 7.51 (d, $J = 8.7$ Hz, 1H, benzofuran-H-7), 7.42 (d, $J = 8.7$ Hz, 1H, benzofuran-H-6), 6.85 (d, 1H, benzofuran-H-3), 6.06 (d, $J = 5.2$ Hz, 1H, H-1'), 5.56 (dd, $J = 5.8, 5.8$ Hz, 1H, H-2'), 5.43 (dd, 1H, H-3'), 4.41 – 4.29 (m, 3H, H-4' and 5'), 2.10 (s, 6H, OAc), 1.85 (s, 3H, OAc). ^{13}C NMR (100 MHz, Methanol- d_4) δ 171.96 (COCH₃), 171.44 (COCH₃), 171.39 (COCH₃), 164.58 (C-4), 156.06 (benzofuran-C-9),

151.78 (C-2), 147.23 (C-6), 139.36 (benzofuran-C-2), 129.00 (benzofuran-C-8), 128.69 (benzofuran-C-5), 126.23 (benzofuran-C-6), 122.52 (benzofuran-C-4), 117.26 (C-5), 112.02 (benzofuran-C-7), 107.65 (benzofuran-C-3), 89.86 (C-1'), 81.41 (C-4'), 74.27 (C-2'), 71.68 (C-3'), 64.26 (C-5'), 20.54 (COCH₃), 20.42 (COCH₃), 20.34 (COCH₃). LC-MS (m/z) [M + H⁺]: calculated 487.2; found 487.4. HPLC: > 99 % purity at 225 nm and 285 nm; *t*_R = 1.8 min; flow rate: 1 mL/min; solvent elution: 90 % MeOH in water.

(2*R*,3*R*,4*R*,5*R*)-2-(acetoxymethyl)-5-(5-(benzofuran-7-yl)-2,4-dioxo-3,4-dihydropyrimidin-1(2*H*)-yl)tetrahydrofuran-3,4-diyl diacetate (8)

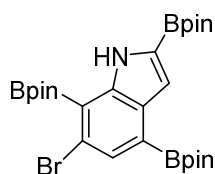


White solid, 84 % yield over 2 steps. ¹H NMR (400 MHz, Methanol-*d*₄) δ 8.18 (s, 1H, H-6), 7.74 (d, 1H, benzofuran-H-2), 7.59 (s, 2H, benzofuran-H-4 and 6), 7.25 (dd, *J* = 7.7, 7.7 Hz, 1H, benzofuran-H-5), 6.87 (d, 1H, benzofuran-H-3), 6.15 (d, 1H, *J* = 5.2, H-1'), 5.53 (dd, *J* = 5.2, 6.1 Hz, 1H, H-2'), 5.44 (dd, *J* = 6.1, 6.1 Hz, 1H, H-3'), 4.42 – 4.28 (m, 3H, H-4' and 5'), 2.09 (s, 6H, H-OAc), 1.59 (s, 3H, H-OAc). ¹³C NMR (101 MHz, Methanol-*d*₄) δ 171.81 (COCH₃), 171.37 (COCH₃), 171.33 (COCH₃), 163.94 (C-4), 153.40 (benzofuran-C-9), 151.61 (C-2), 146.51 (benzofuran-C-2), 140.93 (C-6), 129.27 (benzofuran-C-8), 126.48 (benzofuran-C-6), 123.92 (benzofuran-C-5), 122.20 (benzofuran-C-4), 117.92 (benzofuran-C-7), 111.62 (C-5), 107.94 (benzofuran-C-3), 89.25 (C-1'), 81.36 (C-4'), 74.59 (C-2'), 71.66 (C-3'), 64.26 (C-5'), 20.43 (COCH₃), 20.32 (COCH₃), 20.07 (COCH₃). LC-MS (m/z) [M + H⁺]: calculated 487.2; found 487.4. HPLC: > 99 % purity at 225 nm and 285 nm; *t*_R = 1.8 min; flow rate: 1 mL/min; solvent elution: 90 % MeOH in water.

6.1.2 Chapter 3 compounds: 9 – 43 (Class 2 inhibitors)

Borylation. In a 50 mL Schlenk tube, a solution of 6-bromoindole (2 g, 10.2 mmol), bis(pinacolato)diboron (B_2Pin_2) (9.1 g, 36 mmol), $[Ir(OMe)cod]_2$ (612 mg, 0.92 mmol, 9 mol%) and 4,4-di-tert-butyl bipuridine (dtbpy) (492 mg, 1.8 mmol, 18 mol%) in anhydrous THF was heated to 85 °C for 41 h. The crude 1H NMR showed a mixture of 2,7-diborylindole **9** and 2,4,7-triborylindole **10** in 1:2 ratio from 1H NMR. The reaction was continued for another 24 h. After cooling to room temperature, a few drops of MeOH were added to quench the reaction. The solvent was removed in vacuo. The crude product can be used directly in the next step or purified by column chromatography on silica gel eluting with *n*-hexane-ethyl acetate (10:1) to afford pure **10** as a white solid (84 % yield).

6-bromo-2,4,7-tris(4,4,5,5-tetramethyl-1,3,2-dioxaborolan-2-yl)-1*H*-indole (**10**)¹³⁴

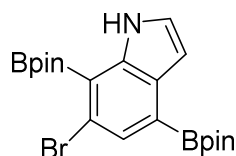


White solid, 84 % yield. 1H NMR (400 MHz, $CDCl_3$) δ 9.64 (s, 1H, NH), 7.75 (s, 1H, H-5), 7.50 (s, 1H, H-3), 1.44 (s, 12H, 4×Me of Bpin), 1.37 (s, 24H, 8×Me of Bpin). ^{13}C NMR (101 MHz, $CDCl_3$) δ 144.12, 132.36 (C-5), 130.59, 124.86, 115.05 (C-3), 84.23 (2C of Bpin), 83.96 (1C of Bpin), 25.13 (4×Me of Bpin), 25.09 (4×Me of Bpin), 24.98 (4×Me of Bpin). 3C are missing. LC-MS (m/z) $[M + H^+]$: calculated 574.2; found 574.4, 576.4.

In a 250 mL Schlenk flask, bismuth triacetate (772 mg, 2 mmol, 20 mol%) was added to a solution of the unpurified triborylindole **10** in 44 mL THF, then 100 mL MeOH was added. The reaction mixture was stirred at 65 °C for 16 h under N_2 . The solution was filtered with

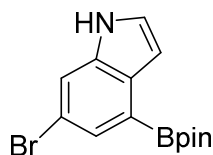
celite, and the solvent was removed in vacuo to give the crude diborylindole **11** and **12**. The crude product was purified by column chromatography on silica gel eluting with *n*-hexane-ethyl acetate (10:1), or crystallised from EtOAc to afford pure **11** and **12**.

6-bromo-4,7-bis(4,4,5,5-tetramethyl-1,3,2-dioxaborolan-2-yl)-1H-indole (11)

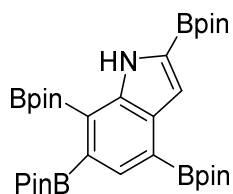


11 was produced more under normal nitrogen atmosphere and with non-anhydrous MeOH-THF. ¹H NMR (400 MHz, CDCl₃) δ 9.51 (s, 1H, NH), 7.78 (s, 1H, H-5), 7.26 (s, 1H, H-2), 6.96 (s, 1H, H-3), 1.40 (s, 24H, 8×Me of Bpin). ¹³C NMR (101 MHz, CDCl₃) δ 142.12 (C-9), 132.01 (C-5), 130.48 (C-8), 125.04 (C-2), 122.99 (C-6), 104.02 (C-3), 84.19 (1C of Bpin), 83.92 (1C of Bpin) 25.15 (4×Me of Bpin), 25.12 (4×Me of Bpin). 2C are missing.

6-bromo-4-(4,4,5,5-tetramethyl-1,3,2-dioxaborolan-2-yl)-1H-indole (12)¹³⁴

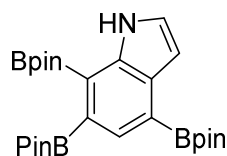


12 was produced more under nitrogen pressure and with anhydrous MeOH-THF. White solid, 80 % yield. ¹H NMR (400 MHz, CDCl₃) δ 8.36 (s, 1H, NH), 7.82 (s, 1H, H-5), 7.64 (d, 1H, H-7), 7.27 (s, 1H, H-2), 7.09 (d, 1H, H-3), 1.47 (s, 12H, 4×Me of BPin). ¹³C NMR (100 MHz, CDCl₃) δ 136.17 (C-9), 131.47 (C-8), 130.40 (C-5), 125.46 (C-2), 116.77 (C-7), 115.29 (C-6), 104.64 (C-3), 83.89(C of Bpin), 25.06 (4×Me of Bpin). 1C is missing. LC-MS (m/z) [M + H⁺]: calculated 322.1; found 322.2, 324.2.

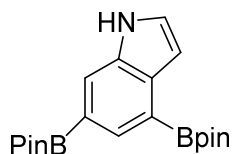
2,4,6,7-tetrakis(4,4,5,5-tetramethyl-1,3,2-dioxaborolan-2-yl)-1H-indole (13)

In a 50 mL Schlenk tube, a solution of 6-bromoindole (100 mg, 0.51 mmol), bis(pinacolato)diboron (B_2Pin_2) (1.27 g, 5.0 mmol), $[Ir(OMe)cod]_2$ (30 mg, 0.046 mmol, 9 mol%) and 4,4-di-tert-butyl bipyridine (dtbpy) (25 mg, 0.09 mmol, 18 mol%) in anhydrous THF was heated to 85 °C for 72 h. After cooling to room temperature, a few drops of MeOH were added to quench the reaction. The solvent was removed in vacuo. The crude product can be used directly in the next step or purified by column chromatography on silica gel eluting with *n*-hexane-ethyl acetate (10:1) to afford **13** as transparent oil with 58 % yield. 1H NMR (400MHz, $CDCl_3$) δ 9.50 (1 H, br s, NH), 7.76 (1 H, s, CH), 7.55 (1H, s, CH), 1.41 (12 H, s, 8 \times Me), 1.37 (24 H, s, 8 \times Me). ^{13}C NMR (100 MHz, $CDCl_3$) δ 142.8 (C), 132.6 (C), 132.3 (C), 131.6 (CH), 115.0 (CH), 84.0 (4 \times C of BPin), 83.7 (2 \times C of BPin), 83.4 (2 \times C of BPin), 25.2 (2 \times Me of BPin), 25.1 (4 \times Me of BPin), 25.0 (4 \times Me of BPin), 24.9 (4 \times Me of BPin), 3 \times C not observed. LC-MS (m/z) $[M + H^+]$: 622.4, found 622.7.

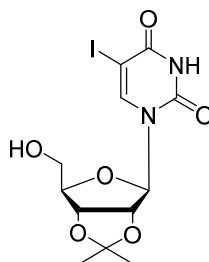
Diprotodeborylation. In a 50 mL Schlenk flask, bismuth triacetate (39 mg, 0.01 mmol, 20 mol%) was added to a solution of the unpurified tetraborindole **13** in 2.2 mL THF, then 5 mL MeOH was added. The reaction mixture was stirred at 65 °C for 16 h under N_2 . The solution was filtered with celite, and the solvent was removed in vacuo to give the crude triborylindole **14** and **15**. The crude product was purified by column chromatography on silica gel eluting with *n*-hexane-ethyl acetate (10:1).

4,6,7-tris(4,4,5,5-tetramethyl-1,3,2-dioxaborolan-2-yl)-1H-indole (14)

14 was produced under nitrogen atmosphere and with non-anhydrous MeOH-THF. ^1H NMR (400 MHz, CDCl_3) δ 9.35 (s, 1H, NH), 7.78 (s, 1H, H-5), 7.30 (d, $J = 2.6$ Hz, 1H, H-2), 7.00 (d, $J = 2.6$ Hz, 1H, H-3), 1.40 (s, 36H, 3 \times Me of Bpin). ^{13}C NMR (101 MHz, CDCl_3) δ 140.85, 132.73, 131.66 (C-5), 125.09 (C-2), 103.87 (C-3), 84.03 (1C of Bpin), 83.73 (1C of Bpin), 83.47 (1C of Bpin), 25.22 (4 \times Me of BPin), 25.20 (4 \times Me of BPin), 25.16 (4 \times Me of BPin). 3C are missing.

4,6-bis(4,4,5,5-tetramethyl-1,3,2-dioxaborolan-2-yl)-1H-indole (15)

15 could be produced more under high pressure of nitrogen and using anhydrous MeOH-THF. ^1H NMR (400 MHz, CDCl_3) δ (400MHz, CDCl_3) 8.23 (1 H, br s, NH), 8.10 (1 H, s, CH), 7.99 (1H, s, CH), 7.30 (1H, d, CH), 7.06 (1H, d, CH) 1.39 (12H, s, 4 \times Me), 1.36 (12 H, 4 \times Me). ^{13}C NMR (101 MHz, CDCl_3) δ (100MHz, CDCl_3) 134.0 (C), 133.9 (C) 132.9 (CH), 124.9 (CH), 119.8 (CH), 103.8 (CH), 82.5 (2 \times C of BPin), 82.3 (2 \times C of BPin), 24.0 (4 \times Me of BPin), 23.9 (4 \times Me of BPin). LC-MS (m/z) $[\text{M}^+ \text{H}]^+$ 370.2, found 370.3.

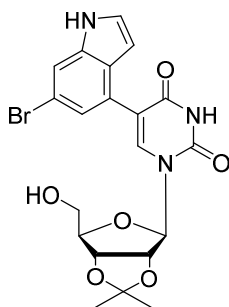
1-((3*aR*,4*R*,6*R*,6*aR*)-6-(hydroxymethyl)-2,2-dimethyltetrahydrofuro[3,4-*d*][1,3]dioxol-4-yl)-5-iodopyrimidine-2,4(1*H*,3*H*)-dione (16)¹⁵⁵

5-iodouridine (100 mg, 0.37 mmol) was stirred in acetone (3.3 mL, 0.08 mmol/mL) and H₂SO₄ (33 μ L) was added dropwise with stirring at rt until TLC showed full conversion (8 h). After completion, the reaction was neutralized with NaHCO₃ powder until no bubbles produced. The solvent was removed and extracted with EtOAc (20 mL \times 3). The organic layer was combined and dried over anhydrous Na₂SO₄. The solvent was removed under vacuo and white powder **16** was obtained (102 mg, 92 % yield) without further purification. ¹H NMR (400 MHz, DMSO-*d*₆) δ 11.74 (s, 1H, NH), 8.32 (s, 1H, H-6), 5.81 (d, *J* = 2.6 Hz, 1H, H-1'), 5.18 (s, 1H, OH-5'), 4.98 – 4.87 (m, 1H, H-2'), 4.81 – 4.70 (m, 1H, H-3'), 4.14 – 4.00 (m, 1H, H-4'), 3.69 – 3.45 (m, 2H, H-5'), 1.47 (s, 3H, CH₃), 1.28 (s, 3H, CH₃). ¹³C NMR (100 MHz, DMSO-*d*₆) δ 160.52 (C-4), 150.01 (C-2), 146.07 (C-6), 112.86 (CCH₃), 91.31 (C-1'), 86.87 (C-4'), 83.85 (C-2'), 80.25 (C-3'), 69.43 (C-5), 61.07 (C-5'), 26.95 (CH₃), 25.12 (CH₃). LC-MS (*m/z*) [M+ H]⁺ 411.0, found 411.2.

In a 50 mL Schlenk tube, 5-iodouridine derivative **16** (100 mg, 0.24 mmol), 6-bromo-4-(BPin)-indole **12** (93 mg, 0.29 mmol) and NaHCO₃ (60 mg, 0.72 mmol) were added into dioxane-DI water (9 mL:3 mL) under N₂. The solution was degassed twice by a freeze-pump-thaw method. PdCl₂(dppf)DCM (9.8 mg, 0.012 mmol, 5 mol%) was then added under N₂ and degassed twice more. The mixture was heated to 130 $^{\circ}$ C for 4 h. The solvent was removed in vacuo. The crude product was extracted with DCM three times. The organic phase was dried by anhydrous

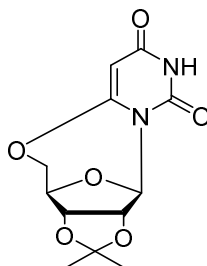
Na_2SO_4 and concentrated in vacuo to give the crude product **17** and **18**. The crude product was purified by column chromatography on silica gel eluting with DCM-MeOH (100:4) to afford pure **17** (69 mg, 60 % yield) as a transparent oil and side product **18**.

5-(6-bromo-1*H*-indol-4-yl)-1-((3*aR*,4*R*,6*R*,6*aR*)-6-(hydroxymethyl)-2,2-dimethyltetrahydrofuro[3,4-*d*][1,3]dioxol-4-yl)pyrimidine-2,4(1*H*,3*H*)-dione (17)



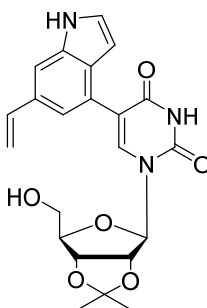
Transparent oil, 60 % yield. ^1H NMR (400 MHz, $\text{DMSO-}d_6$) δ 11.64 (s, 1H, uracil-NH), 11.28 (s, 1H, indoyl-NH), 8.03 (s, 1H, H-6), 7.55 (s, 1H, indoyl-H-7), 7.37 (d, 1H, indoyl-H-2), 7.17 (s, 1H, indoyl-H-5), 6.35 (d, 1H, indoyl-H-3), 5.95 (d, 1H, H-1'), 5.09 – 4.93 (m, 2H, H-2' and OH), 4.81 – 4.67 (m, 1H, H-3'), 4.16 – 4.03 (m, 1H, H-4'), 3.59 – 3.51 (m, 2H, H-5'), 1.50 (s, 3H, CH_3), 1.30 (s, 3H, CH_3). ^{13}C NMR (101 MHz, $\text{DMSO-}d_6$) δ 162.03 (C-4), 150.09 (C-2), 140.44 (C-6), 136.81 (indoyl-C-9), 126.57, 126.39 (indoyl-C-4), 126.29 (indoyl-C-2), 126.09 (indoyl-C-8), 122.56 (indoyl-C-5), 113.45 (indoyl-C-7), 113.18 (indoyl-C-6), 113.07 (CCH_3), 112.77 (C-5), 101.25 (indoyl-C-3), 91.43 (C-1'), 86.57 (C-4'), 83.79 (C-2'), 80.69 (C-3'), 61.36 (C-5'), 27.16 (CH_3), 25.29 (CH_3). LC-MS (m/z) [$\text{M} + \text{H}^+$]: calculated 478.1; found 478.2, 480.2.

(3aR,4R,12R,12aR)-2,2-dimethyl-3a,4,12,12a-tetrahydro-5H,8H-4,12-epoxy[1,3]dioxolo[4,5-e]pyrimido[6,1-b][1,3]oxazocine-8,10(9H)-dione (18)⁹³



Transparent oil. ¹H NMR (400MHz, DMSO-*d*₆) δ 6.49 (1H, s, H-5), 4.91 (2H, m, H1', H2'), 4.67 (1H, d, *J* = 5.2 Hz, H3'), 4.46 (2H, m, H-4', H-5'), 3.72 (1H, d, *J* = 12.8 Hz, H-5'), 4.62 (1H, d, *J* = 12.8 Hz, H-5'), 4.05 (1H, d, *J* = 12.8 Hz, H-5'), 1.42 (3H, s, CH₃), 1.29 (3H, s, CH₃). LC-MS (m/z) [M+ H]⁺ 283.1, found 283.3.

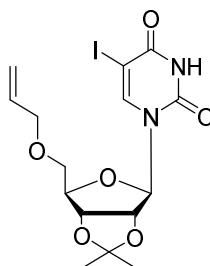
1-((3aR,4R,6R,6aR)-6-(hydroxymethyl)-2,2-dimethyltetrahydrofuro[3,4-d][1,3]dioxol-4-yl)-5-(6-vinyl-1H-indol-4-yl)pyrimidine-2,4(1H,3H)-dione (19)



A 50 mL Schlenk tube was charged with **17** (134 mg, 0.28 mmol) and Cs₂CO₃ (365 mg, 1.12 mmol). 6 mL dioxane and 2 mL DI water were added and degassed twice by a freeze-pump-thaw method. PdCl₂(dppf)DCM (11.4 mg, 0.014 mmol) was added under N₂ and degassed twice more. Vinylboronic acid pinacol ester (0.56 mmol) was quickly added into the Schlenk tube under N₂. The Schlenk tube was sealed, and the reaction proceeded at 115 °C for overnight. The solvent was removed in vacuo and purified by column chromatography on silica gel eluting with DCM-MeOH (100:3.5) to afford pure **19** (108 mg, 91 %) as a colourless oil. ¹H NMR

(400 MHz, DMSO-*d*₆) δ 11.58 (s, 1H, uracil-NH), 11.16 (s, 1H, indoyl-NH), 7.98 (s, 1H, H-6), 7.41 (s, 1H, indoyl-H-7), 7.33 (d, $J = 2.6$ Hz, 1H, indoyl-H-2), 7.18 (s, 1H, indoyl-H-5), 6.82 (dd, $J = 17.7, 11.2$ Hz, 1H, CH=CH₂), 6.29 (d, 1H, $J = 2.6$ Hz, indoyl-H-3), 5.96 (d, $J = 2.8$ Hz, 1H, H-1'), 5.74 (d, $J = 17.7$ Hz, 1H, CH=CH₂), 5.15 (d, $J = 11.2$ Hz, 1H, CH=CH₂), 5.10 – 4.95 (m, 2H, H-2' and OH), 4.82 – 4.70 (m, 1H, H-3'), 4.17 – 4.05 (m, 1H, H-4'), 3.61 – 3.50 (m, 2H, H-5'), 1.50 (s, 3H, CH₃), 1.30 (s, 3H, CH₃). ¹³C NMR (100 MHz, DMSO-*d*₆) δ 162.10 (C-4), 150.12 (C-2), 139.93 (C-6), 137.81 (CH=CH₂), 136.17 (indoyl-C-4), 130.24 (indoyl-C-5), 127.07 (indoyl-C-9), 126.10 (indoyl-C-2), 124.87 (C-5), 118.33 (indoyl-C-5), 114.09 (indoyl-C-8), 113.00 (CCH₃), 111.58 (CH=CH₂), 109.28 (indoyl-C-7), 101.23 (indoyl-C-3), 91.35 (C-1'), 86.52 (C-4'), 83.64 (C-2'), 80.66 (C-3'), 61.33 (C-5'), 27.11 (CH₃), 25.23 (CH₃). LC-MS (m/z) [M + H⁺]: calculated 426.2; found 426.4.

1-((3*aR*,4*R*,6*R*,6*aR*)-6-((allyloxy)methyl)-2,2-dimethyltetrahydrofuro[3,4-*d*][1,3]dioxol-4-yl)-5-iodopyrimidine-2,4(1*H*,3*H*)-dione (20a)

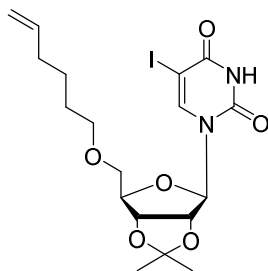


In a 50 ml dry round bottom flask, NaH (60 %, 49 mg, 1.23 mmol) was added to 20 mL dry THF and stirred until NaH dissolved, followed by adding 2', 3'-O-isopropylidene (200 mg, 0.49 mmol). The solution was activated via sonication for 30 min at rt. 6-bromo-1-hexene (50 μ L, 0.59 mmol) was added and the reaction mixture was irradiated for 1.5 h. A few drops of water were added to quench the reaction. The solution was filtered with celite and washed with EtOAc. The filtrate was combined, and the solvent was removed in vacuo. The crude product was purified by column chromatography on silica gel eluting with DCM-MeOH (100:1) to

afford pure **20a** (176 mg, 80 % yield) as a white solid. ^1H NMR (400 MHz, $\text{DMSO-}d_6$) δ 11.77 (s, 1H, br s NH), 8.14 (s, 1H, H-6), 5.90 (m, 1H, $\text{CH}=\text{CH}_2$), 5.78 (d, $J = 2.1$ Hz, 1H, H-1'), 5.26 (dd, $J = 10.5, 1.8$ Hz, 1H), 5.17 (d, $J = 10.5$ Hz, 1H), 4.92 (dd, $J = 6.3, 2.0$ Hz, 1H, H-2'), 4.75 (dd, $J = 6.3, 3.4$ Hz, 1H, H-3'), 4.31 – 4.21 (m, 1H, H-4'), 4.01 (d, $J = 5.6$ Hz, 2H, $\text{CH}=\text{CH}_2$), 3.65 – 3.52 (m, 2H, H-5'), 1.47 (s, 3H, CH_3), 1.28 (s, 3H, CH_3). ^{13}C NMR (100 MHz, $\text{DMSO-}d_6$) δ 160.82 (C-4), 150.17 (C-2), 145.84 (C-6), 134.67 ($\text{CH}_2=\text{CH}$), 117.07 ($\text{CH}_2=\text{CH}$), 112.86 (CCH_3), 92.13 (C-1'), 85.38 (C-4'), 84.18 (C-2'), 80.64 (C-3'), 71.47 ($\text{CH}_2=\text{CH-CH}_2$), 69.61 (C-5'), 69.48 (C-5), 26.97 (CH_3), 25.12 (CH_3). LC-MS (m/z) [$\text{M} + \text{H}^+$]: calculated 451.0; found 451.2.

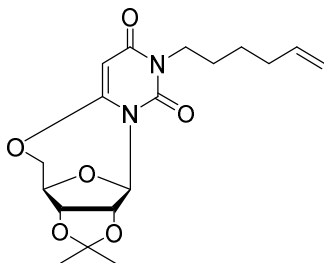
Alkylation. In a 50 ml round bottom flask, uridine derivative **16** (2g, 4.8 mmol), 6-bromohexene (1.6 mL, 12.2 mmol) and NaH (60 %, 488 mg, 12.2 mmol) were added to dry DMF. The solution was stirred in an ice bath for 2 h. After completion, a few drops of water were added to quench the reaction. The solution was filtered with celite and washed with EtOAc. The filtrate was combined, and the solvent was removed in vacuo. The crude product was purified by column chromatography on silica gel eluting with DCM-MeOH (100:1) to afford pure **20d** (1.04 g, 44 % yield), **18**, **23d**, **24** (7 % yield) and **25** (5 % yield).

1-((3a*R*,4*R*,6*R*,6a*R*)-6-((hex-5-en-1-yloxy)methyl)-2,2-dimethyltetrahydrofuro[3,4-*d*][1,3]dioxol-4-yl)-5-iodopyrimidine-2,4(1*H*,3*H*)-dione (20d)



Transparent oil, 44 % yield. ^1H NMR (400 MHz, CDCl_3) δ 9.17 (s, 1H, br s, NH), 8.08 (d, $J = 1.7$ Hz, 1H, H-6), 5.93 (d, $J = 2.4$ Hz, 1H, H-1'), 5.88 – 5.67 (m, 1H, $\text{CH}=\text{CH}_2$), 5.11 – 4.87 (m, 2H, $\text{CH}=\text{CH}_2$), 4.87 – 4.74 (m, 1H, H-3'), 4.74 – 4.65 (m, 1H, H-2'), 4.53 – 4.40 (m, 1H, H-4'), 3.82 – 3.65 (m, 1H, H-5'), 3.65 – 3.52 (m, 2H, H-5' and alkenyl-H-1), 3.44 (t, $J = 7.5$ Hz, 1H, alkenyl-H-1), 2.06 (dd, $J = 7.2$ Hz, 2H, alkenyl-H-4), 1.67 – 1.59 (m, 2H, alkenyl-H-2), 1.58 (s, 3H, CH_3), 1.45 – 1.37 (m, 2H, alkenyl-H-3), 1.35 (s, 3H, CH_3). ^{13}C NMR (100 MHz, CDCl_3) δ 160.31 (C-4), 150.04 (C-2), 145.48 (C-6), 138.48 ($\text{CH}=\text{CH}_2$), 114.95 ($\text{CH}=\text{CH}_2$), 114.06 (CCH_3), 93.15 (C-1'), 85.95 (C-4'), 85.73 (C-2'), 81.10 (C-3'), 71.87 (C-5'), 70.68 (alkenyl-C-1), 67.79 (C-5), 33.50 (alkenyl-C-4), 29.06 (alkenyl-C-2), 27.27 (CH_3), 25.37 (alkenyl-C-3), 25.34 (CH_3). LC-MS (m/z) [$\text{M} + \text{H}^+$]: calculated 493.1; found 493.3.

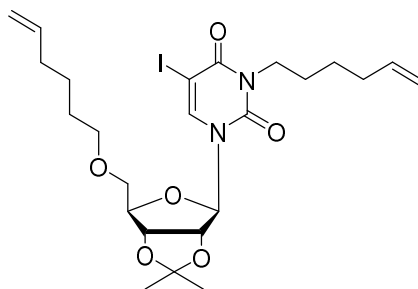
(3a*R*,4*R*,12*R*,12a*R*)-9-(hex-5-en-1-yl)-2,2-dimethyl-3a,4,12,12a-tetrahydro-5*H*,8*H*-4,12-epoxy[1,3]dioxolo[4,5-*e*]pyrimido[6,1-*b*][1,3]oxazocine-8,10(9*H*)-dione (23d)



Transparent oil. ^1H NMR (400 MHz, DMSO) δ 6.31 (s, 1H, H-5), 5.82 – 5.74 (m, 1H, $\text{CH}=\text{CH}_2$), 5.41 (d, $J = 2.6$ Hz, 1H, H-1'), 5.04 – 4.92 (m, 4H, H-2', H-3' and $\text{CH}=\text{CH}_2$), 4.67 – 4.56 (m, 2H, H-4' and H-5'), 4.03 (d, $J = 12.8$ Hz, 1H, H-5'), 3.80 – 3.70 (m, 2H, alkenyl-H-1), 2.08 – 2.00 (m, 2H, alkenyl-H-4), 1.54 – 1.46 (m, 2H, alkenyl-H-2), 1.43 (s, 3H, CH_3), 1.36 – 1.30 (m, 2H, alkenyl-H-3), 1.28 (s, 3H, CH_3). ^{13}C NMR (100 MHz, $\text{DMSO-}d_6$) δ 159.75 (C-2), 150.17 (C-4), 138.44 ($\text{CH}=\text{CH}_2$), 115.02 ($\text{CH}=\text{CH}_2$), 111.57 (CCH_3), 89.99 (C-5), 89.18 (C-1'), 84.52 (C-2'), 83.47 (C-4'), 81.71 (C-3'), 77.37 (C-1'), 40.08 (alkenyl-H-1), 32.84 (alkenyl-

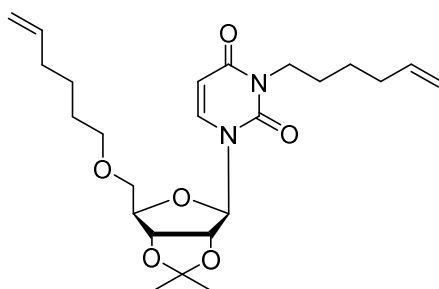
H-4), 26.54 (alkenyl-H-2), 26.02 (CH₃), 25.59 (alkenyl-H-3), 24.30 (CH₃). LC-MS (m/z) [M + H⁺]: calculated 365.2; found 365.4.

3-(hex-5-en-1-yl)-1-((3*aR*,4*R*,6*R*,6*aR*)-6-((hex-5-en-1-yloxy)methyl)-2,2-dimethyltetrahydrofuro[3,4-d][1,3]dioxol-4-yl)-5-iodopyrimidine-2,4(1*H*,3*H*)-dione (24)



Transparent oil, 7 % yield. ¹H NMR (400 MHz, DMSO-*d*₆) δ 8.14 (s, 1H, H-6), 5.89 – 5.64 (m, 3H, H-1' and 2×CH=CH₂), 5.09 – 4.88 (m, 4H, 2×CH=CH₂), 4.86 (d, *J* = 6.1, 1H, H-2'), 4.74 (dd, *J* = 6.1, 2.9 Hz, 1H, H-3'), 4.40 – 4.25 (m, 1H, H-4'), 3.81 (dd, *J* = 7.4, 7.4 Hz, 2H, *N*-alkenyl-H-1), 3.62 (dd, *J* = 11.1 Hz, 1H, H-5'), 3.51 (dd, *J* = 5.7 Hz, 1H, H-5'), 3.43 (dd, *J* = 6.5 Hz, 2H, *O*-alkenyl-H-1), 2.13 – 1.90 (m, 4H, alkenyl-H-4), 1.63 – 1.40 (m, 7H, CH₃ and alkenyl-H-2), 1.41 – 1.21 (m, 7H, CH₃ and alkenyl-H-3). ¹³C NMR (100 MHz, DMSO-*d*₆) δ 159.45 (C-4), 149.89 (C-2), 144.07 (C-6), 138.55 (CH=CH₂), 138.37 (CH=CH₂), 114.95 (CH=CH₂), 114.77 (CH=CH₂), 112.56 (CCH₃), 93.46 (C-1'), 85.75 (C-4'), 84.64 (C-2'), 80.66 (C-3'), 70.6 (*O*-alkenyl-C-1), 70.07 (C-1'), 68.04 (C-5), 41.66 (*N*-alkenyl-C-1), 32.92 (alkenyl-C-4), 32.83 (alkenyl-C-4), 28.55 (*O*-alkenyl-C-2), 26.92 (CH₃), 26.44 (*N*-alkenyl-C-2), 25.60 (*N*-alkenyl-C-3), 25.05 (CH₃), 24.79 (*O*-alkenyl-C-3). LC-MS (m/z) [M + H⁺]: calculated 575.2; found 575.3.

3-(hex-5-en-1-yl)-1-((3a*R*,4*R*,6*R*,6a*R*)-6-((hex-5-en-1-yloxy)methyl)-2,2-dimethyltetrahydrofuro[3,4-*d*][1,3]dioxol-4-yl)pyrimidine-2,4(1*H*,3*H*)-dione (25)

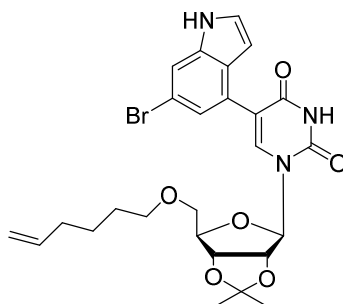


Transparent oil, 5 % yield. ^1H NMR (400 MHz, Methanol-*d*₄) δ 7.79 (d, J = 8.1 Hz, 1H, H-6), 5.88 – 5.76 (m, 3H, 1H for H-1' and 2H for alkenyl-CH=CH₂), 5.73 (d, J = 8.1 Hz, 1H, H-5), 5.04 – 5.00 (m, 1H, alkenyl-CH=CH₂), 4.98 (d, J = 7.4 Hz, 1H, alkenyl-CH=CH₂), 4.94 (d, J = 10.5 Hz, 2H, alkenyl-CH=CH₂), 4.82 (d, J = 1.8 Hz, 2H, H-2', 3'), 4.42 (s, 1H, H-4'), 3.91 (t, J = 7.4 Hz, 2H, alkenyl-NCH₂), 3.70 (dd, J = 10.7, 2.8 Hz, 1H, H-5'), 3.58 (dd, J = 10.7, 4.0 Hz, 1H, H-5'), 3.46 (td, J = 6.5, 3.0 Hz, 2H, alkenyl-OCH₂), 2.12 – 2.03 (m, 4H, alkenyl-H-4), 1.62 (d, J = 7.7 Hz, 2H, alkenyl-H-2), 1.54 (s, 3H, CH₃), 1.51 (s, 2H, alkenyl-H-2), 1.41 (q, J = 7.7 Hz, 4H, alkenyl-H-3), 1.35 (s, 3H, CH₃). ^{13}C NMR (101 MHz, Methanol-*d*₄) δ 165.10 (C-2), 152.19 (C-4), 141.45 (C-6), 139.72 (alkenyl-CH=CH₂), 139.59 (alkenyl-CH=CH₂), 115.23 (alkenyl-CH=CH₂), 115.17 (alkenyl-CH=CH₂), 114.58 (C(CH₃)₂), 101.32 (C-5), 95.90 (C-1'), 87.74 (C-4'), 86.98 (C-2'), 82.81 (C-3'), 72.33 (alkenyl-OCH₂), 71.90 (C-5'), 41.83 (*N*-alkenyl-C-1), 34.60 (alkenyl-C-4), 34.48 (alkenyl-C-4), 30.13 (*O*-alkenyl-C-2), 28.08 (*N*-alkenyl-C-2), 27.48 (*O*-alkenyl-C-3), 27.32 (CH₃), 26.63 (*N*-alkenyl-C-3), 25.43 (CH₃).

Suzuki and Heck couplings. In a 50 mL Schlenk tube, the substrate **20d** (308 mg, 0.63 mmol), indole derivative **12** (227 mg, 0.75 mmol) and NaHCO₃ (158 mg, 1.88 mmol) were added into dioxane-DI water (139 mL:46 mL) under N₂, and then degassed twice by a freeze-pump-thaw method. PdCl₂(dppf)DCM (25.5 mg, 0.03 mmol, 5 mol%) was then added under N₂ and degassed twice more. The reaction was heated to 90 °C for overnight. The solvent was removed

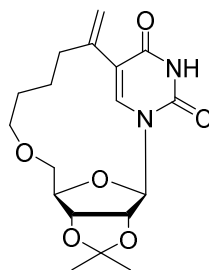
in vacuo. The crude was purified by column chromatography on silica gel eluting with DCM-MeOH (100:2) to afford pure **26** (20 % yield) as a transparent oil, pure **27** (70 % yield) as a white powder and **28** (5 % yield) with some isomers as a yellow oil.

5-(6-bromo-1*H*-indol-4-yl)-1-((3*aR*,4*R*,6*R*,6*aR*)-6-((hex-5-en-1-yl)oxy)methyl)-2,2-dimethyltetrahydrofuro[3,4-*d*][1,3]dioxol-4-yl)pyrimidine-2,4(1*H*,3*H*)-dione (26)



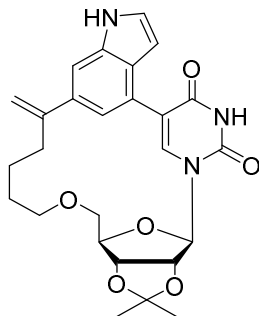
Transparent oil, 20 % yield. ^1H NMR (400 MHz, $\text{DMSO-}d_6$) δ 12.44 (s, 1H, NH, uracil-NH), 12.10 (s, 1H, indoyl-NH), 8.82 (s, 1H, H-6), 8.35 (s, 1H, indoyl-H-7), 8.19 (d, 1H, indoyl-H-2), 7.97 (s, 1H, indoyl-H-5), 7.15 (d, 1H, indoyl-H-3), 6.78 (d, 1H, H-1'), 6.56 – 6.36 (m, 1H, $\text{CH}=\text{CH}_2$), 5.80 – 5.67 (m, 3H, $\text{CH}=\text{CH}_2$ and H-2'), 5.61 – 5.49 (m, 1H, H-3'), 5.11 – 5.02 (m, 1H, H-4'), 4.48 – 4.24 (m, 2H, H-5'), 4.02 – 3.65 (m, 2H, alkenyl-H-1), 2.61 – 2.48 (m, 2H, alkenyl-H-4), 2.31 (s, 3H, CH_3), 2.11 (s, 3H, CH_3), 1.86 – 1.69 (m, 4H, alkenyl-H-2 and 3). ^{13}C NMR (100 MHz, $\text{DMSO-}d_6$) δ 161.93 (C-4), 149.98 (C-2), 139.68 (C-6), 138.54 ($\text{CH}=\text{CH}_2$), 136.78 (indoyl-C-4), 126.54 (indoyl-C-6), 126.29 (indoyl-H-2), 126.05, 122.43 (indoyl-H-5), 114.67 ($\text{CH}=\text{CH}_2$), 113.34 (indoyl-H-7), 113.12 (C-5), 112.88 (CCH_3), 112.48, 100.96 (indoyl-H-3), 91.38 (H-1'), 84.80 (H-4'), 84.17 (H-2'), 80.55 (H-3'), 70.50 (alkenyl-H-1), 70.03 (H-5'), 32.77 (alkenyl-H-4), 28.00 (alkenyl-H-2), 27.10 (CH_3), 25.22 (CH_3), 24.47 (alkenyl-H-3). LC-MS (m/z) [$\text{M} + \text{H}^+$]: calculated 560.1; found 560.3, 562.3.

(3aR,4R,17R,17aR,Z)-2,2-dimethyl-10-methylene-3a,11,12,13,14,16,17,17a-octahydro-4H,6H,10H-4,17-epoxy-5,9-(metheno)[1,3]dioxolo[4,5-d][1]oxa[7,9]diazacyclohexadecane-6,8(7H)-dione (27)



White solid, 70 % yield. ^1H NMR (400 MHz, $\text{DMSO-}d_6$) δ 11.40 (s, 1H, br s, NH), 8.14 (s, 1H, H-6), 6.27 (s, 1H, $\text{C}=\text{CH}_2$), 6.06 (d, 1H, H-1'), 5.13 (s, 1H, $\text{C}=\text{CH}_2$), 4.91 – 4.78 (m, 1H, H-3'), 4.82 – 4.66 (m, 1H, H-2'), 4.47 – 4.31 (m, 1H, H-4'), 3.68 (d, $J = 6.2$ Hz, 2H, H-5'), 3.62 – 3.56 (m, 2H, alkenyl-H-1), 2.37 – 2.29 (m, 1H, alkenyl-H-3), 2.17 – 2.09 (m, 1H, alkenyl-H-3), 1.74 – 1.65 (m, 2H, alkenyl-H-2), 1.57 – 1.44 (m, 5H, alkenyl-H-4 and CH_3), 1.29 (s, 3H, CH_3). ^{13}C NMR (100 MHz, $\text{DMSO-}d_6$) δ 162.37 (C-4), 149.29 (C-2), 139.20 ($\text{C}=\text{CH}_2$), 137.39 (C-6), 115.11 ($\text{C}=\text{CH}_2$), 112.82 (CCH_3), 110.21 (C-5), 89.75 (C-1'), 84.91 (C-2'), 84.54 (C-4'), 79.72 (C-3'), 70.24 (C-5'), 67.55 (alkenyl-C-1), 32.88 (alkenyl-C-3), 27.28 (CH_3), 25.99 (alkenyl-C-2), 25.29 (alkenyl-C-4), 24.14 (CH_3). LC-MS (m/z) $[\text{M} + \text{H}^+]$: calculated 365.3; found 365.2.

(33a*R*,34*R*,36*R*,36a*R*,*Z*)-32,32-dimethyl-10-methylene-21,22,23,24,33a,34,36,36a-octa-hydro-11*H*-5-oxa-1(4,6)-indola-2(5,1)-pyrimidina-3(6,4)-furo[3,4-*d*][1,3]dioxolacyclo-decaphane-22,24-dione (28**)**



Yellow oil, 5 % yield. The yield of **28** was increased to 23 % by increasing the reaction temperature to 130 °C and using a nucleoside derivative concentration of 8 mM. ¹H NMR (400 MHz, Methanol-*d*₄) δ 7.68 (s, 1H, H-6), 7.44 (s, 1H, indoyl-H-7), 7.14 (d, *J* = 3.2 Hz, 1H, indoyl-H-2), 6.87 (d, *J* = 1.5 Hz, 1H, indoyl-H-5), 6.22 (d, *J* = 3.2 Hz, 1H, indoyl-H-3), 6.03 (d, *J* = 3.6 Hz, 1H, H-1'), 5.19 (d, *J* = 2.0 Hz, 1H, C=CH₂), 4.92 (d, *J* = 2.0 Hz, 1H, C=CH₂), 4.80 – 4.66 (m, 4H, H-3' and H-2'), 4.20 (m, 1H, H-4'), 3.70 (d, *J* = 11.3 Hz, 1H, H-5'), 3.53 (m, 1H, alkenyl-H-1), 3.45 – 3.35 (m, 2H, H-5' and alkenyl-H-1), 2.54 (m, 2H, alkenyl-H), 1.54 (m, 4H, alkenyl-H), 1.48 (s, 3H, H-Me), 1.25 (s, 3H, H-Me). ¹³C NMR (101 MHz, Methanol-*d*₄) δ 162.81 (C-4), 150.66 (C-2), 149.40 (indoyl-C-6), 138.60 (C-6), 136.81 (indoyl-C-9), 133.39 (C=CH₂), 126.50 (indoyl-C-8), 124.92 (indoyl-C-2), 124.54 (indoyl-C-4), 118.41 (indoyl-C-5), 116.66 (C-5), 113.95 (C(CH₃)₂), 109.28 (indoyl-C-7), 109.06 (C=CH₂), 101.75 (indoyl-C-3), 89.82 (C-1'), 84.74 (C-2'), 84.39 (C-4'), 79.66 (C-3'), 70.67 (alkenyl-C-1), 69.70 (C-5'), 35.69 (alkenyl-C), 29.16 (alkenyl-C), 26.33 (C-Me), 25.19 (alkenyl-C), 24.30 (C-Me). LC-MS (*m/z*) [*M* + H⁺]: calculated 480.3; found 480.2.

Method A of deprotection (Hydrolysis) of 2'3'-*O*-isopropylideneuridine derivatives with 1N HCl in MeOH¹⁵¹

To a solution of starting material (0.1 mmol) in MeOH (0.1 mL) was added 1N HCl (1 mL). The mixture was stirred at 65 °C until TLC showed full conversion. After completion, the solvent was extracted with EtOAc (5×). The organic layer was combined and dried over anhydrous Na₂SO₄. The solvent was removed under vacuo and the crude product was purified via flash column chromatography.

Method B of deprotection (Hydrolysis) of 2'3'-*O*-isopropylideneuridine derivatives with *p*-TsOH in 1:1 THF/ H₂O¹⁵²

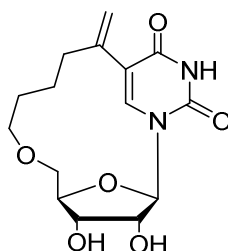
The SM (1 equiv.) was dissolved in 1:1 THF/H₂O and stirred at rt for 5 mins. *p*-TsOH (2 or 4 equiv.) was then added to the reaction. The mixture was stirred at 80 °C until TLC showed full conversion. After completion, the solvent was extracted with EtOAc (5×). The organic layer was combined and dried over anhydrous Na₂SO₄. The solvent was removed under vacuo and the crude product was purified via flash column chromatography.

Method C of deprotection (Hydrolysis) of 2'3'-*O*-isopropylideneuridine derivatives with 10 % TFA in H₂O⁹⁴

To a solution of starting material (1 mmol) was added 10 % TFA in 6 mL H₂O. The mixture was stirred at 70 °C until TLC showed full conversion. After completion, the solvent was extracted with EtOAc (5×). The organic layer was combined and dried over anhydrous Na₂SO₄.

The solvent was removed under vacuo and the crude product was purified via flash column chromatography.

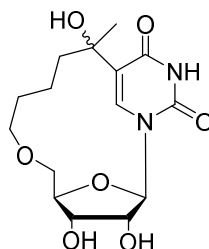
(2*R*,3*R*,4*S*,5*R*)-3,4-dihydroxy-12-methylidene-7,18-dioxa-1,15diazatricyclo[11.3.1.1^{2,5}]octadec-13(17)-ene-14,16-dione (29)



The reaction was complete in 5 h with 0.13 mmol SM using deprotection Method B. The crude product was purified by column chromatography on silica gel eluting with DCM-MeOH (100:4) to afford pure **29** as a white solid (90 % yield). ¹H NMR (400 MHz, Methanol-*d*₄) δ 8.38 (s, 1H, H-6), 6.34 (d, *J* = 2.5 Hz, 1H, C=CH₂), 5.96 (d, *J* = 4.3 Hz, 1H, H-1'), 5.18 (d, *J* = 2.5 Hz, 1H, C=CH₂), 4.24 (d, *J* = 4.5 Hz, 1H, H-3'), 4.17 (m, 2H, H-2' and H-4'), 3.75 (s, 2H, H-5'), 3.66 (m, 2H, alkenyl-H-1), 2.51 (t, *J* = 13.0 Hz, 1H, alkenyl-H-4), 2.18 (dd, *J* = 13.0, 6.0 Hz, 1H, alkenyl-H-4), 1.96 – 1.74 (m, 2H, alkenyl-H-2 and 3), 1.67 – 1.50 (m, 2H, alkenyl-H-3 and 2). ¹³C NMR (101 MHz, Methanol-*d*₄) δ 164.73 (C-4), 151.54 (C-2), 140.48 (C=CH₂), 139.22 (C-6), 116.22 (C=CH₂), 111.94 (C-5), 90.66 (C-1'), 85.67 (C-2'), 77.54 (C-4'), 71.66 (C-3'), 70.99 (C-5'), 69.05 (alkenyl-C-1), 34.20 (alkenyl-C-4), 27.84 (alkenyl-C-2), 25.88 (alkenyl-C-3). LC-MS (*m/z*) [M + H⁺]: calculated 325.3; found 325.1. HPLC: 98 % purity at 254 nm and 290 nm; *t*_R = 6.4 min; flow rate: 1 mL/min; solvent elution: 60 % MeOH in water.

(2*R*,5*R*,12*R*)-3,4,12-trihydroxy-12-methyl-7,18-dioxa-1,15-diazatricyclo[11.3.1.1^{2,5}]octadec-13(17)-ene-14,16-dione (30a)

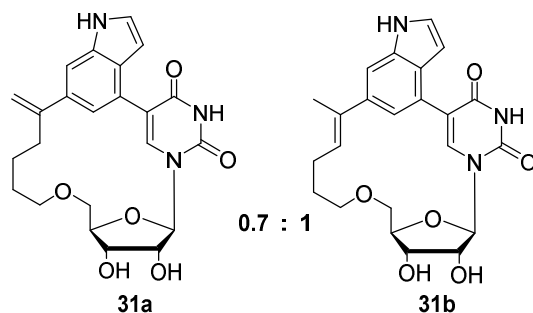
(2*R*,5*R*,12*S*)-3,4,12-trihydroxy-12-methyl-7,18-dioxa-1,15-diazatricyclo[11.3.1.1^{2,5}]octadec-13(17)-ene-14,16-dione (30b)



The reaction was complete in 7 h with 1.1 mmol SM and 54 mM concentration of starting material via Method B of deprotection. The crude product was purified by column chromatography on silica gel eluting with DCM-MeOH (100:5) to afford a mixture of two diastereomers of **30** with total yield of 30 % (the ratio of two isomers was 0.2:1). Main isomer: ¹H NMR (400 MHz, Methanol-*d*₄) δ 8.16 (s, 1H, H-6), 5.83 (d, *J* = 3.6 Hz, 1H, H-1'), 4.26 – 4.15 (m, 3H, H-2', 3' and 4'), 3.80 – 3.73 (m, 2H, H-5'), 3.67 (m, 1H, alkenyl-H-1), 3.60 (m, 1H, alkenyl-H-1), 1.96 (m, 2H, alkenyl-H-3), 1.67 – 1.54 (m, 4H, alkenyl-H-2 and 3), 1.49 (s, 3H, alkenyl-CH₃). ¹³C NMR (101 MHz, Methanol-*d*₄) δ 166.77 (C-4), 151.76 (C-2), 137.78 (C-6), 116.53 (C-5), 91.26 (C-1'), 85.54 (C-2'), 77.59 (C-4'), 74.08 (alkenyl-C-5), 71.11 (C-3'), 70.45 (C-5'), 68.45 (alkenyl-C-1), 36.08(alkenyl-C-4), 30.99 (alkenyl-C-Me), 27.61 (alkenyl-C-2), 19.35 (alkenyl-C-3). LC-MS (*m/z*) [*M* + Na⁺]: calculated 365.1; found 365.1. HPLC: the ratio of two isomers is 12 % to 80 % at 230 nm and 254 nm; *t*_R = 3.9 min and 6.1 min; flow rate: 1 mL/min; solvent elution: 50 % MeOH in water; 8 % is compound **29**, *t*_R = 14.6 min.

(7*R*,8*R*,9*S*,10*R*)-8,9-dihydroxy-17-methylidene-12,26-dioxa-4,6,21-triazapentacyclo
[16.6.1.1^{2,6}.1^{7,10}.0^{20,24}]heptacos-1(24),2(27),18(25),19,22-pentaene-3,5-dione (31a)

(7*R*,8*R*,9*S*,10*R*,16*Z*)-8,9-dihydroxy-17-methyl-12,26-dioxa-4,6,21-triazapentacyclo
[16.6.1.1^{2,6}.1^{7,10}.0^{20,24}]heptacos-1(24),2(27),16,18(25),19,22-hexaene-3,5-dione (31b)

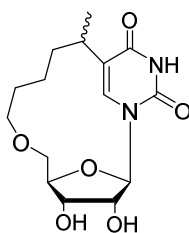


The reaction was complete in 10 h with 0.11 mmol SM and 4 equiv. *p*-TsOH using deprotection Method B. The crude was purified by column chromatography on silica gel eluting with DCM-MeOH (100:3) to afford a mixture of three main isomers of **31** as a light-yellow oil (50 % yield). The mixture was almost separated by HPLC in MeOH/H₂O. **31ab** was used as a mixture of 0.7:1 (**a:b**). **31c** was fully separated. ¹H NMR (400 MHz, Methanol-*d*₄) δ 8.02 (s, 1H, H-6, isomer 2), 7.83 (s, 0.7H, H-6, isomer 1), 7.54 (s, 0.7H, indoyl-H-7, isomer 1), 7.25 (s, 1H, indoyl-H-7, isomer 1), 7.24 (d, *J* = 3.4 Hz, 0.7H, indoyl-H-2, isomer 2), 7.22 (d, *J* = 3.1 Hz, 1H, indoyl-H-2, isomer 2), 6.95 (s, 0.7H, indoyl-H-5, isomer 1), 6.83 (s, 1H, indoyl-H-5, isomer 2), 6.31 (d, *J* = 3.4 Hz, 0.7H, indoyl-H-3, isomer 1), 6.09 (d, *J* = 3.1 Hz, 1H, indoyl-H-3, isomer 2), 6.07 (d, *J* = 5.1 Hz, 0.7H, H-1', isomer 1), 5.52 (t, *J* = 4.9 Hz, 1H, CH₃C=CHCH₂ isomer 2), 5.29 (d, *J* = 2.1 Hz, 0.7H, C=CH₂, isomer 1), 5.03 (s, *J* = 2.1 Hz, 0.7H, C=CH₂, isomer 1), 4.31 – 4.18 (m, 1.4H for isomer 1, 2H for isomer 2, H-2' and H-3'), 4.09 (m, 0.7H for isomer 1, 1H for isomer 2, H-4'), 3.85 (d, *J* = 12.0 Hz, 1 H, H-5', isomer 2), 3.80 (d, *J* = 11.4 Hz, 0.7H, H-5', isomer 1), 3.69 – 3.65 (m, 1H, alkenyl-H-1, isomer 2) 3.62 – 3.60 (m, 0.7H, alkenyl-H-1, isomer 1), 3.46 (d, *J* = 11.4 Hz, 0.7H, H-5', isomer 1) 3.44 (d, *J* = 12.0 Hz, 1 H, H-5', isomer 2), 3.38 (m, 0.7H for isomer 1, 1H for isomer 2, alkenyl-H-1), 2.70 – 2.59

(m, 1.4H, alkenyl-H-4), isomer 1), 0.33 – 2.42 (m, 1H, alkenyl-H-3, isomer 2), 2.10 (s, 3H, CH₃=C, isomer 2), 1.96 (m, 1H, alkenyl-H-3, isomer 2), 1.77 – 1.60 (m, 1.4H for isomer 1, alkenyl-H-2 and 3; 2H for isomer 2, alkenyl-H-2 and 3), 1.35 (m, 1.4H for isomer 1, alkenyl-H-2 and 3; 2H for isomer 2, alkenyl-H-2 and 3). ¹³C NMR (101 MHz, Methanol-*d*₄) δ 164.04 (C-4, isomer 2), 163.34 (C-4, isomer 1), 156.09 (C-2, isomer 1), 155.18 (C-2, isomer 2), 153.56 (indoyl-C-6, isomer 1), 152.87 (indoyl-C-6, isomer 2), 140.08 (C-6 for isomer 1), 139.99 (C-6 for isomer 2), 138.91 (alkenyl-C-5, isomer 2), 138.24 (indoyl-C-9, isomer 1), 138.12 (indoyl-C-9, isomer 2), 136.56 (indoyl-C-8, isomer 1), 136.54 (indoyl-C-8, isomer 2), 127.18 (CH₃Cz=CHCH₂, isomer 2), 126.29 (indoyl-C-2, isomer 1) 125.72 (indoyl-H-2, isomer 2), 121.36 (indoyl-C-5, isomer 2), 119.98 (indoyl-C-5, isomer 1), 119.03 (C-5, isomer 1), 117.89 (C-5, isomer 2), 110.93 (indoyl-C-7, isomer 2), 110.56 (CH₂=CCH₂, isomer 1), 110.49 (indoyl-C-7, isomer 1), 103.03 (indoyl-C-5 for isomer 1 and 2), 89.68 (indoyl-C-3, isomer 2), 88.97 (indoyl-C-3, isomer 1), 85.95 (C-4', isomer 1), 85.89 (C-4', isomer 2), 76.70 (C-2', isomer 2), 76.32 (C-2', isomer 1), 74.05 (alkenyl-C-1, isomer 2), 72.88 (alkenyl-C-1, isomer 1), 72.00 (C-3', isomer 1), 71.81 (C-3', isomer 2), 71.25 (C-5', isomer 1), 71.03 (C-5', isomer 2), 37.60 (alkenyl-C-4, isomer 1), 31.65 (alkenyl-C-2, isomer 2), 30.90 (alkenyl-C-2, isomer 1), 28.65 (alkenyl-C-3, isomer 2), 26.94 (alkenyl-C-3, isomer 1), 25.95 (C-Me, isomer 2). LC-MS (m/z) [M + H⁺]: calculated 440.3; found 440.2. Analytic HPLC: the ratio of three main peaks is 21 %:60 %:14 % at 230 nm and 254 nm; *t*_R = 21.1 min (unknown cmpds), 22.8 min (**31a** & **31b**) and 23.8 min (**31c**); flow rate: 1 mL/min; solvent gradient elution: 40 – 67 % MeOH in water in 23 min. Preparative HPLC for separation of **31**: *t*_R = 27 min (**31a**), 95 min (**31b**) and 98 min (**31c**) at 230 nm and 254 nm; flow rate: 10 mL/min; solvent gradient elution: 10 – 20 % MeCN in 0.1 % TFA of water for 10 min, then 20 % MeCN in 0.1 % TFA of water for 100 min.

Hydrogenation. To a 50 mL round bottom flask, the substrate (0.114 mmol) and the catalyst (Pt₂O or Pd/C) were added to 7 mL MeOH. The flask was the evacuated and backfilled with hydrogen for 3 times. The mixture was stirred under hydrogen at rt for 1 h. After completion, the catalyst was filtered off with celite and washed with EtOAc. The filtrate was combined, and the solvent was removed in vacuo. The crude product was purified via flash column chromatography on silica gel eluting with DCM-MeOH (100:4) to afford **32** (white solid) with a mixture of two isomers in different ratios depending on the catalyst choice. The combined yield of two diastereomers is 85 % when using Pt₂O.

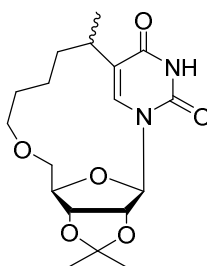
(2*R*,5*R*)-3,4-dihydroxy-12-methyl-7,18-dioxa-1,15-diazatricyclo[11.3.1.1^{2,5}]octadec-13(17)-ene-14,16-dione (32)



isomer1/isomer2=0.5:1. ¹H NMR (400 MHz, Methanol-*d*₄) δ 9.59 (s, 0.5H, H-6, isomer1), 9.56 (s, 1H, H-6, isomer2), 7.63 (d, *J* = 3.8 Hz 0.5H, H-1', isomer1), 7.34 (d, *J* = 3.1 Hz, 1H, isomer2), 5.83 – 5.68 (m, 1.5H for isomer1, 3H for isomer2, H2', 3' and 4'), 5.35 – 5.12 (m, 2H for isomer1, 4H for isomer2, H-5' and alkenyl-H-1), 4.27 (m, 0.5H, alkenyl-H-5, isomer1), 4.18 (m, 1H, alkenyl-H-5, isomer2), 3.48 (s, 1H, alkenyl-H-2, isomer2), 3.22 – 2.90 (m, 3H for isomer1, alkenyl-H-2,3,4; 5H for isomer2, alkenyl-H-2,3,4), 2.73 (d, *J* = 6.8 Hz, 1.5H for isomer1), 2.66 (d, *J* = 6.7, 3H, alkenyl-CH₃ for isomer2). ¹³C NMR of the main (101 MHz, Methanol-*d*₄) δ 165.15, 150.65, 135.42, 116.28, 90.16, 83.98, 76.16, 69.36, 69.00, 67.05, 30.71, 29.06, 26.62, 21.39, 21.00. LC-MS (*m/z*) [*M* + H⁺]: calculated 327.3; found 327.2. HPLC: the

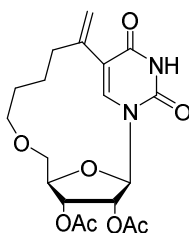
ratio of two isomers is 29 %: 66 % at 254 nm and 290 nm; t_R = 9.6 min and 13.6 min; flow rate: 1 mL/min; solvent elution: 50 % MeOH in water.

(3a*R*,4*R*,17*R*,17a*R*,*Z*)-2,2,10-trimethyl-3a,11,12,13,14,16,17,17a-octahydro-4*H*,6*H*,10*H*-4,17-epoxy-5,9-(metheno)[1,3]dioxolo[4,5-*d*][1]oxa[7,9]diazacyclohexadecine-6,8(7*H*)-dione (33)

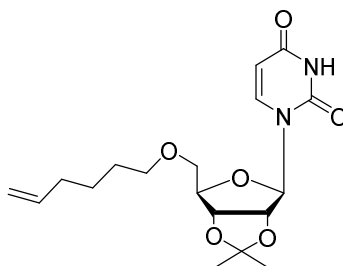


The hydrogenation reaction was complete in 16 h with 0.1 mmol SM and 10 mol% PtO₂. The crude product was not further purified but characterized by NMR and HPLC. isomer1/isomer2 = 0.3: 1 (both NMR and HPLC). ¹H NMR (400 MHz, Methanol-*d*₄) δ 7.91 (s, 0.3H, H-6, isomer1), 7.84 (s, 1H, H-6, isomer2), 6.18 (d, *J* = 3.5 Hz, 1H, H-1', isomer2), 6.04 (d, *J* = 2.6 Hz, 1H, H-1', isomer1), 4.96 (m, 1H, H-3', isomer2), 4.75 (m, 1H, H-2', isomer2), 4.59 (m, 0.3H, H-2', isomer1), 4.42 (m, 0.3H, H-4', isomer1), 4.36 (m, 1H, H-4', isomer2), 3.86 – 3.48 (m, 2.2H for isomer1; 4H for isomer2, alkenyl-H-1 and H-5'), 2.64 (m, 0.3H for isomer1; 1H for isomer2, alkenyl-H-5), 1.92 (m, 0.3H, alkenyl-H-2, isomer1), 1.79 (m, 1H, alkenyl-H-2, isomer2), 1.61-1.30 (m, 1.5H for alkenyl-H 2,3,4 and 0.9H for C(CH₃)₂, isomer1; 5H for alkenyl-H2,3,4 and 3H for C(CH₃)₂, isomer2), 1.12 (d, *J* = 6.8 Hz, 3H, alkenyl-CH₃, isomer2), 1.08 (d, *J* = 6.6 Hz, 1H, alkenyl-CH₃, isomer1). (H-3' for isomer1 was buried in water peak). LC-MS (*m/z*) [*M* + H⁺]: calculated 367.3; found 367.2.

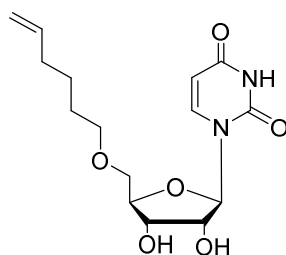
**(2R,5R)-4-(acetyloxy)-12-methylidene-14,16-dioxo-7,18-dioxa-1,15-diazatricyclo
[11.3.1.1^{2,5}]octadec-13(17)-en-3-yl acetate (34)**



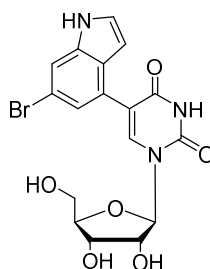
To a solution of **29** (20 mg, 0.06 mmol, 1 equiv.) and DMAP (3.8 mg, 0.031 mmol, 0.05 equiv.) in pyridine (0.5 mL) was added acetic anhydride (15 μ L, 2.5 equiv.). The reaction was stirred at rt until TLC (hexane/EA = 3: 1) indicated complete conversion. The reaction was quenched with several drops water. The solvent was removed by evaporation and the residue was co-evaporated with toluene (3 \times). The crude product was purified by flash silica chromatography (hexane/EA, gradient: 10: 1 to 3: 1) to yield target compound **34** (20 mg, 85 %). ¹H NMR (400 MHz, Chloroform-*d*) δ 8.28 (s, 1H, H-6), 6.42 (d, J = 2.1 Hz, 1H, CH=CH₂), 6.34 (d, J = 7.0 Hz, 1H, H-1'), 5.49 (d, J = 5.2 Hz, 1H, H-3'), 5.36 (dd, J = 7.0, 5.2 Hz, 1H, H-2'), 5.25 (d, J = 2.1 Hz, 1H, CH=CH₂), 4.33 (m, 1H, H-4'), 3.78 – 3.62 (m, 4H, 2H for alkenyl-H-1 and 2H for H-5'), 2.44 (t, J = 13.0 Hz, 1H, alkenyl-H), 2.15 (s, 3H, H-OAc), 2.06 (s, 3H, H-OAc), 1.95 (m, 1H, alkenyl-H), 1.81 – 1.71 (m, 1H, alkenyl-H), 1.63 (m, 3H, alkenyl-H). ¹³C NMR (101 MHz, CDCl₃) δ 170.12 (COCH₃), 169.80 (COCH₃), 162.07 (C-4), 149.75 (C-2), 137.97 (C=CH₂), 137.10 (C-6), 117.11(C=CH₂), 112.05 (C-5), 86.07 (C-1'), 83.29 (C-3'), 74.53 (C-2'), 72.71 (C-3'), 70.86 (C-5'), 68.49 (alkenyl-C-1), 32.87 (alkenyl-C-4), 26.50 (alkenyl-C-2), 24.14, 20.89 (alkenyl-C-3), 20.57 (COCH₃). LC-MS (m/z) [$M + H^+$]: calculated 409.2; found 409.3.

**1-((3a*R*,4*R*,6*R*,6a*R*)-6-((hex-5-en-1-yloxy)methyl)-2,2-dimethyltetrahydrofuro[3,4-
d][1,3]dioxol-4-yl)pyrimidine-2,4(1*H*,3*H*)-dione (35)**

In a 250 ml dry round bottom flask, NaH (60 %, 180 mg, 19.4 mmol) was added to 50 mL dry DMF and was stirred until dissolved, followed by addition of 2', 3'-*O*-isopropylidenuridine (500 mg, 7.76 mmol). The solution was activated by sonicating for 30 min at rt. 6-bromo-1-hexene (300 μ L, 9.3 mmol) was added and the reaction mixture was reacted for another 3 h in an ice bath. A few drops of water were added to quench the reaction. The solution was filtered with celite and washed with EtOAc. The filtrate was combined, and the solvent removed in vacuo. The crude product was purified via column chromatography on silica gel eluting with *n*-hexane-EtOAc (50:50) to afford pure **35** (256 mg, 40 % yield) as a white solid. ^1H NMR (400 MHz, Methanol- d_4) δ 7.80 (d, J = 8.1 Hz, 1H, H-6), 5.85 (d, J = 2.2 Hz, 1H, H-1'), 5.79 (tt, J = 13.6, 5.1 Hz, 1H, alkenyl-CH=CH₂), 5.66 (d, J = 8.1 Hz, 1H, H-5), 4.96 (m, 2H, alkenyl-CH=CH₂), 4.81 (m, 2H, H-2' and 3'), 4.38 (m, H-4', 1H), 3.70 (dd, J = 10.8, 2.9 Hz, 1H, H-5'), 3.59 (dd, J = 10.8, 3.9 Hz, 1H, H-5'), 3.48 (t, J = 6.5, 2H, alkenyl-H-1), 2.06 (q, J = 7.2 Hz, 2H, alkenyl-H-4), 1.62 – 1.50 (m, 2H for alkenyl-H-2 and 3H for C(CH₃)₂), 1.43 (p, J = 7.5 Hz, 2H, alkenyl-H-3), 1.34 (s, 3H, C(CH₃)₂). ^{13}C NMR (101 MHz, Methanol- d_4) δ 164.86 (C-2), 150.67 (C-4), 141.88 (C-6), 138.33 (alkenyl-CH=CH₂), 113.83 (alkenyl-CH=CH₂), 113.36 (C(CH₃)₂), 100.75 (C-5), 93.22 (C-1'), 85.94 (C-4'), 85.19 (C-2'), 81.33 (C-3'), 70.99 (alkenyl-C-1), 70.48 (C-5'), 33.20 (alkenyl-C-4), 28.73 (alkenyl-C-2), 26.15 (C(CH₃)₂), 25.25 (alkenyl-C-3), 24.12 (C(CH₃)₂). LC-MS (m/z) [M + H⁺]: calculated 367.3; found 367.2.

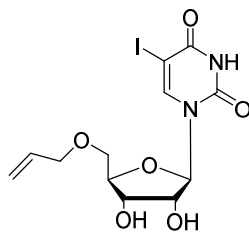
1-((2*R*,3*R*,4*S*,5*R*)-5-((hex-5-en-1-yloxy)methyl)-3,4-dihydroxytetrahydrofuran-2-yl)pyrimidine-2,4(1*H*,3*H*)-dione (36)

The reaction was complete in 1 h with 0.42 mmol SM using deprotection Method A. The crude product was purified by column chromatography on silica gel eluting with DCM-MeOH (100:5) to afford pure **36** as a white solid (61 % yield). ¹H NMR (400 MHz, Methanol-*d*₄) δ 8.01 (d, *J* = 8.1 Hz, 1H, H-6), 5.87 (d, *J* = 3.5 Hz, 1H, H-1'), 5.84 – 5.70 (m, 1H, CH=CH₂), 5.62 (d, *J* = 8.1 Hz, 1H, H-5), 5.02 – 4.88 (m, 2H, CH=CH₂), 4.12 (t, *J* = 3.0 Hz, 2H, H-3', H-2'), 4.06 (dt, *J* = 4.8, 2.5 Hz, 1H, H-4'), 3.73 (dd, *J* = 11.0, 2.5 Hz, 1H, H-5'), 3.57 (dd, *J* = 11.0, 2.5 Hz, 1H, H-5'), 3.50 (td, *J* = 6.4, 4.0 Hz, 2H, alkenyl-H-1), 2.11 – 2.02 (m, 2H, alkenyl-H-4), 1.66 – 1.53 (m, 2H, alkenyl-H-2), 1.53 – 1.39 (m, 2H, alkenyl-H-3). ¹³C NMR (101 MHz, Methanol-*d*₄) δ 172.33, 156.88, 141.39, 139.72, 115.21, 102.83, 90.80, 84.84, 76.27, 72.43, 71.50, 70.96, 34.62, 30.29, 26.78. LC-MS (m/z) [M + H⁺]: calculated 327.2; found 327.3. HPLC: > 98 % purity at 254 nm and 290 nm; *t*_R = 17.3 min; flow rate: 1 mL/min; solvent elution: 50 % MeOH in water.

5-(6-bromo-1*H*-indol-4-yl)-1-((2*R*,3*R*,4*S*,5*R*)-3,4-dihydroxy-5-(hydroxymethyl)tetrahydrofuran-2-yl)pyrimidine-2,4(1*H*,3*H*)-dione (37)

The reaction was complete in 8 h with 0.08 mmol SM using deprotection Method A. The crude product was purified by column chromatography on silica gel eluting with DCM-MeOH (100:13) to afford pure **37** as a yellow oil (50 % yield). Yellow solid can be obtained when washed with Et₂O. ¹H NMR (400 MHz, Methanol-*d*₄) δ 8.22 (s, 1H, H-6), 7.52 – 7.45 (m, 1H, indole-H-7), 7.22 (d, *J* = 3.2 Hz, 1H, indole-H-3), 7.20 (d, *J* = 1.6 Hz, 1H, indole-H-5), 6.38 (d, *J* = 3.1 Hz, 1H, indole-H-2), 6.00 (d, *J* = 5.1 Hz, 1H, H-1'), 4.27 (dd, *J* = 5.1, 4.8 Hz, 1H, H-2'), 4.13 (dd, *J* = 4.8 Hz, 4.8 Hz, 1H, H-3'), 3.99 (dt, *J* = 4.8 Hz, 3.0 Hz, 1H, H-4'), 3.73 (dd, *J* = 12.1, 3.0 Hz, 1H, H-5'), 3.67 (dd, *J* = 12.1, 3.0 Hz, 2H, H-5'). ¹³C NMR (101 MHz, Methanol-*d*₄) δ 164.53 (C-4), 152.25 (C-2), 141.16 (C-6), 138.56 (indole-C-9), 127.51 (indole-C-6), 127.22 (indole-C-4), 126.81 (indole-C-2), 124.19 (indole-C-5), 115.13 (C-5), 114.94 (indole-C-8), 114.83 (indole-C-7), 102.08 (indole-C-3), 90.60 (C-1'), 86.51 (C-4'), 75.86 (C-2'), 71.68 (C-3'), 62.32 (C-5'). LC-MS (m/z) [M + H⁺]: calculated 438.0; found 438.2, 440.2.

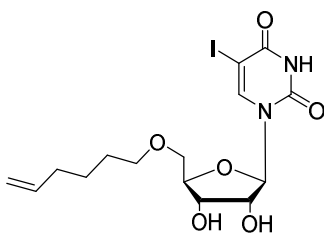
1-((2*R*,3*R*,4*S*,5*R*)-5-((allyloxy)methyl)-3,4-dihydroxytetrahydrofuran-2-yl)-5-iodo pyrimidine -2,4(1*H*,3*H*)-dione (38**)**



The reaction was complete in 6 h with 0.1 mmol SM using deprotection Method A. The crude product was purified by column chromatography on silica gel eluting with DCM-MeOH (100:4.5) to afford pure **38** as a white solid (46 % yield). ¹H NMR (400 MHz, Methanol-*d*₄) δ 8.49 (s, 1H, H-6), 6.05 (ddt, *J* = 17.0, 11.0, 5.8 Hz, 1H, alkenyl-CH=CH₂), 5.89 (d, *J* = 4.2 Hz, 1H, H-1'), 5.42 – 5.29 (d, *J* = 17.0 Hz, 1H), 5.26 (d, *J* = 11.0 Hz, 1H), 4.17 (m, 3H for H-2', 3' and 4'; 2H for alkenyl-H-1), 3.81 (dd, *J* = 11.0, 2.1 Hz, 1H, H-5'), 3.65 (dd, *J* = 11.0, 2.1 Hz,

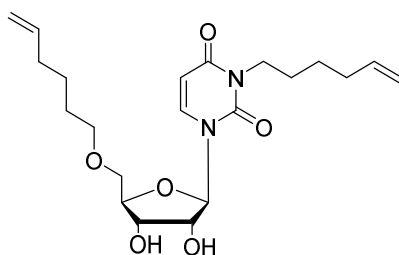
1H, H-5'). ¹³C NMR (101 MHz, Methanol-*d*₄) δ 162.76 (C-2), 152.14 (C-4), 146.83 (C-6), 135.73 (alkenyl-CH=CH₂), 118.33 (alkenyl-CH=CH₂), 90.68 (C-1'), 85.14 (C-4'), 76.34 (C-2'), 73.50 (C-3'), 71.41 (alkenyl-C-1), 69.78 (C-5'), 68.44 (C-5). HPLC: > 99 % purity at 254 nm and 290 nm; *t*_R = 17.3 min; solvent elution: 50 % MeOH in water.

1-((2*R*,3*R*,4*S*,5*R*)-5-((hex-5-en-1-yloxy)methyl)-3,4-dihydroxytetrahydrofuran-2-yl)-5-iodopyrimidine-2,4(1*H*,3*H*)-dione (39)



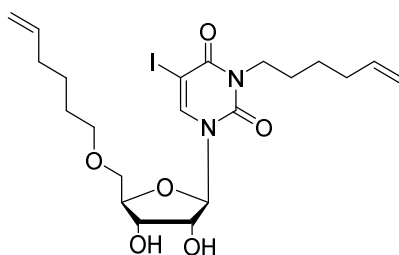
The reaction was complete in 6 h when using 0.26 mmol SM using deprotection Method A. The crude product was purified by column chromatography on silica gel eluting with n-hexane-EtOAc (30:70) to afford pure **39** as a transparent oil (39 % yield). ¹H NMR (400 MHz, Methanol-*d*₄) δ 8.42 (s, 1H, H-6), 5.91 (d, *J* = 3.9 Hz, 1H, H-1'), 5.89 – 5.74 (m, 1H, alkenyl-CH=CH₂), 5.06 – 4.93 (m, 2H, alkenyl-CH=CH₂), 4.21 – 4.08 (m, 3H, H-2', 3' and 4'), 3.79 (dt, *J* = 10.8, 2.2 Hz, 1H, H-5'), 3.67 (dt, *J* = 9.5, 6.9 Hz, 1H, alkenyl-H-1) (3.60 (dt, *J* = 11.1, 2.9 Hz, 1H, H-5'), 3.52 (dt, *J* = 9.5, 6.9 Hz, 1H, alkenyl-H-1), 2.12 (q, *J* = 7.3 Hz, 2H, alkenyl-H-4), 1.79 (m, 2H, alkenyl-H-2), 1.52 (m, 2H, alkenyl-H-3). ¹³C NMR (101 MHz, Methanol-*d*₄) δ 161.35 (C-2), 150.78 (C-4), 145.25 (C-6), 138.44 (CH=CH₂), 113.79 (CH=CH₂), 89.12 (C-1'), 84.05 (C-4'), 75.06 (C-2'), 71.31 (C-3'), 70.36 (alkenyl-C-1), 69.30 (C-5), 67.35 (C-5), 33.29 (alkenyl-C-4), 29.00 (alkenyl-C-2), 25.37 (alkenyl-C-3). LC-MS (*m/z*) [M + H⁺]: calculated 453.1; found 453.2. HPLC: > 99 % purity at 254 nm and 285 nm; *t*_R = 8.5 min; flow rate: 0.5 mL/min; solvent elution: 50 % MeOH in water.

3-(hex-5-en-1-yl)-1-((2*R*,3*R*,4*S*,5*R*)-5-((hex-5-en-1-yloxy)methyl)-3,4-dihydroxytetrahydrofuran-2-yl)pyrimidine-2,4(1*H*,3*H*)-dione (40)

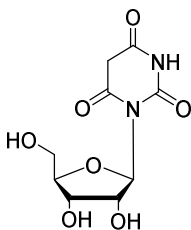


The reaction was complete in 20 h with 0.1 mmol SM and 4 equiv. *p*-TsOH via Method B of deprotection. The crude product was purified via column chromatography on silica gel eluting with n-hexane-EtOAc (40:60) to afford pure **40** as a transparent oil (30 % yield). ¹H NMR (400 MHz, Methanol-*d*₄) δ 8.06 (d, *J* = 8.1 Hz, 1H, H-6), 5.92 (d, *J* = 3.7 Hz, 1H, H-1'), 5.88 – 5.74 (m, 2H, alkenyl-CH=CH₂), 5.71 (d, *J* = 8.1 Hz, 1H, H-5), 5.09 – 4.92 (m, 4H, alkenyl-CH=CH₂), 4.13 (m, 3H, H-2', 3' and 4'), 3.91 (t, *J* = 7.5 Hz, 2H, alkenyl-NCH₂), 3.79 (dd, *J* = 11.0, 2.5 Hz, 1H, H-5'), 3.62 (dd, *J* = 11.0, 2.5 Hz, 1H, H-5'), 3.54 (td, *J* = 6.3, 4.1 Hz, 2H, alkenyl-OCH₂), 2.09 (dt, *J* = 11.4, 5.5 Hz, 4H, alkenyl-H-4), 1.67 – 1.57 (m, 4H, alkenyl-H-2), 1.54 – 1.45 (m, 2H, alkenyl-H-3), 1.45 – 1.38 (m, 2H, alkenyl-H-3). ¹³C NMR (101 MHz, Methanol-*d*₄) δ 164.97 (C-2), 152.38 (C-4), 140.48 (C-6), 139.72 (alkenyl-CH=CH₂), 139.58 (alkenyl-CH=CH₂), 115.25 (alkenyl-CH=CH₂), 115.21 (alkenyl-CH=CH₂), 101.73 (C-5), 91.52 (C-1'), 84.88 (C-4'), 76.20 (C-2'), 72.42 (C-3'), 71.24 (alkenyl-OCH₂), 70.66 (C-5'), 41.92 (*N*-alkenyl-C-1), 34.64 (alkenyl-C-4), 34.47 (alkenyl-C-4), 30.31 (*O*-alkenyl-C-2), 27.98 (*N*-alkenyl-C-2), 27.31 (*O*-alkenyl-C-3), 26.79 (*N*-alkenyl-C-3). LC-MS (*m/z*) [*M* + H⁺]: calculated 409.2; found 409.5. HPLC: > 98 % purity at 254 nm and 265 nm; *t*_R = 17.4 min; flow rate: 1 mL/min; solvent gradient elution: 50 – 80 % MeOH in water in 10 min.

3-(hex-5-en-1-yl)-1-((2*R*,3*R*,4*S*,5*R*)-5-((hex-5-en-1-yloxy)methyl)-3,4-dihydroxytetrahydrofuran-2-yl)-5-iodopyrimidine-2,4(1*H*,3*H*)-dione (41)



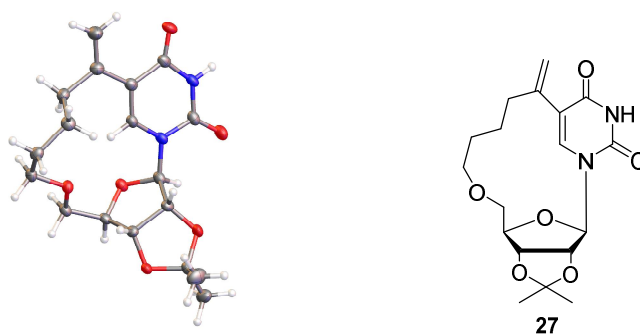
The reaction was complete in 20 h with 0.18 mmol SM and 4 equiv. *p*-TsOH using deprotection Method B. The crude product was purified via column chromatography on silica gel eluting with n-hexane-EtOAc (30:70) to afford pure **41** as a transparent oil (42 % yield). ¹H NMR (400 MHz, Methanol-*d*₄) δ 8.45 (s, 1H, H-6), 5.91 (d, *J* = 3.9 Hz, 1H, H-1'), 5.81 (ddd, *J* = 17.1, 10.2, 6.9 Hz, 2H, alkenyl-CH=CH₂), 5.02 (d, *J* = 17.1 Hz, 2H, alkenyl-CH=CH₂), 4.92 (d, *J* = 10.2 Hz, 2H, alkenyl-CH=CH₂), 4.21 – 4.07 (m, 3H, H-2', 3' and 4'), 3.95 (t, *J* = 7.5 Hz, 2H, alkenyl-NCH₂), 3.81 (dd, *J* = 11.0, 2.2 Hz, 1H, H-5'), 3.72 – 3.63 (m, 1H, alkenyl-OCH₂), 3.61 (dd, *J* = 11.0, 2.0 Hz, 1H, H-5'), 3.58 – 3.47 (m, 1H, alkenyl-OCH₂), 2.10 (m, 4H, alkenyl-H-4), 1.78 (m, 2H, *O*-alkenyl-H-2), 1.66 – 1.57 (m, 2H, *N*-alkenyl-H-2), 1.51 (m, *O*-alkenyl-H-3), 1.42 (m, *N*-alkenyl-H-3). ¹³C NMR (101 MHz, Methanol-*d*₄) δ 161.64 (C-2), 152.03 (C-4), 144.93 (C-6), 139.80 (alkenyl-CH=CH₂), 139.52 (alkenyl-CH=CH₂), 115.25 (alkenyl-CH=CH₂), 115.16 (alkenyl-CH=CH₂), 91.54 (C-1'), 85.24 (C-4'), 76.50 (C-2'), 72.68 (C-3'), 71.33 (alkenyl-OCH₂), 70.37 (C-5'), 68.03 (C-5), 43.60 (*N*-alkenyl-C-1), 34.64 (alkenyl-C-4), 34.43 (alkenyl-C-4), 30.34 (*O*-alkenyl-C-2), 27.87 (*N*-alkenyl-C-2), 27.27 (*O*-alkenyl-C-3), 26.72 (*N*-alkenyl-C-3). LC-MS (*m/z*) [*M* + *H*⁺]: calculated 535.1; found 535.2. HPLC: > 98 % purity at 254 nm and 285 nm; *t*_R = 23.1 min; flow rate: 1 mL/min; solvent gradient elution: 50 – 80 % MeOH in water in 10 min.

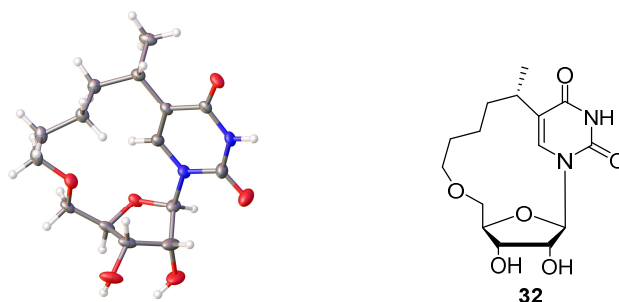
1-((2*R*,3*R*,4*S*,5*R*)-3,4-dihydroxy-5-(hydroxymethyl)tetrahydrofuran-2-yl)pyrimidine-2,4,6(1*H*,3*H*,5*H*)-trione (42)¹⁵⁶

The reaction was complete in 3 h with 0.14 mmol SM using deprotection Method C. The crude product was recrystallized from MeOH to afford **42** as a white solid (20 % yield). ¹H NMR (400 MHz, Methanol-*d*₄) δ 6.13 (d, *J* = 3.3 Hz, 1H, H-1'), 4.54 (dd, *J* = 6.2, 3.3 Hz, 1H, H-2'), 4.34 (dd, 1H, H-3'), 3.87 – 3.82 (m, 1H, H-4'), 3.79 (dd, *J* = 11.8, 6.1 Hz, 1H, H-5'), 3.64 (dd, *J* = 11.8, 6.1 Hz, 1H, H-5').

6.2 Crystallography

Crystals of **27** and **32** (Figure 60) were grown from MeOH at room temperature. The detailed crystallography data was shown in Table 21. Single-crystal X-ray diffraction data (XRD) were collected at a temperature of 100.0 K using a SuperNova instrument equipped with an EosS2 diffractometer, employing Cu-K α radiation ($\lambda = 1.54184 \text{ \AA}$). Using Olex2 software¹⁵⁷, the structure was resolved with ShelXT program¹⁵⁸ and refined with ShelXL program¹⁵⁹.



**Figure 60** Crystal structures of **27** and **32****Table 21** Crystallography data of compound **27** and **32**

Compound	27	32
Empirical formula	C18 H24 N2 O6	C15 H22 N2 O6
Formula weight (g/mol)	364.39	326.34
Temperature (K)	99.98(13)	99.97(16)
Wavelength (Å)	1.54184	1.54184
Completeness	99.76	99.94
Crystal system	hexagonal	hexagonal
Space group	P 64	P 61
Unit cell dimensions	a = 15.9231(3) Å b = 15.9231(3) Å c = 12.0737(2) Å $\alpha = 90^\circ \beta = 90^\circ \gamma = 120^\circ$	a = 24.22416(14) Å b = 24.22416(14) Å c = 5.07959(3) Å $\alpha = 90^\circ \beta = 90^\circ \gamma = 120^\circ$
Volume (Å³)	2651.10 (11)	2581.41(3)
Z	6	6
Theta max.	71.025	71.2800
Theta min.	4.85	4.1990
Density (Mg/m³)	1.369	1.260
Absorption coefficient (mm⁻¹)	0.861	0.821

F (000)	1164	1044
Absorption correction	multi-scan	multi-scan
Goodness-of-fit on F^2	1.046	1.099
R1 (for all data)	0.0424	0.0692

6.3 Malachite-Green inhibition assays

General. All reagents were obtained commercially and used as received, unless otherwise stated. Absorbance measurements were conducted using a BMG Labtech POLARstar Optima multiplate reader. The colorimetric glycosyltransferase assay was modified from Tedaldi *et al.*⁹⁸ All experiments were performed in Nunc clear, flat-bottom 96-well plates.

Assay protocol. Final concentrations are provided for all assay components. β -1,4-GalT (1 μ g/mL) or activated LgtC (1 μ g/mL, incubated with 5 mM DTT at 30 °C for 20 min); the final concentration of DTT is 2 μ M, CIP (10 U/mL), lysozyme (1 mg/mL), GlcNAc (10 mM), Triton X (0.01 %), MnCl₂ (5 mM), KCl (50 mM, not in the LgtC inhibition assay), HEPES (PH 7.5, 10 mM), DMSO (10 %), UDP-Gal donor (33 mM) and inhibitors series dilutions were added into 96-well plate in triplicate. The reaction started by the addition of UDP in the UDP-calibration wells (**Table 22**, column 1 – 3) and UDP-Gal in the GalT inhibition experiments (**Table 22**, column 4 – 9), followed by incubation at 30 °C for 20 mins (with 5 min shaking). The reaction was stopped by the addition of malachite reagents, and the absorbance was recorded at 620 nm for 1 hour (with 5 min shaking).

Table 22 Schematic table of Malachite-Green components in 96-well plate.

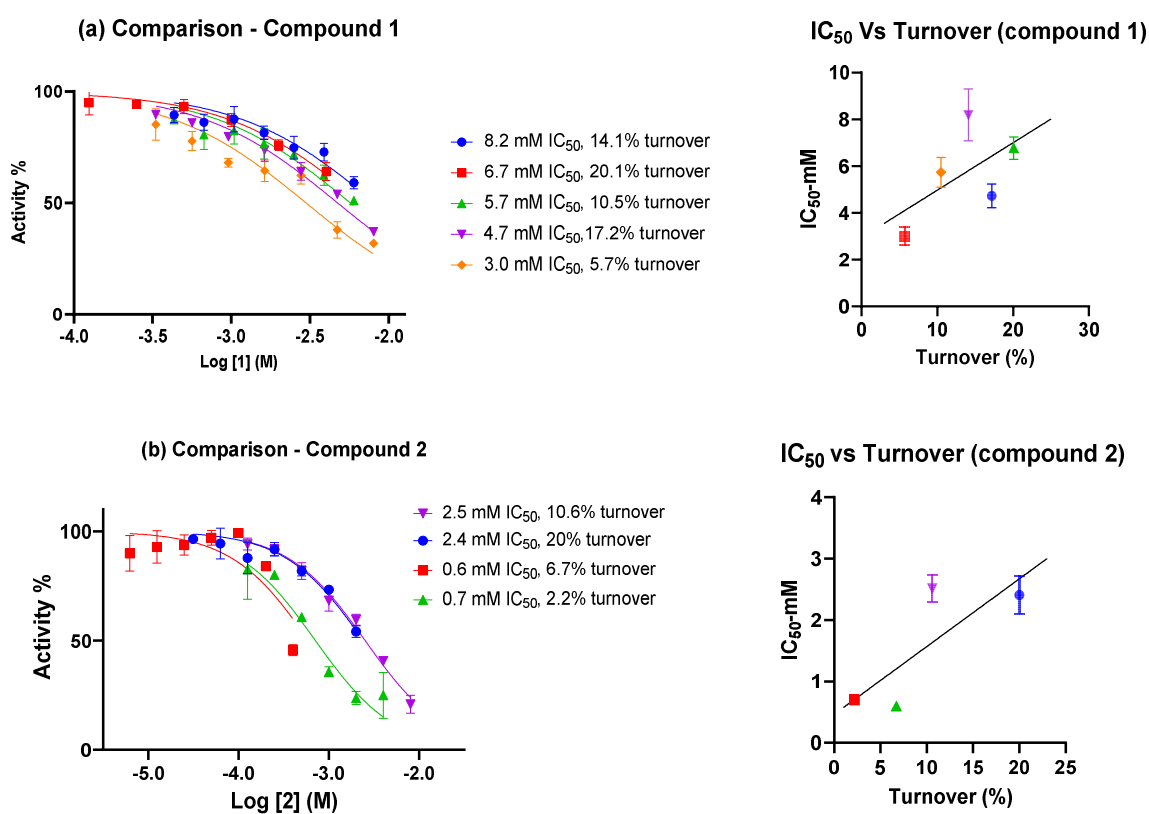
96-well plate	Column 1 – 3	Column 4 – 6	Column 7 – 9
Wells A-H	UDP-Calibration	Inhibitor test	Background-no GalT
	All components	All components	All components
Components	with UDP series dilution	with inhibitor series dilution	with inhibitor series dilution
	without UDP-Gal and GalT	without UDP	without UDP and GalT

Data analysis. Data was analysed using GraphPad Prism 9. The timepoint where the data was stable amongst UDP-Calibration, inhibitor, and background wells was chosen (usually at 30 min). The absorbance of inhibitor and background was transformed to [UDP] (μM) using linear regression from a calibration curve (around 0 – 7.18 μM). Corrected values were obtained by subtracting corresponding background reading from the inhibitor wells. The corrected value of the negative control (0 μM inhibitor, wells 4A – 6A) was normalized to 100 %, the values of inhibitor wells were normalized to corresponding percentage. This percentage was plotted against log [inhibitor] to afford relative IC_{50} values. To calculate the donor turnover: the donor concentration (33 μM in this assay) was divided by the corrected UDP concentration of the blank (assay window, wells 4A – 6A).

Relationship between IC_{50} and turnover

Due to the enzyme sensitivity, precise control over its concentration can be challenging. Consequently, the assay occasionally yielded turnover of the UDP-Gal donor below 10 %. However, an interesting observation emerged from these circumstances: a low donor turnover rate (below 10 %) appeared to correspond to relatively low IC_{50} values (**Figure 61a** and **Figure**

61b). In the case of 5-FT UDP-Gal (**Figure 61c**), this phenomenon was not observed. The IC_{50} values for low turnover rates fell within the error range of the high turnover rates. This could potentially be influenced by trace contamination of nucleoside inhibitors in the phosphatase. Such minor contamination may have a more pronounced impact on the results when dealing with low turnovers with a narrow assay window (below 10 % turnover), whereas its effect might be less significant in cases with a larger assay window (10 % – 20 % turnover). This also provides another rationale for the inability to accurately determine IC_{50} values when the turnover of the donor molecule is less than 10 %. The presence of nucleoside inhibitor contamination in the phosphatase can significantly impact results in such cases.



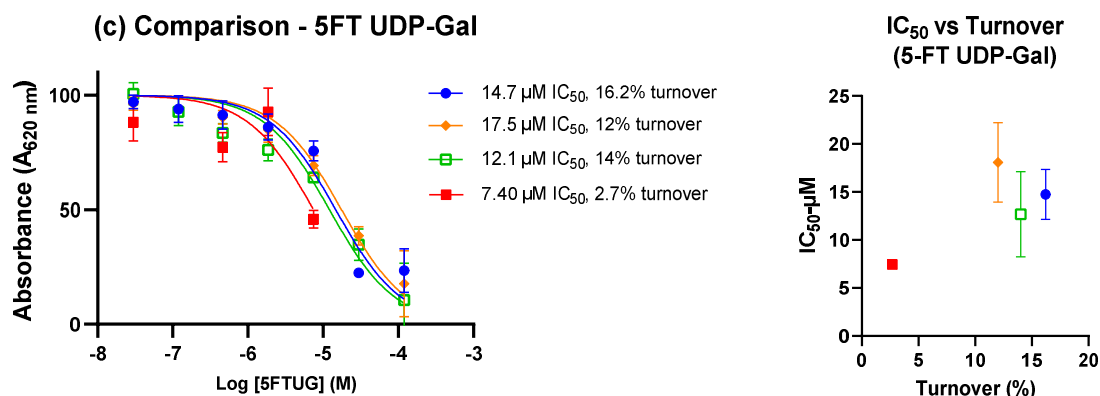


Figure 61 IC_{50} values in different donor turnovers. Reagents and conditions: $\beta 4\text{GalT1}$ ($1 \mu\text{g/mL}$), UDP-Gal (33 mM), GlcNAc (10 mM), CIP (10 U/mL), MnCl_2 (5 mM), lysozyme (1 mg/mL), Triton X (0.01%), MnCl_2 (5 mM), KCl (50 mM), HEPES (PH 7.5, 10 mM), DMSO (10%) and inhibitors series dilutions were incubated on a 96-well plate at $30 \text{ }^\circ\text{C}$ with shaking for 20 min. The reaction was stopped by adding malachite reagents. The absorbance was measured at 620 nm in 1 h. Bars indicate mean values \pm S.D. of the triplicates in a single experiment.

UDP-Calibration curve

The UDP-Calibration is linear up to $7.18 \mu\text{M}$ UDP in the assay (**Figure 62**), which means the turnover (donor concentration is $33 \mu\text{M}$) should be less than 22% under this condition. all the turnovers are around 10% – 20% , less than 10% turnover gave low assay window, more than 20% turnover are outside the linearity of UDP detection. Therefore, we set the turnover range around 10% – 20% under these experimental conditions.

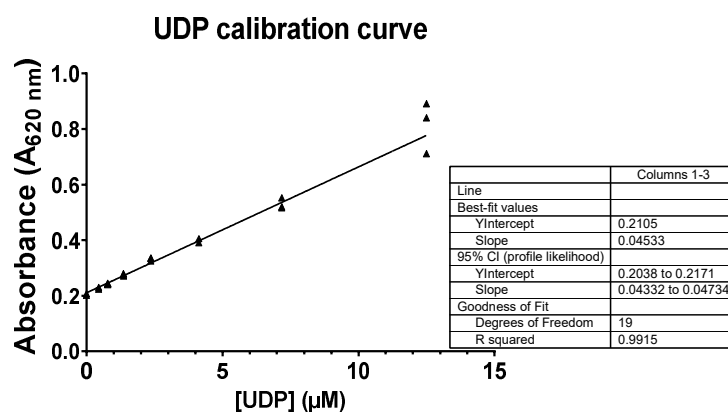


Figure 62 UDP calibration curve. Conditions: GlcNAc (10 mM), CIP (10 U/mL), MnCl₂ (5 mM), lysozyme (1 mg/mL), Triton X (0.01 %), MnCl₂ (5 mM), KCl (50 mM), HEPES (PH 7.5, 10 mM), DMSO (10 %) and UDP (0 – 12.5 µM) were incubated on a 96-well plate at 30 °C with shaking for 20 min. The reaction was stopped by adding malachite reagents. The absorbance was measured at 620 nm in 1 h. The experiment was carried out in triplicate. Bars indicate mean values ± S.D. of the triplicates in a single experiment. The experiment was repeated three times.

Control experiments

Positive control 5-FT UDP-Gal has potent inhibition towards β4GalT1 and therefore served as a positive control in our experiment. Values were similar to those from literature, which meant this protocol was feasible.

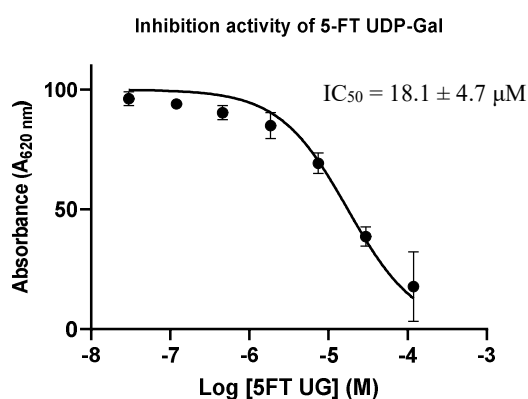


Figure 63 Determination of IC₅₀ values for 5-FT UDP-Gal against β4GalT1. Reagents and conditions: β4GalT1 (1 µg/mL, turnover: 12%), UDP-Gal (33 mM), GlcNAc (10 mM), CIP (10 U/mL), MnCl₂ (5 mM), lysozyme (1 mg/mL), Triton X (0.01 %), MnCl₂ (5 mM), KCl (50 mM), HEPES (PH 7.5, 10 mM), DMSO (10 %) and inhibitors series dilutions were incubated on a 96-well plate at 30 °C with shaking for 20 min. The reaction was stopped by adding malachite reagents. The absorbance was measured at 620 nm in 1 h. Bars indicate mean values ± S.D. of the triplicates in a single experiment. The experiment was repeated three times.

Potential inhibition of CIP by inhibitors

To confirm that the activity of these compounds in the assay is not due to inhibition of the phosphatase (CIP), UDP-Gal was replaced with 5 μ M UDP whilst all the conditions remained the same as GalT inhibition experiments. The results showed no apparent CIP inhibitory activity under the given UDP and inhibitor concentrations in any of these experiments (**Figure 64**).

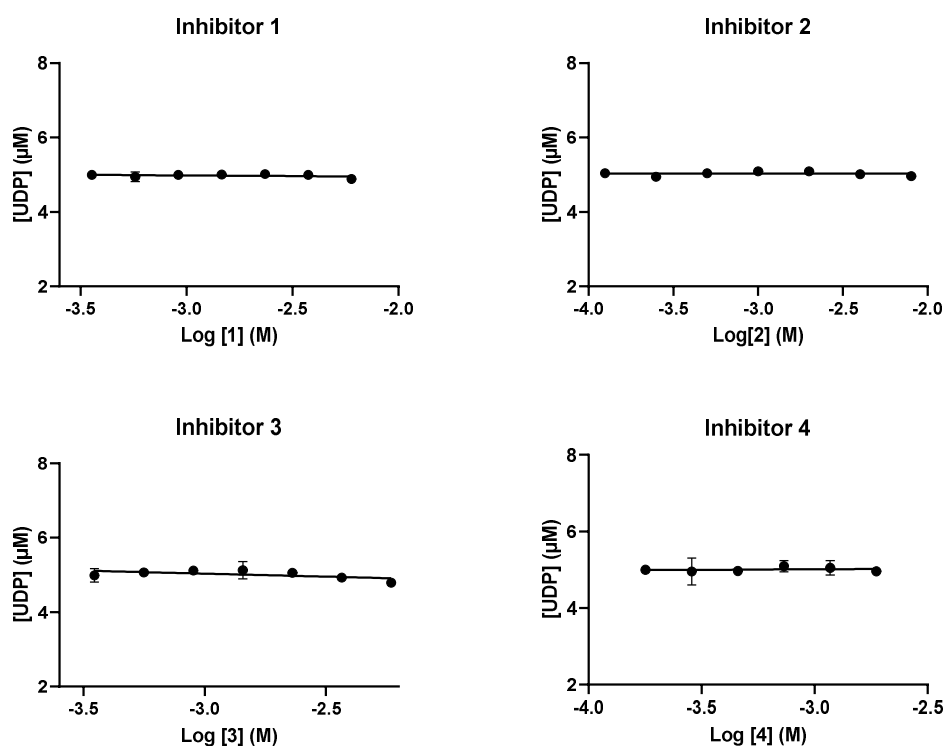


Figure 64 Potential inhibition of CIP by inhibitors. Reagents and conditions: β 4GalT1 (1 μ g/mL, turnover: 12 %), UDP (5 μ M), GlcNAc (10 mM), CIP (10 U/mL), $MnCl_2$ (5 mM), lysozyme (1 mg/mL), Triton X (0.01 %), $MnCl_2$ (5 mM), KCl (50 mM), HEPES (PH 7.5, 10 mM), DMSO (10 %) and inhibitors series dilutions were incubated on a 96-well plate at 30 $^{\circ}$ C with shaking for 20 min. The reaction was stopped by adding malachite reagents. The absorbance was measured at 620 nm in 1 h. The experiment was carried out in triplicate. Bars indicate mean values \pm S.D. of the triplicates in a single experiment.

Potential Donor-hydrolysis acceleration by inhibitors 2 and 3

Interestingly, high inhibitor concentration might accelerate the hydrolysis rate of the donor, fortunately, this extra background value could be corrected by the background control (**Figure 65**).

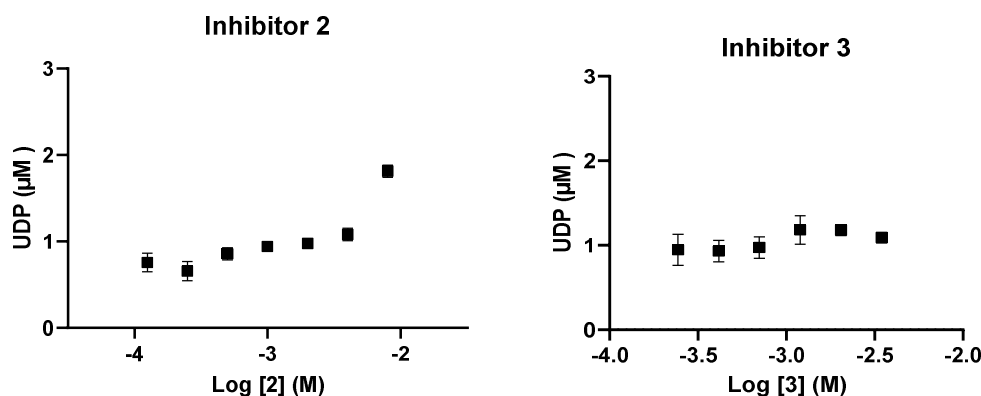


Figure 65 Potential donor-hydrolysis acceleration by 2 and 3

Enzyme activity prediction

In principle, turnover rates can be controlled through enzyme concentration. Early control experiments indicated that increasing the concentration of enzyme increased the turnover of donor substrate. However, as is known, enzyme can easily lose activity at rt while it's inevitable we take it out from freezer for assays. This means it can be practically difficult to exactly control turnover rates with the required accuracy. Based on this, the freeze-thaw cycles were recorded of two batches of β 4GalT1 in different dates and the corresponding turnovers ($[\text{GalT}] = 2 \text{ mU/mL}$). Interestingly, a common principle emerged for both batches of enzymes. There was a negative correlation between the freeze-thaw cycle and the associated turnover, with a slope of -2.4, ultimately reaching a plateau of 6.5 % donor turnover (**Figure 66**). This suggests a possibility to predict turnover based on the number of freeze-thaw cycles.

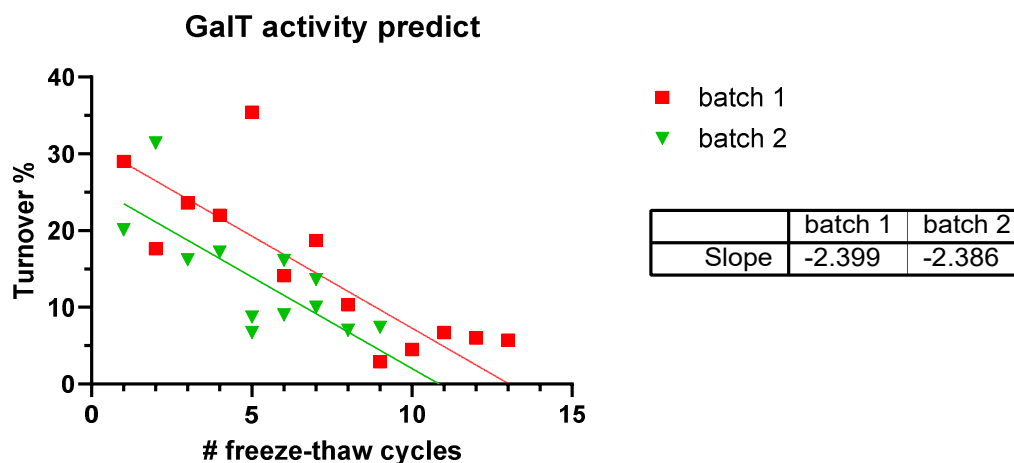


Figure 66 GalT activity prediction

6.4 β 4GalT7 inhibition assays

General. The β 4GalT7 inhibition assays were conducted by Roberto Mastio (Lund University, Sweden). Human β 4GalT7 was expressed as a 6xHIS+GST fusion protein, following the previously reported method¹⁰⁷. Instead of utilizing a HisTrap HP (GE Life Sciences) column and manual purification¹⁰⁷, the purification now involved an ACE C4 column (ACE-113-1046, 3 μ m, 100 \times 4.6 mm) and a Dionex ultimate 3000 (Thermo Fisher) chromatography system. The determination of β 4GalT7 activity followed the established protocol¹⁰⁷ but was adapted to a 96-well format.¹⁶⁰ Simply, 50 ng of β 4GalT7 was combined with 1 mM UDP-Gal and varying concentrations of inhibitors in a 50 μ L MES buffer (20 mM, pH 6.2) containing MnCl₂ (10 mM). The reaction took place in a 96-well polypropylene plate, covered with a PES/silicone sealing film, and incubated at 37 $^{\circ}$ C for 30 min using an Eppendorf Thermomixer C, with shaking at 800 rpm. Subsequently, the plate was quickly transferred to a 4 $^{\circ}$ C cooling block, and 5 μ L from each well was transferred to a new 96-well polypropylene plate containing 100 μ L HPLC eluent (70 % NH₄OAc (60 mM, pH 5.6) – 30 % CH₃CN (v/v)) in each well. After

manual mixing and brief centrifugation, the plate underwent HPLC analysis, consistent with the previously described procedure¹⁰⁷.

6.5 Cell assays

The cell assays were performed by Alex McCraw.

Cell viability

The samples were dissolved in a 40 % DMSO solution. Expi293 cells expressing to Chondroitin Sulfate Proteoglycan 4 (CSPG4)-IgE were cultured in 6-well plates at a concentration of approximately 5×10^6 cells/mL, with a final volume of 3 mL per well. Inhibitors were introduced at concentrations ranging from 100 – 1000 μ M, except for **31**, which was used in the range of 100 – 500 μ M. Controls included cells seeded without additives or with an equivalent volume of a 40 % DMSO solution. Cell counts were conducted immediately after seeding, around 24 hours later (Day 1), and approximately 48 hours after seeding (Day 2). Live and dead cell counts, as well as viability, were recorded at each time point. On Day 2, cultures were harvested by centrifugation at 2500 rpm for 5 minutes. Supernatants were transferred to Eppendorf tubes and stored at -80 °C, while cell pellets were lysed and also stored at -80 °C.

IgE production

An Anti-IgE ELISA (IgE production) was performed using cell supernatants. Expi293F cells, stably transfected to express IgE specific to CSPG4, were utilized for the production of all CSPG4 IgE-based glycovariants.¹⁶¹ The cells were cultured in 124 mL Erlenmeyer Flasks at a density of 5×10^6 cells/mL and incubated for 3 days with shaking. On Day 3, cell counting was performed, and supernatants were collected. Subsequently, the supernatants were filtered twice through 0.45 μm and 0.2 μm filters before the purification of the antibodies.

Degranulation

RBL-SX38 cell degranulation was assessed by measuring the release of β -hexosaminidase.¹⁶¹ Cells were initially seeded at a density of 1×10^4 cells/well in culture medium overnight. Subsequently, the cells were sensitized with 200 ng/mL IgE, control antibody, or medium alone, with incubation for 1 h at 37 °C. After 3 washes with stimulation buffer (HBSS + 2 % FBS), the cells were stimulated for 1 h at 37 °C with either stimulation buffer alone or rabbit anti-IgE (1.5 $\mu\text{g}/\text{mL}$). To quantify β -hexosaminidase, 25 μL culture supernatant was mixed with 1:1 with stimulation buffer and transferred to black 96-well plates containing 50 μL of a fluorogenic substrate per well (1 mmol/L 4-methylumbelliferyl N-acetyl- β -D-glucosaminide, 0.1 % dimethyl sulfoxide, 200 mmol/mL sodium citrate, pH 4.5) The plates were incubated for 1 h in the dark at 37 °C, and the reaction was quenched with 100 μL 0.5 M Tris per well. The plates were then read using a FLUOstar Omega Microplate Reader ($\lambda_{\text{ex}} = 350 \text{ nm}$, $\lambda_{\text{em}} = 450 \text{ nm}$; BMG Labtech, Ortenberg, Germany). Degranulation was represented as a percentage relative to Triton X-100 release (100 %).

Lectin blot

The antibodies were prepared in stock solutions with a concentration of 20 µg/ml. After mixing the samples with Reducing Buffer, they were incubated at 95 °C for 5 minutes, cooled, and loaded onto Mini-PROTEAN TGX Gels (15-well, 15 µL). Electrophoresis was conducted at 150V for 45 minutes using a Mini-PROTEAN Tetra Vertical Electrophoresis Cell. Subsequently, the gels were transferred to Trans-Blot Turbo Mini 0.2 µm PVDF membranes using a Trans-Blot Turbo Transfer System. To separate the sections containing the heavy and light chains, the membranes were horizontally cut just below the 37 kDa mark on the protein marker ladder. For the light chain, membranes were blocked for 1 h using either Kappa Blocking Buffer or Superblock Blocking Buffer. For the heavy chain, membranes were blocked for 1 h using Kappa Blocking Buffer.

Membranes containing the heavy chain were subjected to a 30-min incubation with relevant lectins on a rotator. An α -human Kappa Chain antibody, prepared at a 1:5000 dilution in Kappa Blocking Buffer/SuperBlock Blocking Buffer, was incubated as specified. Subsequently, membranes were washed with Wash Buffer for 5 minutes, repeating the process three times. Heavy chain membranes underwent incubation with Streptavidin-HRP at a 1:2000 dilution in Lectin Blocking Buffer, while light chain membranes were incubated with α -rabbit-HRP at a 1:2000 dilution in Kappa Blocking Buffer or SuperBlock Blocking Buffer. The membranes were incubated for 30 minutes on a rotator and then washed as previously described.

For visualization, membranes were developed using ECL Western Blotting Detection Reagent. Densitometric quantification was carried out using ImageJ software [National Institutes of Health], with values normalized using the kappa light chain as a loading control.

Glycoanalysis using HPLC-FD-MS

Samples were utilized without cleanup and were dried before application. For N-glycan release, samples underwent treatment with PNGase F and were subsequently cleaned up before procainamide labeling. After labeling, excess reagents were removed, and the samples were eluted in water from the cleanup plate, concentrated, and analyzed using HPLC-FD-MS.¹⁶²

Hydrophilic Interaction Liquid Chromatography (HILIC) HPLC was employed for separation and analysis, utilizing a Dionex Ultimate 3000 UHPLC instrument with a BEH-Glycan 1.7 μm , 2.1×150 mm column (Waters) and a fluorescence detector ($\lambda_{\text{ex}} = 310$ nm, $\lambda_{\text{em}} = 370$ nm), controlled by Bruker HyStar 3.2 and Chromeleon data software version 7.2. MS analysis was conducted with a Bruker Mazon Speed ETD electrospray mass spectrometer directly coupled after the UHPLC FD without splitting.

HPLC-ESI-MS chromatogram analysis utilized Bruker Compass DataAnalysis 4.4 or Xcalibur Data Acquisition and Interpretation Software version 4.3, along with GlycoWorkbench software. The assignment of glucose unit values to peaks was performed using Chromeleon Data software, version 7.2, or Xcalibur Data Acquisition and Interpretation Software version 4.3.

6.6 HPLC-based cell permeability assessment

The cell permeability evaluation followed the previously reported method.⁵³ The material was used from the cell-viability experiments. All samples (cell pellet or supernatant) were analyzed by reverse-phase high performance liquid chromatography on an Agilent 1220 infinity LC

system with an Agilent ZORBAX eclipse XDB-C18 column (5 μm , 4.6 \times 250 mm). Detection wavelength was 254 nm. Flow rate, gradient and retention time were in the synthesis section (see 6.1, HPLC data of individual compound). The cell pellets or supernatants were filtered through a 2 μm filter, and the filter membrane was washed twice with 5 μL MeOH. The filtrate was completely dried in vacuo. The concentrated sample was dissolved in 600 μL MeOH and 5 μL was loaded into HPLC system. The cell permeability (intracellular proportion) of compounds **29** to **36** were determined as a percentage of the total concentration. The concentration of the compounds in the cell pellet or supernatant was calculated based on the area under the curve in HPLC.

6.7 Differential Scanning Fluorimetry (DSF) binding assays

General. All reagents were obtained commercially and used as received, unless otherwise stated. The DSF binding assays were modified from Vivoli M. *et al.*¹⁶⁰ All experiments were performed in 96-well PCR plates on a Lightcycler[®]480 system. Data was analysed using LightCycler[®] Thermal Shift Analysis software and GraphPad Prism 10.

Assay protocol. All assay components are provided as final concentrations. LgtC, SetA or LtpM (0.22 mg/mL), DTT (5 mM), MnCl₂ (5 mM), HEPES (PH 7.5, 10 mM) and SYPRO Orange dye (5 mM), ligand (0 – 2 mM). All components, excluding the dye agent, were combined and incubated at 30 °C for 20 min. Subsequently, SYPRO Orange dye and inhibitors were added.

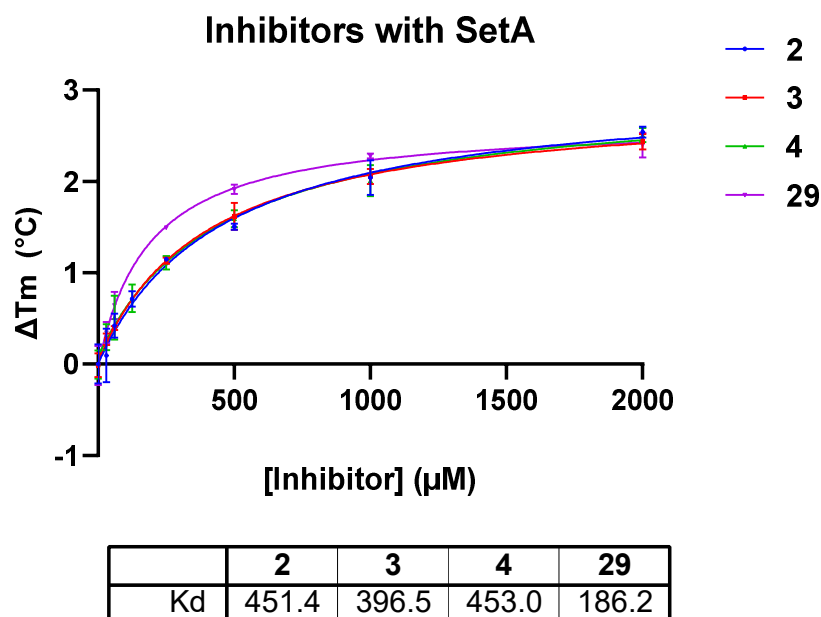


Figure 67 Class 1 and Class 2 inhibitors with SetA in DSF assays. All assay components are provided as final concentrations. LgtC, SetA or LtpM (0.22 mg/mL), DTT (5 mM), MnCl₂ (5 mM), HEPES (PH 7.5, 10 mM) and SYPRO Orange dye (5 mM), ligand (0 – 2 mM). All components, excluding the dye agent, were combined and incubated at 30 °C for 20 min. Subsequently, SYPRO Orange dye and inhibitors were added. Run a thermal denaturation on a Lightcycler®480 system. Bars indicate mean values ± S.D. of the triplicates in a single experiment. Each experiment was repeated twice.

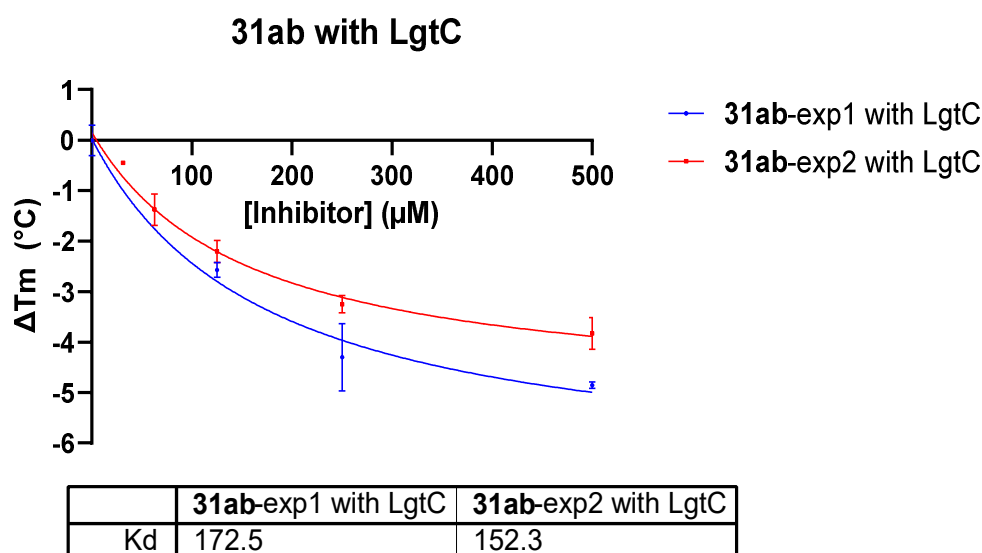


Figure 68 Compound **31ab** with LgtC in DSF assays. **31ab** was used as a 0.7:1 mixture of two isomers. All assay components are provided as final concentrations. LgtC, SetA or LtpM (0.22 mg/mL), DTT (5 mM), MnCl₂ (5 mM), HEPES (PH 7.5, 10 mM) and SYPRO Orange dye (5 mM), ligand (0 – 0.5 mM). All components, excluding the dye agent, were combined and incubated at 30 °C for 20 min. Subsequently, SYPRO Orange dye and inhibitors were added. Run a thermal denaturation on a Lightcycler®480 system. Bars indicate mean values ± S.D. of the triplicates in a single experiment.

6.8 Molecular Modelling

General protocol. The previously reported structures of UDP with bovine β 4GalT1 (PDB: 1FR8), human β 4GalT7 (PDB: 4IRP), LgtC from *E. coli* (PDB: 1G9R) were employed to generate substrate-enzyme complexes. SetA and LtpM were AlphaFold models generated by Gunnar Neels Schroeder. The ligand was drawn in 3D with hydrogen atoms using either MarvinSketch 20.21.0 or Schrodinger 2021-1¹⁶³ and then saved as a mol2 file. The prepared ligand was docked into the binding site of the prepared protein using the Glide module¹⁶⁴ of Schrodinger. The chosen outcome was subsequently subjected to Molecular dynamics (MD) simulations. The solution was built using Charmm-Gui¹⁶⁵⁻¹⁶⁷ and simulations conducted using the GPU-accelerated version of the PMEMD program¹⁶⁸ in the Amber20 package¹⁶⁹.

In MD simulations, the initial phase involved 5000 steepest descent steps followed by 5000 conjugated gradient steps for energy minimization. The system was then heated to 308 K over 25 ps in the NVT ensemble. Equilibration and production runs utilized a Langevin thermostat with a friction coefficient of 1.0 ps⁻¹. The equilibration phase, incorporating pressure control and a 1 fs timestep, had five steps sequentially releasing positional restraints on lipid phosphate atoms, waters and ions, and the protein and ligand. A brief 50 ns simulation (NPT, 2 fs timestep) concluded the equilibration, followed by production runs in the NPT ensemble with semi-isotropic pressure control using the Monte Carlo barostat.¹⁷⁰ The nonbonded force cutoff for van der Waals and electrostatic interactions was set at 10 Å. Trajectories were saved every 100 ps, resulting in 1000 frames over 100 ns. Triplicate simulations were conducted for inhibitor **31** with GalTs (β 4GalT1, β 4GalT7, and LgtC). Different production runs began from the same equilibrated structure, maintaining consistent initial velocities and coordinates. Only different

seeds were used for the Langevin thermostat. All generated replicas were employed for trajectory analyses.

Analysis of trajectories, involving Root Mean Square Deviation (RMSD) and hydrogen bond occupancy, was performed utilizing VMD 1.9.3.¹⁷¹ The calculation of interaction energy between residues and ligands utilized the "namdenergy.tcl" script v1.6 from NAMD,¹⁷² specifically considering residues within a 5 Å distance from the ligand. Model images were visualized using Schrodinger 2021-1 and VMD 1.9.3.

7 References

1. Lu, R. M. *et al.* Development of therapeutic antibodies for the treatment of diseases. *J. Biomed. Sci.* **27**, 1–30 (2020).
2. Hayes, J. M. *et al.* Glycosylation and Fc receptors. *Current Topics in Microbiology and Immunology* vol. 382, 165–199 (2014).
3. de Haan, N., Falck, D. & Wuhrer, M. Monitoring of immunoglobulin N- And O-glycosylation in health and disease. *Glycobiology* **30**, 226–240 (2021).
4. Plomp, R. *et al.* Site-specific N-glycosylation analysis of human immunoglobulin e. *J. Proteome Res.* **13**, 536–546 (2014).
5. Abès, R. & Teillaud, J. L. Impact of glycosylation on effector functions of therapeutic IgG. *Pharmaceuticals* **3**, 146–157 (2010).
6. Huang, W., Giddens, J., Fan, S. Q., Toonstra, C. & Wang, L. X. Chemoenzymatic glycoengineering of intact IgG antibodies for gain of functions. *J. Am. Chem. Soc.* **134**, 12308–12318 (2012).
7. Hunt, J. *et al.* Disulfide linkage controls the affinity and stoichiometry of IgE Fcε3-4 binding to FcεRI. *J. Biol. Chem.* **280**, 16808–16814 (2005).
8. Björklund, J. E. M., Karlsson, T. & Magnusson, C. G. M. N-glycosylation influences epitope expression and receptor binding structures in human IgE. *Mol. Immunol.* **36**, 213–221 (1999).
9. Shade, K. T. C. *et al.* A single glycan on IgE is indispensable for initiation of anaphylaxis. *J. Exp. Med.* **212**, 457–467 (2015).
10. Shade, K. T. C. *et al.* Sialylation of immunoglobulin E is a determinant of allergic pathogenicity. *Nature* **582**, 265–270 (2020).
11. Montero-Morales, L. *et al.* In planta glycan engineering and functional activities of IgE

- antibodies. *Front. Bioeng. Biotechnol.* **7**, 1–11 (2019).
12. Ashwell, G. & Harford, J. CARBOHYDRATE-SPECIFIC RECEPTORS OF THE LIVER. *Ann. Rev. Biochem.* **51**, 531–554(1982).
 13. Louie, S. *et al.* FX knockout CHO hosts can express desired ratios of fucosylated or afucosylated antibodies with high titers and comparable product quality. *Biotechnol. Bioeng.* **114**, 632–644 (2017).
 14. Strasser, R. *et al.* Generation of glyco-engineered *Nicotiana benthamiana* for the production of monoclonal antibodies with a homogeneous human-like N-glycan structure. *Plant Biotechnol. J.* **6**, 392–402 (2008).
 15. Jennewein, M. F. & Alter, G. The Immunoregulatory Roles of Antibody Glycosylation. *Trends Immunol.* **38**, 358–372 (2017).
 16. Mikkola, S. Nucleotide sugars in chemistry and biology. *Molecules* **25**, 1–27 (2020).
 17. Lairson, L. L., Henrissat, B., Davies, G. J. & Withers, S. G. Glycosyl transferases: Structures, functions, and mechanisms. *Annu. Rev. Biochem.* **77**, 521–555 (2008).
 18. Taujale, R. *et al.* Deep evolutionary analysis reveals the design principles of fold a glycosyltransferases. *Elife* **9**, 1–24 (2020).
 19. Albesa-Jové, D., Giganti, D., Jackson, M., Alzari, P. M. & Guerin, M. E. Structure-function relationships of membrane-associated GT-B glycosyltransferases. *Glycobiology* **24**, 108–124 (2014).
 20. Wagner, G. K. & Pesnot, T. Glycosyltransferases and their assays. *ChemBioChem* **11**, 1939–1949 (2010).
 21. Hennet, T. The galactosyltransferase family. *Cell. Mol. Life Sci.* **59**, 1081–1095 (2002).
 22. Tsutsui, Y., Ramakrishnan, B. & Qasba, P. K. Crystal structures of β -1,4-galactosyltransferase 7 enzyme reveal conformational changes and substrate binding. *J. Biol. Chem.* **288**, 31963–31970 (2013).

23. Takaya, K. *et al.* Rational design, synthesis, and characterization of novel inhibitors for human β 1,4-galactosyltransferase. *J. Med. Chem.* **48**, 6054–6065 (2005).
24. Furukawa, K., Clausen, H. & Sato, T. UDP-Gal: BetaGlcNAc Beta 1,4-Galactosyltransferase, Polypeptide 2-6; Xylosylprotein Beta 1,4-Galactosyltransferase, Polypeptide 7 (Galactosyltransferase I) (B4GALT2-7). *Handb. Glycosyltransferases Relat. Genes, Second Ed.* 63–72 (2014).
25. Ujita, M. *et al.* Synthesis of poly-N-acetyllactosamine in core 2 branched O-glycans. *J. Biol. Chem.* **273**, 34843–34849 (1998).
26. McDonald, A. G. *et al.* Galactosyltransferase 4 is a major control point for glycan branching in N-linked glycosylation. *J. Cell Sci.* **127**, 5014–5026 (2014).
27. Kumagai, T. *et al.* Involvement of murine β -1,4-galactosyltransferase v in lactosylceramide biosynthesis. *Glycoconj. J.* **27**, 685–695 (2010).
28. Qasba, P., Ramakrishnan, B. & Boeggeman, E. Structure and Function of β -1,4-Galactosyltransferase. *Curr. Drug Targets* **9**, 292–309 (2008).
29. Tsutsui, Y., Ramakrishnan, B. & Qasba, P. K. Crystal structures of β -1,4-galactosyltransferase 7 enzyme reveal conformational changes and substrate binding. *J. Biol. Chem.* **288**, 31963–31970 (2013).
30. Huang, K. *et al.* Biochemical characterisation of an α 1,4 galactosyltransferase from: *Neisseria weaveri* for the synthesis of α 1,4-linked galactosides. *Org. Biomol. Chem.* **18**, 3142–3148 (2020).
31. Erwin, A. L. *et al.* Role of LgtC in resistance of nontypeable *Haemophilus influenzae* strain R2866 to human serum. *Infect. Immun.* **74**, 6226–6235 (2006).
32. Xu, Y. *et al.* Covalent inhibitors of LgtC: A blueprint for the discovery of non-substrate-like inhibitors for bacterial glycosyltransferases. *Bioorganic Med. Chem.* **25**, 3182–3194 (2017).

33. Persson, K. *et al.* Crystal structure of the retaining galactosyltransferase LgtC from *Neisseria meningitidis* in complex with donor and acceptor sugar analogs. *Nat. Struct. Biol.* **8**, 166–175 (2001).
34. Šnajdrová, L., Kulhánek, P., Imberty, A. & Koča, J. Molecular dynamics simulations of glycosyltransferase LgtC. *Carbohydr. Res.* **339**, 995–1006 (2004).
35. Jank, T. *et al.* Domain organization of *Legionella* effector SetA. *Cell. Microbiol.* **14**, 852–868 (2012).
36. Gao, L. *et al.* *Legionella* effector SetA as a general O-glycosyltransferase for eukaryotic proteins. *Nat. Chem. Biol.* **15**, 213–216 (2019).
37. Heidtman, M., Chen, E. J., Moy, M. Y. & Isberg, R. R. Large-scale identification of *Legionella pneumophila* Dot/Icm substrates that modulate host cell vesicle trafficking pathways. *Cell. Microbiol.* **11**, 230–248 (2009).
38. Levanova, N. *et al.* The *Legionella* effector LtpM is a new type of phosphoinositide-activated glycosyltransferase. *J. Biol. Chem.* **294**, 2862–2879 (2019).
39. Takaya, K. *et al.* Rational Design, Synthesis, and Characterization of Novel Inhibitors for Human β 1,4-Galactosyltransferase II. *J. Med. Chem.* **48**, 6054–6065 (2005).
40. Vidal, S., Bruyère, I., Malleron, A., Augé, C. & Praly, J. P. Non-isosteric C-glycosyl analogues of natural nucleotide diphosphate sugars as glycosyltransferase inhibitors. *Bioorganic Med. Chem.* **14**, 7293–7301 (2006).
41. Pesnot, T., Jørgensen, R., Palcic, M. M. & Wagner, G. K. Structural and mechanistic basis for a new mode of glycosyltransferase inhibition. *Nat. Chem. Biol.* **6**, 321–323 (2010).
42. Jiang, J. *et al.* Uncharged nucleoside inhibitors of β -1,4-galactosyltransferase with activity in cells. *Chem. Commun.* **52**, 3955–3958 (2016).
43. Torrey, N., Road, P. & Jolla, L. Department of Chemistry and The Skaggs Institute for

- Chemical Biology, The Scripps Research Institute, 10550 North Torrey Pines Road, La Jolla, CA 92037, USA. **8**, 3359–3364 (1998).
44. Jiang, J. & Wagner, G. K. An acceptor analogue of β -1,4-galactosyltransferase: Substrate, inhibitor, or both? *Carbohydr. Res.* **450**, 54–59 (2017).
 45. Okeley, N. M. *et al.* Development of orally active inhibitors of protein and cellular fucosylation. *Proc. Natl. Acad. Sci. U. S. A.* **110**, 5404–5409 (2013).
 46. Allen, J. G. *et al.* Facile Modulation of Antibody Fucosylation with Small Molecule Fucostatin Inhibitors and Cocrystal Structure with GDP-Mannose 4,6-Dehydratase. *ACS Chem. Biol.* **11**, 2734–2743 (2016).
 47. Burkart, M. D., Vincent, S. P. & Wong, C. An efficient synthesis of CMP-3-fluoroneuraminic acid for sialyltransferases, has been efficiently synthesized using sialic acid glycal. *Chem. Biol.* 1525–1526 (1999).
 48. Montgomery, A., Szabo, R., Skropeta, D. & Yu, H. Computational characterisation of the interactions between human ST6Gal I and transition-state analogue inhibitors: Insights for inhibitor design. *J. Mol. Recognit.* **29**, 210–222 (2016).
 49. Rillahan, C. D. *et al.* Global metabolic inhibitors of sialyl- and fucosyltransferases remodel the glycome. *Nat. Chem. Biol.* **8**, 661–668 (2012).
 50. Heise, T. *et al.* Potent Metabolic Sialylation Inhibitors Based on C-5-Modified Fluorinated Sialic Acids. *J. Med. Chem.* **62**, 1014–1021 (2019).
 51. Urbaniak, M. D., Yashunsky, D. V., Crossman, A., Nikolaev, A. V. & Ferguson, M. A. J. Probing enzymes late in the trypanosomal glycosylphosphatidylinositol biosynthetic pathway with synthetic glycosylphosphatidylinositol analogues. *ACS Chem. Biol.* **3**, 625–634 (2008).
 52. Pesnot, T., Jørgensen, R., Palcic, M. M. & Wagner, G. K. Structural and mechanistic basis for a new mode of glycosyltransferase inhibition. *Nat. Chem. Biol.* **6**, 321–323

- (2010).
53. Kanabar, V. *et al.* Base-modified UDP-sugars reduce cell surface levels of P-selectin glycoprotein 1 (PSGL-1) on IL-1 β -stimulated human monocytes. *Glycobiology* **26**, 1059–1071 (2016).
 54. Mallinson, J. & Collins, I. Macrocycles in new drug discovery. *Future Med. Chem.* **4**, 1409–1438 (2012).
 55. Fang, Z. Conformational restriction: an effective tactic in ‘follow-on’-based drug discovery. *Future Med. Chem.* **6**, 885–901 (2014).
 56. Lipinski, C. A., Lombardo, F., Dominy, B. W. & Feeney, P. J. Experimental and computational approaches to estimate solubility and permeability in drug discovery and development settings. *Adv. Drug Deliv. Rev.* **64**, 4–17 (2012).
 57. Augustijns, P. F. *et al.* Hydration changes implicated in the remarkable temperature-dependent membrane permeation of cyclosporin A. *Biochemistry* **39**, 7621–7630 (2000).
 58. Stachel, S. J. *et al.* Macrocyclic inhibitors of β -secretase: Functional activity in an animal model. *J. Med. Chem.* **49**, 6147–6150 (2006).
 59. Tron, A. E. *et al.* Discovery of Mcl-1-specific inhibitor AZD5991 and preclinical activity in multiple myeloma and acute myeloid leukemia. *Nat. Commun.* **9**, (2018).
 60. Delorbe, J. E., Clements, J. H., Whiddon, B. B. & Martin, S. F. Thermodynamic and structural effects of macrocyclic constraints in protein-ligand interactions. *ACS Med. Chem. Lett.* **1**, 448–452 (2010).
 61. Ettmayer, P. *et al.* Structural and conformational requirements for high-affinity binding to the SH2 domain of Grb21. *J. Med. Chem.* **42**, 971–980 (1999).
 62. Nie, Z. *et al.* Structure-based design and synthesis of novel macrocyclic pyrazolo[1,5-a][1,3,5]triazine compounds as potent inhibitors of protein kinase CK2 and their anticancer activities. *Bioorganic Med. Chem. Lett.* **18**, 619–623 (2008).

63. Ishikawa, M. & Hashimoto, Y. Improvement in aqueous solubility in small molecule drug discovery programs by disruption of molecular planarity and symmetry. *J. Med. Chem.* **54**, 1539–1554 (2011).
64. Lovering, F., Bikker, J. & Humblet, C. Escape from flatland: Increasing saturation as an approach to improving clinical success. *J. Med. Chem.* **52**, 6752–6756 (2009).
65. Díaz-Rodríguez, A. *et al.* Synthesis and anti-HIV activity of conformationally restricted bicyclic hexahydroisobenzofuran nucleoside analogs. *Org. Biomol. Chem.* **7**, 1415–1423 (2009).
66. Figueras, A. *et al.* Synthesis, Anti-HIV Activity Studies, and insilico Rationalization of Cyclobutane-Fused Nucleosides. *ChemMedChem* **7**, 1044–1056 (2012).
67. Frieden, M., Giraud, M., Reese, C. B. & Song, Q. Synthesis of 1-[cis-3-(hydroxymethyl)cyclobutyl]-uracil, -thymine and -cytosine. *J. Chem. Soc. - Perkin Trans. 1* 2827–2832 (1998).
68. Koshkin, A. A. *et al.* LNA (Locked Nucleic Acids): Synthesis of the adenine, cytosine, guanine, 5-methylcytosine, thymine and uracil bicyclonucleoside monomers, oligomerisation, and unprecedented nucleic acid recognition. *Tetrahedron* **54**, 3607–3630 (1998).
69. Sung, W. L. Synthesis of 4-(1,2,4-Triazol-1-yl)pyrimidin-2(1H)-one Ribonucleotide and Its Application in Synthesis of Oligoribonucleotides. *J. Org. Chem.* **47**, 3623–3628 (1982).
70. Hřebabecký, H. *et al.* Synthesis and biological evaluation of conformationally restricted adenine bicycloribonucleosides. *Org. Biomol. Chem.* **13**, 9300–9313 (2015).
71. Salinas, J. C., Yu, J., Østergaard, M., Seth, P. P. & Hanessian, S. Conception and Synthesis of Oxabicyclic Nucleoside Phosphonates as Internucleotidic Phosphate Surrogates in Antisense Oligonucleotide Constructs. *Org. Lett.* **20**, 5296–5299 (2018).

72. Chen, Q. & Davidson, A. Synthesis, conformational study and antiviral activity of L-like neplanocin derivatives. *Bioorganic Med. Chem. Lett.* **27**, 4436–4439 (2017).
73. Soengas, R. G., Da Silva, G. & Estévez, J. C. Synthesis of spironucleosides: Past and future perspectives. *Molecules* **22**, (2017).
74. Jonckers, T. H. M. *et al.* 2'-deoxy-2'-spirocyclopropylcytidine revisited: A new and selective inhibitor of the hepatitis C virus NS5B polymerase. *J. Med. Chem.* **53**, 8150–8160 (2010).
75. De Castro, S. *et al.* Unprecedented lability of the 5'-O-tert-butyldimethylsilyl group from 3'-spiro-5''-(4''-acylamino-1'',2''-oxathiole- 2'',2''-dioxide) nucleoside derivatives via neighboring group participation of the 4''-acylamino residue. *J. Org. Chem.* **71**, 1407–1415 (2006).
76. Kumar, M., Kumar, R., Rana, N. & Prasad, A. K. Chemo-enzymatic Synthesis of 3'-azido/-amino-C-4'-spirooxetano-xylo nucleosides. *Curr. Green Chem.* **7**, 120–127 (2020).
77. Jonckers, T. H. M. *et al.* Nucleotide prodrugs of 2'-deoxy-2'-spirooxetane ribonucleosides as novel inhibitors of the HCV NS5B polymerase. *J. Med. Chem.* **57**, 1836–1844 (2014).
78. Lennox, A. J. J. & Lloyd-Jones, G. C. Selection of boron reagents for Suzuki-Miyaura coupling. *Chem. Soc. Rev.* **43**, 412–443 (2014).
79. Macharia, J. M. *et al.* The catalytic mechanism of the Suzuki-Miyaura reaction. (2021).
80. D'Alterio, M. C. *et al.* Mechanistic Aspects of the Palladium-Catalyzed Suzuki-Miyaura Cross-Coupling Reaction. *Chem. - A Eur. J.* **27**, 13481–13493 (2021).
81. Amatore, C. *et al.* Rates and Mechanism of the Formation of Zerovalent Palladium Complexes from Mixtures of Pd(OAc)₂ and Tertiary Phosphines and Their Reactivity in Oxidative Additions. *Organometallics* **14**, 1818–1826 (1995).

82. Miyaura, N. & Suzuki, A. Palladium-Catalyzed Cross-Coupling Reactions of Organoboron Compounds. *Chem. Rev.* **95**, 2457–2483 (1995).
83. Liu, C., Ji, C. L., Hong, X. & Szostak, M. Palladium-Catalyzed Decarbonylative Borylation of Carboxylic Acids: Tuning Reaction Selectivity by Computation. *Angew. Chemie - Int. Ed.* **57**, 16721–16726 (2018).
84. Hopkinson, M. N., Richter, C., Schedler, M. & Glorius, F. An overview of N-heterocyclic carbenes. *Nature* **510**, 485–496 (2014).
85. Amann, N., Pandurski, E., Fiebig, T. & Wagenknecht, H. A. Electron injection into DNA: Synthesis and spectroscopic properties of pyrenyl-modified oligonucleotides. *Chem. - A Eur. J.* **8**, 4877–4883 (2002).
86. Kohyama, N., Katashima, T. & Yamamoto, Y. Synthesis of novel 2-aryl AICAR derivatives. *Synthesis (Stuttg.)*. 2799–2804 (2004).
87. Collier, A. & Wagner, G. K. Suzuki-Miyaura cross-coupling of unprotected halopurine nucleosides in water - Influence of catalyst and cosolvent. *Synth. Commun.* **36**, 3713–3721 (2006).
88. Fresneau, N., Hiebel, M. A., Agrofoglio, L. A. & Berteina-Raboin, S. Efficient synthesis of unprotected C-5-Aryl/Heteroaryl-2'-deoxyuridine via a suzuki-miyaura reaction in aqueous media. *Molecules* **17**, 14409–14417 (2012).
89. Western, E. C., Daft, J. R., Johnson, E. M., Gannett, P. M. & Shaughnessy, K. H. Efficient one-step Suzuki arylation of unprotected halonucleosides, using water-soluble palladium catalysts. *J. Org. Chem.* **68**, 6767–6774 (2003).
90. Hervé, G., Sartori, G., Enderlin, G., MacKenzie, G. & Len, C. Palladium-catalyzed Suzuki reaction in aqueous solvents applied to unprotected nucleosides and nucleotides. *RSC Adv.* **4**, 18558–18594 (2014).
91. Serrano, J. L. *et al.* Quadrol-Pd(ii) complexes: Phosphine-free precatalysts for the room-

- temperature Suzuki-Miyaura synthesis of nucleoside analogues in aqueous media. *Dalt. Trans.* **51**, 2370–2384 (2022).
92. Mieczkowski, A., Peltier, P., Zevaco, T. & Agrofoglio, L. A. Preparation of C5-substituted O6,5'-cyclouridine. *Tetrahedron* **65**, 4053–4059 (2009).
93. Mieczkowski, A., Blu, J., Roy, V. & Agrofoglio, L. A. Preparation of C-5-substituted 6,5'-O-anhydrouridine by Sn-Pd transmetallation-coupling process and their use. *Tetrahedron* **65**, 9791–9796 (2009).
94. Lakshman, M. K. *et al.* Palladium catalysis for the synthesis of hydrophobic C-6 and C-2 aryl 2'-deoxynucleosides. Comparison of C-C versus C-N bond formation as well as C-6 versus C-2 reactivity. *J. Am. Chem. Soc.* **123**, 7779–7787 (2001).
95. Bookser, B. C., Matelich, M. C., Ollis, K. & Ugarkar, B. G. Derivatives . Synthesis , Conformation , and Enzyme Inhibition. *Society* **1**, 3389–3399 (2005).
96. Amann, N. & Wagenknecht, H. A. Preparation of pyrenyl-modified nucleosides via Suzuki-Miyaura cross-coupling reactions. *Synlett* 687–691 (2002).
97. Hocek, M., Holý, A., Votruba, I. & Dvořáková, H. Synthesis and cytostatic activity of substituted 6-phenylpurine bases and nucleosides: Application of the Suzuki-Miyaura cross-coupling reactions of 6-chloropurine derivatives with phenylboronic acids. *J. Med. Chem.* **43**, 1817–1825 (2000).
98. Tedaldi, L., Evitt, A., Göös, N., Jiang, J. & Wagner, G. K. A practical glycosyltransferase assay for the identification of new inhibitor chemotypes. *Medchemcomm* **5**, 1193–1201 (2014).
99. Afratis, N. *et al.* Glycosaminoglycans: Key players in cancer cell biology and treatment. *FEBS J.* **279**, 1177–1197 (2012).
100. Hua, S. H., Viera, M., Yip, G. W. & Bay, B. H. Theranostic Applications of Glycosaminoglycans in Metastatic Renal Cell Carcinoma. *Cancers (Basel)*. **15**, (2023).

101. Köwitsch, A., Zhou, G. & Groth, T. Medical application of glycosaminoglycans: a review. *J. Tissue Eng. Regen. Med.* **12**, e23–e41 (2018).
102. Vitale, D. *et al.* Proteoglycans and glycosaminoglycans as regulators of cancer stem cell function and therapeutic resistance. *FEBS J.* **286**, 2870–2882 (2019).
103. Ghiselli, G. Drug-Mediated Regulation of Glycosaminoglycan Biosynthesis. *Med. Res. Rev.* **37**, 1051–1094 (2017).
104. Robinson, H. C., Brett, M. J., Tralaggan, P. J., Lowther, D. A. & Okayama, M. The effect of D xylose β d xylosides and β D galactosides on chondroitin sulphate biosynthesis in embryonic chicken cartilage. *Biochem. J.* **148**, 25–34 (1975).
105. Schwartz, N. B., Galligani, L., Ho, P. L. & Dorfman, A. Stimulation of synthesis of free chondroitin sulfate chains by β D xylosides in cultured cells. *Proc. Natl. Acad. Sci. U. S. A.* **71**, 4047–4051 (1974).
106. Siegbahn, A. *et al.* Synthesis, conformation and biology of naphthoxylosides. *Bioorganic Med. Chem.* **19**, 4114–4126 (2011).
107. Siegbahn, A. *et al.* Rules for priming and inhibition of glycosaminoglycan biosynthesis; Probing the β 4GalT7 active site. *Chem. Sci.* **5**, 3501–3508 (2014).
108. Bruce, D., Cardew, E., Freitag-Pohl, S. & Pohl, E. How to Stabilize Protein: Stability Screens for Thermal Shift Assays and Nano Differential Scanning Fluorimetry in the Virus-X Project. *J. Vis. Exp.* **2019**, 1–11 (2019).
109. Schrock, R. R. High-Oxidation-State Molybdenum and Tungsten Alkylidyne Complexes. *Acc. Chem. Res.* **19**, 342–348 (1986).
110. Gregory, C. & Grubbs, R. H. Synthesis of Cycloalkenes via Alkylidene-Mediated Olefin Metathesis and Carbonyl Olefination. *J. Am. Chem. Soc.* **115**, 3800–3801 (1993).
111. Herndon, J. W. The chemistry of the carbon-transition metal double and triple bond: Annual survey covering the year 2008. *Coord. Chem. Rev.* **254**, 103–194 (2010).

112. Zieliński, G. K., Majteczak, J., Gutowski, M. & Grela, K. A Selective and Functional Group-Tolerant Ruthenium-Catalyzed Olefin Metathesis/Transfer Hydrogenation Tandem Sequence Using Formic Acid as Hydrogen Source. *J. Org. Chem.* **83**, 2542–2553 (2018).
113. Tao, Z. F., Sowin, T. J. & Lin, N. H. Synthesis of macrocyclic urea kinase inhibitors. *Synlett.* **118**, 2855–2858 (2007).
114. Malcolmson, S. J., Meek, S. J., Sattely, E. S., Schrock, R. R. & Hoveyda, A. H. Highly efficient molybdenum-based catalysts for enantioselective alkene metathesis. *Nature* **456**, 933–937 (2008).
115. Schrock, R. R. *et al.* Synthesis of Molybdenum Imido Alkylidene Complexes and Some Reactions Involving Acyclic Olefins. *J. Am. Chem. Soc.* **112**, 3875–3886 (1990).
116. Dias, E. L., Nguyen, S. B. T. & Grubbs, R. H. Well-defined ruthenium olefin metathesis catalysts: Mechanism and activity. *J. Am. Chem. Soc.* **119**, 3887–3897 (1997).
117. Sanford, M. S., Love, J. A. & Grubbs, R. H. Mechanism and activity of ruthenium olefin metathesis catalysts. *J. Am. Chem. Soc.* **123**, 6543–6554 (2001).
118. Ogba, O. M., Warner, N. C., O’Leary, D. J. & Grubbs, R. H. Recent advances in ruthenium-based olefin metathesis. *Chem. Soc. Rev.* **47**, 4510–4544 (2018).
119. Vougioukalakis, G. C. & Grubbs, R. H. Ruthenium-Based Heterocyclic Carbene-Coordinated Olefin Metathesis. *Chemical Reviews.* **110**, 1746–1787 (2010).
120. Hoye, T. R. *et al.* Total synthesis of peloruside a through kinetic lactonization and relay ring-closing metathesis cyclization reactions. *Angew. Chemie - Int. Ed.* **49**, 6151–6155 (2010).
121. Si, D. & Kaliappan, K. P. A concise total synthesis of (+)-cladospolide D. *Synlett* **23**, 2822–2826 (2012).
122. Kobayashi, Y. Total Synthesis of Macrosphelides. *有機合成化学協会誌.* **190**, 4–13

- (2004).
123. Dakas, P. Y., Jogireddy, R., Valot, G., Barluenga, S. & Winssinger, N. Divergent syntheses of resorcylic acid lactones: L-783277, LL-Z1640-2, and hypothemycin. *Chem. - A Eur. J.* **15**, 11490–11497 (2009).
 124. Toma, T., Kita, Y. & Fukuyama, T. Total Synthesis of (+)-Manzamine A. *J. Am. Chem. Soc.* **132**, 10233–10235 (2010).
 125. Shiina, I. *et al.* Enantioselective total synthesis of octalactin a using asymmetric aldol reactions and a rapid lactonization to form a medium-sized ring. *Chem. - A Eur. J.* **11**, 6601–6608 (2005).
 126. Shiina, I., Ibuka, R. & Kubota, M. A new condensation reaction for the synthesis of carboxylic esters from nearly equimolar amounts of carboxylic acids and alcohols using 2-methyl-6-nitrobenzoic anhydride. *Chem. Lett.* 286–287 (2002).
 127. Simonot, B. & Rousseau, G. Preparation of Seven-Membered and Medium-Ring Lactones by Iodo Lactonization. *J. Org. Chem.* **58**, 4–5 (1993).
 128. Lumbroso, A., Abermil, N. & Breit, B. Atom economic macrolactonization and lactonization via redox-neutral rhodium-catalyzed coupling of terminal alkynes with carboxylic acids. *Chem. Sci.* **3**, 789–793 (2012).
 129. Zhang, W. Heck macrocyclization in natural product total synthesis. *Nat. Prod. Rep.* **38**, 1109–1135 (2021).
 130. Geng, X., Miller, M. L., Lin, S. & Ojima, I. Synthesis of novel C2-C3'N-linked macrocyclic taxoids by means of highly regioselective heck macrocyclization. *Org. Lett.* **5**, 3733–3736 (2003).
 131. Carr, J. L. *et al.* Total synthesis of (±)-aspercyclide A and its C19 methyl ether. *Chem. Commun.* **46**, 1824–1826 (2010).
 132. Breslin, H. J. *et al.* Design, synthesis, and anaplastic lymphoma kinase (ALK) inhibitory

- activity for a novel series of 2,4,8,22-tetraazatetracyclo[14.3.1.1 3,7.1 9,13]docosa-1(20),3(22),4,6,9(21),10,12,16,18-nonaene macrocycles. *J. Med. Chem.* **55**, 449–464 (2012).
133. Shen, F. *et al.* Bismuth Acetate as a Catalyst for the Sequential Protodeboronation of Di- and Triborylated Indoles. *Org. Lett.* **18**, 1554–1557 (2016).
134. Nabi, A. A., Liyu, J., Lindsay, A. C. & Sperry, J. C4–H alkoxylation of 6-bromoindole and its application to the synthesis of breitfussin B. *Tetrahedron* **74**, 1199–1202 (2018).
135. Pesnot, T. & Wagner, G. K. Novel derivatives of UDP-glucose: Concise synthesis and fluorescent properties. *Org. Biomol. Chem.* **6**, 2884–2891 (2008).
136. Malkowski, S. N. *et al.* Design, modeling & synthesis of 1,2,3-triazole-linked nucleoside-amino acid conjugates as potential antibacterial agents. *Molecules* **22**, (2017).
137. Qu, G. R., Ren, B., Niu, H. Y., Mao, Z. J. & Guo, H. M. A novel one-step method for the synthesis of C-5-substituted O 6,5'-cyclopyrimidine nucleoside analogues in ammonia water. *J. Org. Chem.* **73**, 2450–2453 (2008).
138. Gao, Y., Osman, S. & Koide, K. Total synthesis and biological studies of TMC-205 and analogues as anticancer agents and activators of SV40 promoter. *ACS Med. Chem. Lett.* **5**, 863–867 (2014).
139. Pubill-Ulldemolins, C. *et al.* Heck Diversification of Indole-Based Substrates under Aqueous Conditions: From Indoles to Unprotected Halo-tryptophans and Halo-tryptophans in Natural Product Derivatives. *Chem. - A Eur. J.* **25**, 10866–10875 (2019).
140. Liu, Z. *et al.* Selective and efficient synthesis of trans-arylvinylboronates and trans-hetarylvinylboronates using palladium catalyzed cross-coupling. *New J. Chem.* **41**, 3172–3176 (2017).
141. Roy, V., Colombeau, L., Zerrouki, R. & Krausz, P. One step selective 5'-O-allylation of thymidine using microwave or ultrasound activation. *Carbohydr. Res.* **339**, 1829–1831

- (2004).
142. Pisár, M. *et al.* Modification of boc-protected CAN508 via acylation and suzuki-miyaura coupling. *Molecules* **23**, 1–14 (2018).
143. Yamashita, T., Kawai, N., Tokuyama, H. & Fukuyama, T. Stereocontrolled Total Synthesis of (-)-Eudistomin C. *J. Am. Chem. Soc.* **127**, 15038–15039 (2005).
144. Xue, F. & Silverman, R. B. An alkoxide anion-triggered tert-butyloxycarbonyl group migration. Mechanism and application. *Tetrahedron Lett.* **51**, 2536–2538 (2010).
145. Lawton, G. R. *et al.* Analogues of 2-aminopyridine-based selective inhibitors of neuronal nitric oxide synthase with increased bioavailability. *Bioorganic Med. Chem.* **17**, 2371–2380 (2009).
146. Dominique, P., Schnurr, M. & Lewandowski, B. Chiral recognition of amino-acid esters by a glucose-derived macrocyclic receptor. *Chem. Commun.* **57**, 3476–3479 (2021).
147. Tsuchimoto, T., Iketani, Y. & Sekine, M. Zinc-catalyzed dehydrogenative N-silylation of indoles with hydrosilanes. *Chem. - A Eur. J.* **18**, 9500–9504 (2012).
148. Martin, J. S., Mackenzie, C. J. & Gilbert, I. H. Synthesis of a Series of Diaminoindoles. *J. Org. Chem.* **86**, 11333–11340 (2021).
149. Teste, K. *et al.* Solvent-controlled regioselective protection of 5'-O-protected thymidine. *Carbohydr. Res.* **343**, 1490–1495 (2008).
150. Liu, J., Leonard, P., Müller, S. L., Daniliuc, C. & Seela, F. Nucleoside macrocycles formed by intramolecular click reaction: Efficient cyclization of pyrimidine nucleosides decorated with 5'-azido residues and 5-octadiynyl side chains. *Beilstein J. Org. Chem.* **14**, 2404–2410 (2018).
151. Sun, J. *et al.* Synthesis and anti-HIV activity of triazolo-fused, medium-sized cyclic nucleoside analogs prepared by an intramolecular huisgen 1,3-dipolar cycloaddition. *Helv. Chim. Acta* **97**, 733–743 (2014).

152. Van Brabandt, W., Vanwalleghem, M., D'Hooghe, M. & De Kimpe, N. Asymmetric synthesis of 1-(2- and 3-haloalkyl)azetididin-2-ones as precursors for novel piperazine, morpholine, and 1,4-diazepane annulated beta-lactams. *J. Org. Chem.* **71**, 7083–7086 (2006).
153. Otter, B. A., Falco, E. A. & Fox, J. J. Nucleosides. LVIII. Transformations of Pyrimidine Nucleosides in Alkaline Media. III. The Conversion of 5-Halogenouridines into Imidazoline and Barbituric Acid Nucleosides. *J. Org. Chem.* **34**, 1390–1396 (1969).
154. Otter, B. A., Falco, E. A. & Fox, J. J. Nucleosides. LII. Transformations of Pyrimidine Nucleosides in Alkaline Media. I. The Conversion of 5-Halogenoarabinosyluracils into Imidazoline Nucleosides. *J. Org. Chem.* **33**, 3593–3600 (1968).
155. Camacho-García, J. *et al.* Synthesis and complementary self-association of novel lipophilic π -conjugated nucleoside oligomers. *Org. Biomol. Chem.* **13**, 4506–4513 (2015).
156. Receptors, P. Y., El-tayeb, A., Qi, A. & Mu, C. E. Synthesis and Structure - Activity Relationships of Uracil Nucleotide Derivatives and Analogues as Agonists at Human P2Y₂, P2Y₄, and P2Y₆ Receptors. *J. Med. Chem.* **49**, 7076–7087 (2006).
157. Dolomanov, O. V., Bourhis, L. J., Gildea, R. J., Howard, J. A. K. & Puschmann, H. OLEX2: A complete structure solution, refinement and analysis program. *J. Appl. Crystallogr.* **42**, 339–341 (2009).
158. Sheldrick, G. M. SHELXT - Integrated space-group and crystal-structure determination. *Acta Crystallogr. Sect. A Found. Crystallogr.* **71**, 3–8 (2015).
159. Sheldrick, G. M. Crystal structure refinement with SHELXL. *Acta Crystallogr. Sect. C Struct. Chem.* **71**, 3–8 (2015).
160. Thorsheim, K. *et al.* Hydroxylated oxanes as xyloside analogs for determination of the minimal binding requirements of β 4GalT7. *Tetrahedron Lett.* **58**, 3466–3469 (2017).

161. Crescioli, S. *et al.* Engineering and stable production of recombinant IgE for cancer immunotherapy and AllergoOncology. *J. Allergy Clin. Immunol.* **141**, 1519-1523.e9 (2018).
162. McCraw, A. J. *et al.* Generation and Characterization of Native and Sialic Acid-Deficient IgE. *Int. J. Mol. Sci.* **23**, (2022).
163. Schrodinger Release 2021-1: Maestro, Schrodinger, LLC, New York, NY, 2021-1.
164. Friesner, R. A. *et al.* Glide: A New Approach for Rapid, Accurate Docking and Scoring. 1. Method and Assessment of Docking Accuracy. *J. Med. Chem.* **47**, 1739–1749 (2004).
165. Jo, S., KIM, T., Iyer, R. S. & Im, W. Software News and Updates CHARMM-GUI: A Web-Based Graphical User Interface for CHARMM. *J. Comput. Chem.* **29**, 1859–1865 (2008).
166. Lee, J. *et al.* CHARMM-GUI Input Generator for NAMD, GROMACS, AMBER, OpenMM, and CHARMM/OpenMM Simulations Using the CHARMM36 Additive Force Field. *J. Chem. Theory Comput.* **12**, 405–413 (2016).
167. Lee, J. *et al.* CHARMM-GUI supports the Amber force fields. *J. Chem. Phys.* **153**, (2020).
168. Götz, A. W. *et al.* Routine microsecond molecular dynamics simulations with AMBER on GPUs. 1. generalized born. *J. Chem. Theory Comput.* **8**, 1542–1555 (2012).
169. Salomon-Ferrer, R., Case, D. A. & Walker, R. C. An overview of the Amber biomolecular simulation package. *Wiley Interdiscip. Rev. Comput. Mol. Sci.* **3**, 198–210 (2013).
170. Paquet, E. & Viktor, H. L. Molecular dynamics, monte carlo simulations, and langevin dynamics: A computational review. *Biomed Res. Int.* **2015**, (2015).
171. Humphrey, W., Dalke, A. & Schulten, K. Sartorius products. *J. Mol. Graph.* **14**, 33–38 (1996).

172. Phillips, J. C. *et al.* Scalable molecular dynamics with NAMD. *J. Comput. Chem.* **26**, 1781–1802 (2005).

8 Appendix (^1H and ^{13}C NMR spectra)